GLOBAL AND REGIONAL TRENDS OF AEROSOL OPTICAL THICKNESS DERIVED USING SATELLITE- AND GROUND-BASED OBSERVATIONS

vorgelegt von

Jongmin Yoon

vom Fachbereich Physik und Elektrotechnik

der Universität Bremen

Universität Bremen

Bremen, 19.04.2012

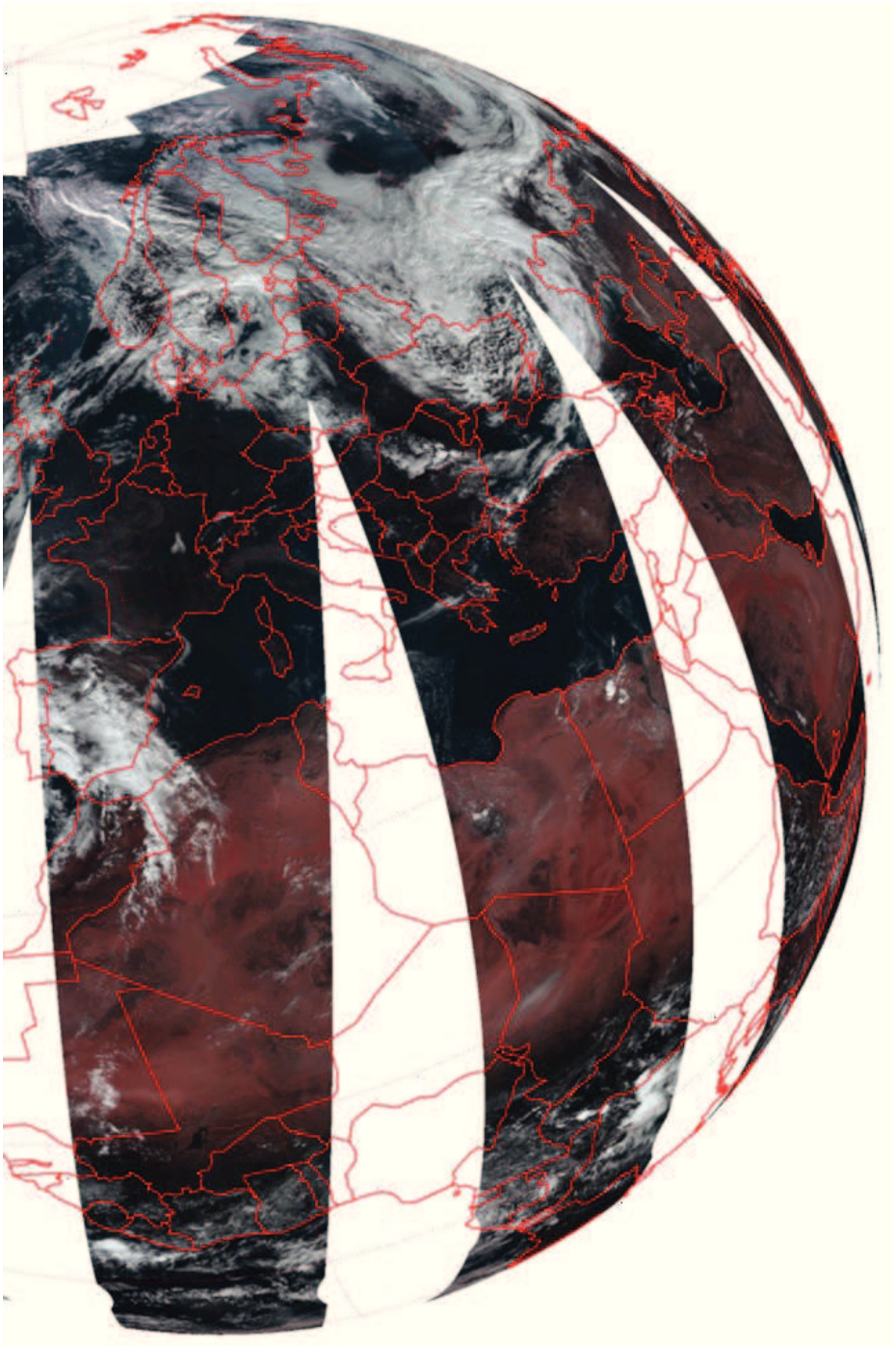

** RGB composite image from SeaWiFS observation at 12/Oct./2001.*

Global and regional trends of Aerosol Optical Thickness derived using satellite- and ground-based observations

Dissertation von Jongmin Yoon

vom Fachbereich für Physik und Elektrotechnik der Univerität Bremen zur Erlangung des akademischen Grades eines Doktor der Naturwissenschaften (Dr. rer. nat.) genehmigte Dissertation

Ausgabetermin:	01.03.2009
Abgabetermin:	19.04.2012
Zuständige Hochschullehrer:	Prof. J. P. Burrows, IUP
	Prof. J. Notholt, IUP

Institut für Umweltphysik
Fachbereich Physik/Elektrotechnik (FB 1)
Postfach 33 04 40
D-28334 Bremen

Ich versichere, dass ich die Dissertation selbständig verfaβt und keine anderen als die angegebenen Quellen und Hilfsmittel benutzt habe.

Bremen, 19.04.2011

. . . . . .

Abstract

Atmospheric aerosol plays a critical role for human health, air quality, long range transport of pollution, and the Earth's radiative balance, thereby influencing global climate change. To test our scientific understanding and provide an evidence base for policymakers, long-term temporal changes of local, regional, and global aerosols are needed. Remote sensing from satellite borne and ground based observations offers unique opportunities to provide such data. However, only a few studies have discussed the limitations, associated with unrepresentative sampling originating from large/persistent cloud disturbance and limited/different sampling (limited orbital periods and different sampling times) in the trend analysis. Using a linear weighted model, the long-term trends of global AOTs from various polar orbiting satellites and ground observations: MODIS (aboard Terra), MISR (Terra), SeaWiFS (OrbView-2), MODIS (Aqua), and AERONET have been analyzed. In this manner, the present study attempts to minimize the influence of unrepresentative sampling in the trend analysis. Throughout terrestrial and marine regions, temporal increase of cloud-free AOTs were dominat over the globe (GL), northern (NH), and southern hemisphere (SH) (up to +0.00348±0.00185 for GL, +0.00514±0.00272 for NH, and +0.00232±0.00124 yr^{-1} for SH). Generally, consistently in all observations, the weighted trends over Eastern US and OECD Europe showed a strong decreasing AOT (up to -0.00376±0.00174 for Eastern US and -0.00530±0.00304 yr^{-1} for OECD Europe) attributed to the recent environmental legislation and resulting regulation of emissions. A significant increase was observed over Saharan/Arabian deserts, South, and East Asia (up to +0.00618±0.00326, +0.01452±0.00615, and +0.01939±0.00986 yr^{-1} respectively). These in part dramatic increases are caused by the enhanced amount of aerosol transported/emitted from industrialization, urbanization,

deforestation, desertification, and climate change. Overall large/persistent cloud disturbance all year round and the limited/different sampling of polar orbiting satellites represent a challenge, which has been addressed successfully in this study for the accurate determination of aerosol amount and its trends.

List of publications

a. Articles in peer-reviewed journals

As first author:

1. **Yoon, J.** , Vountas, M., von Hoyningen-Huene, W., Chang, D. Y., and Burrows, J. P.: Trend analysis of global AOT derived from polar orbiting satellites: Terra (MODIS and MISR), OrbView-2 (SeaWiFS), and Aqua (MODIS), *Geophysical Research Letters*, in preparation, 2012.
2. **Yoon, J.**, von Hoyningen-Huene, W., Kokhanovsky, A. A., Vountas, M., and Burrows, J. P.: Trend analysis of the Aerosol Optical Thickness and Ångström Exponent derived from the global AERONET spectral observations, *Atmospheric Measurement Techniques*, **5**, 1271-1299, doi:10.5194/amt-5-1271-2012, 2012.
3. **Yoon, J.** , von Hoyningen-Huene, W., Vountas, M., and Burrows, J. P.: Analysis of linear long-term trend of Aerosol Optical Thickness derived from SeaWiFS using BAER over Europe and South China, *Atmospheric Chemistry and Physics*, **11**, 12149-12167, doi:10.5194/acp-11-12149-2011, 2011.
4. **Yoon, J. -M.**, Kim, J., Lee, J. H., Cho, H. K., Shon, B. J., and Ahn, M. H.: Retrieval of Aerosol Optical Depth over East Asia from a Geostationary Satellite, MTSAT-1R, *Journal of the Korean Meteorological Society*, **43**, 133-142, 2007.

As co-author:

5. von Hoyningen-Huene, W., **Yoon, J.**, Vountas, M., Istomina, L. G., Rohen, G., Dinter, T., Kokhanovsky, A. A., and Burrows, J. P.: Retrieval of spectral aerosol optical thickness over land using ocean colour sensors MERIS and SeaWiFS, *Atmospheric Measurement Techniques*, **4**, 151-171, doi:10.5194/amt-4-151-2011, 2011.
6. Kim, J., **Yoon, J. -M.**, Ahn, M. H., Sohn, B. J., and Li, H. S.: Retrieving aerosol optical depth using visible and mid-IR channels from geostationary satellite MTSAT-1R, *International Journal of Remote Sensing*, **29**, 6179-6190, doi:10.1080/01431160802175553, 2008.
7. Yoo , J. M., Jeong, M. J., Lee, K. T., Kim, J., Rhee, J. E., Hur, Y. M., Kim, B. M., Lee, Y. G., Lee, J. H., **Yoon, J. M.**, and Lee, W. H.: Intercomparison of shortwave radiative transfer models for aerosol-laden atmospheres, *The Journal of the Korean Earth Science Society*, **29**, 128-139, 2008.
8. Yoo, J. M., Jeong, M. J., Lee, K. T., Kim, J., Ho, C. H., Ahn, M. H., Hur, Y. M., Rhee, J. E., Yoo, H. L., Chung, C. Y., Shin, I. C., Choi, Y. S., Kim, Y. M., Lee, Y. G., Lee, J. H., **Yoon, J. M.**, and Lee, W. H.: Intercomparison of shortwave radiative transfer models for a Rayleigh atmosphere, *The Journal of the Korean Earth Science Society*, **28**, 298-310, 2007.

b. Selected oral and poster presentations

1. **Jongmin Yoon,** Marco Vountas, Wolfgang von Hoyningen-Huene, Dong Yeong Chang, and John P. Burrows, Global Trend Analysis of MODIS (Terra), MISR (Terra), SeaWiFS (OrbView-2), and MODIS (Aqua) AOTs, ATMOS 2012: Advances in Atmospheric Science and Applications, Bruges, Belgium, 18 - 22 June, 2012.
2. **Jongmin Yoon,** Marco Vountas, Wolfgang von Hoyningen-Huene, Dong Yeong Chang, and John P. Burrows, Trend Analysis of Global AOT based on various Polar Orbiting Satellites Observations: MODIS (Terra), MISR (Terra), SeaWiFS (OrbView-2), and MODIS (Aqua), European Geosciences Union General Assembly 2012, Vienna, Austria, 22 - 27 April, 2012.
3. Luca Lelli, **Jongmin Yoon,** Alexander A. Kokhanovsky. Vladimir Rozanov, Marco Vountas, and John P. Burrows, Global and regional trends of cloud properties derived by hyperspectral measurements in the O2 A-band, European Geosciences Union General Assembly 2012, Vienna, Austria, 22 - 27 April, 2012.
4. John P. Burrows, Andreas Richter, Andreas Hilboll, Marco Vountas, **Jongmin Yoon**, and Wolfgang von Hoyningen-Huene, The use of satellite remote sensing of trace gases and aerosols to study megacities within CITYZEN, European Geosciences Union General Assembly 2012, Vienna, Austria, 22 - 27 April, 2012.
5. **Jongmin Yoon,** Marco Vountas, Wolfgang von Hoyningen-Huene, Dong Yeong Chang, and John P. Burrows, Trend Analysis of Global AOT derived from Polar Orbiting Satellites Observations: Terra (MODIS and MISR), OrbView-2 (SeaWiFS), and Aqua (MODIS), Planet Under Pressure 2012, London, United Kingdom, 26 - 29 March, 2012.
6. Marco Vountas, **Jongmin Yoon,** Wolfgang von Hoyningen-Huene, and John P. Burrows, Refined Long-Term Analysis of Aerosol Optical Thickness from Satellite Retrievals over Megacities, Planet Under Pressure 2012, London, United Kingdom, 26 - 29 March, 2012.
7. **Jongmin Yoon**, Wolfgang von Hoyningen-Huene, Marco Vountas, and John P. Burrows, Linear Long-term Trend of Aerosol Optical Thickness derived from SeaWiFS and MERIS using BAER over Several Regions, European Geosciences Union General Assembly 2011, Vienna, Austria, 03 - 08 April, 2011.
8. **Jongmin Yoon**, Wolfgang von Hoyningen-Huene, Alexander A. Kokhanovsky, Marco Vountas, and John P. Burrows, Trend Analysis of the Aerosol Optical Thickness and Ångström Exponent Derived from the Global AERONET Spectral Observations, European Geosciences Union General Assembly 2011, Vienna, Austria, 03 - 08 April, 2011.
9. Marco Vountas, Wolfgang von Hoyningen-Huene, **Jongmin Yoon**, and John P. Burrows, Analysis of Aerosol Optical Thickness Retrievals from Satellite Data over large urban Agglomerations, European Geosciences Union General Assembly 2011, Vienna, Austria, 03 - 08 April, 2011.
10. **Jongmin Yoon**, Wolfgang von Hoyningen-Huene, Alexander A. Kokhanovsky, Marco Vountas, and John P. Burrows, Statistical Analysis of Aerosol Optical Thickness from Satellite Retrievals using BAER and AERONET over Several Regions, DPG Spring Meeting of the Section AMOP, Hannover, Germany, March 08 - 12, 2010.
11. **Jongmin Yoon**, Wolfgang von Hoyningen-Huene, Marco Vountas, and John P. Burrows, Linear Long-term Trend of Aerosol Optical Thickness from Satellite Retrievals using BAER over Several Regions, European Geosciences Union General

Assembly 2010, Vienna, Austria, May 02 - 07, 2010.

12. **Jongmin Yoon**, Wolfgang von Hoyningen-Huene, Alexander A. Kokhanovsky, and John P. Burrows, Climatology of Atmospheric Aerosol derived from AERONET Observations, European Geosciences Union General Assembly 2010, Vienna, Austria, May 02 - 07, 2010.
13. Wolfgang von Hoyningen-Huene, Cornelia Martinecz, **Jongmin Yoon**, Alexander A. Kokhanovsky, and John P. Burrows, Iceland Volcano Ash Cloud over Bremen, European Geosciences Union General Assembly 2010, Vienna, Austria, May 02 - 07, 2010.
14. Marco Vountas, Wolfgang Von Hoyningen-Huene, **Jongmin Yoon**, John P. Burrows, Long-term Analysis of Aerosol Optical Thickness from Satellite Retrievals over selected large agglomerations, 38th COSPAR Scientific Assembly, Bremen, Germany, July 18 - 24, 2010.
15. **Jongmin Yoon**, Wolfgang von Hoyningen-Huene, Marco Vountas, and John P. Burrows, Linear Long-term Trend of Aerosol Optical Thickness using Bremen AErosol Retrieval (BAER) , The 3rd Asia Pacific Radiation Symposium, Seoul, South Korea, August 25 - 28, 2010.
16. Mijin Kim, Jhoon Kim, **Jongmin Yoon**, and Jaehwa Lee, AOD Retrieval from Geostationary Satellite with MODIS BRDF, The 3rd Asia Pacific Radiation Symposium, Seoul, South Korea, August 25 - 28, 2010.
17. **Jongmin Yoon**, Jhoon Kim, and Mijin Kim, Satellite-based algorithm for retrieving Aerosol Optical Depth (AOD) using geostationary satellites (GMS-5 and MTSAT-1R), Determination of Atmospheric Aerosol Properties Using Satellite Measurements, Bad Honnef, Germany, August 16 - 19, 2009.
18. Jhoon Kim, Jaehwa Lee, **Jongmin Yoon** and Dong Wu, Background aerosol optical depth from AERONET and MISR, MISR Data Users Science Symposium, Pasadena, CA, USA, December 10 - 11, 2009.

Contents

List of figures

List of tables

1. Introduction

1.1 Motivation and objectives

Aerosol is defined as a suspension of liquid/solid particles in air [Burrows et al., 2011]. The airborne aerosols are minor constituents of the atmosphere by mass, but a critical component in terms of impacts on the human health, Earth's radiative balance, global climate change [Global Climate Observing System (GCOS), 2006; World Health Organization (WHO), http://www.who.int/en/; United Nations Economic Commission for Europe (UNECE), http://www.unece.org/env/lrtap/; Intergovernmental Panel on Climate Change (IPCC), http://www.ipcc.ch/; United Nations Framework Convention on Climate Change (UNFCCC), http://unfccc.int/2860.php]. They are generally classified as two types (i.e., natural and anthropogenic) by composition of coarse- and fine- dominant sources (e.g., mineral dust, industrial pollutants, sea-salt, smoke, secondary aerosol, biological aerosol, and volcanic ash). Recently, a considerable temporal variation of anthropogenic and natural aerosols caused by human activity and climate change has been an issue [WHO, 1987, 2000, 2005]. Especially, the anthropogenic aerosols from rapid urbanization and industrialization in/around newly industrializing countries are identified as the most uncertain climate forcing constituent [IPCC, 2007]. Therefore, long-term trend analyses of global and regional aerosols using remote sensing from ground-based and satellite borne observations are needed to monitor the global aerosols for our scientific understanding and regulate the emission of anthropogenic aerosols as air pollutants for environmental control.

Aerosol was described as a mysterious phenomenon (i.e., "土雨" in Chinese, which means dust-fall or dust-rain in English) in the oriental records in the past [Chun, 2000]. Indeed, some aerosols have somewhat beneficial effects to human. For instances, the calcite ($CaCO_3$)

content in mineral dusts can neutralize the acid soil and rain when dissolved in water [Wang et al., 2002; Kikuchi et al., 2006; Larssen and Carmichael, 2000]. Another example is that the deposition of volcanic aerosols enhances the biological activity in the marine environment by providing micronutrients for some oceanic phytoplankton species [Arimoto et al, 2002; Frogner Kockum et al., 2006]. However, despite these advantages, the aerosol as an air pollutant generally has a bad influence in human health and life.

Fig. 1.1 is the British Parliament painted by Claude Monet (1840-1926) [http://www.newscientist.com]. He potentially considered the Victorian smog and atmospheric states in this painting [Baker and Thornes, 2006]. The smog is a typical catastrophe of the air pollution severely influencing human health. As well-known, the "Great Smog" during December 1952 in London mostly from coal combustion made approximately 100,000 people get pulmonary and cardiovascular diseases and took away the lives of people over 12,000. This terrible accident was enough to stir particularly in environmental research,

Fig. 1.1 Houses of Parliament painted by Claude Monet (1840-1926) [http://www.newscientist.com]. The orange sky is caused by the scattering out of short wavelength components in the solar light.

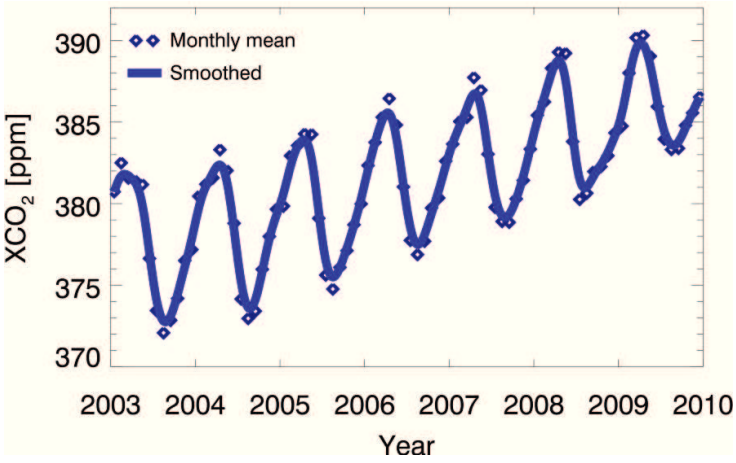

Fig. 1.2 Column averaged mixing ratio of atmospheric carbon dioxide (CO_2) over the northern hemisphere during 2003-2009, which is retrieved from Scanning Imaging Absorption Spectrometer for Atmospheric CHartographY (SCIAMACHY) measurements [http://www.iup.uni-bremen.de/sciamachy/].

government regulation, and public awareness of the relationship between air quality and health [Bell et al., 2004]. Furthermore, more recent research found that particulate matter can adversely affects on human affective and cognitive processes by aerosols [Fonken et al., 2011]. Despite of these threats, many people are still exposed to serious air pollution, especially in the largest urban agglomerations (aka, megacity) [Léon et al., 1995, 2001; Ortore and Francione, 2008].

Recently, climate change has been attracting public attention because the cost of damage caused by severe and extreme weather events are increasing rapidly and a dramatic global warming continues to threaten human survival. Apparently, various greenhouse gases and aerosols are the primary agents in forcing climate change [GCOS, 2011]. The greenhouse gases (typically, H_2O, CO_2, CH_4, N_2O, and O_3), which are released into the atmosphere by burning fossil fuels, increase the Earth temperature. Fig. 1.2 illustrates the long-term time series of column averaged mixing ratio of atmospheric carbon dioxide (CO_2), which have been increasing in recent. Based on such observations of the greenhouse gases, many scientists forecasted a temperature rise of 2.5° to 10°F over the next century [IPCC, 2007] due to the positive radiative forcing of the greenhouse gases (see Fig. 1.3). The rising temperatures bring a significant reduction in Earth's albedo by reducing glaciers and snow

cover. Despite of little contribution, soot particles on snow can not only decrease the snow albedo, but also affect snowmelt [Hansen et al., 2000; Hansen and Nazarenko, 2004]. A positive feedback through the chain of phenomena makes the global temperature more rapidly increased. On the other side of the coin, aerosols generally have a cooling effect (negative feedback) on the Earth radiative system. Firstly, aerosols directly reflect (or absorb, but little) incoming solar radiation to space (for example: see negative radiative forcing in Fig. 1.3). For instance, in June 1991, the massive ashes from volcanic eruption of Mountain Pinatubo (the second largest volcanic eruption of the twentieth century) reduced the global temperature up to 0.5°C at the surface and 0.6°C in the troposphere [Parker et al., 1996; Ward, 2009]. A significant increase in sulfur emissions from Chinese economic expansion since 1998 could be a possible explanation why global surface temperatures did not rise rapidly in the past decade [Kaufmann et al., 2011]. Secondly, aerosols can influence the cloud formation and persistency [GCOS, 2011], so that a higher cloud reflectivity contributes to atmospheric cooling [Twomey, 1977; Ackerman et al., 2000; Haywood and Shine, 1997;

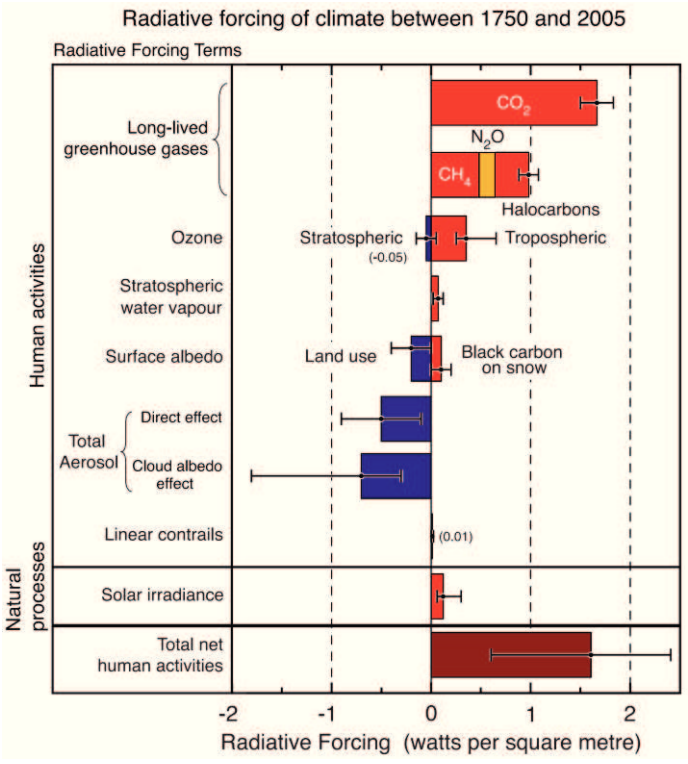

Fig. 1.3 Summary of the principal components of the radiative forcing on climate change. All these radiative forcings result from one or more factors that affect climate and are associated with human activities and natural processes [IPCC, 2007].

Haywood and Boucher, 2000; Penner et al., 2001; Ramanathan et al., 2001] (see Fig. 1.3).

Certainly, the Earth has the ability to maintain equilibrium in terms of greenhouse gases. However, the climate change has been accelerated due to huge human activity losing the balance between sources and sinks of greenhouse gases. In order to regulate greenhouse gas emissions, the "Kyoto Protocol" was adopted on 11 December 1997. Under the Protocol, various studies have been performed using satellite observation, which is one of the most effective to detect the global gas changes. Aerosol in the atmosphere is a major source of uncertainty for the gas retrievals with several percent of error because it interacts with radiation [Leitão et al., 2010; Butz et al., 2009]. In conclusion, leading researches about the atmospheric aerosols can assist in monitoring the global change of greenhouse gas.

The ground observation (e.g., AErosol RObotic NETwork (AERONET)) aims to validate satellite retrievals because it has continuously long-term data based on fine temporal resolution as well as high retrieval accuracy [Holben et al., 1998, 2001; Eck et al., 1999; Smirnov et al., 2000]. Additionally, it could provide various aerosol optical properties (e.g., volume size distribution, complex index of refraction, phase functions, Single Scattering Albedo (SSA)), which are inverted using measurements at all available wavelengths and scattering angles [Dubovik and King, 2000; Dubovik et al., 2000, 2002a, 2002b, 2006; Sinyuk et al., 2007]. In despite of these advantages, both small spatial coverage and different observation history at each station are hampering progress in the research of global aerosols.

Recently, abundant satellite retrievals based on well-validated aerosol retrieval algorithms and well-calibrated sensors (e.g., Sea-viewing Wide Field-of-view Sensor (SeaWiFS), MEdium Resolution Imaging Spectrometer (MERIS), Multi-angle Imaging SpectroRadiometer (MISR), and Moderate Resolution Imaging Spectroradiometer (MODIS)) have contributed significantly to the understanding of global aerosols in various studies [Li et al., 2009; Yu et al., 2009; Zhang and Reid, 2010; Street et al., 2009; Karnieli et al., 2009;

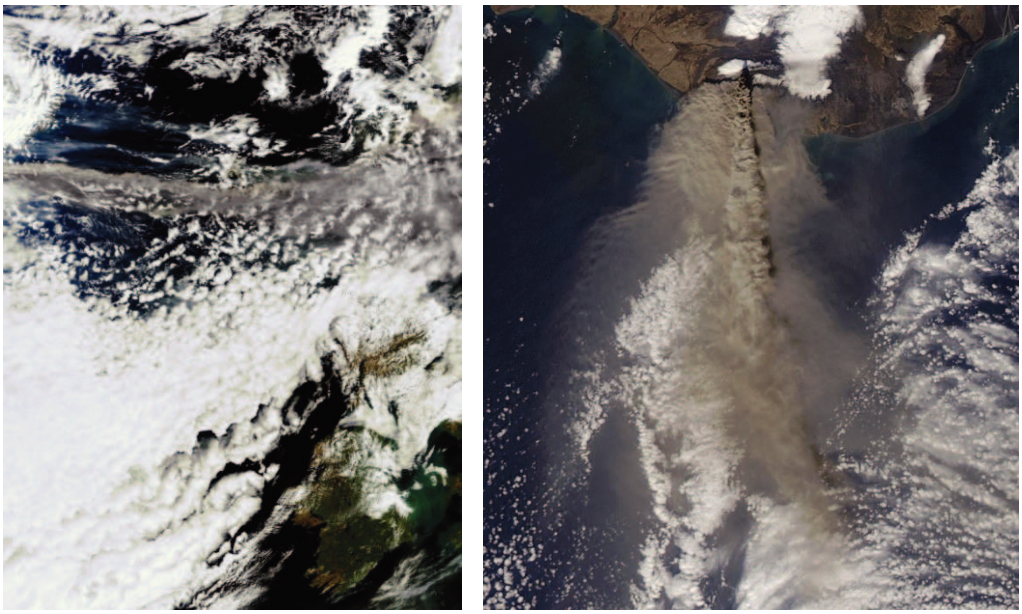

Fig. 1.4 RGB composite images of Iceland's Eyjafjallajökull Volcano observed from Medium Resolution Imaging Spectrometer (MERIS) on 15 April 2010 (left) and Moderate Resolution Imaging Spectroradiometer (MODIS) on 17 April 2010 (right).

Mishchenko et al., 2007; Mishchenko and Geogdzhayev, 2007; Zhao et al., 2008; Massie et al., 2004; Remer et al., 2005; Kaufman et al., 1997a; Higurashi and Nakajima, 1999; Mishchenko et al., 1999a; Jeong et al., 2005; Higurashi et al., 2000; Stowe et al., 1999; Heidinger et al., 2004; Torres et al., 2002; DiGirolamo and Wilson, 2003; Martonchik et al., 2004; Diner et al., 2006; Martins et al., 2002; von Hoyningen-Huene et al., 2011; Yoon et al., 2007; Kim et al., 2008]. In particular, long-term data from a series of satellite observations are good for monitoring as well as modeling regional and global climate change, atmospheric circulation, and mesoscale weather forecasting. Therefore, for improving the capability of model simulations, GCOS (2007) suggests the guideline for aerosol optical depth derived from the satellite observations such as an accuracy: 0.01, spatial and temporal resolution: 1 km horizontal resolution and daily observing cycle, and stability: 0.005/decade. Although the present aerosol products from space-born instrument do not fully meet the target requirements due to the uncertainties caused by instrument calibration and assumptions in the

algorithms [Li et al., 2009; Higurashi and Nakajima, 1999; Ignatov and Stowe, 2002], its long-term observation based on a broad geographical coverage can provide the most appropriate data for monitoring the temporal variations of global aerosols. Fig. 1.4 gives two example pictures of Iceland's Eyjafjallajökull Volcano eruption observed by the satellites observations. Oxford Economics (2011) reported that Air Travel disruptions caused by the eruption cost nearly $5 billion in global Gross Domestic Product (GDP). This kind of natural disaster only can be monitored by the space-born satellites, and thereby it is possible to predict its global impact. Therefore, the present study used multiple satellite observations for trend analysis of global/regional aerosols, and validated them with the trends derived from AERONET observations at global stations in order to overcome the shortcoming in satellite retrievals.

1.2 State of knowledge

The retrieval technique using satellite observations is potentially one of the most effective ways to obtain the global distribution and temporal variation of aerosol amounts. Several algorithms using, for example, Advanced Very High Resolution Radiometer (AVHRR), Total Ozone Mapping Spectrometer (TOMS)/Ozone Monitoring Instrument (OMI), Along Track Scanning Radiometer (ATSR), Multi-angle Imaging SpectroRadiometer (MISR), Moderate Resolution Imaging Spectroradiometer (MODIS), and Sea-viewing Wide Field-of-view Sensor (SeaWiFS) on polar-orbiting satellites [Remer et al., 2005; Kaufman et al., 1997a; Higurashi and Nakajima, 1999; Mishchenko et al., 1999; Jeong et al., 2005; Higurashi et al., 2000; Stowe et al., 1999; Heidinger et al., 2004; Torres et al., 2002; Veefkind et al., 1998; Grey et al., 2006; Thomas et al., 2009; Di Girolamo and Wilson, 2003; Martonchik et al., 2004; Diner et al., 2006; Martins et al., 2002; Robbinson et al., 2003; Wang and Shi, 2005] have been developed to retrieve the global Aerosol Optical Thickness (AOT), which is defined as a term of aerosol transparency in Appendix B. Up to now AVHRR, TOMS/OMI, ATSR, MISR, and MODIS have been used in the analysis of global and regional aerosol

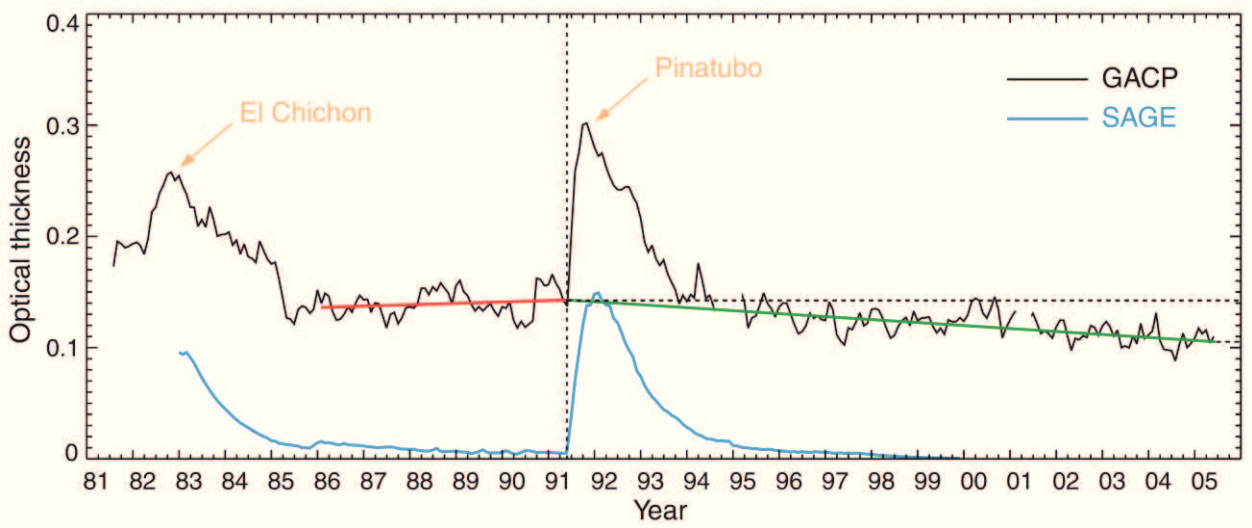

Fig. 1.5 Global Aerosol Climatology Project (GACP) record of the globally averaged column AOT over the oceans, and Stratospheric Aerosol and Gas Experiment (SAGE) record of the globally averaged stratospheric AOT [Mishchenko et al., 2007].

Tab. 1.1 List of references to AOT trend analysis.

References	Sensor/Model /Instrument	Research Regions	Limitations
Mishchenko et al. (2007) **Mishchenko and Geogdzhayev (2007)** **Zhao et al. (2008)**	AVHRR	Global oceans	· No onboard calibration device · Orbital drift · Only ocean · Sampling bias · No consideration of cloud disturbance · No validation with ground observation
Zhang and Reid (2010)	MODIS, MISR	Global oceans	· Only ocean · Sampling bias · No consideration of cloud disturbance · No validation with ground observation
Yu et al. (2009)	MODIS	Global oceans	· Only ocean · Sampling bias · No consideration of cloud disturbance · No validation with ground observation
Kishcha et al. (2009)	MODIS, MISR	Global oceans	· Only ocean · Sampling bias · No consideration of cloud disturbance · No validation with ground observation
Thomas et al. (2010)	ATSR-2	Global oceans	· Only ocean · Sampling bias · No consideration of cloud disturbance · No validation with ground observation
Papadimas et al. (2008)	MODIS Sunphotometer in-situ measurement	Regional ocean (Mediterranean basin)	· Only regional ocean · Sampling bias · No consideration of cloud disturbance
Massie et al. (2004)	TOMS	Global regions	· Poor retrieval accuracy over land · Sampling bias · No consideration of cloud disturbance · No validation with ground observation
Xie and Xia (2008)	TOMS	north China	· Poor retrieval accuracy over land · Only specific regions · Sampling bias · No consideration of cloud disturbance · No validation with ground observation
Karnieli et al. (2009)	MODIS, Sunphotometer, in-situ measurement	Central/ Eastern Europe	· Only specific regions · Sampling bias · No consideration of cloud disturbance
de Meij et al. (2010)	MODIS, MISR, Sunphotometer	Global regions	· Sampling bias · No consideration of cloud disturbance
Koukouli et al. (2010)	MODIS	Southern Balkan/Eastern Mediterranean	· Only specific regions · Sampling bias · No consideration of cloud disturbance · No validation with ground observation
Kaskaoutis et al. (2011)	MODIS	South Asia	· Only specific regions · Sampling bias · No consideration of cloud disturbance · No validation with ground observation
Dey and Di Girolamo (2011)	MISR	Indian subcontinent	· Only specific regions · Sampling bias · No consideration of cloud disturbance · No validation with ground observation
Streets et al. (2009)	GOCART model	Global regions	· Simulation limits · No validation with satellite/ground observations
Leibensperger et al. (2011)	GEOS-Chem CTM, GISS GCM	US	· Simulation limits · Only specific regions · No validation with satellite/ground observations
Lei et al. (2011)	PM/TSP simulation	China	· Simulation limits · Only specific regions · No validation with satellite/ground observations

trends because they have continuous and long-term observation histories. Mishchenko et al. (2007) and Mishchenko and Geogdzhayev (2007) derived aerosol trends from long-term satellite records, utilizing AVHRR channels 1 and 2 over global oceans. In their publications, they provided a comprehensive data set and global/regional trends of tropospheric aerosol from August 1981 to June 2005 (see Fig. 1.5). They concluded that the decrease of the global AOT in the troposphere may have contributed to the upward trend in surface solar fluxes. As a result, the increasing incoming sunlight on the ground surface more evidently supported the climate warming during the past decade. Zhao et al. (2008) provided a more elaborate analysis for global and regional AOT trends using the AVHRR Pathfinder Atmosphere (PATMOS) climate data set. They added uncertainty tests (i.e., the effects of grid size, uncertainty in aerosol retrieval algorithm, and sensor calibration) to the AOT trend analysis and found that the difference between grid sizes when comparing monthly averaged AOT can be neglected while improper assumptions in the algorithm may produce a spurious AOT long-term trend, especially in regions dominated by industrial pollutants, biomass burning, and mineral dust. They observed negative tendencies of AOT in the regions influenced by emissions from industrialized countries or Saharan desert particles, and positive tendencies in the regions influenced by emissions from fast developing countries or smoke from biomass burning. However, although AVHRR could provide continues and long-term observations because it has been mounted on various platforms (i.e., TIROS-N, NOAA-6~19, MetOp-A), the absence of on-board calibration devices as well as the orbital drift could make a serious bias in trend analysis [Thomas, et al., 2010].

Zhang and Reid (2010) explained both regional and global aerosol trends above oceans using MODIS and MISR aerosol products (2000-2009), which included both level 2 (orbital swath data) and level 3 (monthly global product) data sets from Collection 5 (one of the latest reprocessing campaigns). They found that both MODIS and MISR observed statistically

significant increasing trends over the Indian Bay of Bengal, east coast of Asia, and Arabian Sea even though their magnitudes were slightly different. Yu et al. (2009) examined the seasonal and geographical variability of marine aerosol fine-mode fraction from MODIS collection 5 data. They found that MODIS-derived anthropogenic AOT at 550 nm was increasing over a 7-year period (2001-2007) in different latitude ranges (i.e., 30N-60N, EQ-30N, 30S-EQ, and 60S-60N), but it was insignificant. They also attempted to show seasonal and geographical variations, which are consistent with the Goddard Chemistry Aerosol Radiation Transport (GOCART) and Global Modelling Initiative (GMI) model simulations. By using 8-year MISR and MODIS-Terra data sets from March 2000 to February 2008, Kishcha et al. (2009) showed the time series of aerosol data averaged over the ocean in the latitudinal zone (30-60°N), and found the opposite trends of AOT and fine mode AOT with less statistical significance (i.e., negative trend for MISR and positive for MODIS). Thomas et al. (2010) investigated the long-term global AOT trend over the ocean using ATSR-2 instrument covering time period from 1995 to 2001. They derived a positive trend over the ocean which is opposite to the negative with respect to previous AVHRR analyses. Papadimas et al. (2008) investigated the temporal variability of AOT over the Mediterranean basin, where MODIS-Terra could monitor well aerosols over water due to dark surface. They suggested a decreasing tendency in MODIS AOT from 2000 to 2006, which is in good agreement with corresponding AOT trends from AERONET and Particulate Matter (PM_{10}) measurements.

Up to this point, all mentioned publications focused on AOT trend derivation and analysis of the datasets, which are limited to retrievals over oceans only. In spite of relatively high accuracy of aerosol retrieval using remote sensing over ocean due to the dark and stable surface (as compared to land), frequent cloud disturbance for regular measurements makes it difficult to estimate the exact change in aerosol. Furthermore, if considering the relatively

short lifetime and high variability of aerosols, the findings over ocean are hardly to be generalized to global trends of anthropogenic and natural aerosols mainly emitted over land.

Massie et al. (2004) attempted to derive some regional aerosol patterns and their temporal trends over land and ocean surfaces using TOMS data from 1979 to 2000. They related the trends to regional sulphur dioxide emissions, and found that AOT increased clearly between 1979 and 2000 over the China coastal plain and the Ganges River basin in India. Xie and Xia (2008) examined the temporal variations of monthly AOT at 500 nm using TOMS from 1980 to 2001 in north China. They observed a striking feature that AOT variation during 1997-2001 showed a clear increasing trend (especially, in spring), though a reverse tendency was revealed during 1980-1991. However, aerosol layer height and sub-pixel cloud contamination have a serious influence on the retrieval accuracy of aerosol using the near ultraviolet channel of TOMS [Herman, 1997; Torres et al., 1998, 2002].

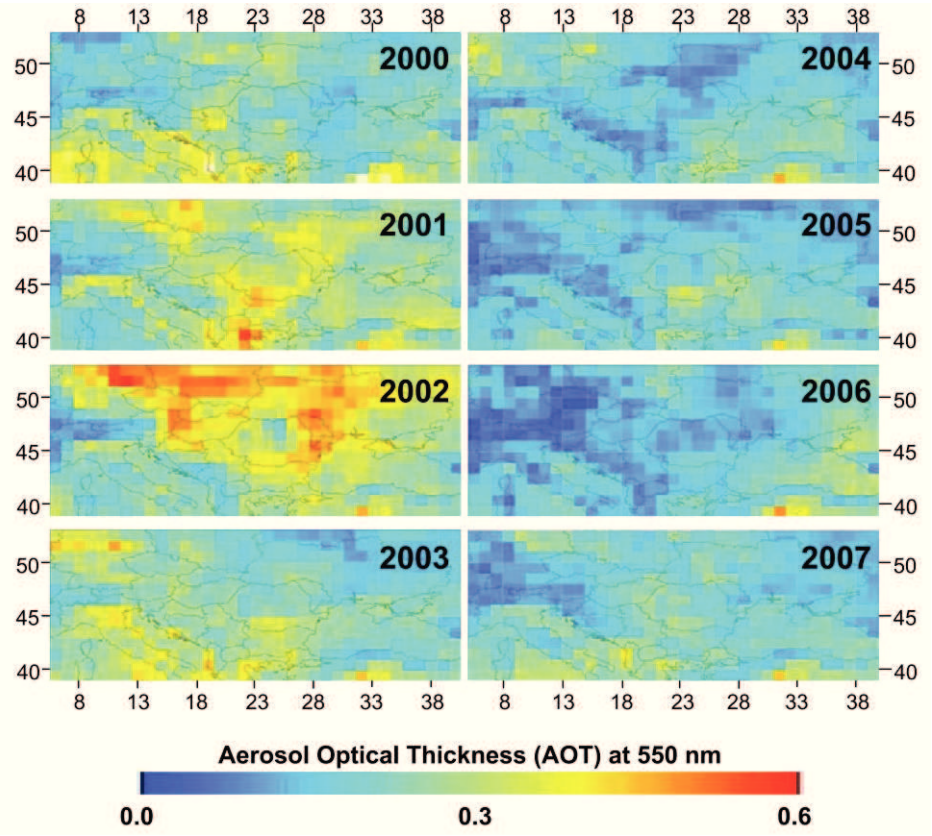

Fig. 1.6 Spatial distribution (7°E-41°E; 40°N-53°N) and temporal variation (monthly means for July and August) of MODIS-Terra-derived AOT at 550 nm [Karnieli et al., 2009].

Karnieli et al. (2009) provided temporal trends of anthropogenic sulphur aerosol transported from central/Eastern Europe to Israel with independent data sets such as MODIS-Terra, CIMEL sun/sky photometer, and PM_{10} Stacked Filter Unit sampler. For each research periods between 1995 to 2007, MODIS-Terra (2000-2007) observed 38% reduction of fine AOT over central and Eastern Europe (see Fig. 1.6), a ground-based sun/sky photometer (1998-2007) showed 43% reduction in southern Israel, and the aerosol sampler (1995-2004) obtained 25% reduction of fine aerosols mass. de Meij et al. (2010) investigated the global and regional trends of AOT over land for the period of a decade (2000-2009) derived from MODIS-Terra, MISR-Terra, and AERONET as well as the emission estimates from the Co-operative Programme for Monitoring and Evaluation of the Long-range Transmission of Air Pollutants (EMEP) for Europe, the Region Emission Inventory for Asia (REAS) and the Intergovernmental Panel on Climate Change (IPCC, RCP 3PD) for North America and the entire globe. They found generally negative trends over Europe and North America, while mostly positive ones over South and East Asia. Koukouli et al. (2010) found a negative trend from MODIS-Terra AOTs (2000-2006) over the Southern Balkan and Eastern Mediterranean. They concluded that the negative trend is going back to the decrease of local aerosol emission or the transported aerosol and the change in the wind patterns of the area in the past decade. Kaskaoutis et al. (2011) focused on analysis of aerosol amount over south Asia using MODIS-Terra AOT data during the period from 2000 to 2009, and found an increasing AOT trend of 10.17%. Dey and Di Girolamo (2011) used ten years of MISR observations from Mar./2000 to Feb./2010, and found seasonal increase in AOT in a range of 0.1-0.4 over the Indian subcontinent due to human activity. However, without a validation with ground observations, these findings over land based on satellite remote sensing can face a general doubt about the accuracy because it is still a challenging task to retrieve accurate AOTs over land using satellite observations (AOT retrieval uncertainty; $\pm 0.20 \sim 0.30 \times \mathrm{AOT}$ for TOMS

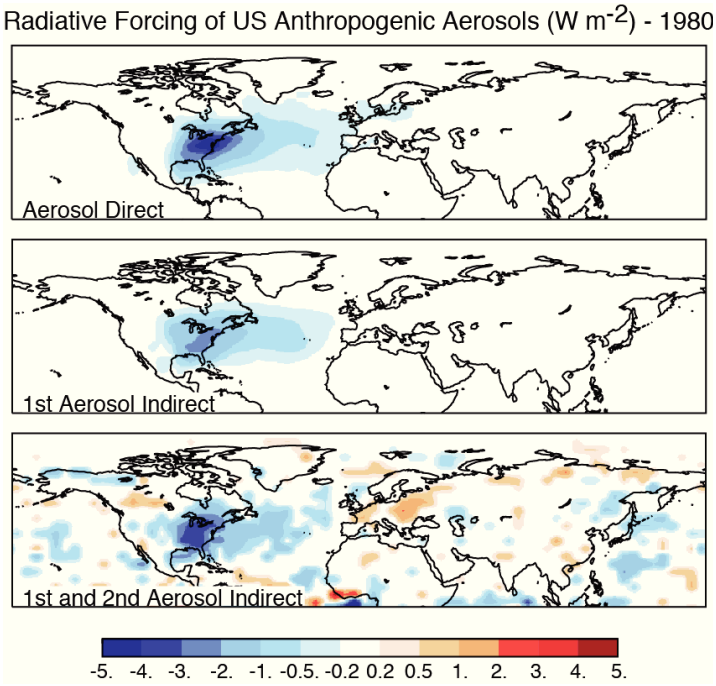

Fig. 1.7 Annual mean aerosol direct (top), first indirect (middle), and total indirect (bottom) radiative forcing from US anthropogenic sources for year 1980 [Leibensperger et al., 2011].

[Torres et al., 2002], $\pm 0.05 \pm 0.20 \times \mathrm{AOT}$ for MISR [Kahn et al., 2005a, 2010], and $\pm 0.05 \pm 0.15 \times \mathrm{AOT}$ for MODIS [Remer et al., 2008; Levy et al., 2010]) due to the high spatial and temporal variability of the surface contribution, aerosol loading, and aerosol characteristics. Besides, the AOT trend analysis based on polar orbiting satellite measurements is impossible to avoid a bias caused by unrepresentative sampling (i.e., cloud disturbance, limited orbital periods, and different sampling times). Therefore, in order to analyze more reliable AOT trends observed from the satellites, it is necessary not only to derive AOT trends from various samplings, but also to validate them with ground-based observation over land.

Recently, there have been several analyses of aerosol trends by means of model studies. For instance, Streets et al. (2009) examined the hypothesis that AOT changes are caused by the changing patterns of anthropogenic emissions of aerosol and its precursors from 1980 to 2006 using the Goddard Chemistry Aerosol Radiation and Transport (GOCART) model. They concluded that the main contributions of aerosol changes are from industrial and

economic activities. A step further, Leibensperger et al. (2011) simulated the aerosol direct and indirect (warm cloud) radiative forcings from US anthropogenic sources over the 1950-2050 period based on historical emission inventories (see Fig. 1.7) and future projections from the IPCC A1B scenario [Nakićenović and Swart, 2000]. They used the GEOS-Chem Chemical Transport Model (CTM) combined with the GISS General Circulation Model (GCM), and found that a dramatic decrease in US anthropogenic aerosol forcing has the potential to induce strong warming over the US. Lei et al. (2011) derived the primary anthropogenic aerosol emission trend in China from 1990 to 2005 using model framework. They estimated the $PM_{2.5}/PM_{10}$ and Total Suspended Particulate (TSP) increased from 1990 to 1996, and decreased until 2000, then increased again in the following years. However, in spite of the plausible conclusions, the simulations can be easily damaged by a large unexpectable error caused by many assumptions in the models.

To the best of my knowledge, several researches have analyzed the global aerosol trends using satellite-based observation generally because of its wide spatial coverage. Nonetheless, there is still much to consider the uncertainty factors for estimating a significant trend as to be summarized in Tab. 1.1 (especially, no consideration of unrepresentative sampling). Therefore, the present study attempted to derive more accurate and reliable global and regional trends of cloud-free AOT by minimizing the uncertainties. The next section outlines the content of this dissertation following the research approaches.

1.3 Outline of the dissertation

Several studies discussed in the previous section have some obvious limits caused by the unrepresentative sampling in the global and regional AOT trend analyses using satellite observations. Therefore, a basic approach to a more accurate and reliable analysis in this study is to minimize the uncertainty effect of unrepresentative sampling caused by cloud disturbance, limited orbital periods, and different sampling times.

First of all, the uncertainty caused by limited orbital periods and different sampling times could be minimized by using the several satellite-based observations: Terra (MODIS and MISR), Aqua (MODIS), and OrbView-2 (SeaWiFS), which are crossing the equator at the different local times of 10:30 a.m. for Terra, 01:30 p.m. for Aqua, and 12:20 p.m. for OrbView-2. Additionally, it is necessary to validate the satellite retrievals with the ground-based observation (AERONET) having better retrieval accuracy (AOT accuracy: ±0.01 [Holben et al., 1998]). Chapter 2 describes the research data sets of SeaWiFS, MODIS, MISR, and AERONET, which were adopted in this study for the purposes.

Even though SeaWiFS has provided a long-term and well-calibrated radiance since August 1997, it never has been used in previous investigations for the AOT trends. However, it is important to mention that SeaWiFS observations are imperative to minimize the error in insufficient aerosol sampling. Therefore, this study uses the latest version of Bremen AErosol Retrieval (BAER) algorithm, which successfully retrieved the global AOTs for the trend analysis [von Hoyningen-Huene et al., 2011]. The BAER algorithm improved recently is the most appropriate retrieval method using SeaWiFS because its retrieval performance was verified convincingly based on various observations (SeaWiFS, MERIS, and MODIS) [von Hoyningen-Huene et al., 2003, 2006, 2011; Lee et al., 2004]. Chapter 3 explains in detail about the retrieval techniques of the latest version of BAER with scientific backgrounds. In addition, this chapter provides some possible attempts to improve BAER performance by

reducing the uncertainties, which arise from unscreened thin clouds, the relatively strong surface reflectance over land, and the various aerosol types over global regions.

Chapter 4 reports on the validation of AOT retrieved by BAER using SeaWiFS data from 10/1997 to 05/2008 in order to verify BAER's retrieval accuracy over land. The main focus for the validation lies on the Europe and South China regions (Belgium/Netherlands/Luxemburg, Po Valley, Eastern Europe, Eastern Mediterranean, and Pearl River Delta), which were assigned within the CityZen project (megaCITY - Zoom for the Environment: EU 24 Framework Programme 7 of European Commission) as being of particular significance [Colette et al., 2011; Gerasopoulos et al., 2011; Lelieveld et al., 2002; Zhang et al., 2008]. Even though the previous validations show good agreement between BAER and AERONET AOTs within the research regions, it does not mean that BAER AOT trends retrieved using SeaWiFS observations are highly reliable. Therefore, in order to demonstrate the feasibility and uncertainty of AOT trends, BAER AOT trends are compared with AERONET AOT trends by applying inter-correction method for non-representative monthly AOTs, which are calculated based on small number of observation due to cloud disturbance. Through the trend comparison, the uncertainty effect of cloud disturbance can be estimated in cloud-free AOT trend.

Chapter 5 firstly aims to investigate and analyze the long-term trends of AOT (440, 675, 870, and 1020 nm) and Ångström Exponent (ÅE) (440-870 nm) using more accurate and spectral AERONET observations. Furthermore, the trend analysis based on Coarse- and Fine-mode dominant AOTs classified by a newly introduced criterion in this study, a 50% of fine volume fraction of total AOT, can contribute to find out the major sources for the temporal changes. The second objective of this chapter is to figure out a way to consider the significant uncertainty of cloud disturbance mentioned in Chapter 4. Since the effect of cloud disturbance clearly shows in the possible number of AERONET observations, the present

study introduces and examines a linear trend model weighted by the monthly numbers for cloud disturbance. Additionally, using AERONET inversion data (e.g., water vapor contents, volume size distribution, refractive index, SSA, and phase function), the last part in this chapter is a climatological study of regional aerosol types, which can provide a priori for Look-Up Table (LUT) approach based on satellite observations.

Chapter 6 analyzes the global AOT derived from multiple polar orbiting satellites observations: Terra (MODIS and MISR), OrbView-2 (SeaWiFS), and Aqua (MODIS), which can minimize the uncertainty caused by limited orbital period (roughly 100 minutes for each orbit) and different sampling times of polar-orbiting platforms. Furthermore, by applying the verified method of weighted least squares regression in the previous chapter, the influence of cloud disturbance can be reduced. The regions of interest are basically divided by land only, ocean only, and both land and ocean because of high temporal variability and spatial heterogeneity of cloud disturbance by different region. For the same reason mentioned above, the regional trends have been estimated by weighted averaging of the trends on a grid scale (1° × 1° for MODIS and SeaWiFS or 0.5° × 0.5° for MISR).

Chapter 7 summarizes major findings from this study, and offers a brief outlook.

The present dissertation is largely composed of the scientific articles published or submitted by von Hoyningen-Huene et al. in *Atmospheric Measurement Techniques* (2011), Yoon et al. in *Atmospheric Chemistry and Physics* (2011), Yoon et al. in *Atmospheric Measurement Techniques* (2012), and Yoon et al. in *Geophysical Research Letters* (2012) during the PhD periods.

2. Instruments and data sets

High scientific quality of observations is a prerequisite for analyzing the climatological AOT change. Therefore, the aspect of radiance calibration should be examined, which is a well-known major source of uncertainty in AOT retrievals [Higurashi and Nakajima, 1999; Ignatov and Stowe, 2002]. Recently, the calibration accuracies have been improved remarkably by several calibration methods (e.g., pre- or post-launch calibrations using deep convective clouds, vicarious calibration, inter-satellite calibration, lunar calibration, and comparison with in-situ data) and discussed thoroughly by Li et al. (2009). The data sets used in this study, SeaWiFS, MODIS, MISR, and AERONET are introduced and their calibration accuracies are discussed in this chapter.

2.1 Sea-viewing Wide Field Sensor (SeaWiFS)

After launched in August 1997, SeaWiFS on OrbView-2 (see Figs. 2.1 and 2.2) has been almost continuously measuring well-calibrated radiances (accuracy: 0.5% and stability: 0.3% [Li et al., 2009]) from the perspective of on-board, lunar [Barnes et al., 2001], and vicarious calibrations [Gordon, 1998; Eplee et al., 2001]. In this study, SeaWiFS Level 1B (L1B), Global-Area Coverage data (GAC) subsampled from full-resolution data with every fourth pixel of a scan line and every fourth scan line being recorded, were used for AOT retrieval over several regions. SeaWiFS provides six visible (412, 443, 490, 510, 555, and 670 nm) and two near-infrared wavelengths (765 and 865 nm). The spatial resolution is approximately 4.5 km at nadir with a swath width of 1,502 km (±45.0°) at equator. A scanner tilt mechanism allows the instruments to avoid sun glint on the sea surface. More detailed information on the major characteristics of SeaWiFS [Hooker et al., 1992; Cracknell et al., 2001] is summarized

in Tab. 2.1.

An example of SeaWiFS normalized radiances by applying the lunar calibration in the fifth reprocessing for bands 2, 5, 6, and 8 (443, 555, 670, and 865 nm, respectively) is depicted in Fig. 2.3. The band 2 and 5 (443 and 555 nm), which are slightly influenced by land surface, were used to retrieve AOT using BAER algorithm. The band 6 and 8 (670 and 865 nm) were utilized to estimate the surface contribution using Normalized Differential Vegetation Index (NDVI). The degradation in band 8 might induce an error to account for the surface contribution in the AOT retrieval. A detailed account of BAER's AOT retrieval based on SeaWiFS data are given in Chapter 3.

Tab. 2.1 SeaWiFS bandwidths and mission characteristics [http://oceancolor.gsfc.nasa.gov].

Instrument Bands		**Mission Characteristics**	
Band	**Wavelength [nm]**	**Orbit Type**	Sun Synchronous at 705 km
1	402-422	**Equator Crossing**	Noon +20 min, descending
2	433-453	**Orbital Period**	99 minutes
3	480-500	**Swath Width**	2,801 km LAC (58.3 degrees)
4	500-520	**Swath Width**	1,502 km GAC (45 degrees)
5	545-565	**Spatial Resolution**	1.1 km LAC, 4.5 km GAC
6	660-680	**Real-Time Data Rate**	665 kbps
7	745-785	**Revisit Time**	1 day
8	845-885	**Digitization**	10 bits

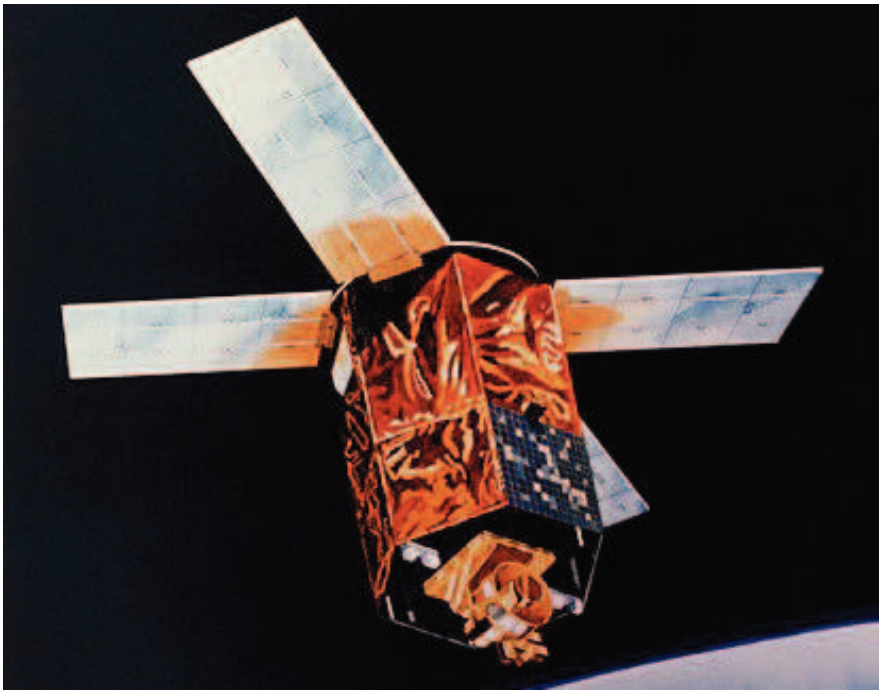

Fig. 2.1 GeoEye's OrbView-2 (aka SeaStar) satellite [http://www.sciencephoto.com].

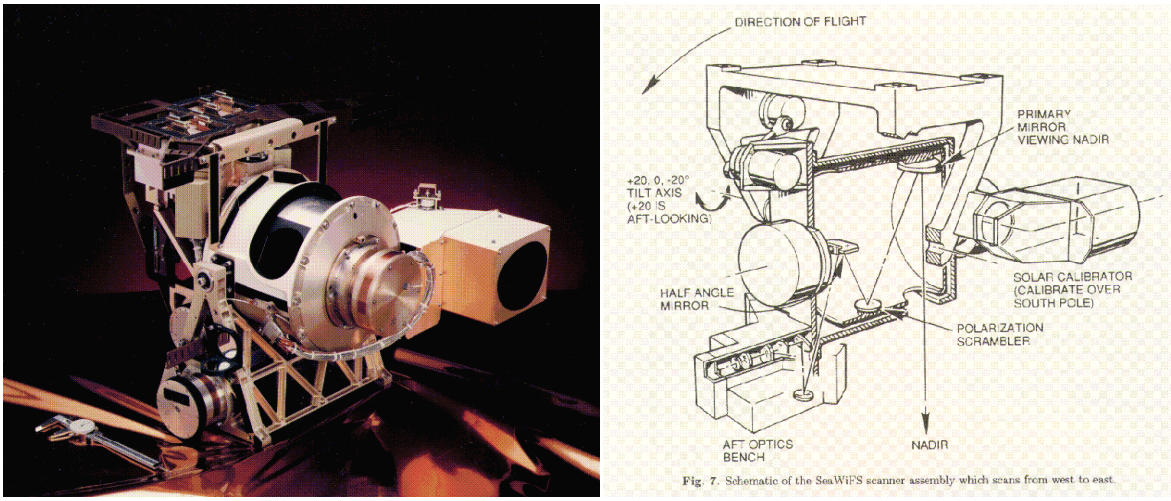

Fig. 2.2 SeaWiFS instrument (left) and line drawing (right). It consists of an optical scanner and an electronics module [http://oceancolor.gsfc.nasa.gov].

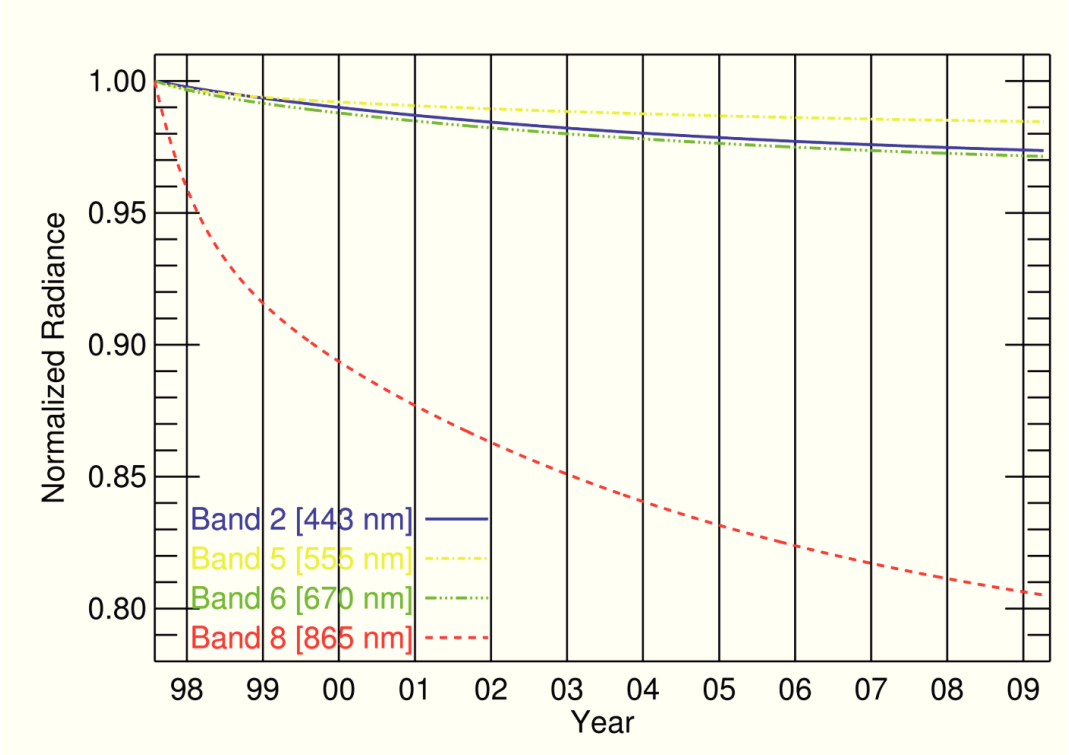

Fig. 2.3 SeaWiFS normalized radiances by lunar calibration in the fifth reprocessing at bands 2, 5, 6, and 8 (443, 555, 670, and 865nm, respectively) after launched.

2.2 Moderate-Resolution Imaging Spectroradiometer (MODIS)

Among many sensors on-board polar orbiting satellites for observing Earth system, MODIS on Terra and Aqua spacecrafts (see Figs. 2.4 and 2.5) have largely contributed to monitor global aerosols. The first MODIS instrument is mounted on Terra, which was launched successfully on December 18, 1999. Afterwards, the second one mounted on Aqua was started to observe global aerosols on May 4, 2002. The main objectives of these instruments are to improve the understandings of global dynamics and processes occurring on the land, in the oceans, and in the lower atmosphere [http://modis.gsfc.nasa.gov]. The MODIS instrument provides visible and infrared radiation in 36 spectral bands (i.e., lights emitted or reflected by the Earth ranging in wavelength from 400 to 14400 nm), which are well calibrated (~2 % absolute, ~1 % precision [Li et al., 2009]). They could cover the global area every one to two days. Further information of MODIS instrument characteristics and calibration status is summarized in Tab. 2.2. In this study, monthly AOTs at 550 nm and Cloud Fractions (CFs) in daytime from Level 3 Collection 5 global products (1°×1°) are used for analysis of the global aerosol trends in Chapter 6.

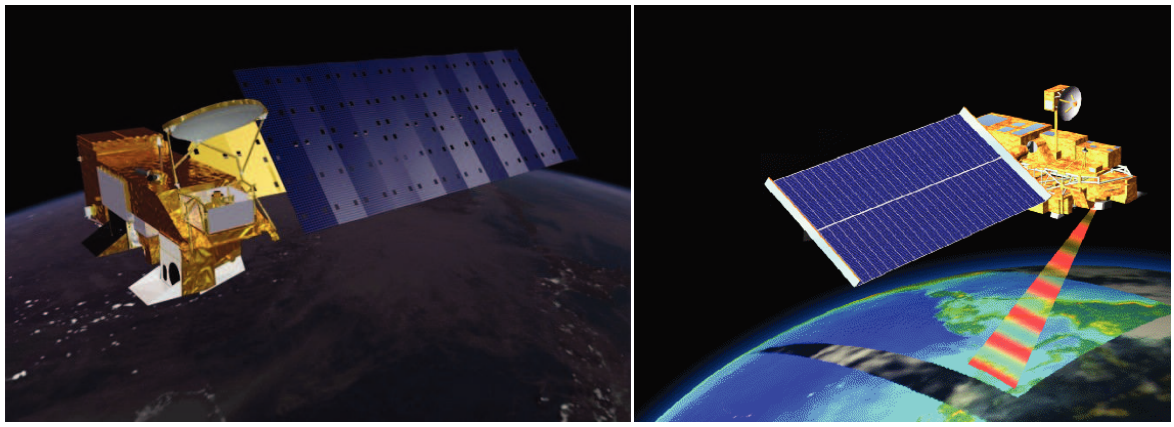

Fig. 2.4 NASA's Terra (left) and Aqua (right) satellites over the Earth [http://oceanmotion.org; http://earthobservatory.nasa.gov].

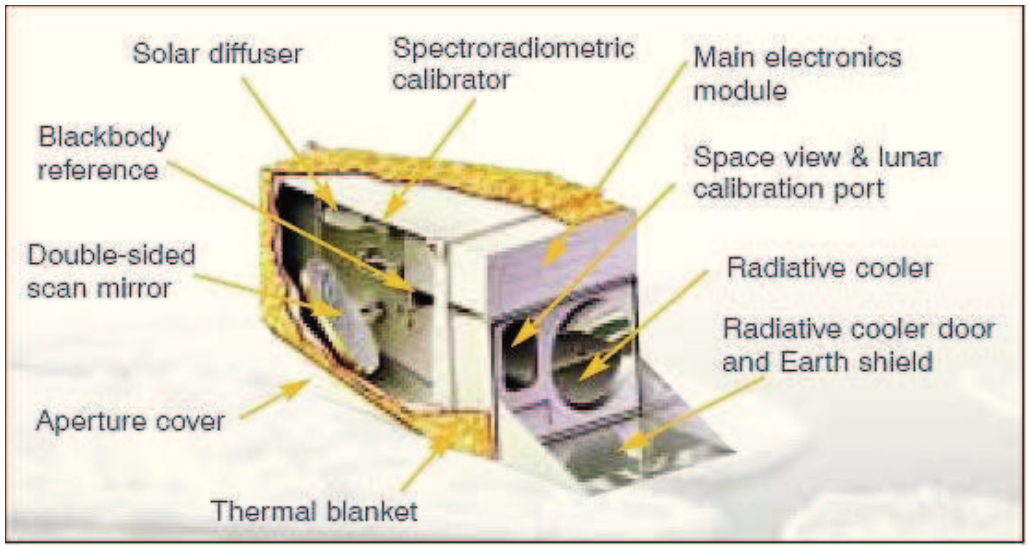

Fig. 2.5 Schematic MODIS instrument [http://www.sciencephoto.com].

Tab. 2.2 MODIS instrument characteristics and calibration status.

Sensor	**MODIS (Moderate Resolution Imaging Spectroradiometer)**	
Satellite	Terra	Aqua
Orbit	descending node	ascending node
Local Equatorial Crossing Time	10:30 a.m.	01:30 p.m.
Launch Date	1999/12/18	2002/05/04
Swath	2330 km	
Number of Bands	36	
Resolution	250 m (bands 1-2) 500 m (bands 3-7) 1000 m (bands 8-36)	
Spectral Coverage	405-14385 nm	
Quantization	12 bits	
Sensor Calibration Method	On-board, Vicarious, and Lunar	
Calibration Accuracy/Precision	~2 % absolute, ~1 % precision	
Reference Source	Li et al. (2009), http://modis.gsfc.nasa.gov	

2.3 Multiangle Imaging SpectroRadiometer (MISR)

The MISR instrument, one of the sensors on-board the Terra spacecraft (see Figs. 2.6 and 2.7), can distinctively provide the viewings of the sunlit Earth (446, 558, 672 and 866 nm) simultaneously at nine widely spaced angles (nadir, forward, and backward view angles at 26.1°, 45.6°, 60.0°, and 70.5°). These unique features are able to distinguish different types of atmospheric aerosols, cloud forms, and land surface covers, which support MISR science goals. In addition, the instrument provides a global coverage with high spatial resolutions (i.e., 275 m × 275 m, 275 m × 1.1 km, 1.1 km × 1.1 km), but it takes around 9 days to cover the entire Earth's surface [http://www-misr.jpl.nasa.gov]. The imagery sensor is carefully calibrated (~3 % absolute, 1-2 % channel-to-channel relative, 1 % precision [Kahn et al., 2005b; Bruegge et al., 2007]) using On-board, Vicarious, and Lunar methods to provide accurate measures of reflected sunlight. Further information of MISR instrument characteristics and calibration status is summarized in Tab. 2.3. In this study, monthly AOTs (558 nm) from Level 3 Component Global Aerosol Product version F15 (CGAS-F15) products (0.5°×0.5°) are used for analysis of the global aerosol trends in Chapter 6.

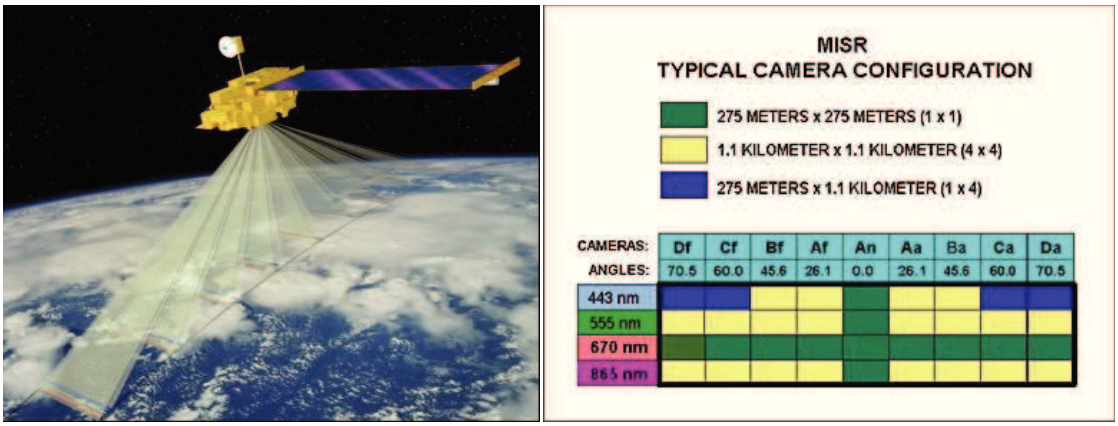

Fig. 2.6 MISR observing concept (left) and typical camera configuration (right) [http://www-misr.jpl.nasa.gov].

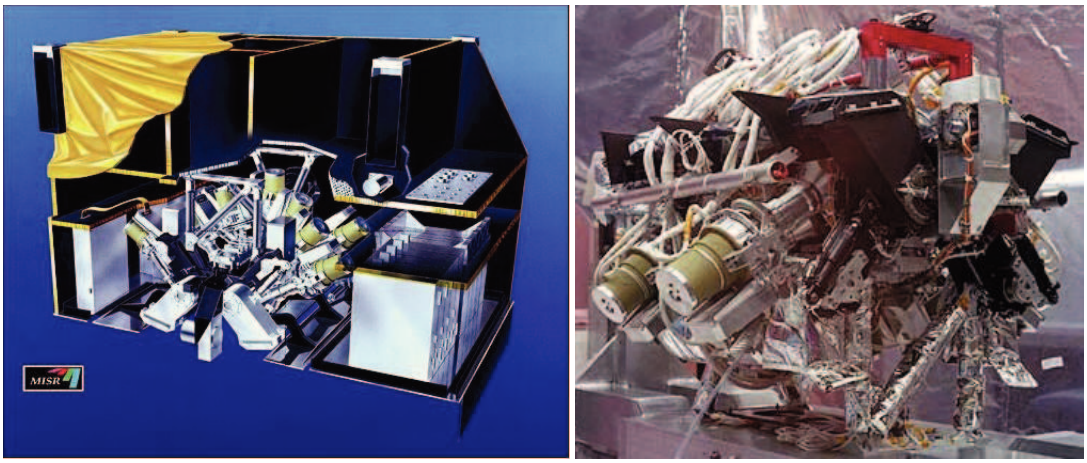

Fig. 2.7 Cut-away drawing of the MISR Instrument (left) and MISR optical bench (right) [http://www-misr.jpl.nasa.gov].

Tab. 2.3 MISR instrument characteristics and calibration status.

Sensor	**MISR (Multiangle Imaging SpectroRadiometer)**
Satellite	Terra
Orbit	descending node
Local Equatorial Crossing Time	10:30 a.m.
Launch Date	1999/12/18
Swath	360 km
Number of Bands	4
Resolution	275 m × 275 m 275 m × 1.1 km 1.1 km × 1.1 km
Spectral Coverage	446, 558, 672 and 866 nm
View Angles	0°, ±26.1°, ±45.6°, ±60.0°, and ±70.5°
Sensor Calibration Method	On-board, Vicarious, and Lunar
Calibration Accuracy/Precision	~3 % absolute, 1-2 % channel-to-channel relative, 1 % precision
Reference Source	Kahn et al. (2005b), Bruegge et al. (2007), http://www-misr.jpl.nasa.gov

2.4 AErosol RObotic NETwork (AERONET)

The networks based on the earth's surface measurements have played an important role in monitoring aerosol optical properties around the world. The AERONET program, which aims to assess aerosol optical properties and validate satellite retrievals of aerosol optical properties, is an inclusive federation of ground-based remote sensing aerosol networks established by the AERONET and PHOTONS (French sunphotometer network), and greatly expanded by AEROCAN (Canadian sunphotometer network), other agency, institute, and university partners [http://aeronet.gsfc.nasa.gov]. This program has globally provided aerosol products (generally at four wavelengths: 440, 675, 870, and 1020 nm) for the past decades over roughly 850 stations (see Fig. 2.8). Despite aerosols below clouds are underrepresented in the database [Remer et al., 1997; Dubovik et al., 2002a], the continuous long-term AOTs data with high temporal resolution and retrieval accuracy (pre- and post-field calibration applied) are suitable for trend analysis [Holben et al., 1998, 2001; Eck et al., 1999; Smirnov et al., 2000]. Additionally, AERONET inversion products from sky radiances at all available wavelengths and scattering angles are useful to investigate climatological aerosol optical properties. The AERONET inversion process and research activities were described by Dubovik and King (2000), Dubovik et al. (2000, 2002a, 2002b, 2006), and Sinyuk et al. (2007). In this study, Level 2.0 (cloud-screened and quality-assured) AERONET data [Holben et al., 1998, 2001; Eck et al., 1999; Smirnov et al., 2000] are mainly used for validating the satellite retrievals (i.e. AOT and AOT trend), estimating the cloud-free AOT trends, and investigating the climatological aerosol optical properties at several global stations.

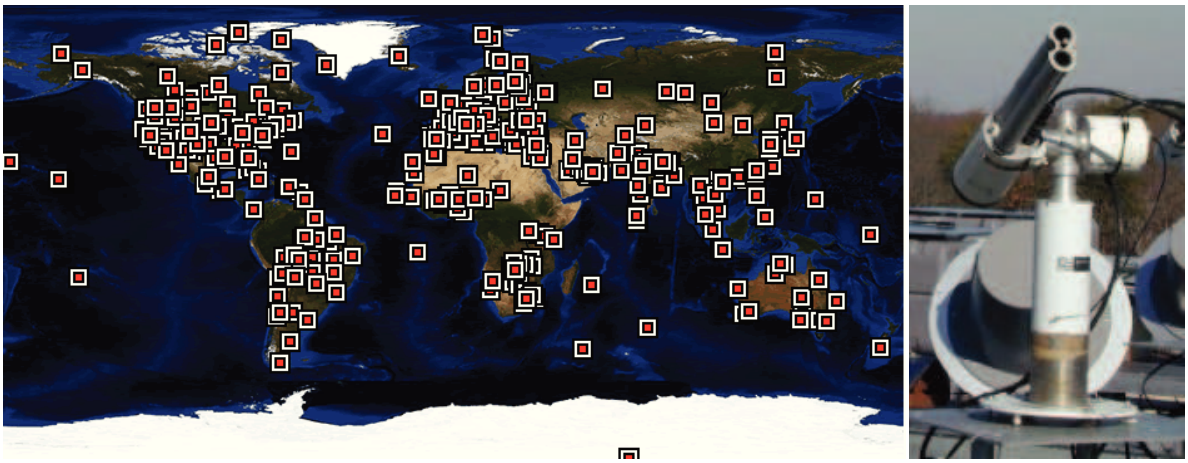

Fig. 2.8 Global AERONET stations (left) and sunphotometer (right) [http://aeronet.gsfc.nasa.gov].

3. Bremen AErosol Retrieval (BAER) Algorithm

A long-term and well-calibrated observation is an essential requirement for the trend analysis. Even though SeaWiFS observations fully meet the condition, it is difficult to investigate the global AOT trends because there was a lack of research on the atmospheric aerosol using SeaWiFS observations, which was mainly designed to study the ocean colors. Therefore, this study used the Bremen AErosol Retrieval (BAER) to retrieve AOTs over land and ocean using SeaWiFS observations. This retrieval approach has been demonstrated convincingly in previous studies using various sensors (i.e., MEdium Resolution Imaging Spectrometer (MERIS), SeaWiFS, and MODIS) [von Hoyningen-Huene et al., 2003, 2006, 2011; Lee et al., 2004]. The main characteristics of BAER are the use of multi-spectral separation techniques to discriminate spectral surfaces and atmospheric properties. This chapter is mainly based on the paper published by von Hoyningen-Huene et al. in *Atmospheric Measurement Techniques*, 2011.

3.1 Radiative transfer equation for TOA reflectance

Nadir viewing sensors measure the up-welling directed radiance ($L^{\uparrow}$), which is expressed in terms of Top Of Atmosphere (TOA) reflectance (ρ_{TOA}) defined as:

$$\rho_{TOA} = \frac{\pi L^{\uparrow}}{E_0} \cdot M(z_0) \tag{3.1}$$

where the solar irradiation (E_0), the air mass ($M(z_0)$), and the solar zenith angle (z_0). In order to consider the atmospheric curvature effect when the solar zenith angle is large enough, the air mass is defined by the following approximation formula [Kasten and Young, 1989].

$$M(z_0) = \frac{1}{\cos(z_0)+0.50572\cdot(6.07795-z_0)^{-1.6364}} \quad (3.2)$$

In Kaufman et al. (1997a), TOA reflectance is defined as two main parts, atmospheric path and surface contributions. The atmospheric path reflectance (ρ_{Atmos}^{Black}) is based on a "black" surface (i.e., no contribution from the surface). It depends on Aerosol and Rayleigh Optical Thickness (AOT (δ_{Aer}) and ROT (δ_{Ray})), the atmospheric phase function ($p(\theta)$), the SSA of atmosphere (ω_0), and the geometry conditions (z_0, z_s, ϕ). The surface part is determined by multiple scattering between the atmosphere and surface. It is expressed by the surface albedo (A_{Surf}), the total transmission (t_{tot}) for the illumination/viewing geometry (z_0, z_s), and the hemispheric reflectance (r_{Hem}).

$$\begin{aligned}
&\rho_{TOA}(z_0, z_s, \phi\,) \\
&\quad = \rho_{Atmos}^{Black}\big(z_0, z_s, \phi, \delta_{Aer}, \delta_{Ray}, p(\theta), \omega_0, 0\,\big) \\
&\quad + \Big(t_{tot}(z_0)\cdot A_{surf}(z_0, z_s)\cdot t_{tot}(z_s)\Big)\Big\{1 + r_{Hem}(\delta_{tot}, g)\cdot A_{Surf}(z_0, z_s) \\
&\quad + \Big(r_{Hem}(\delta_{tot}, g)\cdot A_{Surf}(z_0, z_s)\Big)^2 + \Big(r_{Hem}(\delta_{tot}, g)\cdot A_{Surf}(z_0, z_s)\Big)^3 + \cdots\Big\} \\
&\quad = \rho_{Atmos}^{Black}\big(z_0, z_s, \phi, \delta_{Aer}, \delta_{Ray}, p(\theta), \omega_0, 0\,\big) + \frac{t_{tot}(z_0)\cdot A_{surf}(z_0,z_s)\cdot t_{tot}(z_s)}{1-r_{Hem}(\delta_{tot},g)\cdot A_{Surf}(z_0,z_s)}\ , \quad (3.3)
\end{aligned}$$

where, θ is scattering angle, δ_{tot} is total optical thickness, and g is asymmetric factor. All parameters, except the geometry angles, have a spectral dependence. Over ocean, the equation is quite simple because the ocean surface is almost "black" (see Fig. 3.1). However, the multiple scattering terms need to be considered over the land surface. Furthermore, it is difficult to separate the aerosol reflectance simply from the atmospheric path reflectance combined with the Rayleigh and multiple scatterings.

Fig. 3.1 RGB composite image from SeaWiFS TOA reflectances over Europe and North Africa at 12/Oct./2001.

3.2 Aerosol reflectance over land and ocean

In order to retrieve the aerosol reflectance, the Rayleigh path reflectance and the multiple scattering terms are subtracted from TOA reflectance.

$$\rho_{Aer}(z_0, z_s, \phi, \delta_{Aer}, p_{Aer}(\theta), \omega_0) =$$

$$\rho_{TOA}(z_0, z_s, \phi) - \rho_{Ray}\left(z_0, z_s, \phi, \delta_{Ray}(p, T)\right) - \frac{t_{tot}(z_0) \cdot A_{Surf}(z_0, z_s) \cdot t_{tot}(z_s)}{1 - r_{Hem}(\delta_{tot}, g) \cdot A_{Surf}(z_0, z_s)} \quad (3.4)$$

The Rayleigh path reflectance is calculated by a radiative transfer model using ROT for the corresponding wavelengths [Buchholz, 1995], Rayleigh phase function, illumination and viewing geometry angles, surface temperature, and pressure. Using the Barometric height equation and dry adiabatic lapse rate in conjunction with GTOPO30 (which is a global digital elevation model with a horizontal grid spacing of 30 arc seconds (approximately 1 km)), the ROT could be corrected for the actual conditions (i.e., temperature and pressure) by the following equation.

$$\delta_{Ray}(\lambda, p, T) = \frac{p}{p_0} \cdot \frac{T_0}{T} \cdot \delta_{Ray}(\lambda) \quad (3.5)$$

The surface term needs an additional adjustment using the application of the surface model in respect of the spectral and geometry conditions of the satellite scene. If the surface could be assumed as Lambertian (e.g. full moon and white paper), the adjustment requires only the knowledge of the spectral surface albedo ($A_{Surf}(\lambda)$). However, over most of the land surface (i.e. a non-Lambertian ground), the spectral surface albedo has to be considered by a directed spectral surface reflectance.

$$\rho_{Surf}(z_0, z_s, \phi, \lambda) = BRDF(z_0, z_s, \phi, \lambda) \cdot A_{Surf}(\lambda) \quad (3.6)$$

$BRDF(z_0, z_s, \phi, \lambda)$ is the normalized Bi-directional Reflection Distribution Function (BRDF) to the nadir position based on the Raman-Pinty-Verstraete model (RPV) [Maignan et al, 2004]. The RPV model describes the relative deviation of the reflectance for the given illumination and viewing conditions. Fig. 3.2 presents the normalized BRDF, which shows a

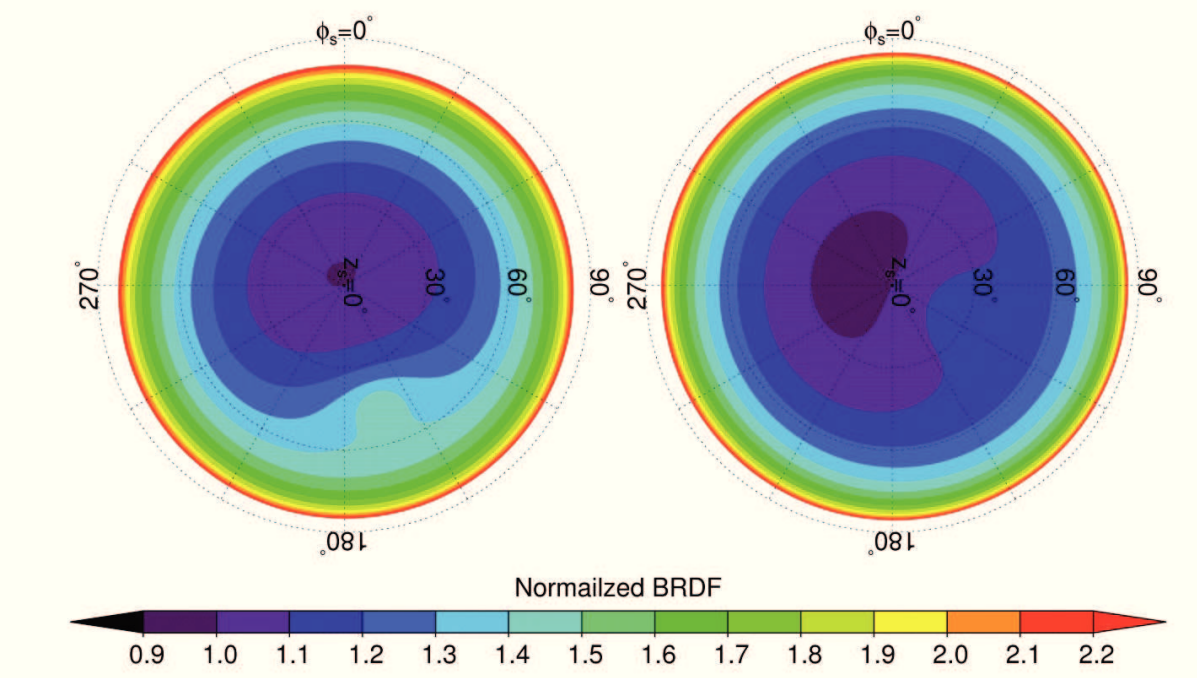

Fig. 3.2 Normalized BRDF by the Lambertian conditions for two illumination conditions (solar zenith 43.11° and 22.39°, solar azimuth 163.71° and 112.72°) and the RPV parameters (k=0.65, φ=-0.06).

significant deviation from the Lambertian conditions ($BRDF_{Lamb}(z_0, z_s, \phi, \lambda) = const = 1.0$). The RPV parameters depending on the type of surface, are quite variable globally. Therefore, an error in the BRDF adjustment can lead to a bias in AOT along the viewing geometry. In this study, the normalized BRDF is used as

$$BRDF(z_0, z_s, \phi, \lambda) = \frac{BRDF^*(z_0, z_s, \phi, \lambda)}{BRDF^*(z_0, z_s=0, \phi, \lambda)} \tag{3.7}$$

where $BRDF^*(z_0, z_s, \phi, \lambda)$ is calculated applying the RPV model:

$$BRDF^*(z_0, z_s, \phi, \lambda) = \rho_{Surf}(\lambda) \cdot \frac{\cos^{k-1} z_0 \cdot \cos^{k-1} z_s}{(\cos z_0 + \cos z_s)^{1-k}} \cdot \frac{1-\varphi^2}{[1+\varphi^2-2\varphi\cos(\pi-\theta)]^{1.5}} \cdot \left(1 + \frac{1-\rho_{Surf}(\lambda)}{1+G}\right) \tag{3.8}$$

where

$$G = \sqrt{\tan^2 z_0 + \tan^2 z_s - 2 \cdot \tan z_0 \cdot \tan z_s \cdot \cos\phi}. \tag{3.9}$$

$\rho_{Surf}(\lambda)$ is estimated under Lambertian conditions ($BRDF(z_0, z_s, \phi, \lambda) = 1.0$) taken from the Eq. (3.10). k and φ describe the surface anisotropy and the forward-backward

scattering of the surface, respectively. With these input parameters ($k = 0.65$ and $\varphi = -0.06$), the deviation caused by difference between Lambertian and non-Lambertian grounds can be minimized.

The surface reflectances are described by the spectral albedo, which is expressed by a linear mixing model with two basic spectra of "green vegetation" ($\rho_{veg}(\lambda)$) and "bare soil" ($\rho_{Soil}(\lambda)$):

$$\rho_{Surf}(\lambda) = \frac{SF}{BRDF(z_0, z_s, \phi, \lambda)} \cdot \{C_{veg} \cdot \rho_{veg}(\lambda) + (1 - C_{veg}) \cdot \rho_{Soil}(\lambda)\}. \quad (3.10)$$

The vegetation fraction (C_{veg}) is determined by $NDVI^*$ which is the corrected from $NDVI$. The scaling factor (SF) is used to adapt the spectrum to the radiation conditions by the following equations.

$$C_{veg} = NDVI^* = \frac{\rho^*(0.865\mu m) - \rho^*(0.665\mu m)}{\rho^*(0.865\mu m) + \rho^*(0.665\mu m)} \quad (3.11)$$

$$SF = \frac{\rho^*(\lambda)}{C_{veg} \cdot \rho_{veg}(\lambda) + (1 - C_{veg}) \cdot \rho_{Soil}(\lambda)}, \ \lambda = 0.665\mu m \quad (3.12)$$

$$\rho^*(\lambda) = \rho_{TOA}(\lambda) - \rho_{Ray}(\lambda) - \rho_{Aer}^{Guess}(\lambda) \quad (3.13)$$

In order to derive the atmospheric corrected reflectance ($\rho^*(\lambda)$), a guess of the aerosol reflectance ($\rho_{Aer}^{Guess}(\lambda)$) is needed. It is estimated by assuming a "black" surface at 412 nm and constant Ångström Exponent (ÅE (α) = 1.0). Finally, the aerosol reflectance in Eq. (3.4) is calculated using the surface model in Eq. (3.14).

$$A_{Surf}(\lambda, z_0, z_s, \phi) = \frac{\rho_{Surf}(\lambda)}{BRDF(z_0, z_s, \phi, \lambda)} \quad (3.14)$$

The spectra of both surface types, "green vegetation" and "bare soil", are shown in Fig. 3.3. Averages of the spectral surface reflectance from the Lindenberg Aerosol Characterization Experiment-98 (LACE-98) [Bundke et al., 2002; Ansmann et al., 2002; von Hoyningen-Huene et al., 2003] were combined with measurement of the Airborne Visible/ Infrared Imaging Spectrometer (AVIRIS) instrument to cover the whole spectral range.

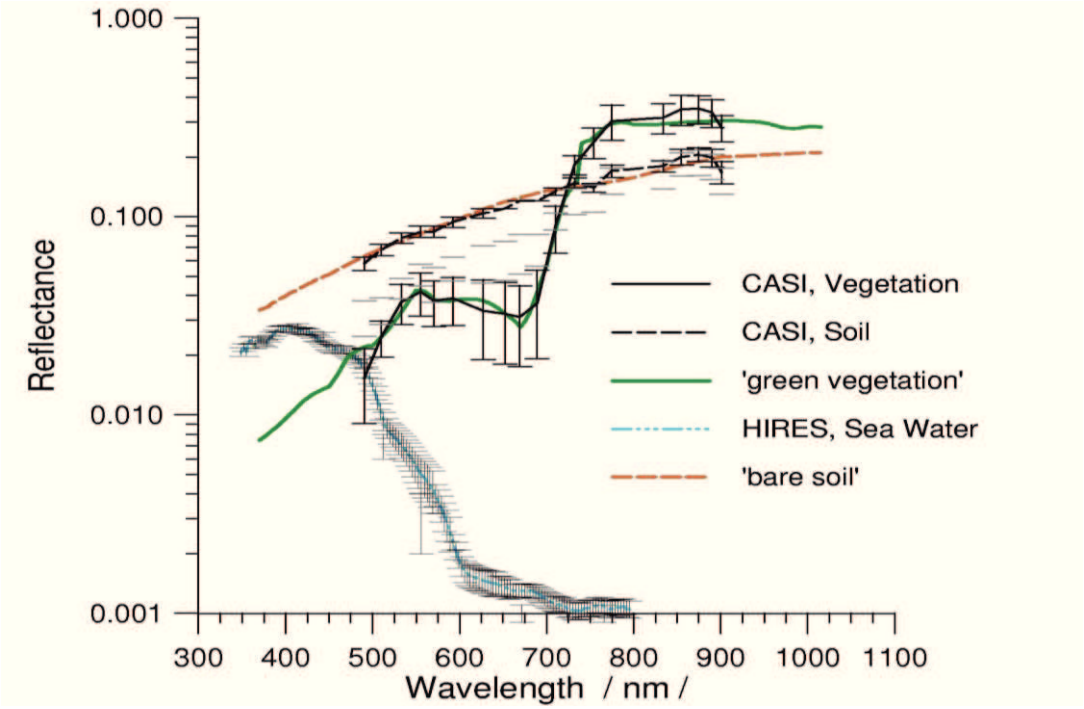

Fig. 3.3 Main surface reflectance spectra as "green vegetation" ($\rho_{veg}(\lambda)$) and "bare soil" ($\rho_{Soil}(\lambda)$) in comparison with experimental data [von Hoyningen-Huene et al., 2011].

For the ocean ground, the main change in Eq. (3.3) is the term of surface albedo, which is nearly "black" in the red and near IR ranges shown in Fig. 3.3 because it is only determined by a water leaving reflectance. Additionally, the glint effect (i.e. specular reflection), which could disturb AOT retrieval significantly, needs to be corrected or flagged out in BAER's AOT retrieval. Nonetheless, it is almost negligible based on the SeaWiFS observation in this study since a scanner tilt mechanism (about 20° tilt away) of the SeaWiFS instrument allows to minimize it on the sea surface [Hooker et al., 1992]. Over ocean, the surface albedo is tuned by the Normalized Differential Pigment Index (NDPI) using the spectra of "clean" and "coastal water". The $NDPI^*$ is defined as

$$NDPI^* = \frac{\rho^*(0.443\mu m) - \rho^*(0.560\mu m)}{\rho^*(0.490\mu m)}. \tag{3.15}$$

3.3 Aerosol Optical Thickness (AOT) retrieval

After separating the aerosol reflectance from the TOA reflectance in Eq. (3.4), the AOT can be determined using Look-Up Tables (LUTs), which were pre-processed by radiative transfer modeling with aerosol and surface characteristics, Rayleigh scattering, and geometry conditions.

$$\delta_{Aer}(\lambda) = f\left(\rho_{Aer}(z_0, z_s, \phi, \lambda)\right) \tag{3.16}$$

Fig. 3.4 gives a graphical example of the LUT by plotting AOT as function of the aerosol reflectance for experimental aerosol properties (i.e., SSA and phase function shown in Fig. 3.5) observed during the LACE-98.

The spectral smoothness of retrieved AOTs is checked by an iterative process of modifying the surface reflectance using Ångström power law. This process continues until the root mean square deviation (RMSD) of the spectral AOTs is smaller than 0.005.

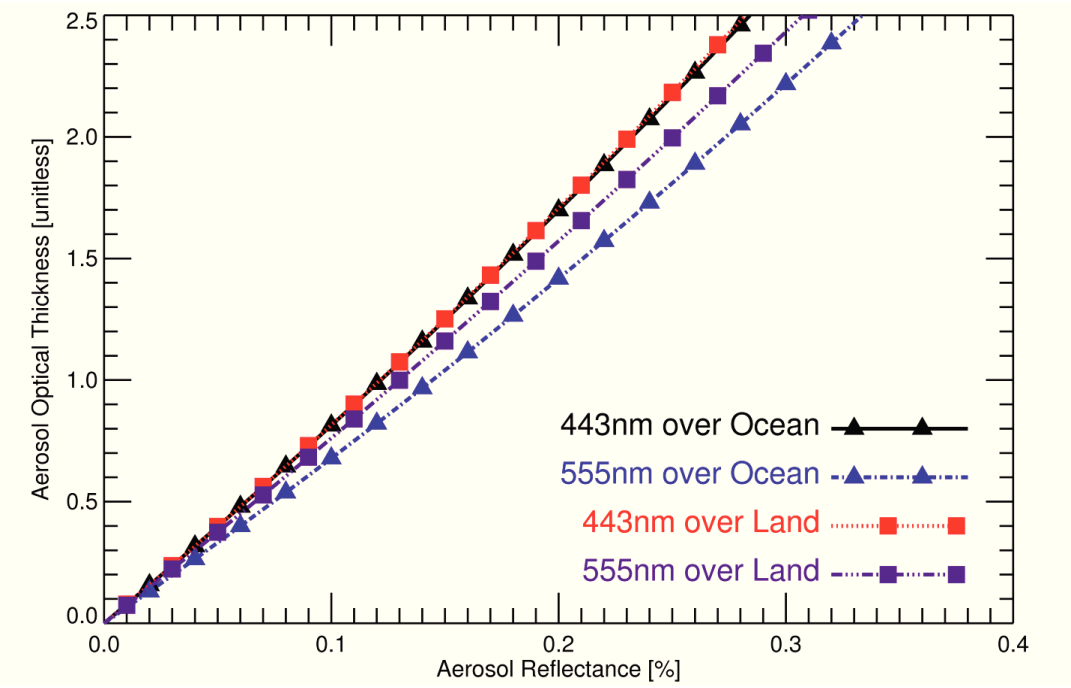

Fig. 3.4 Look-Up Table for SeaWiFS channel 2 (443 nm) and 5 (555 nm), giving relationship between AOT and aerosol reflectance ($\rho_{Aer}(z_0, z_s, \phi, \lambda)$).

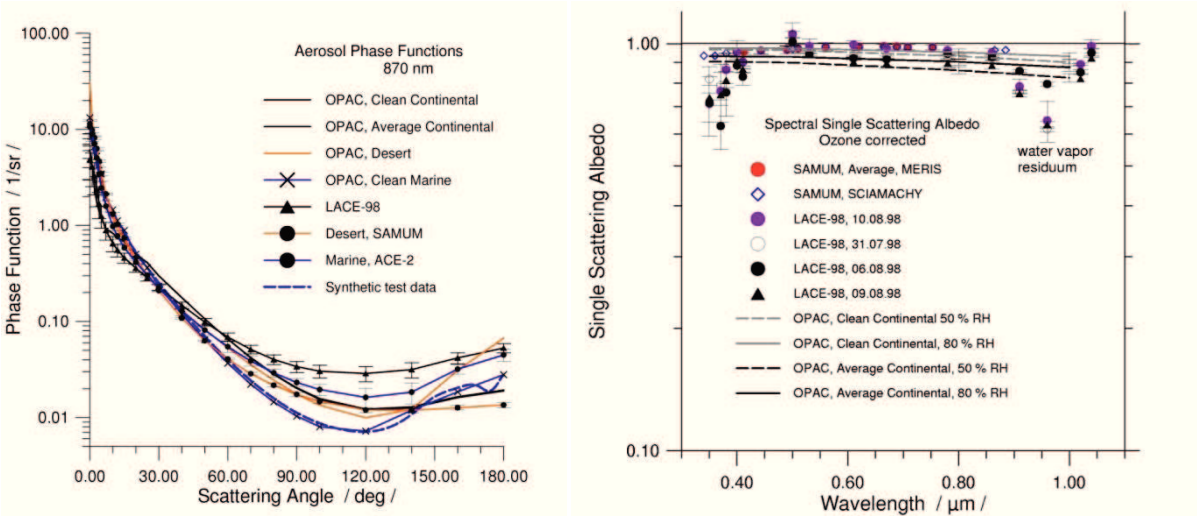

Fig. 3.5 Experimental phase functions (left) and single scattering albedo (right) observed from the experiments, Aerosol Characterization Experiment-2 (ACE-2), LACE-98 and Saharan Mineral Dust Experiment (SAMUM) in comparison with the Optical Properties of Aerosols and Clouds (OPAC) aerosol models. Additionally the dashed line (left) gives the phase function for the synthetic data of the algorithm inter-comparison by Kokhanovsky et al. (2010) [von Hoyningen-Huene et al., 2011].

The final step in this aerosol retrieval deals with cloud screening in order to identify and remove cloud-contaminated pixels from the satellite retrievals. Cloudy pixels are screened out by 1) a reflectance threshold for the minimum cloud reflectance [Kokhanovsky, 2001], 2) checking for decreased spectral TOA reflectance in the blue bands, 3) checking for increased heterogeneity within 5×5 pixels, and 4) adjacency effects around clouds [von Hoyningen-Huene et al., 2011].

Moreover, bright surfaces (like snow and desert surfaces usually having low NDVI) are also removed because the aerosol reflectance is not sensitive over such bright surfaces. Fig. 3.6 shows the global RGB image and AOTs at 443 nm retrieved by BAER. Many pixels are removed as clouds or bright surface. However, despite rigorous cloud-masking schemes, clouds can still remain one of the most serious factors in the uncertainty of aerosol retrieval. Generally, the AOTs are larger over land (especially, close to desert, agricultural, and industrial regions) where mineral dust, biomass burning, and anthropogenic pollutants occur

frequently. The major steps for retrieving AOT based on SeaWiFS data are illustrated as a flowchart in Fig. 3.7.

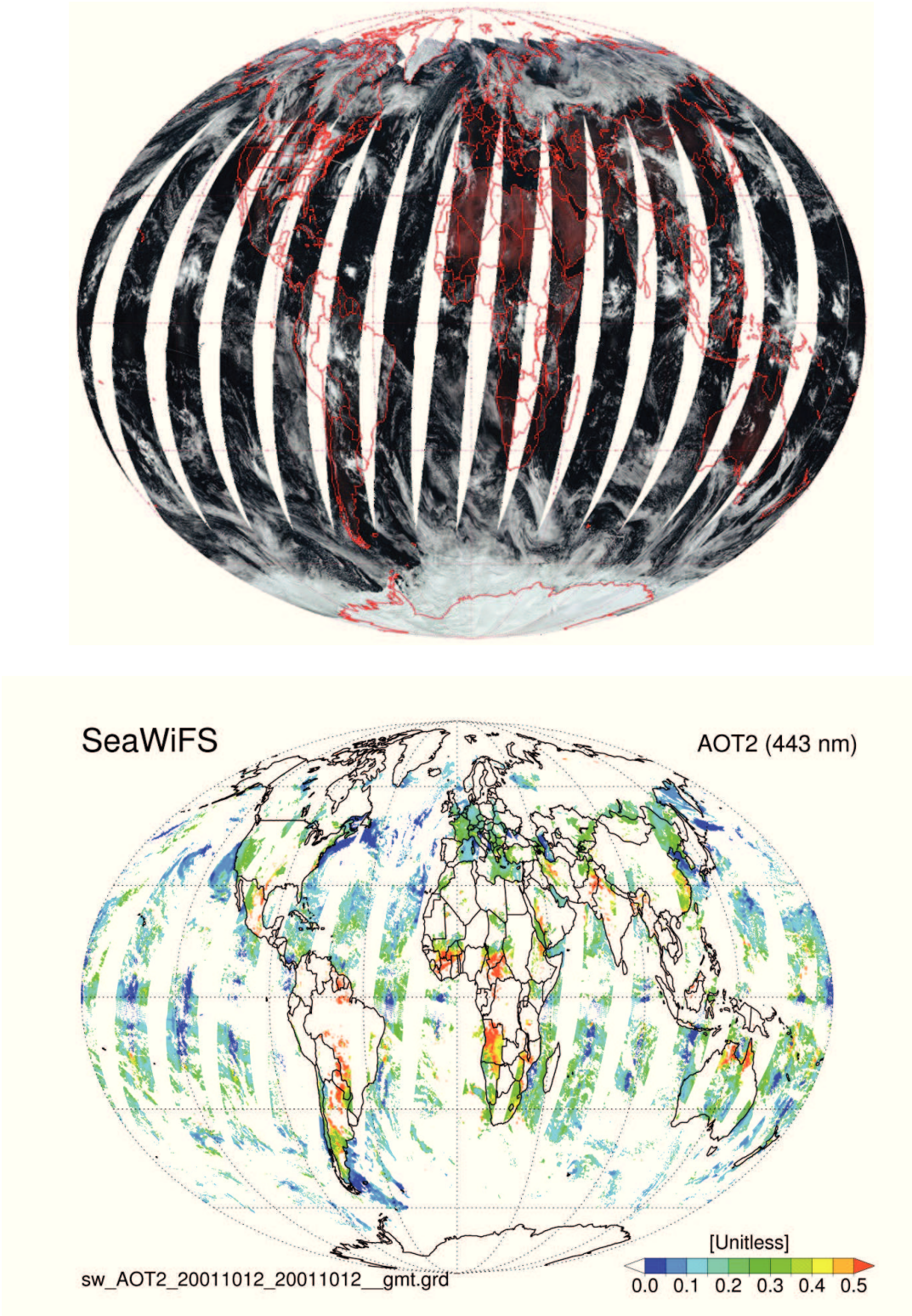

Fig. 3.6 Global RGB composite image (upper) and AOTs at 443 nm retrieved by BAER (lower) using SeaWiFS observations at 12/Oct./2001.

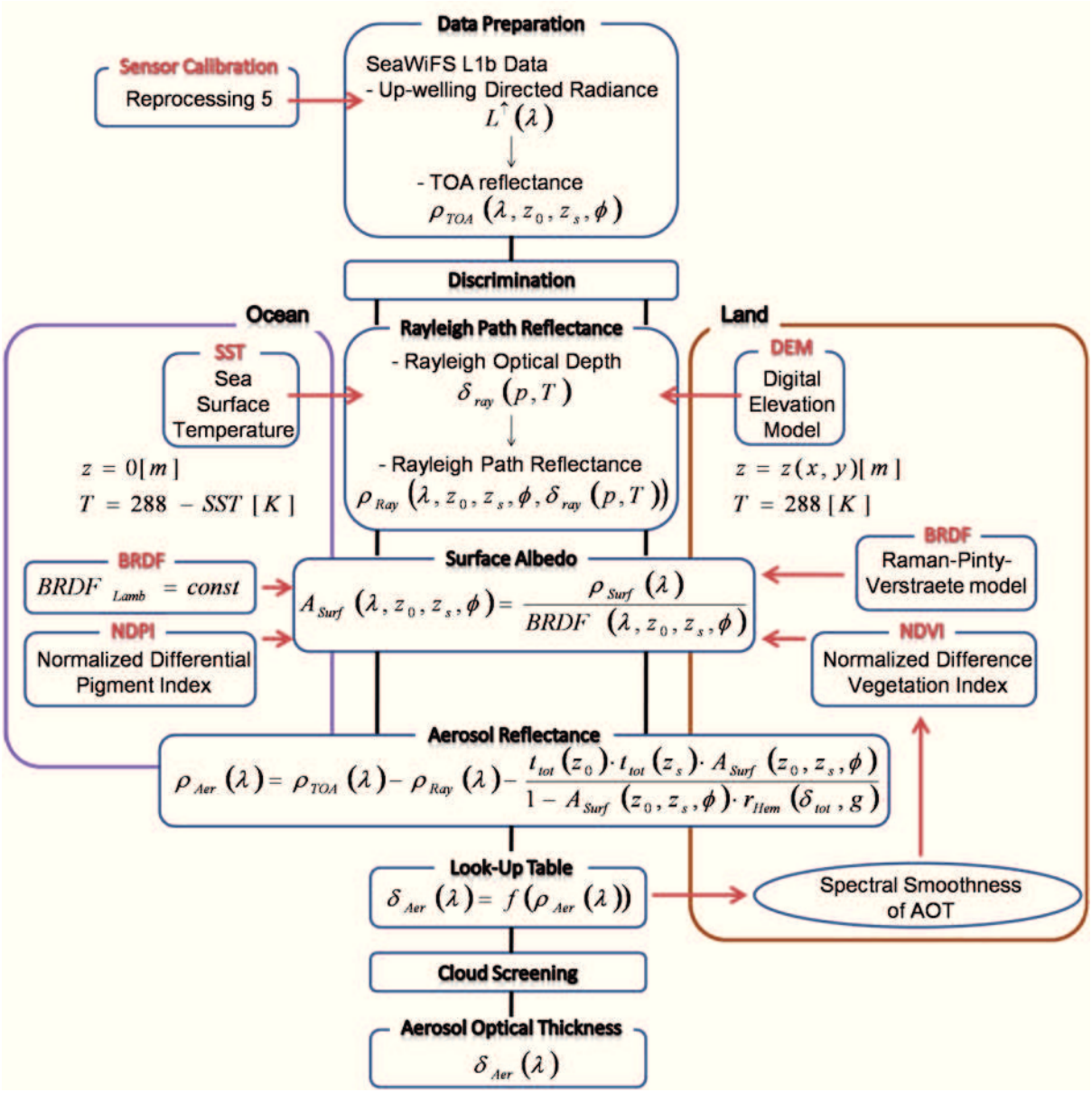

Fig. 3.7 Flowchart of BAER using SeaWiFS data.

3.4 Possible attempts for improving the retrieval accuracy

Recently, many AOT retrieval algorithms have been developed using space-borne measurements offering the capability to cover distributions and variations of global aerosols. However, they have a serious limit in retrieval accuracy due to many assumptions in the algorithm or lack of information observed by sensors. The main error sources in BAER are 1) unscreened clouds, 2) incorrect surface reflectance, and 3) inadequate a priori of aerosol optical properties assumed in the aerosol retrieval. This section suggests some possible attempts for improving the accuracy of BAER.

Cloud screening

The presence of clouds influences AOT retrievals in three ways [Husar et al., 1997; Haywood et al., 2001; Jeong and Li, 2005; Jeong et al., 2005] by 1) thin cloud contamination in aerosol retrieval, 2) misclassification of strong aerosol loading as clouds, and 3) bias in aerosol sampling due to a lack of retrievals in presence of clouds.

Thin cloud contamination causes the retrieved AOT to be overestimated. Therefore, to distinguish thin cloud pixels, many algorithms have adopted very rigid filtering methods. However, this strategy causes another side effect linked to the lack of possible retrievals. The second effect leads to an underestimated AOT due to the removal of pixels dominated by heavy aerosol loading. This underestimation cannot easily be quantified because misclassified aerosols were already removed by cloud masking. In particular, the second effect can induce more serious errors to calculate climatological data (e.g., monthly, seasonal, or annual averages of global and regional AOTs) and their corresponding trends. The third effect introduces a random-like error. The uncertainty from the third effect leads to an over- or underestimation of AOT because cloudy days are underrepresented in the database [Remer et al., 1997; Dubovik et al., 2002a]. Overall, the three superimposed cloud effects can have a

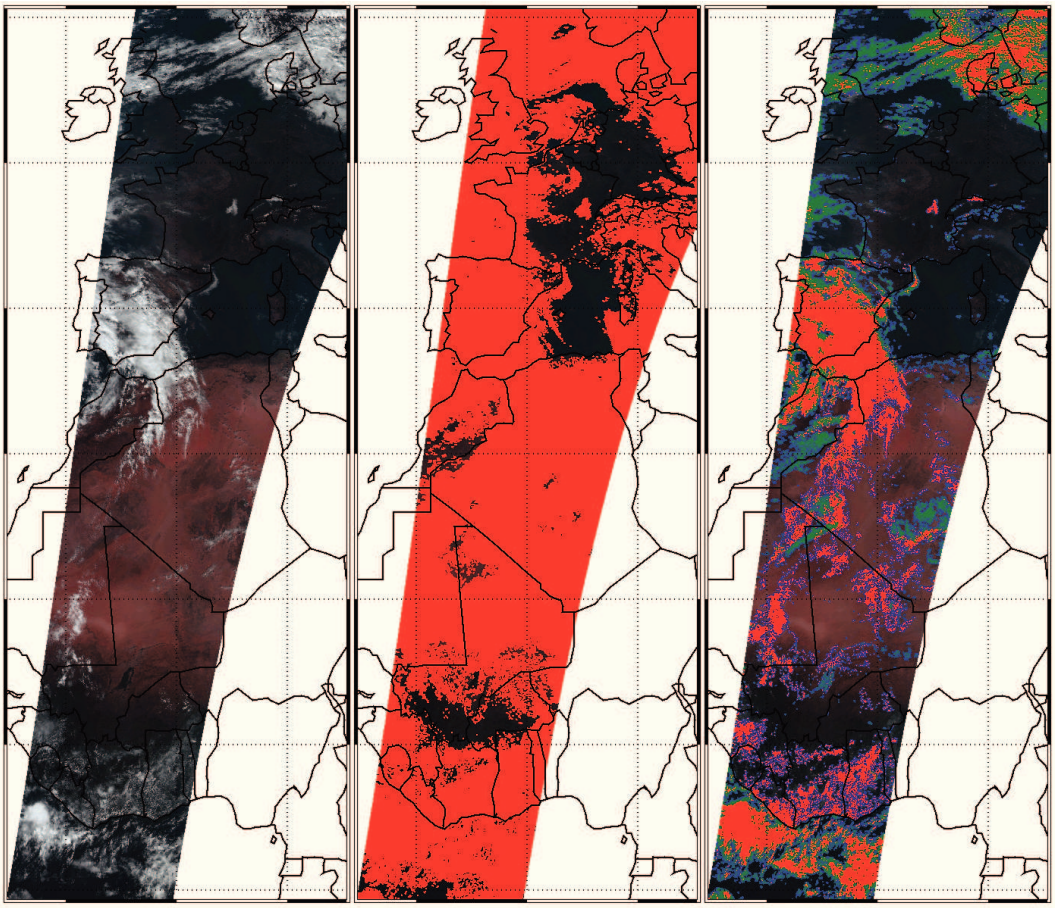

Fig. 3.8 RGB composite image (left), BAER cloud masking (middle), and new cloud masking (right) over Western Europe and North Africa from SeaWiFS observations at 12/Oct./2001.

complicated influence on the accuracy of AOT retrievals.

Fig. 3.8 shows an example of RGB composite image from SeaWiFS TOA reflectances, cloud masking in the latest version of BAER in Section 3.3, and new cloud masking as a possible suggestion. As mentioned above, BAER adopts various and rigid cloud screening methods for more accurate aerosol retrieval. However, compared to the RGB image, they are too strict to detect cloud-free (non-red) pixels. This can lead to the lack of possible aerosol retrievals so that they can be a bias in climatological averaging. The new cloud screening (right one in Fig. 3.8) is better as compared to the middle. In the new method, the whiteness and brightness of clouds are checked using spectral slope, mean, and standard deviation of SeaWiFS TOA reflectances. Red, green, and blue colors in the right figure are represented as

thick, thin clouds, and adjacency effects around clouds, respectively. Clearly, this method can improve the cloud screening in the future BAER, and minimize non-retrievals caused by cloud disturbance, so that it is possible to derive more reliable trend of cloud-free AOT.

Aerosol optical properties

Aerosol optical properties as a priori used for LUT pre-calculation are very important in satellite-based retrievals because they are dependent on various aerosol sources and regional meteorological conditions. Nonetheless, many algorithms have adopted a few kinds of the properties observed from ground-based experiments. Fig. 3.9 demonstrates some examples of the aerosol properties (i.e., spectral AOTs, SSAs, and phase function at 440 nm) from AERONET observations. The stations Lille, Ispra, and Venise over Europe regions are influenced by a typical type of industrial aerosols (spectral increase of SSA by longer wavelengths) while the FORTH_CRETE station is influenced by maritime aerosol or desert dust (spectral decrease of SSA by longer wavelengths). The aerosol properties at the station

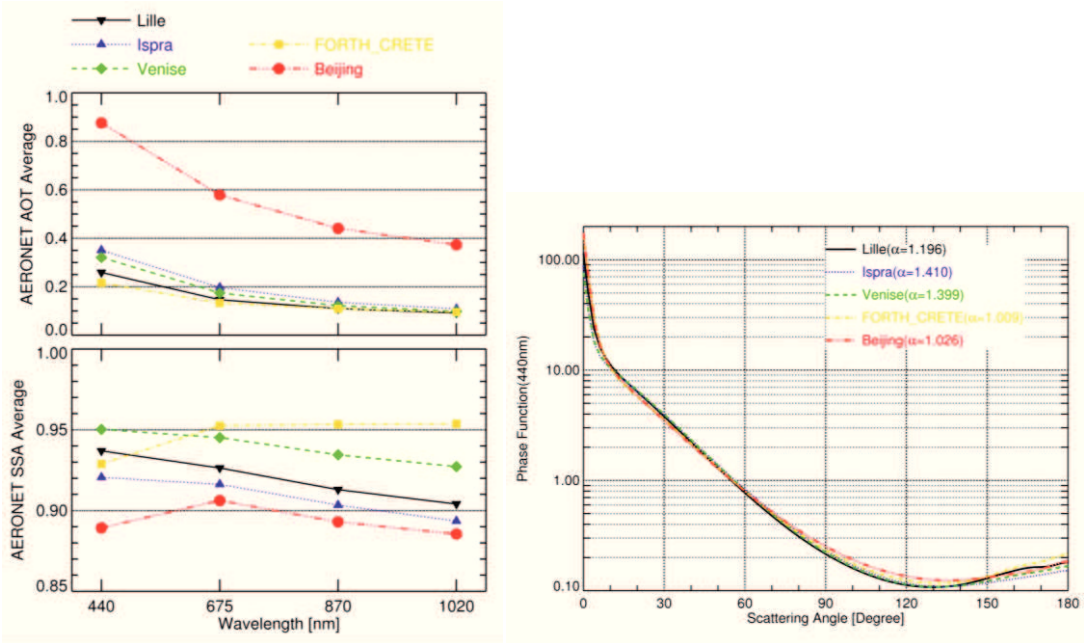

Fig. 3.9 Total mean of spectral AERONET AOTs, SSAs (440, 675, 870, and 1020 nm), and phase function (440 nm) at Lille, Ispra, Venise, FORTH_CRETE, and Beijing stations.

Beijing show the complicated combinations of natural and anthropogenic aerosols due to desertification, industrialization, and urbanization over China. Therefore, it is necessary to set up a database of global aerosol properties for better retrieval accuracy using satellite observations. In the following Section 5.3, various aerosol optical properties (i.e., AOT, SSA, volume size distribution, and phase function) at several AERONET stations with long-term observations will be provided for building a database of global aerosol properties.

Surface reflectance

The multiple scattering between surface and atmosphere is very important over land surfaces, where the surface reflectance varies significantly due to human activity and natural variation. Thus, separating the exact aerosol reflectance from the surface reflectance is directly connected to an accurate AOT retrieval over land using satellite remote sensing (see Section 3.2). Therefore, the evaluation of the surface reflectance modeled by BAER is a prerequisite to improve the retrieval accuracy.

Firstly, the surface reflectance is simulated by the BAER surface model using MODIS radiances, and then the simulated surface reflectance is compared to the MODIS surface

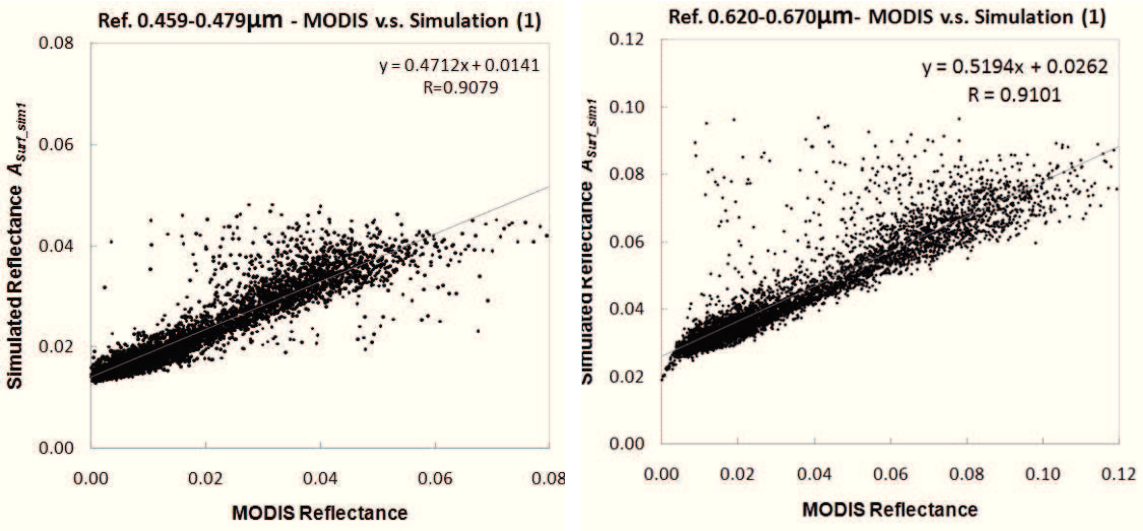

Fig. 3.10 Comparison between MODIS surface reflectance and simulated reflectance by BAER approach at 459-479 nm (left) and 620-670 nm channels (right) [Chiang et al., 2012].

reflectance. Fig. 3.10 shows the comparisons between the MODIS surface reflectances (459-479 nm and 620-670 nm) and simulated reflectance by BAER [Chiang et al., 2012]. They are in good agreement providing high correlation coefficients (R = 0.9079 and 0.9101). However, the BAER surface model tends to overestimate surface reflectance (thereby, underestimate AOT) for low reflectance, and to underestimate it (overestimate AOT) for high. These differences can cause a discrepancy between BAER and MODIS AOTs.

Another evaluation method of BAER surface reflectance is to model the surface reflectance using Radiative Transfer Model (RTM) with SeaWiFS TOA reflectances, various AERONET aerosol properties (i.e., AOT, size distribution, and refractive index), and absorbing gas contents (i.e., total ozone from Global Ozone Monitoring Experiment (GOME), Scanning Imaging Absorption Spectrometer for Atmospheric CHartographY (SCIAMACHY),

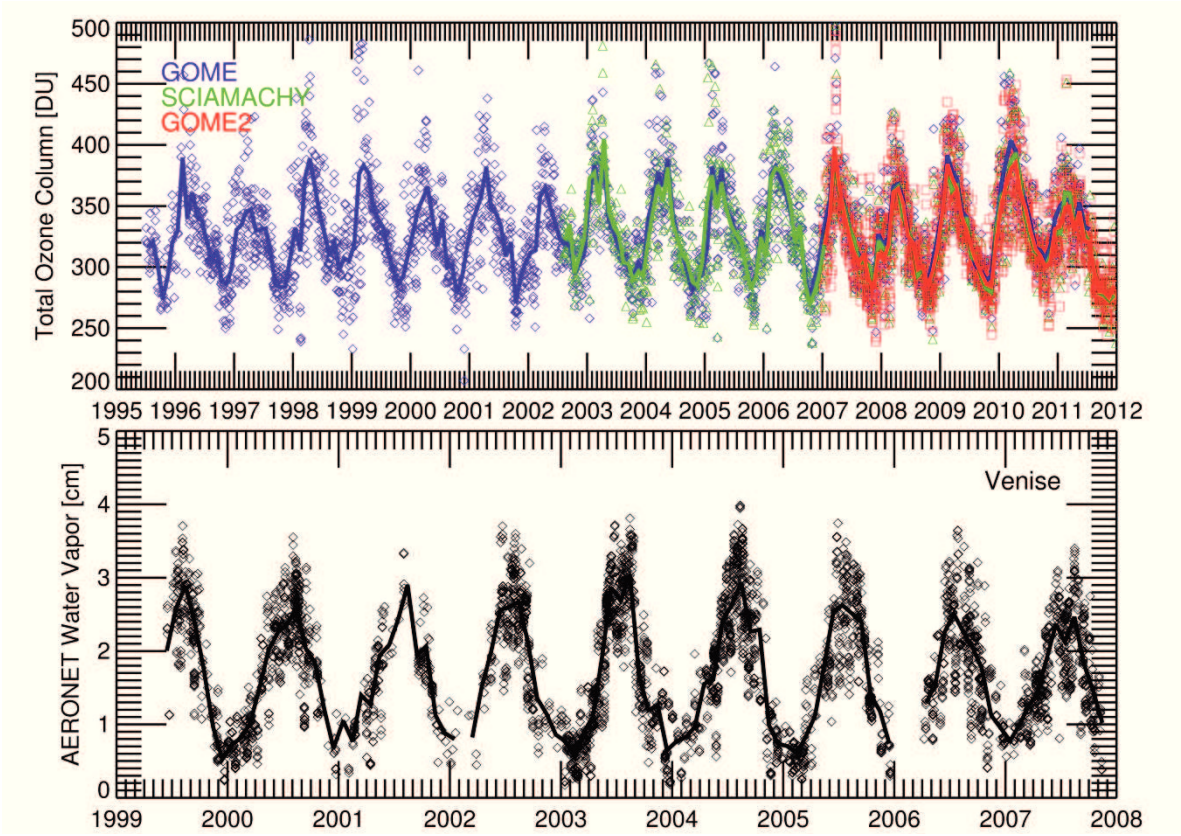

Fig. 3.11 Long-term time series of ozone and water vapor observed by Global Ozone Monitoring Experiment (GOME), Scanning Imaging Absorption Spectrometer for Atmospheric CHartographY (SCIAMACHY), GOME-2, and AERONET over Venise region.

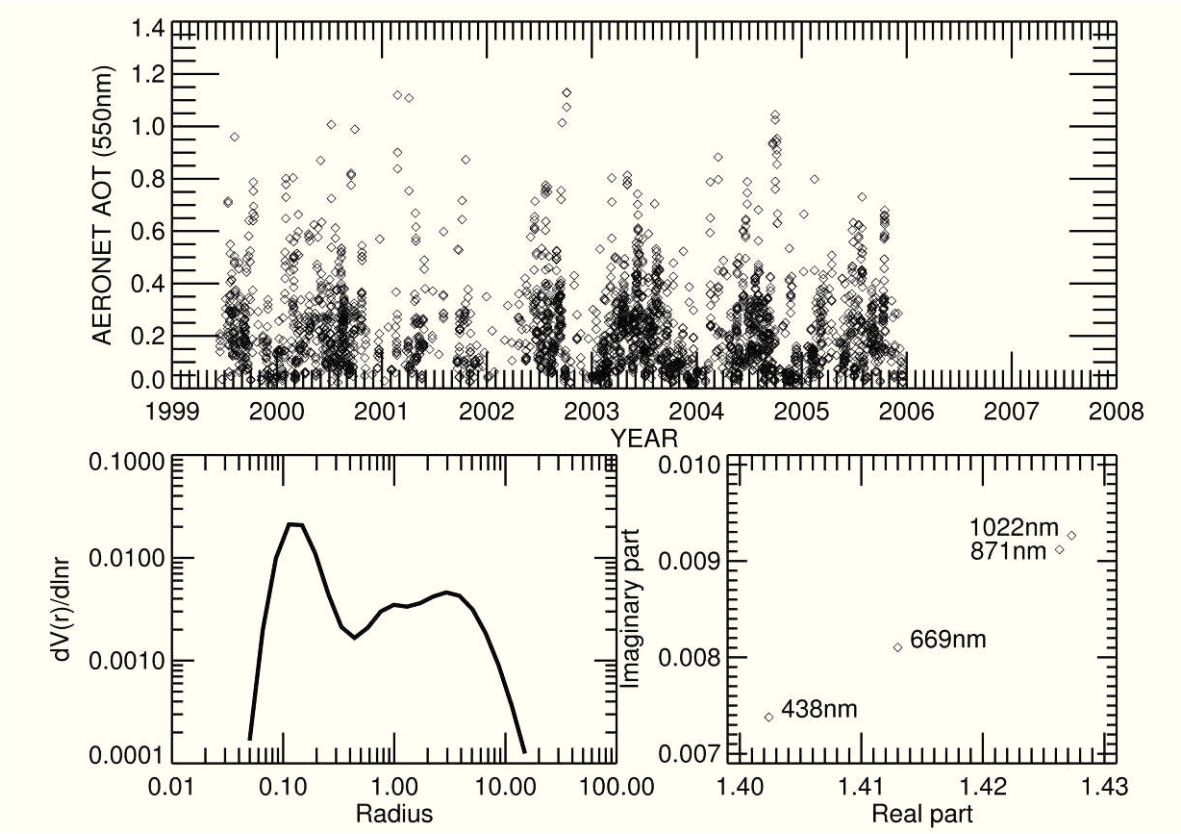

Fig. 3.12 Long-term time series of AERONET AOT (550 nm), and aerosol size distribution and spectral refractive indices (438, 669, 871, and 1022 nm) on 12/10/2001.

GOME-2, and water vapor from AERONET). Fig. 3.11 illustrates long-term time series of total ozone and water vapor observed from GOME, SCIAMACHY, GOME-2, and AERONET over the region including the station Venise. Using these input parameters, the spectral surface reflectances are simulated by RTM for the case of 12/10/2001, 12:13:33 UTC. As drawn in Fig. 3.13, the spectral surface reflectances retrieved by BAER surface model are generally overestimated in comparison to the simulated reflectance, which is consistent with the comparisons in Chiang et al. (2012) (see Fig. 3.10). In other words, the overestimated surface reflectance can influence the underestimation of AOT in BAER retrievals. Therefore, for better AOT retrieval accuracy over land, the BAER surface model will be improved through such various evaluations.

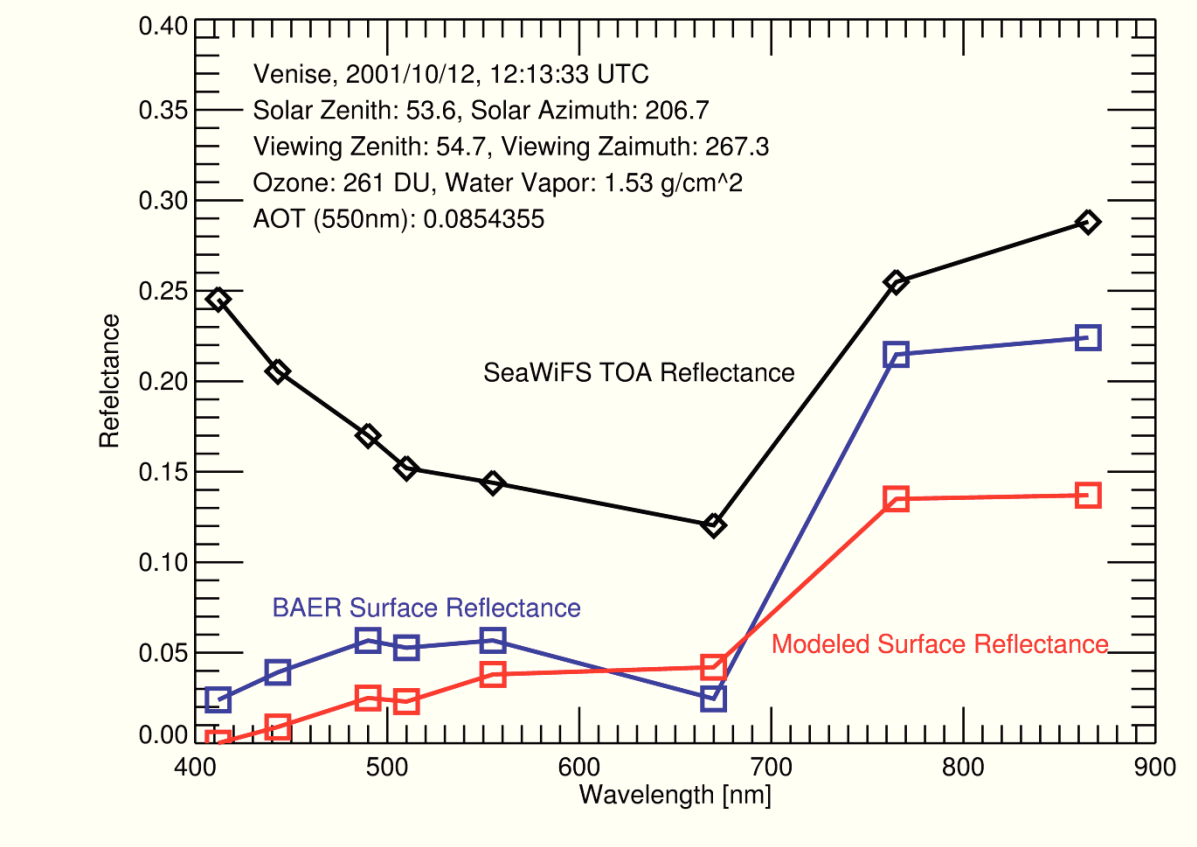

Fig. 3.13 Spectral SeaWiFS TOA reflectances and surface reflectances retrieved by BAER and RTM with various input parameters: geometry angles (i.e. Solar Zenith, Solar Azimuth, Viewing Zenith, Viewing Azimuth angles), ozone, water vapor, and aerosol optical properties.

4. Analysis of linear long-term trend of AOT derived from SeaWiFS

Before going on with the analysis of the BAER AOT trends using SeaWiFS observations, it is important to verify BAER's retrieval accuracy through the comparison with ground-based observations, AERONET AOT. Furthermore, since the verified retrieval accuracy does not guarantee to estimate a reliable cloud-free AOT trend due to cloud disturbance, the trend comparison is also an essential prerequisite for the trend analysis. Therefore, based on the two validations of BAER AOTs and corresponding trends, this chapter deals with the analysis of the BAER AOT trends over Europe and South China regions (BeNeLux (Belgium/Netherlands/Luxemburg), Po Valley, Eastern Europe, Eastern Mediterranean, and Pearl River Delta, shown by Fig. 4.1 and listed in Tab. 4.1), and has been published by Yoon et al. in *Atmospheric Chemistry and Physics*, 2011. These centers of population have been assigned within the CityZen project (megaCITY - Zoom for the Environment: EU 24 Framework Programme 7 of European Commission) as being of particular significance. Especially, most of European regions are air pollution hotspots constituted by densely populated cluster of large cities [Colette et al., 2011]. Eastern Mediterranean has been received much interest with regard to the effects of aerosol [Gerasopoulos et al., 2011] because of particularly large aerosol loading in the area [Lelieveld et al., 2002]. Pearl River Delta is one of the three areas in China which have experienced extremely fast economic development [Xiao et al., 2011]. Rapid urbanization and industrialization over the last few decades have introduced more complexity to air pollution issues in this area [Zhang et al., 2008]. CityZen has aimed to determine air pollution distribution and corresponding changes in and around the selected areas over the last decade [http://wiki.met.no/cityzen/start].

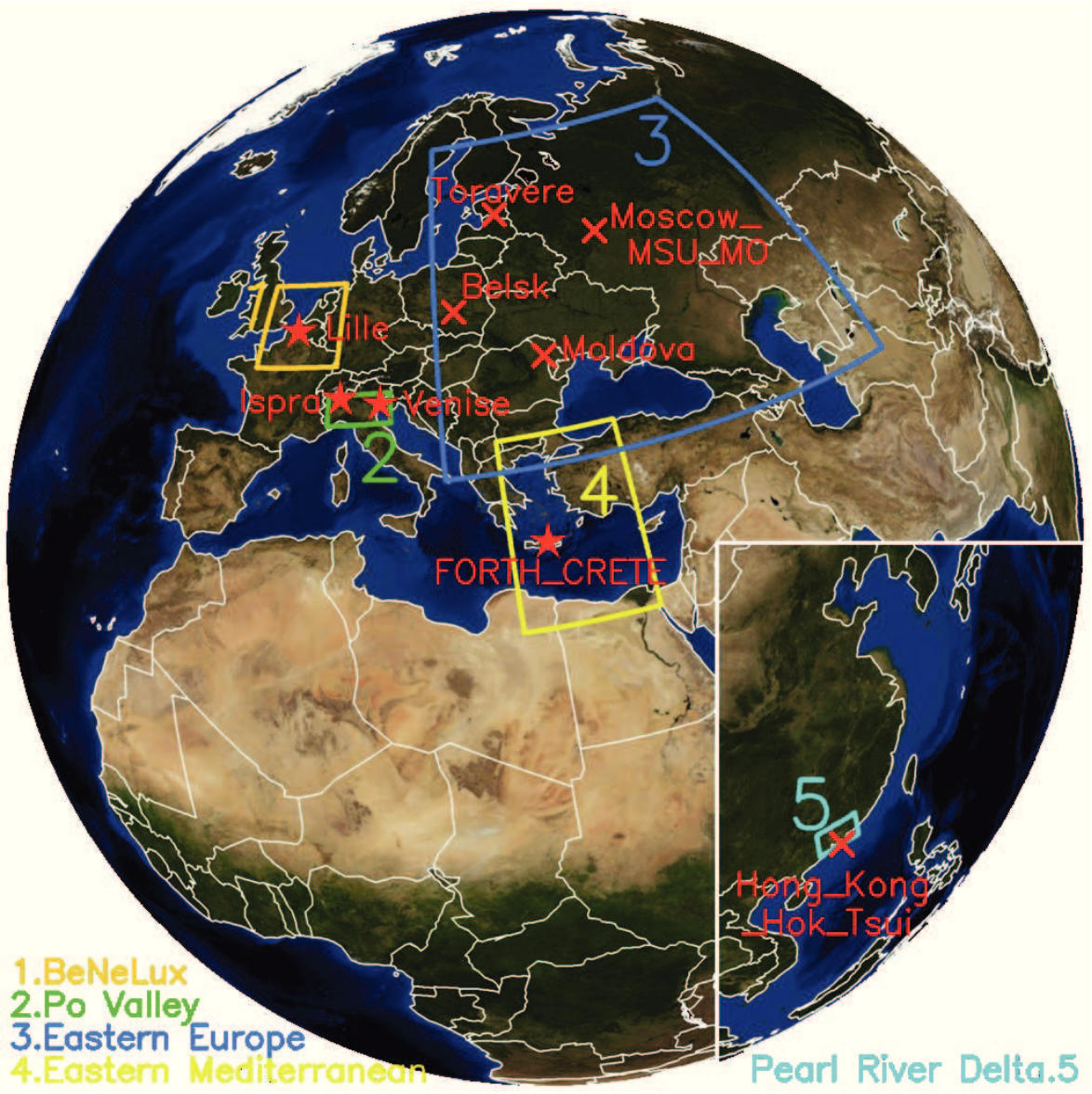

Background RGB source: http://visibleearth.nasa.gov/

Fig. 4.1 Several regions (BeNeLux (Belgium/Netherlands/Luxemburg), Po Valley, Eastern Europe, Eastern Mediterranean, and Pearl River Delta in South China) for analysis of linear long-term trends of AOTs retrieved by BAER, and AERONET stations (red star or cross symbols) for three purposes described in Tab. 4.1.

Tab. 4.1 Geolocations of several regions for linear long-term trend of BAER AOT and information summary of AERONET data.

Regions for BAER AOT trend	Geolocations lon.(min/max)/lat.(min/max)[°]	AERONET stations (regions)	Geolocation lon.[°]/lat.[°]/alt.[m]	Purpose*	Observation Period
1.BeNeLux	(-1.0/8.0)/(48.0/54.0)	Lille (-)	3.142/50.612/60	I, III	1994-NOV~2008-JUN
2.Po Valley	(7.5/13.5)/(44.0/46.0)	Ispra (-)	8.627/45.803/235	I, II, III	1997-JUN~2008-FEB
		Venise (Venice)	12.508/45.314/10	I, II, III	1999-JUN~2009-NOV
3.Eastern Europe	(18.0/60.0)/(40.0/65.0)	Toravere (-)	26.460/58.255/70	III	2002-JUN~2008-NOV
		Moscow_MSU_MO (Moscow)	37.510/55.700/192	III	2001-SEP~2008-NOV
		Moldova (-)	28.816/47.000/205	III	1999-SEP~2009-MAY
		Belsk (-)	20.792/51.837/190	III	2002-APR~2008-OCT
4.Eastern Mediterranean	(22.5/32.5)/(30.0/42.0)	Forth_Crete (Crete)	25.282/35.333/20	I, II, III	2003-JAN~2008-MAR
5. Pearl River Delta	(112.0/115.5)/(22.0/24.0)	Hong_Kong_Hok_Tsui (Hong Kong)	114.258/22.210/80	III	2007-NOV~2009-AUG

* The AERONET data were mainly used for three purposes, which are (I) validation of BAER retireved AOTs, (II) validation of BAER AOT trends, and (III) investigation of climatological aerosol characteristics. For purpose I and II, AERONET Level 2.0 (pre- and post-field calibration applied, cloud-screened, and quality-assured) all-point and monthly AOTs were employed respectively. For purpose III, Level 2.0 inversion all-point data (volume size distribution and SSA) were used for analysis of aerosol characteristics.

As mentioned before, the validation process of AOT retrievals based on satellite observations is essential because there are many uncertainty factors of satellite retrievals especially over land. Therefore, a validation of the reliability and accuracy of BAER retrieved AOTs at 443 and 555 nm is required by comparison to independent data. In this study, AERONET Level 2 AOTs at selected stations (locations labeled with red stars in Fig. 4.1) having a long observation history (more than five years) are used for the validation. Even though there are a lot of AERONET stations within the regions of interest, not all stations are suitable for the validations of AOTs and AOT trends because they do not distribute sufficiently long-term and continuous data records. Furthermore, BAER is still limited in the retrieval of AOT using SeaWiFS data (in visible wavelength range) over some regions, which are affected by frequent cloud disturbance or/and high surface reflectance. Especially, at some AERONET stations in Pearl River Delta (Hong Kong) and at higher latitude over the Eastern Mediterranean it is difficult to compare BAER with AERONET AOTs. Thus, only four AERONET stations can be used for this validation. The AERONET AOT at 555 nm is derived using AERONET ÅE (computed by two AOTs at 440 and 675 nm) and AOT at 675 nm because major wavelengths of AERONET AOT are 440, 675, 870, and 1020 nm. Prior to the validation process, an essential step is to identify and remove cloud-contaminated scenes from the satellite retrievals. Despite the rigorous cloud-masking schemes in BAER, clouds could still remain one of the most serious uncertainties in the aerosol retrieval. In order to reduce the remaining impact caused by cloud contamination, an additional cloud filtering method is applied for cases that the averaged AOT exhibits high standard deviation.

4.1 Validations of BAER AOTs and corresponding trends

BAER retrieved AOTs

In Fig. 4.2 (a) - (d), AOTs retrieved using BAER are compared with AERONET AOTs at 443 (diamond symbol) and 555 nm (square symbol) over stations located in Lille, Ispra, Venice, and Crete for the observation periods available, as listed in Tab. 4.1. In order to make a comparison between AERONET and BAER data, this study uses the temporal averages of AERONET AOTs within ±30 minutes compared with the SeaWiFS over-passing time and the spatial averages of $0.12° \times 0.12°$ pixels of BAER AOTs co-located with the AERONET station. The correlation coefficient (R), Relative Root-Mean-Square Difference (RMSD),

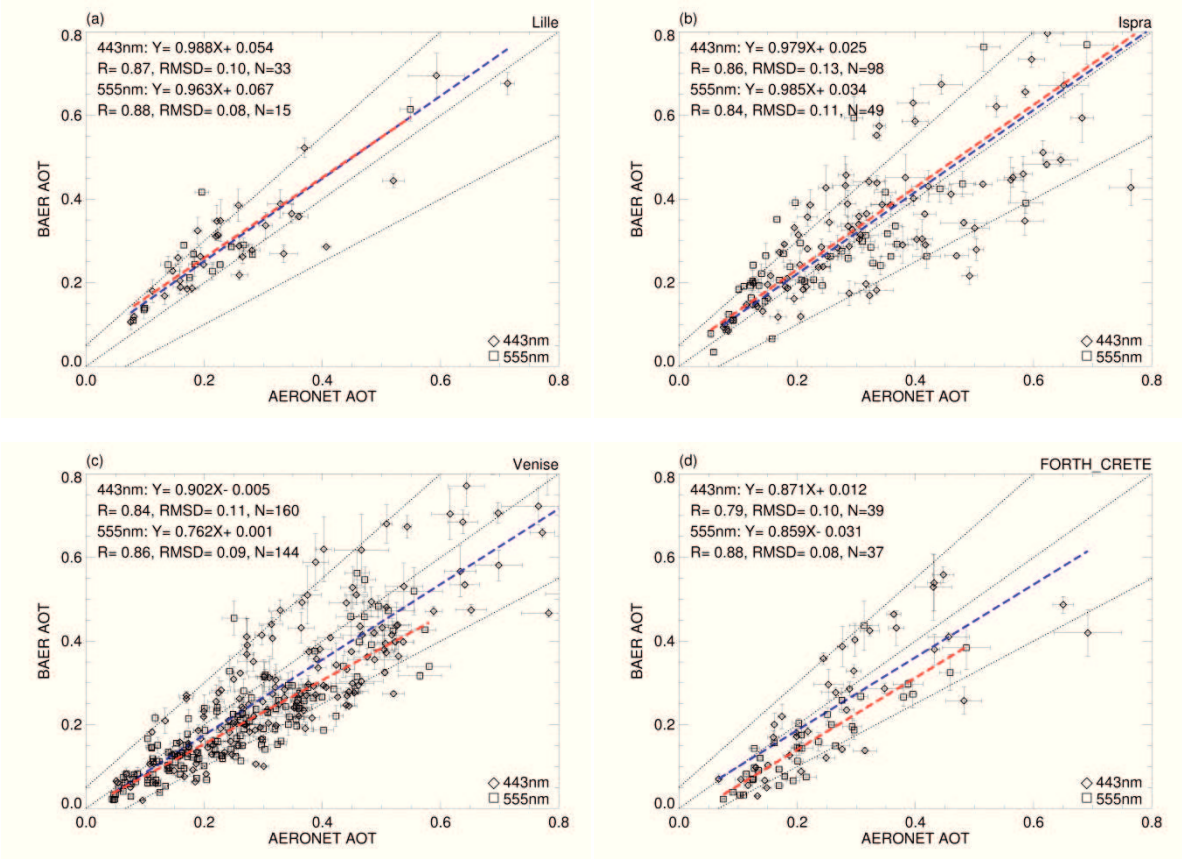

Fig. 4.2 Validation between BAER and AERONET AOTs (443 and 555 nm) at (a) Lille, (b) Ispra, (c) Venice (Venise), and (d) Crete (Forth_Crete). Linear correlation equations between them are shown as correlation blue and red lines at 443 and 555 nm. The guide dot-lines [von Hoyningen-Huene et al., 2011] indicates the error range of BAER AOT retrieval: $\pm 0.05 \pm 0.25 \times \mathrm{AOT}$.

and linear correlation equation ($y = Ax + B$) between them reveal good agreement ($0.79 \leq R \leq 0.88$, $0.08 \leq RMSD \leq 0.13$, $0.762 \leq A \leq 0.988$, and $-0.031 \leq B \leq 0.067$) at all stations. In general, the retrieval accuracy is following the guide dot-lines in Fig. 4.2, which present the error range or uncertainty of BAER AOT retrieval: $\pm 0.05 \pm 0.25 \times AOT$ [von Hoyningen-Huene et al., 2011]. Slope (A) closer to 1 means the appropriateness of aerosol properties used for the pre-calculation of LUT. Intercept (B) closer to 0 indicates how accurate surface contribution is considered in aerosol retrieval. Furthermore, a large error bar on the points can present the possibility of cloud contamination. Clearly, there are still some discrepancies, caused by three main factors: 1) unscreened clouds, 2) incorrect surface reflectance, and 3) inadequate aerosol optical properties assumed in BAER.

BAER AOT trends

Even though previous validations indicated that BAER and AERONET AOTs are in good agreement, it is important to ensure that AOT trends retrieved using satellite observations are highly reliable. This is achieved by undertaking an additional validation of BAER and AERONET AOT trends. First, a simple linear model, which is used to minimize chi-square error statistics, is adopted for the estimation of both trends. In order to analyze accurate trends, the simple model needs to be analyzed with respect to AOT variability, which is usually autocorrelated [Zhao et al., 2008]. Even this linear model might be far away from the reality, it allows a simple approximation of direction and magnitude of the changes in the data for many practical purposes [Weatherhead et al., 1998]. Previous studies also have adopted the simple linear model for AOT trend analysis [Mishchenko et al., 2007; Mishchenko and Geogdzhayev, 2007; Zhao et al., 2008; Papadimas et al., 2008; Yu et al., 2009; Xie and Xia, 2008; Kishcha et al., 2009; Karnieli et al., 2009; de Meij et al., 2010; Kaskaoutis et al., 2011b].

Let Y_t be the monthly AOT values, which are calculated with daily AOTs in a month. The linear trend model is given by Eq. (4.1), where μ is a constant term and ω is the magnitude of the trend per year ($\mathrm{X_t} = \mathrm{t}/12$).

$$Y_t = \mu + \omega \mathrm{X_t} + \mathrm{N_t},\ t = 1 \ldots T \tag{4.1}$$

To investigate the effects of the magnitude and autocorrelation of noise on the estimated trend, the noise N_t is assumed to be autoregressive of first order like in Eq. (4.2), where ε_t is an independent random variable and ϕ is autocorrelation coefficient with $-1 < \phi < 1$ [Weatherhead et al., 1998]:

$$N_t = \phi \mathrm{N_{t-1}} + \varepsilon_t. \tag{4.2}$$

The estimated trend ($\hat{\omega}$) is determined by minimizing the chi-square error statistics.

The variance (σ_N^2) of the noise ($\mathrm{N_t}$) is obtained, and also related to the variance (σ_ε^2) of the white noise (ε_t) by the following equation:

$$\sigma_N^2 = Var(\mathrm{N_t}) = \frac{\sigma_\varepsilon^2}{(1-\phi^2)}. \tag{4.3}$$

Finally, the precision or uncertainty of the trend is given by the following equation:

$$\sigma_{\hat{\omega}} \approx \frac{\sigma_\varepsilon}{(1-\phi)} \frac{1}{\mathrm{n}^{3/2}} = \frac{\sigma_N}{\mathrm{n}^{3/2}} \sqrt{\frac{1+\phi}{1-\phi}}, \tag{4.4}$$

where $\mathrm{n} = T/12$ denotes the number of years. Additionally, a common decision rule is adopted that the trend is supposed to be real when the significance ($|\hat{\omega}/\sigma_{\hat{\omega}}|$) of the trend is larger than two at a 5% significance or 95% confidence level [Tiao et al., 1990]. Fig. 4.3 depicts the linear trends of BAER and AERONET monthly AOTs at 443 and 555 nm. Generally, negative trends are similar for both data sets, but their magnitudes are quite different. Especially, the significance values of BAER trends are poor ($|\hat{\omega}/\sigma_{\hat{\omega}}| << 2$), except for the values from Venice ($|\hat{\omega}/\sigma_{\hat{\omega}}|$= 1.58 and 1.72 at 443 and 555 nm) due to small variability of monthly AOTs

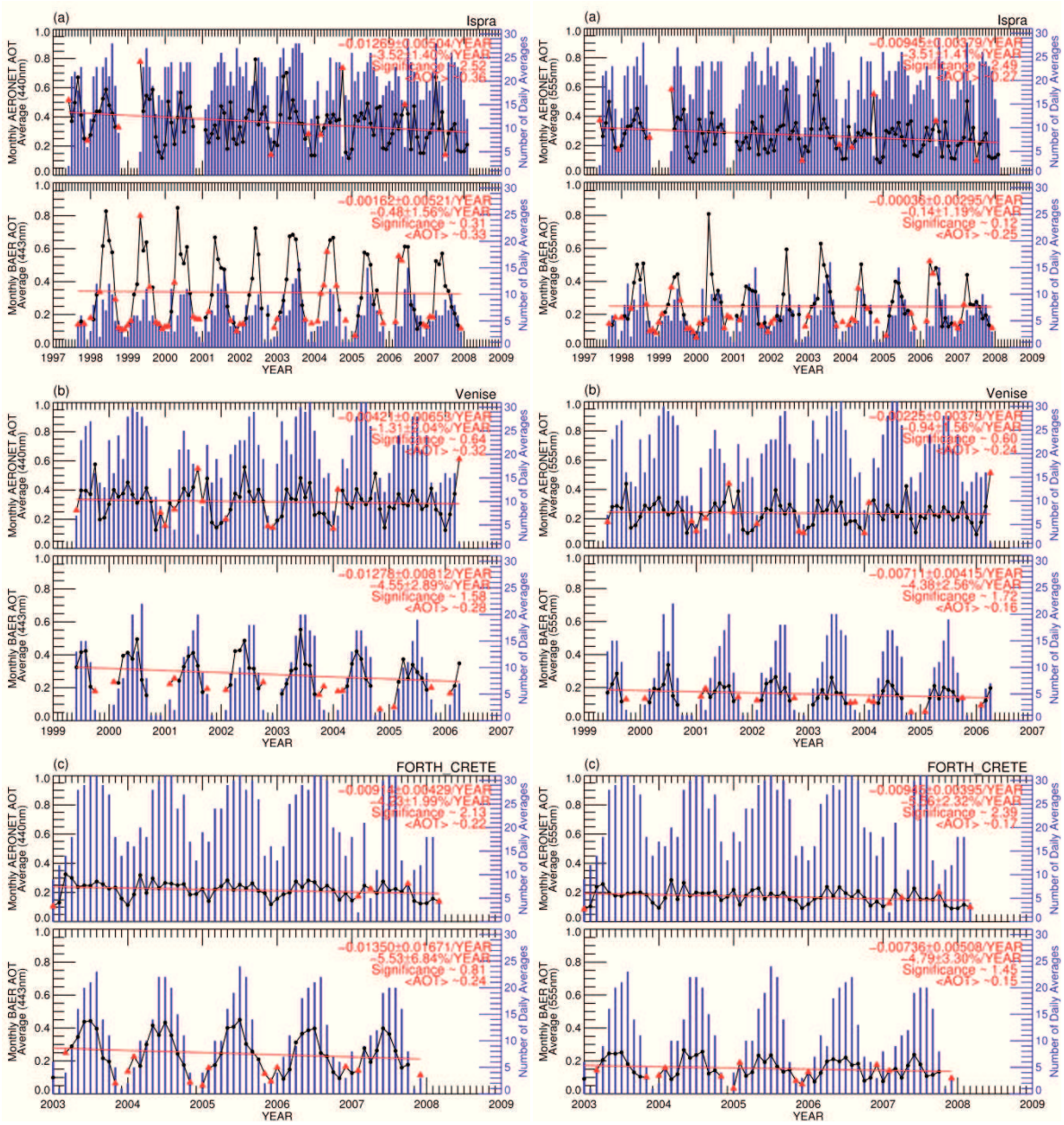

Fig. 4.3 Total AOT averages (<AOT>) and statistical parameters for linear long-term trends of AERONET and BAER AOTs at 443 nm (left-hand black circle and red triangle symbols) and 555 nm (right-hand) at (a) Ispra, (b) Venice (Venise), and (c) Crete (Forth_Crete). Non-representative monthly AOTs (red triangle symbol) were defined as the average of less than five daily AOTs from BAER and ten from AERONET. Blue histograms show daily observation number per each month (right axis).

In order to achieve statistical significance, a sufficient number of observations are needed. As mentioned in Section 3.4, the presence of clouds can seriously influence the observation number in AOT retrievals. As seen the trends on the upper-right hand side in Fig. 4.3, it can also make a difference between AERONET and BAER AOT trends in spite of good retrieval accuracy of BAER as demonstrated in Fig. 4.2. For the consideration of the cloud effects, a histogram analysis is introduced (right axis in Fig. 4.3). Based on statistical and visual analysis, non-representative monthly AOTs are defined (shown as red triangle symbols in Fig. 4.3) when having less than five daily AOTs for BAER retrievals and ten for AERONET. According to these criteria, the AERONET station of Lille has been excluded from this approach because most of the BAER AOTs are identified as non-representative.

For a direct comparison between the trends of AERONET and BAER under the same conditions, non-representative monthly AOTs are inter-corrected from the opposite data set (representative values) using the linear correlation equations (blue and red correlation lines shown in Fig. 4.2). This approach derives a better agreement between BAER and AERONET AOT trends. Fig. 4.4 illustrates both trends based on inter-corrected (blue diamond symbol) and representative monthly AOT (black circle symbol) at 443 and 555 nm including their statistical significance. Magnitudes of both trends now agree much better with higher statistical significances. Most of the inter-corrections have been performed in winter time because it is the cloudy season over Europe.

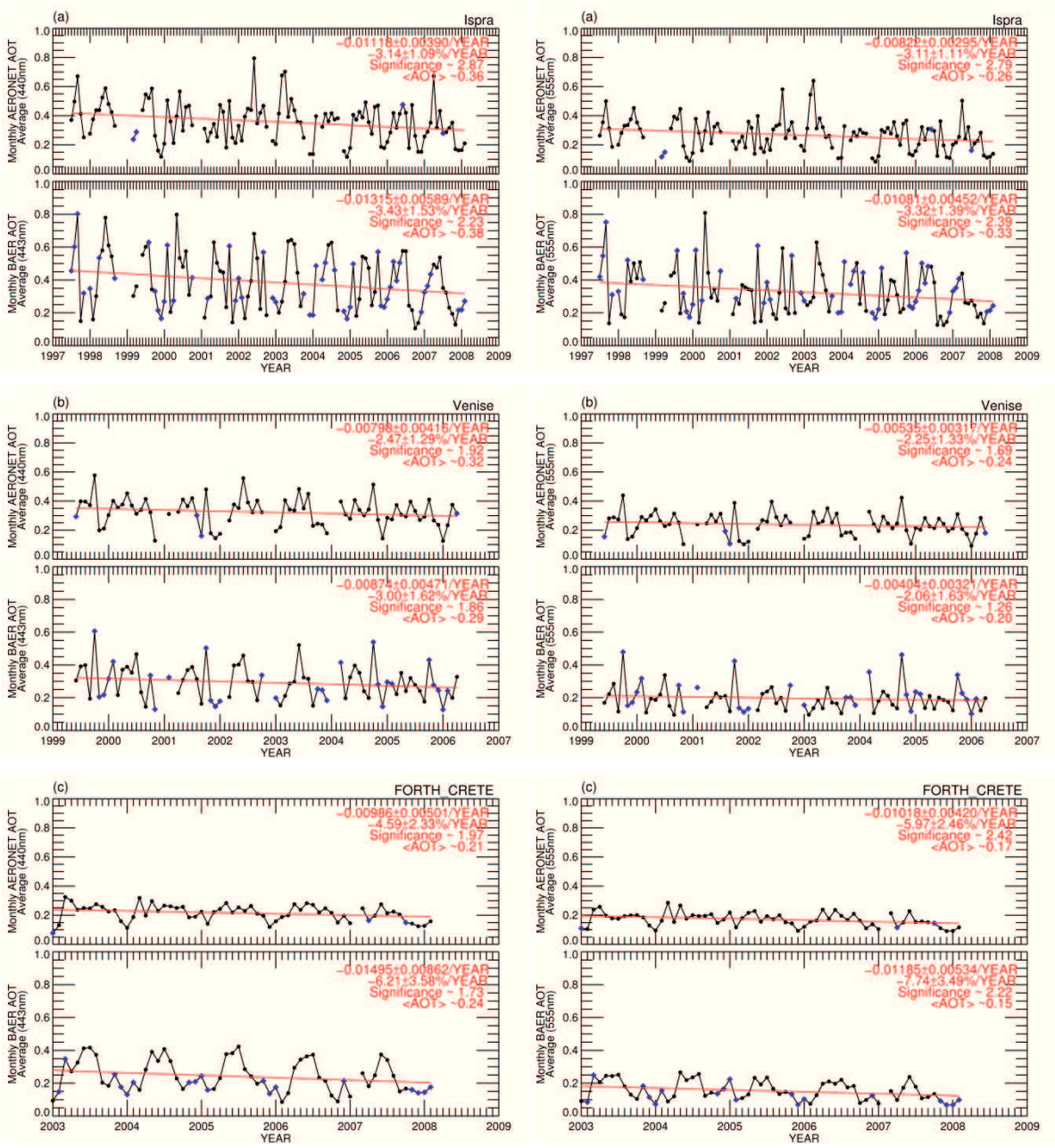

Fig. 4.4 Total AOT averages (<AOT>) and statistical parameters for linear long-term trends of representative and inter-corrected AOTs at 443 nm (left-hand black circle and blue diamond symbols) and 555 nm (right-hand) from AERONET and BAER at (a) Ispra, (b) Venice (Venise), and (c) Crete (Forth_Crete). The non-representative monthly AOTs (red triangle symbols in Fig. 4.2) are inter-corrected using the linear correlation equations in Fig. 4.1.

Fig. 4.5 demonstrates the linear long-term AOT trends before (red) and after (blue) applying the inter-correction method described above. Clearly, the trends of BAER and AERONET AOTs agree within error (for example: average of relative difference ~25.19%) after application of the method. Through the trend validation, it can be concluded that one of the most serious factors leading to the difference of trend magnitudes is cloud disturbance reducing the numbers of possible retrievals.

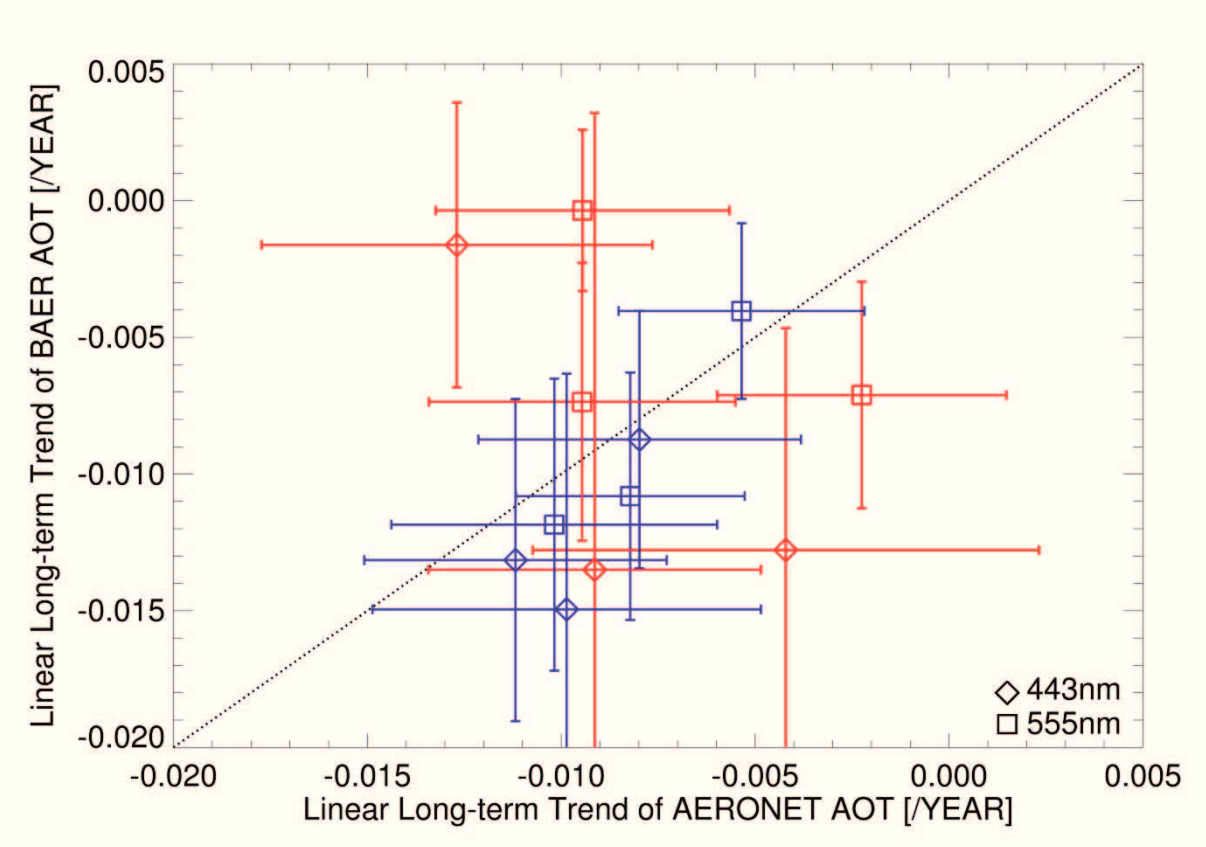

Fig. 4.5 Trend validations of AERONET and BAER AOTs (443 and 555 nm) based on comparison between before (red) and after applying the inter-correction method (blue) at Ispra, Venice (Venise), and Crete (Forth_Crete).

4.2 Linear long-term AOT trends over Europe and South China

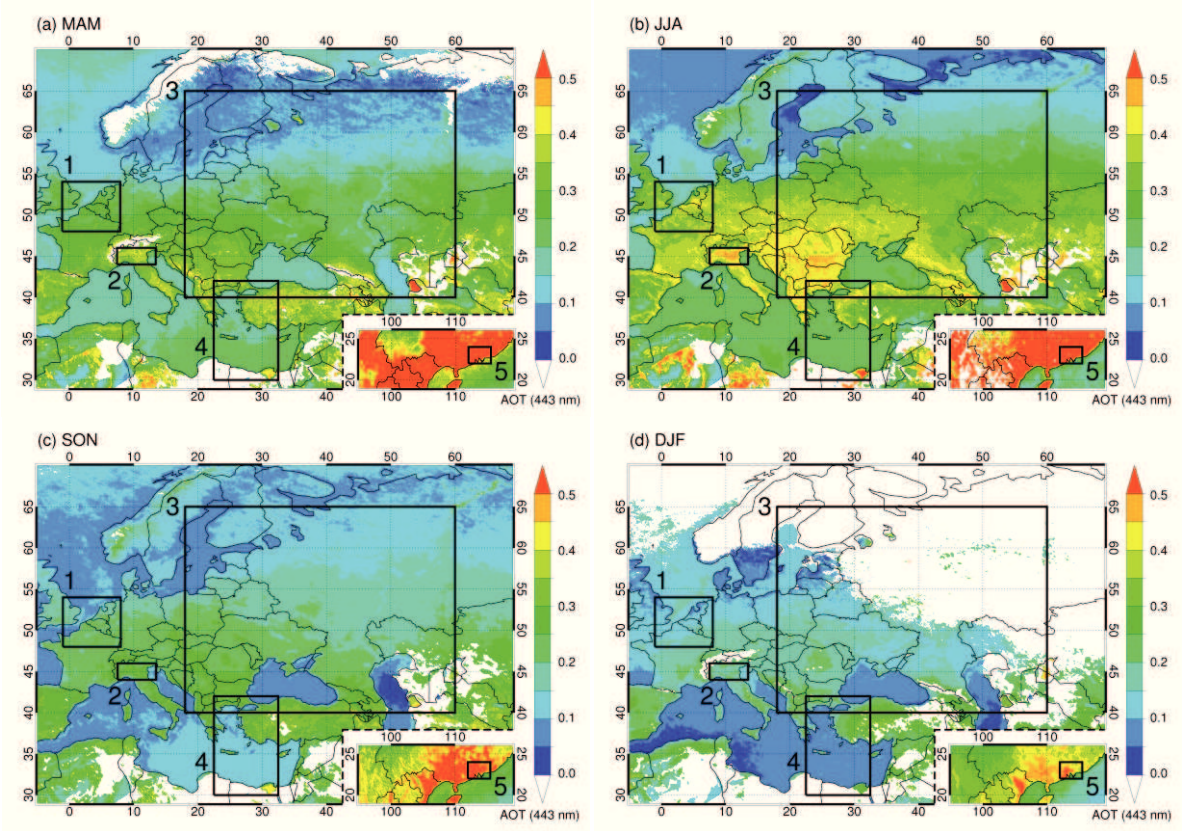

Fig. 4.6 Seasonal distribution of BAER AOT at 443 nm in (a) MAM, (b) JJA, (c) SON, and (d) DJF over the specific regions. The BAER AOTs over bright surface (e.g. Northern African deserts and the Anatolian plateau) or under frequent cloud disturbance are not retrieved.

Aerosols have temporally and regionally variable characteristics because of different aerosol sources (e.g., aerosol types and emission intensity) and atmospheric conditions (e.g., relative humidity and boundary layer height). The regions defined at the beginning of this chapter according to the selection in the CityZen project are affected by huge human activity. Fig. 4.6 shows the seasonal distributions of BAER AOTs at 443 nm, which are good to understand the seasonal variation of AOT in the regions. Over European regions (BeNeLux, Po Valley, Eastern Europe, and Eastern Mediterranean), a strong seasonal variation can be observed because industrial pollution composed of sulphur is enhanced during summer, when solar radiation is at maximum [Marmer et al., 2007; Karnieli et al., 2009]. Furthermore, forest

fires in Southern Europe, occurring mostly in summer, may well contribute to seasonal variation [Pace et al., 2006; Tafuro et al., 2008] and significant dust loadings coming from northern African deserts are frequently observed over Mediterranean in spring and summer [Hatzianastassiou et al., 2009]. Additionally, the absence of removal processes (e.g., rain and monsoon) as well as a high boundary layer height cause higher AOTs in summer over Europe [Hatzianastassiou et al., 2009; Gerasopoulos et al., 2003; Bergamo et al., 2008; Venzac et al., 2009]. Over Pearl River Delta in South China, seasonal aerosol variations are mainly influenced by anthropogenic aerosols, caused by urbanization and industrialization as well as a hygroscopic growth with stagnant synoptic meteorological patterns in summer [Xiao et al., 2011; Zhang et al., 2008].

Fig. 4.7 illustrates the linear long-term trends of retrieved AOTs using BAER over several regions (BeNeLux: -0.00453 and -0.00484, Po Valley: -0.00386 and -0.00440, Eastern Europe: -0.00055 and -0.00019, Eastern Mediterranean: -0.00079 and -0.00054, and Pearl River Delta: +0.00761 and +0.00625 yr^{-1} at 443 and 555 nm, respectively). Except for the case of Pearl River Delta in South China, negative trends are generally observed in all analyzed regions. These are comparable to Zhang and Reid (2010), which estimated the negative trends of MODIS-Terra and MISR-Terra AOTs (-0.009 ~ -0.022 per decade) over Mediterranean Sea and positive (+0.002 ~ +0.014 per decade) ones over Southeast Asia from March 2000 to December 2009. de Meij et al. (2010) also found that AOT is decreasing (-0.00042 ~ -0.00011 yr^{-1}) over Europe and increasing (+0.00063 ~ +0.00189 yr^{-1}) over Asia observed from AERONET, MODIS-Terra, and MISR-Terra during 10 years (2000-2009). Especially for Mediterranean basin, Papadimas et al. (2008) reported a negative MODIS-Terra AOT trend (-0.00002 yr^{-1}) from 2000 to 2005. Koukouli et al. (2010) estimated the downward trends of MODIS-Terra AOTs from 2000 to 2006: -1.85%, -3.50%, -4.18%, and -4.20% per annum at Aegean Sea, Heraklion, Mount Athos, and Thessaloniki over Southern

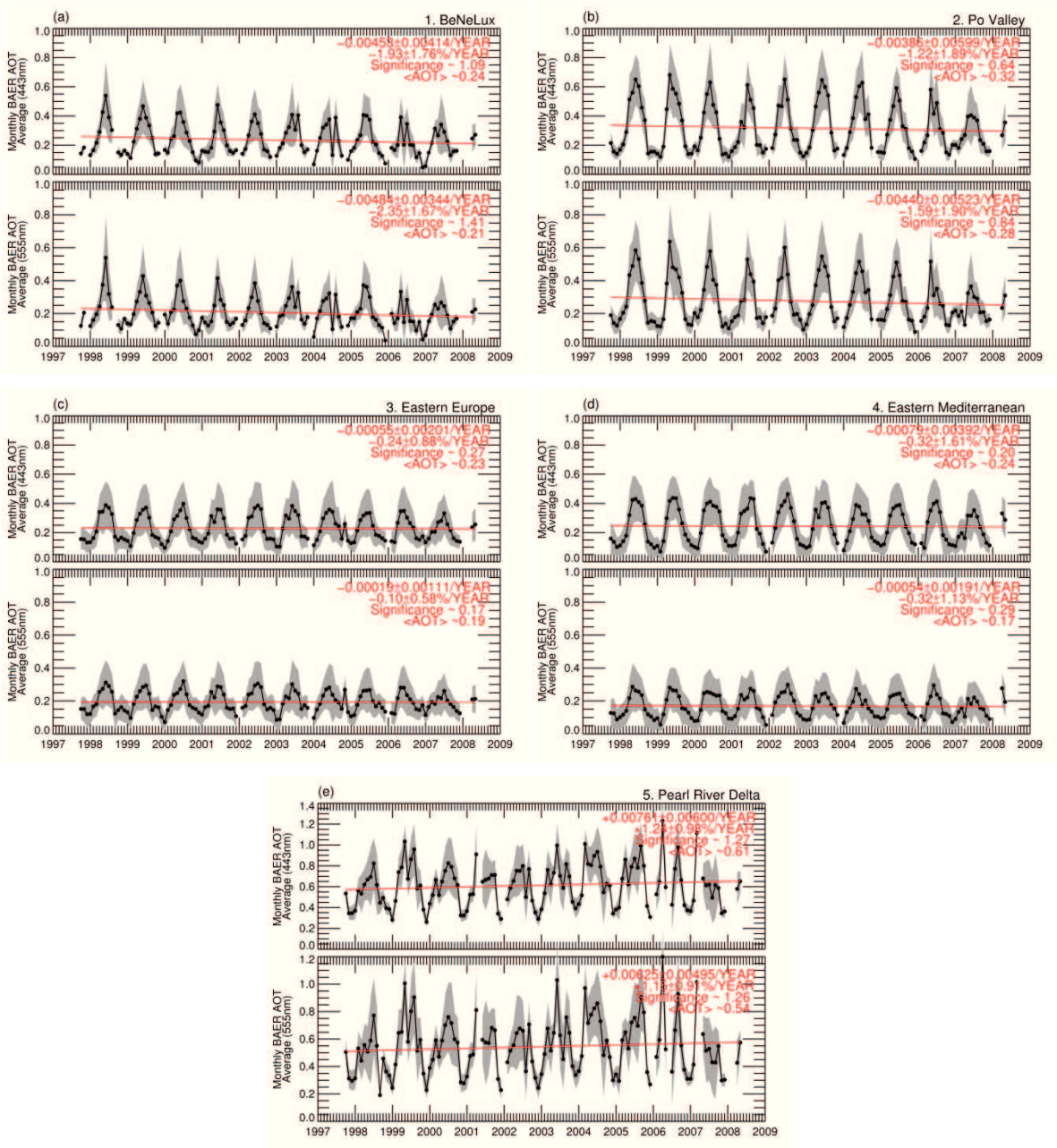

Fig. 4.7 Total averages (<AOT>) and linear long-term trend of BAER monthly AOTs (black circle symbol) including monthly standard deviation (shaded area) over (a) BeNeLux, (b) Po Valley, (c) Eastern Europe, (d) Eastern Mediterranean in Europe, and (e) Pearl River Delta in South China shown in Fig. 4.1. The bottom figures for each region correspond to 555 nm whereas the top figures to 443 nm.

Balkan/Eastern Mediterranean. Additionally, using TOMS data from 1980 to 2001, Hatzianastassiou et al. (2009) found a significant decrease of AOT (-3.8% ~ -20.9%) in eastern Mediterranean basin. Definitely, the AOT trends from different studies are difficult to be compared directly with each other because of different research periods, sampling times, sensor calibrations, aerosol retrieval accuracies, and so on. Nevertheless, the findings of the previous studies are consistent with the BAER AOT trends in the present study.

As already mentioned, practically all AOT trends based on satellite observations are hampered by the influence of cloud disturbance and thereby, need to be corrected. However, the inter-correction as applied in Section 4.1 ignores the difference in spatial resolution of the two data sets. Therefore, the cloud uncertainties are roughly estimated by a separate analysis of trends for each season (as shown in Fig. 4.8 and Tab. 4.2).

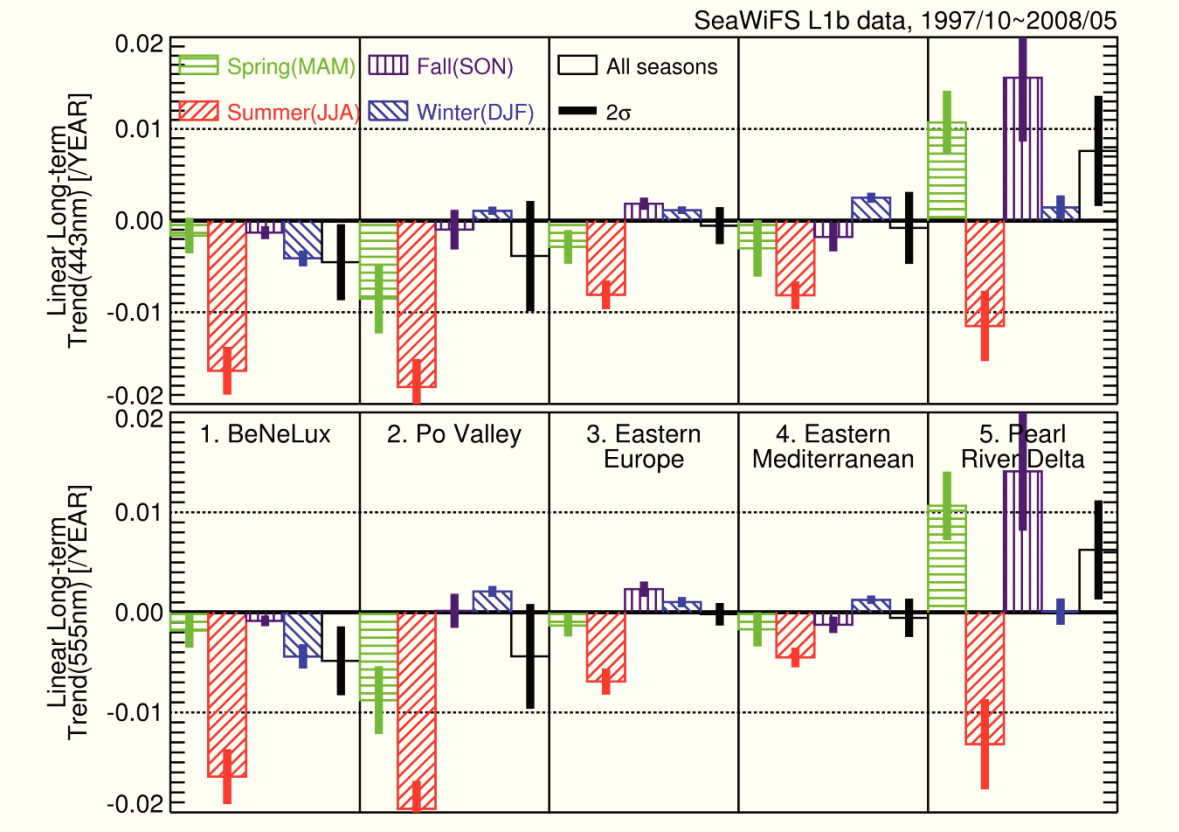

Fig. 4.8 Annual and seasonal trends ($\hat{\omega}$) of BAER monthly AOTs at 443 and 555 nm including their standard deviation ($\sigma_{\hat{\omega}}$) for the several regions.

Tab. 4.2 Statistical parameters for linear long-term trends of AOTs (443 and 555nm) retrieved by BAER over several regions.

Regions	Seasons*	$\langle\delta_\lambda\rangle^a$ (443/555nm) **[dimensionless]**	$\hat{\omega}_\lambda{}^b$ (443/555nm) **[dimensionless/year]**	**[%/year]**	$\sigma_{\hat{\omega}_\lambda}{}^c$ (443/555nm) **[dimensionless]**	**[%]**	Sig.^{d} (443/555nm)* **[dimensionless]**
1.BeNeLux	MAM (Spring)	0.28/0.24	-0.00163/-0.00181	-0.59/-0.75	0.00192/,0.00172	0.69/0.71	0.85/1.05
	JJA (Summer)	0.34/0.29	-0.01636/-0.01643	-4.77/-5.72	0.00259/0.00273	0.75/0.95	**6.32**/**6.03**
	SON (Fall)	0.16/0.14	-0.00130/-0.00085	-0.81/-0.60	0.00070/0.00052	0.43/0.37	1.87/1.64
	DJF (Winter)	0.13/0.14	-0.00411/-0.00441	-3.07/-3.23	0.00085/0.00120	0.64/0.88	**4.82**/**3.68**
	All Seasons	0.24/0.21	-0.00453/-0.00484	-1.93/-2.35	0.00414/0.00344	1.76/1.67	1.09/1.41
2.Po Valley	MAM (Spring)	0.38/0.33	-0.00850/-0.00877	-2.22/-2.69	0.00379/0.00337	0.99/1.03	**2.25**/**2.60**
	JJA (Summer)	0.50/0.43	-0.01815/-0.01964	-3.60/-4.62	0.00304/0.00278	0.60/0.65	**5.96**/**7.07**
	SON (Fall)	0.21/0.19	-0.00098/+0.00015	-0.47/+0.08	0.00215/0.00169	1.03/0.91	0.46/0.09
	DJF (Winter)	0.16/0.16	+0.00108/+0.00209	+0.67/+1.32	0.00044/0.00054	0.28/0.34	**2.43**/**3.90**
	All Seasons	0.32/0.28	-0.00386/-0.00440	-1.22/-1.59	0.00599/0.00523	1.89/1.90	0.64/0.84
3.Eastern Europe	MAM (Spring)	0.27/0.22	-0.00287/-0.00132	-1.08/-0.61	0.00182/0.00109	0.68/0.50	1.58/1.21
	JJA (Summer)	0.33/0.26	-0.00808/-0.00691	-2.42/-2.63	0.00156/0.00129	0.47/0.49	**5.20**/**5.34**
	SON (Fall)	0.18/0.16	+0.00184/+0.00232	+1.05/+1.42	0.00066/0.00076	0.37/0.47	**2.80**/**3.05**
	DJF (Winter)	0.14/0.13	+0.00113/+0.00103	+0.83/+0.81	0.00040/0.00049	0.29/0.39	**2.84**/**2.08**
	All Seasons	0.23/0.19	-0.00055/-0.00019	-0.24/-0.10	0.00201/0.00111	0.88/0.58	0.27/0.17

* Cloudy seasons are represented in ***bold-italic*** type and Significance values (Sig.) larger than two are expressed in **bold** type.

$\langle\delta_\lambda\rangle^a$: AOT average, $\hat{\omega}_\lambda{}^b$: linear long-term trend of AOTs, $\sigma_{\hat{\omega}_\lambda}{}^c$: Standard deviation of the AOT trends, Sig.^{d}: Significance, $|\hat{\omega}/\sigma_{\hat{\omega}}|$.

Tab. 4.2 (*Continued*)

Regions	Seasons*	$\langle\delta_\lambda\rangle^a$ (443/555nm) **[dimensionless]**	$\hat{\omega}_\lambda{}^b$ (443/555nm) **[dimensionless/year]**	**[%/year]**	$\sigma_{\hat{\omega}_\lambda}{}^c$ (443/555nm) **[dimensionless]**	**[%]**	Sig.^{d} (443/555nm)* **[dimensionless]**
4.Eastern Mediterranean	MAM (Spring)	0.29/0.20	-0.00301/-0.00169	-1.04/-0.84	0.00308/0.00170	1.07/0.85	0.98/0.99
	JJA (Summer)	0.38/0.24	-0.00814/-0.00450	-2.12/-1.88	0.00149/0.00097	0.39/0.40	**5.48**/**4.65**
	SON (Fall)	0.18/0.14	-0.00178/-0.00124	-0.96/-0.89	0.00157/0.00082	0.85/0.59	1.13/1.52
	DJF (Winter)	0.11/0.09	+0.00240/+0.00125	+2.24/+1.34	0.00054/0.00042	0.49/0.44	**4.62**/**3.02**
	All Seasons	0.24/0.17	-0.00079/-0.00054	-0.32/-0.32	0.00392/0.00191	1.61/1.13	0.20/0.29
5. Pearl River Delta	MAM (Spring)	0.74/0.65	+0.01071/+0.01066	+1.46/+1.64	0.00345/0.00342	0.47/0.53	**3.11**/**3.12**
	JJA (Summer)	0.74/0.66	-0.01149/-0.01318	-1.56/-2.01	0.00382/0.00450	0.52/0.69	**3.01**/**2.93**
	SON (Fall)	0.57/0.51	+0.01560/+0.01411	+2.72/+2.75	0.00696/0.00594	1.21/1.16	**2.24**/**2.37**
	DJF (Winter)	0.40/0.35	+0.00144/+0.00008	+0.36/+0.02	0.00130/0.00132	0.32/0.37	1.10/0.06
	All Seasons	0.61/0.54	+0.00761/+0.00625	+1.24/+1.15	0.00600/0.00495	0.98/0.91	1.27/1.26

* Cloudy seasons are represented in ***bold-italic*** type and Significance values (Sig.) larger than two are expressed in **bold** type.

$\langle\delta_\lambda\rangle^a$: AOT average, $\hat{\omega}_\lambda{}^b$: linear long-term trend of AOTs, $\sigma_{\hat{\omega}_\lambda}{}^c$: Standard deviation of the AOT trends, Sig.^{d}: Significance, $|\hat{\omega}/\sigma_{\hat{\omega}}|$.

Strong downward trends of BAER AOTs in the spring and summer appear over most European regions. They are similar with Zhao et al. (2008), which discussed the negative trend of AVHRR AOTs during 25 years (1981-2004) over oceans near the regions in spring and summer, and magnitude was up to -0.1 per decade. Karnieli et al. (2009) found very similar results, namely decreasing trends of MODIS-Terra AOTs (-0.01 yr^{-1}) and fine AOTs (-0.009 yr^{-1}) for July and August over central and Eastern Europe. The strong decrease of AOT over the BeNeLux and Po Valley regions is attributed to the strict environmental regulations for mitigating climate change and improving air quality [Smith et al., 2001; Streets et al., 2006; Zhao et al., 2008]. Especially, for the large Mediterranean basin, Papadimas et al. (2008) reported a similar tendency that MODIS-Terra AOTs decreased (-0.0014 yr^{-1}) in summer and increased (+0.0012 yr^{-1}) in winter from 2000 to 2006, which was explained with seasonal trends of precipitation. However, in comparison with the BeNeLux and Po Valley regions, no significant trend is found over Eastern Mediterranean and Eastern Europe regions probably due to various aerosol sources (e.g., sea salt, dust, industrial, and biomass burning).

Over Pearl River Delta region, almost in all seasons (except summer), the seasonal trends of BAER AOT are positive due to a fast development in the economy and associated enhancement of industrial emissions of the surrounding countries [Streets et al., 2006; Smith et al., 2001]. Zhao et al. (2008) reported similar results that positive seasonal trends of AVHRR AOTs from 1981 to 2004 prevailed in all seasons except summer, and maximal magnitude was +0.04 per decade (while it is very close to zero for summer). Similar positive trends were also discussed by Massie et al. (2004) using TOMS AOTs from 1979 to 2000 in Asia.

Generally speaking, clouds frequently occur in winter over Europe and summer over South China. As explained in Section 4.1, in order to get a more reliable trend of cloud-free

aerosol, cloud disturbance should be taken care of. The trends in summer over most of the European regions (BeNeLux, Po Valley, Eastern Mediterranean, and Eastern Europe) are strongly negative with high significance, while some positive trends in cloudy seasons are also observed. This positive trend in winter can be explained with the change of removal processes (i.e., negative trend of precipitation) and atmospheric circulation [Papadimas et al., 2008]. Realistically, the trend in cloudy season is easily contaminated by clouds (not only overestimated AOT in retrieval, but also poorly representative monthly AOT due to less observation) as demonstrated in Section 4.1. Therefore, if the cloud-contaminated trends in winter can be excluded or ignored, only negative trends over European regions are dominant.

Surprisingly, over the Pearl River Delta, a negative trend in summer with highly significant values is opposite to positive trends in other seasons. Clearly, the removal processes of aerosol (e.g., strong monsoon and frequent rain) influences the decrease of AOT in summer. In contrast, frequent cloud occurrence in summer disturbs the observation of cloud-free aerosol, and misclassification between aerosols and clouds can easily happen under high relative humidity or meteorological stagnation of the atmosphere [Kim et al., 2007]. Therefore, the summer trend of BAER AOT over the Pearl River Delta may be problematic with clouds, despite the significance value in summer was larger than two ($|\hat{\omega}/\sigma_{\hat{\omega}}|$= 3.01 and 2.93 at 443 and 555 nm, respectively). To conclude, the annual AOT trend can be influenced strongly by this uncertainty in summer. Detailed values of BAER AOT trends and statistical parameters over the regions are summarized in Tab. 4.2.

Fig. 4.9 depicts seasonal and annual aerosol optical characteristics (i.e. volume size distribution and SSA) from Level 2.0 inversion all points data at the AERONET stations (red star and cross symbols in Fig. 4.1) within the selected regions. The volume size distribution and SSA were retrieved only under the conditions: AOT (440 nm) > 0.4 and solar zenith angle > 50° because of the theoretical limitations in forward model and inversion

assumptions [Dubovik et al., 2000]. Through the investigations of these seasonal aerosol properties, it enables to classify aerosol types and to explain why there are some discrepancies between BAER and AERONET AOTs in Fig.4.2. von Hoyningen-Huene et al. (2011) discussed that BAER could retrieve AOT underestimated up to 20% in the very strong pollution (i.e., high AOT having strong absorbing).

The size distributions over most AERONET stations are dominated by accumulation mode with spectral decrease of SSA towards longer wavelengths. They are typical for an industrial aerosol type [Dubovik et al., 2002a]. The aerosol optical properties over Crete (dominant coarse mode and spectral decrease of SSA by longer wavelengths) reveal that maritime aerosol or desert dust are predominant. Kalivitis et al. (2007) and Fotiadi et al. (2005) reported that desert dust could potentially reach Crete. In contrast, the aerosol properties in Hong Kong, located within the Pearl River Delta, have typical anthropogenic characteristics. Especially interesting is a noticeable increase of aerosol fine-mode radius in summer. This circumstance was explained by stagnant synoptic meteorological patterns, secondary aerosol formation, and hygroscopic growth [Kotchenruther et al., 1999; Dubovik et al., 2002a]. Therefore, the aerosol optical characteristics at Hong Kong supports that the main source of the increase in AOT is industrial aerosol, and that cloud uncertainties can have a large impact on the estimation of the summer trend over the Pearl River Delta.

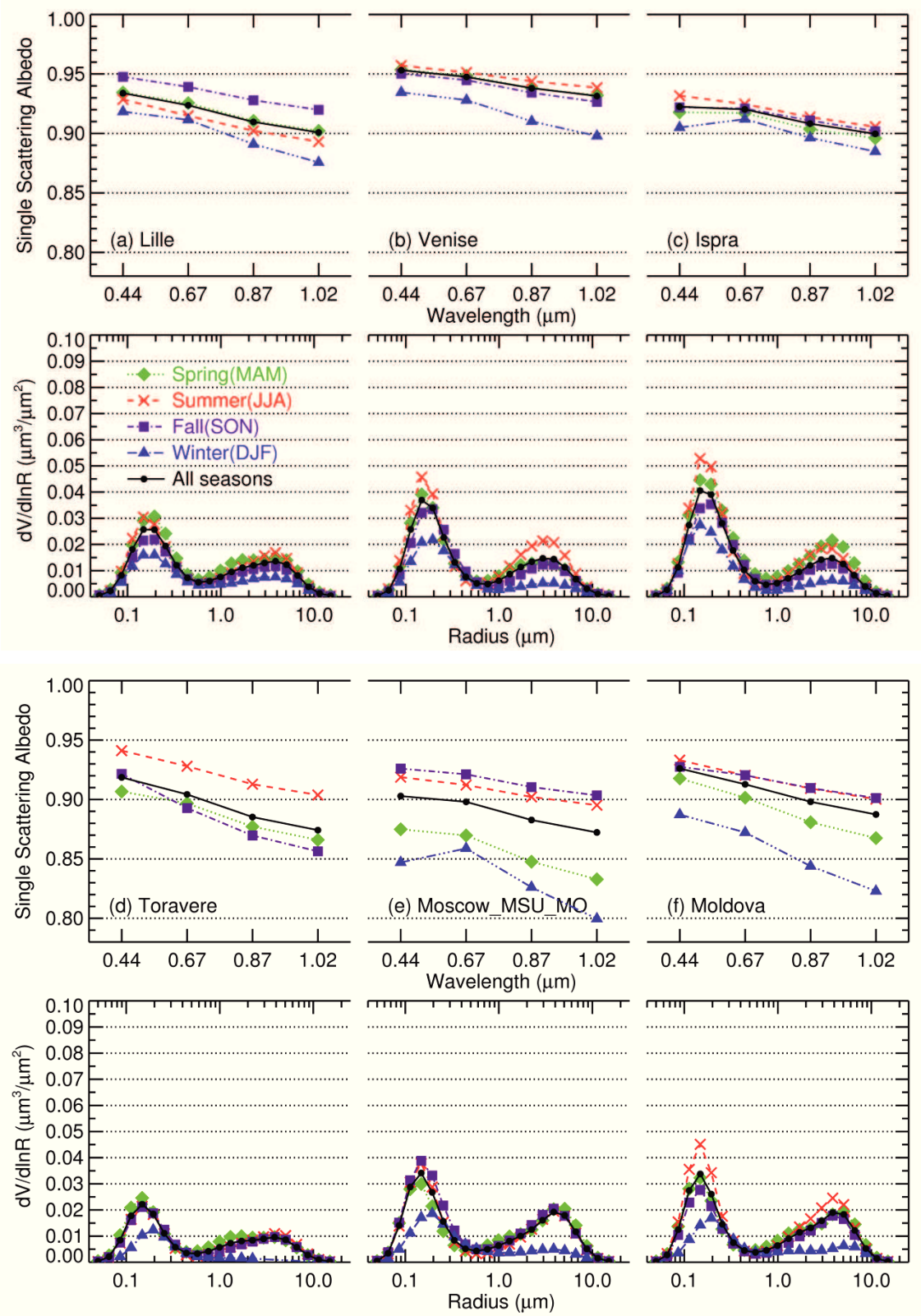

Fig. 4.9 Annual and seasonal aerosol characteristics (i.e. volume size distribution and SSA) from AERONET Level 2 inversion data at (a) Lille, (b) Venice (Venise), (c) Ispra, (d) Toravere, (e) Moscow (Moscow_MSU_MO), (f) Moldova, (g) Belsk, (h) Crete (Forth_Crete), and (i) Hong Kong (Hong_Kong_Hok_Tsui) within the specific regions.

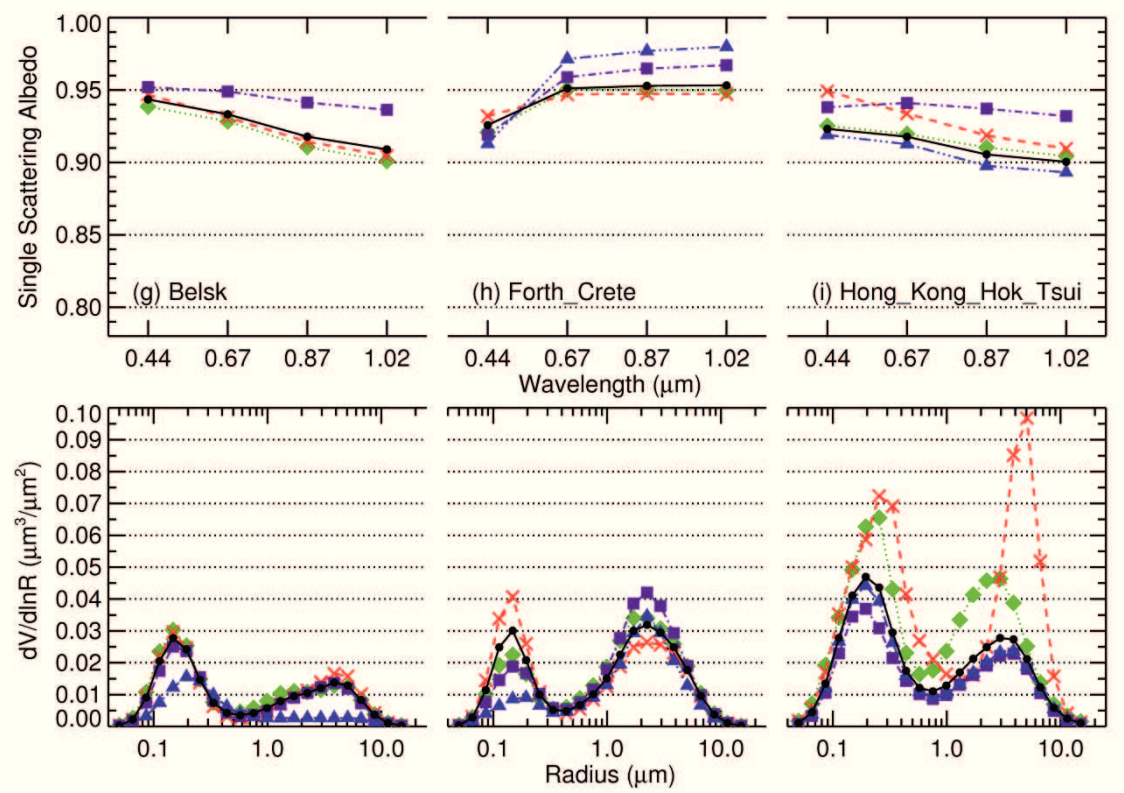

Fig. 4.9 (*Continued*)

5. Trend analysis and climatological average of aerosol optical properties derived from AERONET spectral observations

Recently, several studies based on well-validated aerosol retrieval algorithms using both well-calibrated observations and long-term records from space borne instruments have contributed significantly to the understanding of global aerosol trends. Related to these trends, a hypothesis of global brightening or dimming has been discussed as well [Wild et al., 2005, 2007; Ohmura, 2006; Stanhill, 2007; Norris and Wild, 2007]. However, as discussed in the previous chapter, the trend analysis of cloud-free AOT derived from satellite observations often have serious uncertainties caused by cloud disturbance and aerosol optical properties (as a priori within the algorithms). Therefore, using more accurate and spectral AERONET observations, this chapter attempts to figure out a way to minimize the uncertainties in trend analysis. Firstly, a weighted least squares regression based on the number of observations sensitive to the cloud disturbance is introduced for the long-term trends analysis of AERONET AOT (440, 675, 870, and 1020 nm) and ÅE (440-870 nm). Additionally, a new method for aerosol classification using ÅE and ÅED in this study allows to understand what major sources are influencing the AOT changes. Secondly, even though AERONET inversion products are only valid under strict conditions: AOT (440nm) > 0.4 and solar zenith angle > 50° [Dubovik et al., 2000], they are useful for various kinds of aerosol optical properties (e.g., volume size distribution, SSA, phase function, and radiative forcing) for setting up a database of aerosol climatological properties. The database can reduce the uncertainty in AOT retrievals by providing more practical a priori estimates of aerosol optical

properties for LUT approach based on satellite observations. Most of the content in this chapter is from the paper published by Yoon et al. in *Atmospheric Measurement Techniques*, 2012.

5.1 Methodology

For a reliable analysis of aerosol trends and climatological properties based on AERONET observations, there are four approaches needed: 1) the selection criteria for the AERONET stations having sufficient and nearly-complete multi-year data sets, 2) the weighted least squares regression to consider cloud uncertainty, 3) the bootstrap resampling for the error study of the trends, and 4) the classification of coarse- and fine-mode dominant aerosols.

Selection criteria for suitable AERONET stations

The AERONET program provides high quality aerosol products for the past decades over roughly 850 stations, globally. However, not all stations distribute a sufficiently large temporal record suitable for a trend analysis. Firstly, suitable AERONET stations are distinguished by checking the number of observations per month (n_t). n_t basically depends on the seasonal daytime length, the station's location, the operational instrument status, the cloud disturbance, and the data quality verification process. For statistically meaningful monthly average values, a large n_t is required since the sample average based on a larger sample number is closer to the real average. Another important issue in the trend analysis is that the annual data should be complete yearly sets in order to avoid a bias in particular seasons. In other words, the absence of continuous monthly averages in the yearly data sets can cause a significant uncertainty in the trend analysis. Basically, this study has established the following set of criteria to choose suitable AERONET stations:

a. The qualified monthly average is calculated with a n_t larger than 300 per month (around 10 observations per day).
b. The complete yearly data set is composed of more than seven qualified monthly averages.
c. A suitable AERONET station needs to have more than five complete years of observation history.

Although a five-years time series may be insufficiently short for a statistically significant trend analysis, it is a first, pragmatic time span to investigate aerosol temporal change from AERONET observations. Fig. 5.1 indicates n_t since 1993 for suitable AERONET stations listed in Tab. 5.1. Because each station has a different observation history as well as differently qualified data sets (with respect to the above listed conditions), it is difficult to perform the investigation of aerosol trends during the same period. The research periods whenever data sets satisfy the selection criteria for each station are indicated by blue fields in Fig. 5.1. Detailed information about the geolocation and the research periods for the selected AERONET stations are listed in Tab. 5.1.

Tab. 5.1 Geolocations and research periods of the suitable AERONET stations for aerosol trend analysis in alphabetical order.

Selected AERONET Stations	**Regions**	**Countries**	**Geolocations (lat.[°]/lon.[°]/ alt.[m])**	**Research Periods**
(a) Avignon	Western Europe	France	43.93/4.88/32	2001~2005
(b) Banizoumbou	West Africa	Niger	13.54/2.66/250	2002~2008
(c) Beijing	East Asia	China	39.98/116.38/92	2003~2007
(d) Dakar	West Africa	Senegal	14.39/-16.96/0	2004~2008
(e) GSFC	North America	USA	38.99/-76.84/87	1995~2008
(f) Ispra	Western Europe	Italy	45.80/8.63/235	2001~2007
(g) Mauna_Loa	Free troposphere (Pacific)	USA	19.54/-155.58/3397	1998~2009
(h) MD_Science_Center	North America	USA	39.28/-76.62/15	2000~2006
(i) Mongu	South Africa	Zambia	-15.25/23.15/1107	2000~2004
(j) Ouagadougou	West Africa	Burkina Faso	12.20/-1.40/290	2000~2004
(k) SEDE_BOKER	Middle East	Israel	30.86/34.78/480	2003~2008
(l) Sevilleta	North America	USA	34.35/-106.89/1477	1998~2002
(m) Shirahama	East Asia	Japan	33.69/135.36/10	2003~2009
(n) Skukuza	South Africa	South Africa	-24.99/31.59/150	2000~2007
(o) Solar_Village	Middle East	Saudi Arabia	24.91/46.40/764	2001~2007

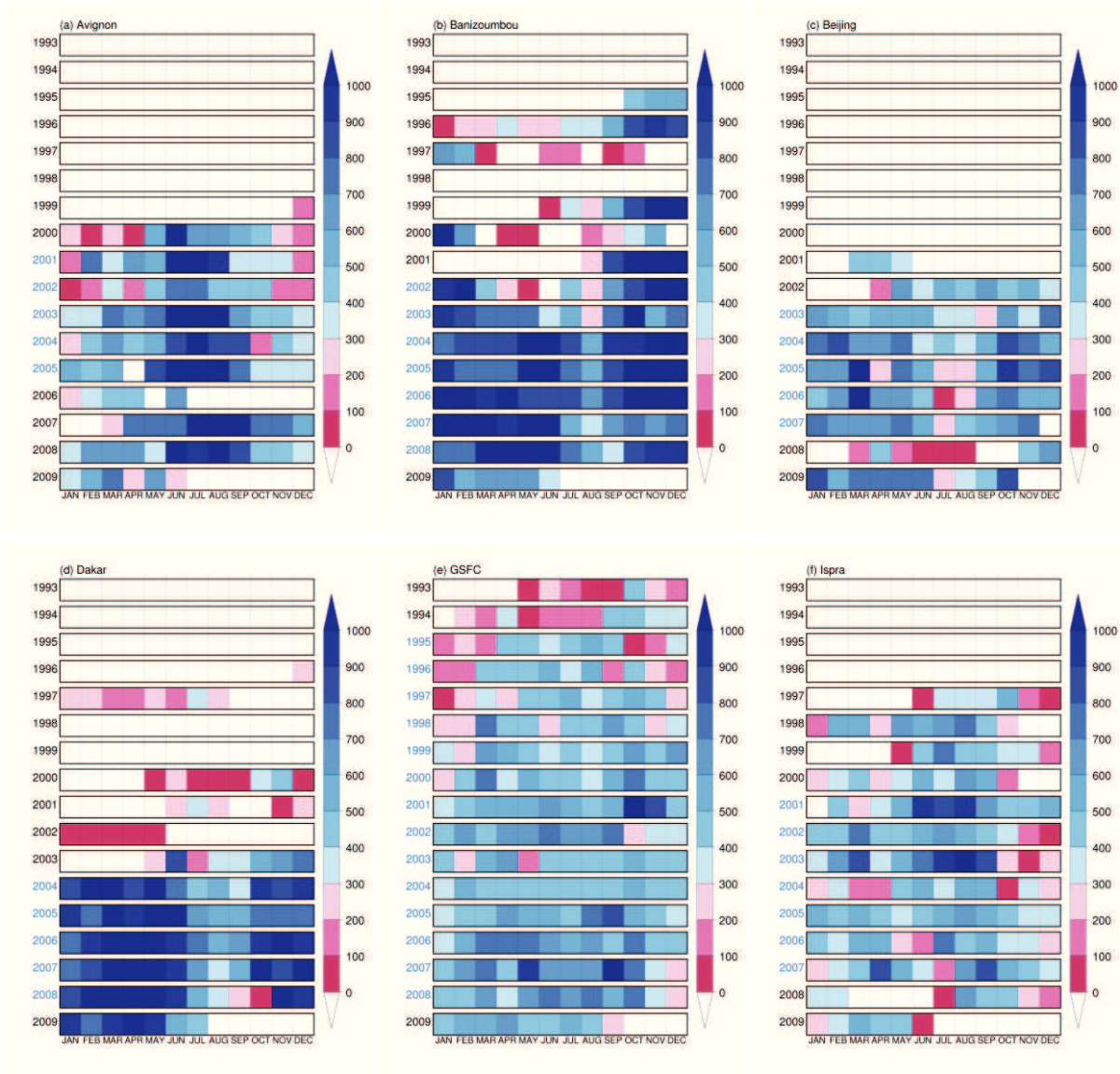

Fig. 5.1 Monthly observation numbers (n_t) at the AEROET stations: (a) Avignon, (b) Banizoumbou, (c) Beijing, (d) Dakar, (e) GSFC, (f) Ispra, (g) Mauna_Loa, (h) MD_Science_Center, (i) Mongu, (j) Ouagadougou, (k) SEDE_BOKER, (l) Sevilleta, (m) Shirahama, (n) Skukuza, and (o) Solar_Village since 1993. The research period for each station is shown by the blue years at the left vertical axis.

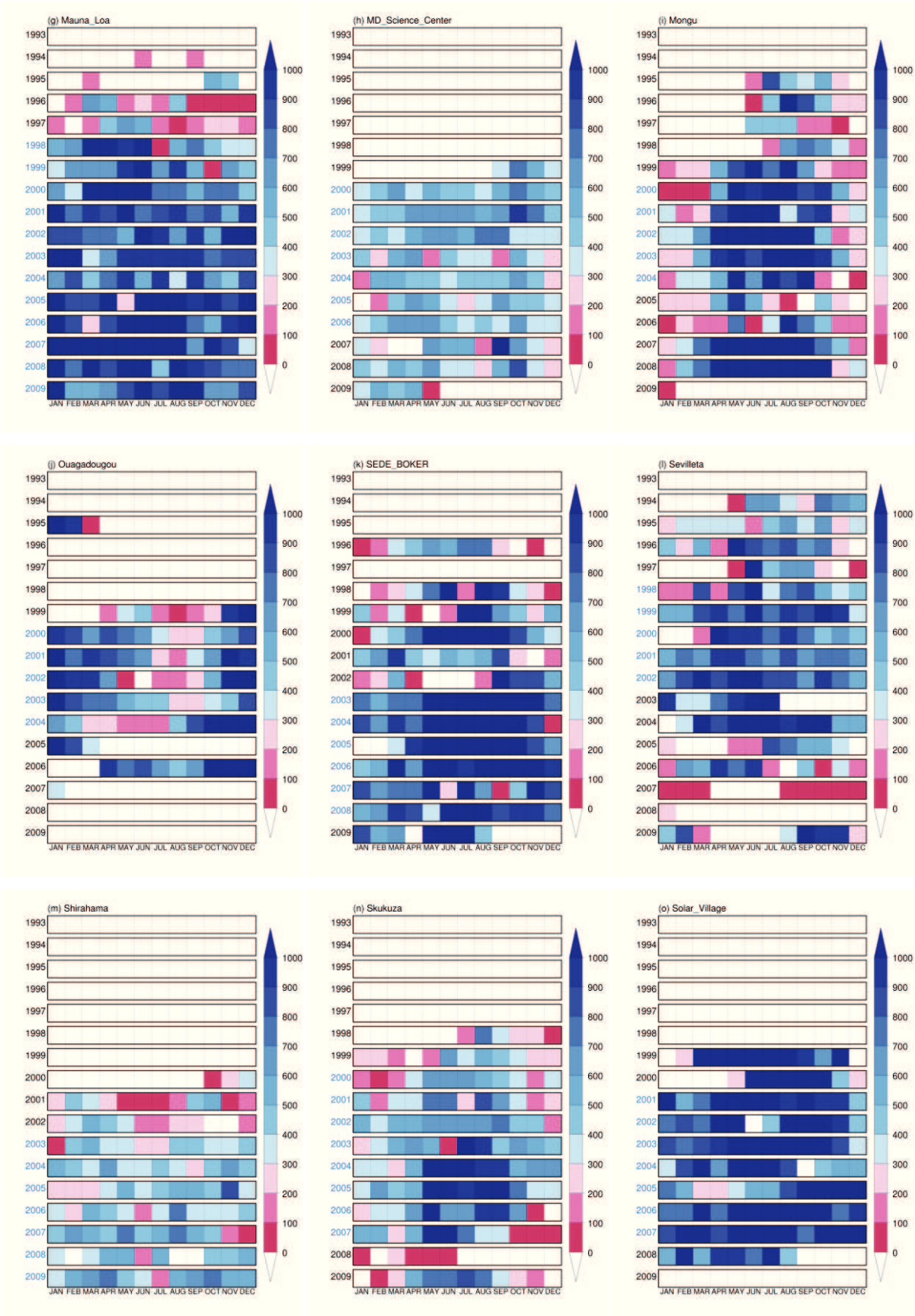

Fig. 5.1 (*Continued*)

Weighted least squares regression

For many practical purposes (e.g., establishing environmental regulations and estimating future climate changes using model simulation), a simple linear trend model has been used in many previous studies [Mishchenko et al., 2007; Mishchenko and Geogdzhayev, 2007; Zhao et al., 2008; Papadimas et al., 2008; Yu et al., 2009; Xie and Xia, 2008; Kishcha et al., 2009; Karnieli et al., 2009; de Meij et al., 2010; Kaskaoutis et al., 2011] even though the linear model might be far away from the reality. This study has also adopted the linear model for AOT trend analysis based on monthly anomaly in order to consider the AOT seasonality. The monthly anomaly of AOT ($\tilde{y}_t$) is given by the following equation:

$$\tilde{y}_t = \mathrm{y}_\mathrm{t}^\mathrm{m} - \bar{\mathrm{y}}^\mathrm{m} \;\text{ with }\; \bar{\mathrm{y}}^\mathrm{m} = \frac{1}{\mathrm{N}}\sum_{\mathrm{n}=1}^{\mathrm{N}} \mathrm{y}_\mathrm{n}^\mathrm{m} \tag{5.1}$$

where, $\mathrm{y}_\mathrm{t}^\mathrm{m}$ is the monthly AOTs for research periods ($t = 1 \ldots T$) and $\bar{\mathrm{y}}^\mathrm{m}$ is total mean of monthly AOTs in same month ($m = 1 \ldots 12$). These monthly anomalies of AOTs are used for fitting the linear model weighted by a factor given by

$$\chi^2(A,B) = \sum_{\mathrm{t}=1}^{\mathrm{T}} \left(\mathrm{wt_t} \times (\tilde{\mathrm{y}}_\mathrm{t} - \mathrm{A} - \mathrm{Bx_t})\right)^2$$

$$\text{with }\; \mathrm{wt_t} = \begin{cases} 1, & \text{for simple linear (unweighted) trend} \\ (\sqrt{\mathrm{n_t}}/\sigma_\mathrm{t}), & \text{for weighted trend} \end{cases} \tag{5.2}$$

where, A is a constant term, B is the magnitude of the trend per year ($\mathrm{x_t} = \mathrm{t}/12$), $\mathrm{wt_t}$ is the monthly weighting factor defined as ratio of square root of $\mathrm{n_t}$ ($\sqrt{\mathrm{n_t}}$) and standard deviation of monthly AOT (σ_t). As mentioned above, a simple linear model ($\mathrm{wt_t} = 1$) needs to take into account cloud disturbance using $\mathrm{n_t}$. Fundamentally, each monthly AOT average has been calculated with different $\mathrm{n_t}$, which is directly related to the number of cloud occurrence. The trend analysis based on monthly average during cloudy season may strongly be biased due to poor temporal sampling, so that a weighting factor is used to derive the respective trends. Fig. 5.2 depicts the removal ratio of cloud (red line) and quality-unassured

(yellow line) observations of AERONET data. If n_t is large enough to ignore the other effects from daytime length, station location, and operational instrument status, then the main factors affecting n_t can be the cloud screening and the data quality verification process. Especially, n_t correlates negatively with the cloud removal ratio for most of the stations in Fig. 5.2. In addition, monthly standard deviation (σ_t) is by itself a suitable weight as it statistically represents the variability or diversity of the average. Therefore, it is possible to minimize the uncertainty caused by cloud disturbance in the trend analysis of cloud-free AOT using the weighting factor consisted of n_t and σ_t.

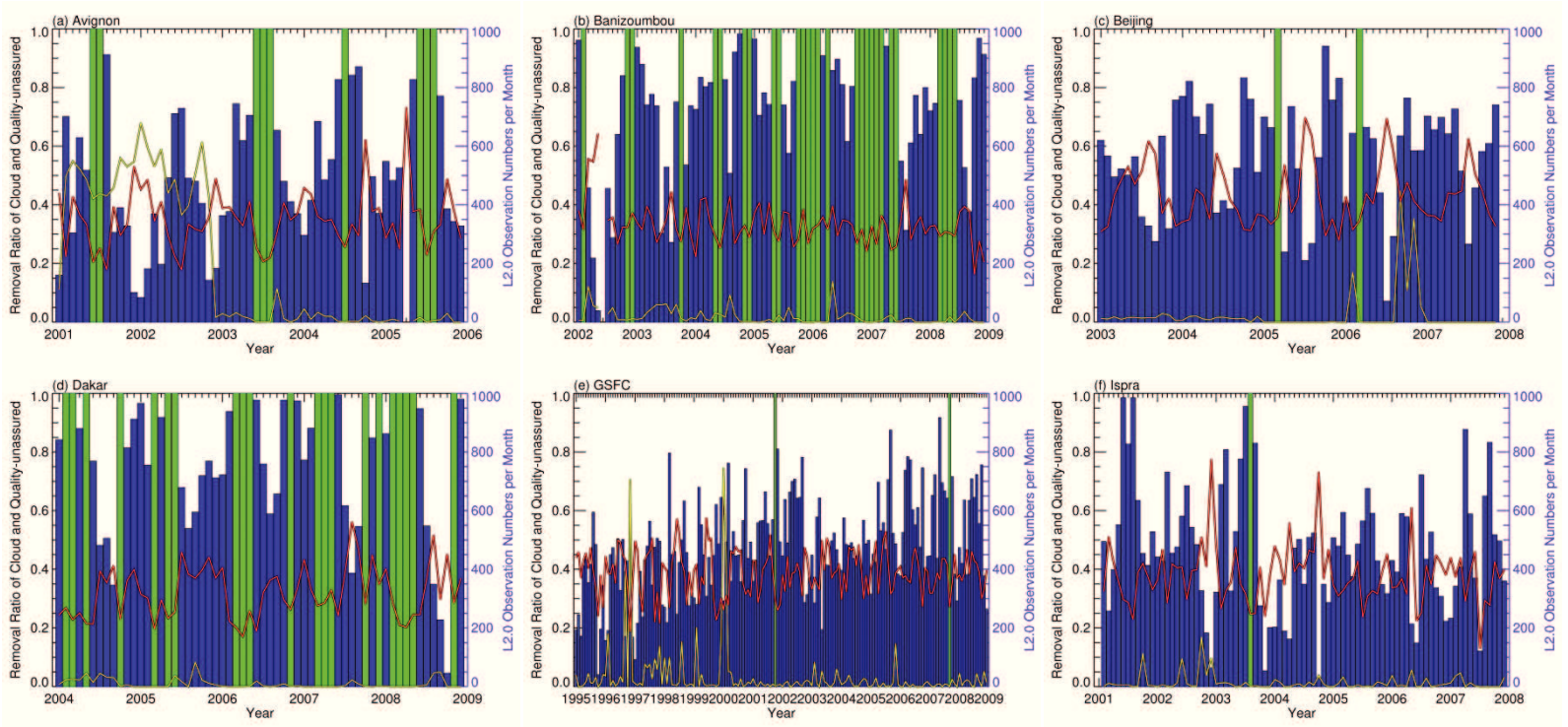

Fig. 5.2 Removal ratios of cloud (red line) and quality-unassured (yellow line) cases to AERONET level 2.0 data (blue bar) within each of research period at the several AERONET stations. Green bars mean that the observation numbers per month are over 1000 times.

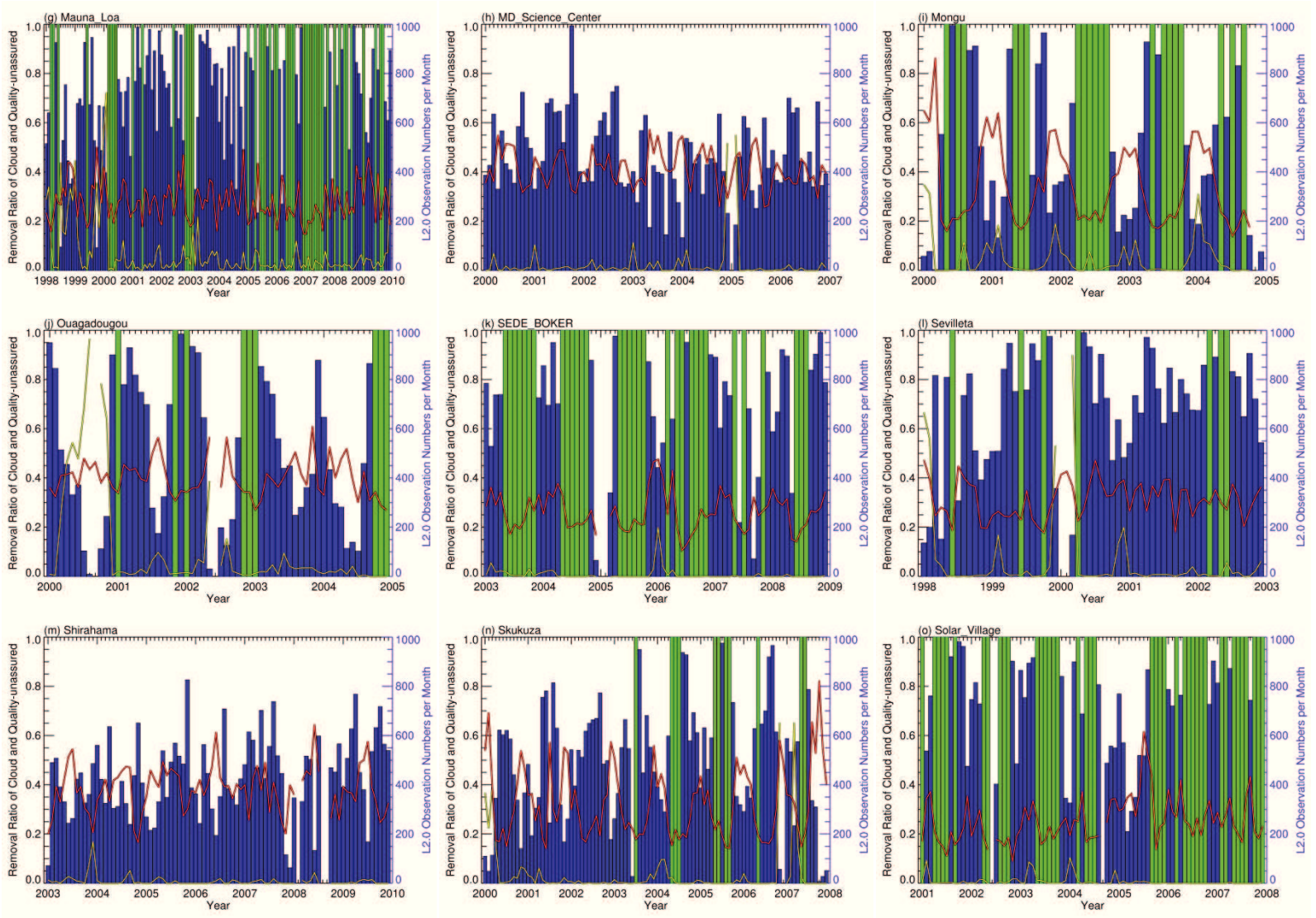

Fig. 5.2 (*Continued*)

Bootstrap resampling

In order to analyze statistically significant trends, the uncertainty ranges need to be estimated. However, the uncertainty test [Weatherhead et al., 1998] adopted in Chapter 4 can hardly be utilzed for a weighted least squares regression because it is based on an autocorrelation between consecutive two monthly values with same statistical confidence. Therefore, for the uncertainty test of AOT trends, this chapter introduces a so-called bootstrap method (Monte Carlo error bars analysis), which is a nonparametric method being applicable to any dataset without knowing distributional parameters of probability density function [Mudelsee, 2010]. Let us suppose the observations (red-cross symbols) shown in Fig. 5.3. From these original observations, randomly resampled data with replacement are grouped to derive the trend (green lines). A group of trends can be obtained by more iterative resampling (N), and used for estimating a confidence interval [Wilcox, 2009]. The number of bootstrap iterations depending on the conditional distribution of the original set ranges typically from 250 to 2000 times [Zhu et al., 2008]. In the present study, the Monte Carlo resampling has been repeated 5000 times for a more reasonable estimate of the distribution.

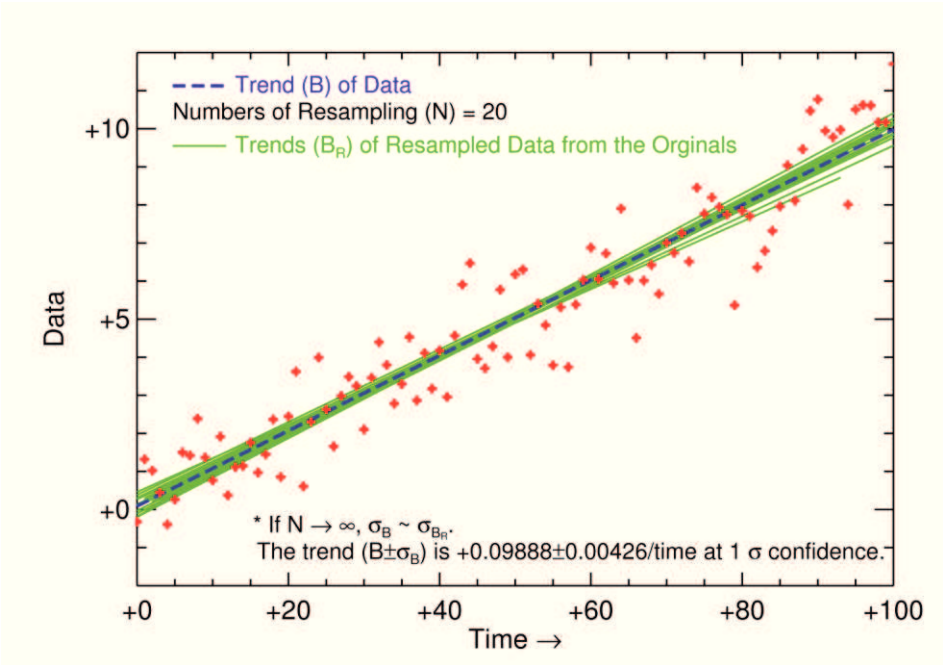

Fig. 5.3 Example of the bootstrap resampling for the uncertainty test of AOT trend analysis.

Classification of coarse- and fine-mode dominant aerosols

In order to quantify the change in anthropogenic (generally, fine-mode dominant) and natural (coarse-mode dominant) aerosols, an aerosol classification needs to be applied as well. The AERONET inversion process [Dubovik and King, 2000; Dubovik et al., 2000, 2002a, 2002b, 2006; Sinyuk et al., 2007] generates various aerosol characteristics such as volume size distribution and SSA. However, the data are only provided when satisfying the following conditions: AOT (440 nm) > 0.4 and solar zenith angle > 50° [Dubovik et al., 2000]. Fig. 5.4 illustrates the normalized frequency of the AOT at 440 nm (δ_{440}) and solar zenith angle (θ) at the selected AERONET stations. Generally, the normalized frequency (histogram) distributions of δ_{440} are skewed and have long tails towards larger aerosol loadings. The percentage of AERONET level 2.0 inversion data to the total observations is indicated as a pie chart on the lower-left hand side in Fig. 5.4. In most cases, it is difficult to use the AERONET inversion data for the aerosol classification because of a low proportion to total observations meeting the conditions mentioned above. Alternatively, a new classification of coarse- and fine-mode dominant aerosols is suggested in this study using ÅE and ÅED retrievals from AERONET level 2.0 direct sun data. ÅE and ÅED are defined as:

$$\text{ÅE} = -\frac{\log(\delta_{\lambda 1}/\delta_{\lambda 2})}{\log(\lambda 1/\lambda 2)}, \tag{5.3}$$

$$\text{ÅED} = -\frac{\log(\delta_{\lambda 1}/\delta_{\lambda 3})}{\log(\lambda 1/\lambda 3)} + \frac{\log(\delta_{\lambda 3}/\delta_{\lambda 2})}{\log(\lambda 3/\lambda 2)}, \tag{5.4}$$

where, δ_λ is the AOT at wavelengths ($\lambda 1 = 440$ nm, $\lambda 2 = 870$ nm, and $\lambda 3 = 675$ nm).

Several investigations have previously been devoted to the curvature of the spectral dependence of the optical depth in order to derive more accurate aerosol size information. For example, Kaufman (1993) found that the spectral curvature shows a transition from mixed accumulation and coarse particle modes to a dominant accumulation mode. Eck et al. (1999) investigated the wavelength dependence of the optical depth of biomass burning, urban, and

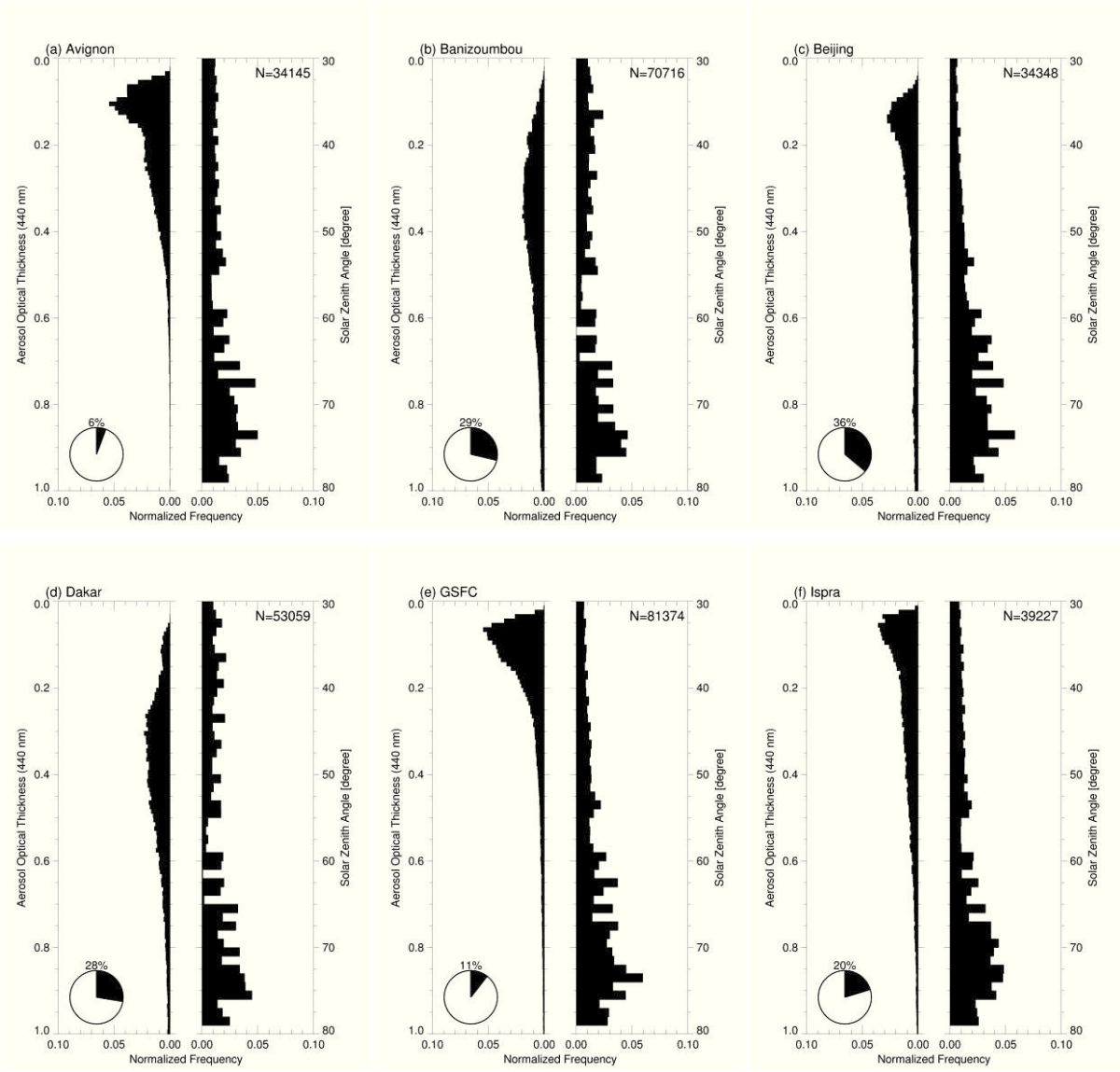

Fig. 5.4 Normalized frequency of Aerosol Optical Thickness at 440 nm (δ_{440}) and solar zenith angle (θ) to total observation number (N) at the AERONET stations. The bin sizes for δ_{440} and θ are 0.01 and 1.0°, respectively. The circle diagram on the lower-left hand means the percentage of AERONET level 2.0 inversion data (e.g. volume size distribution and SSA) to total observations. The AERONET inversion data are provided under the criteria; $\delta_{440} > 0.4$ and $\theta > 50°$.

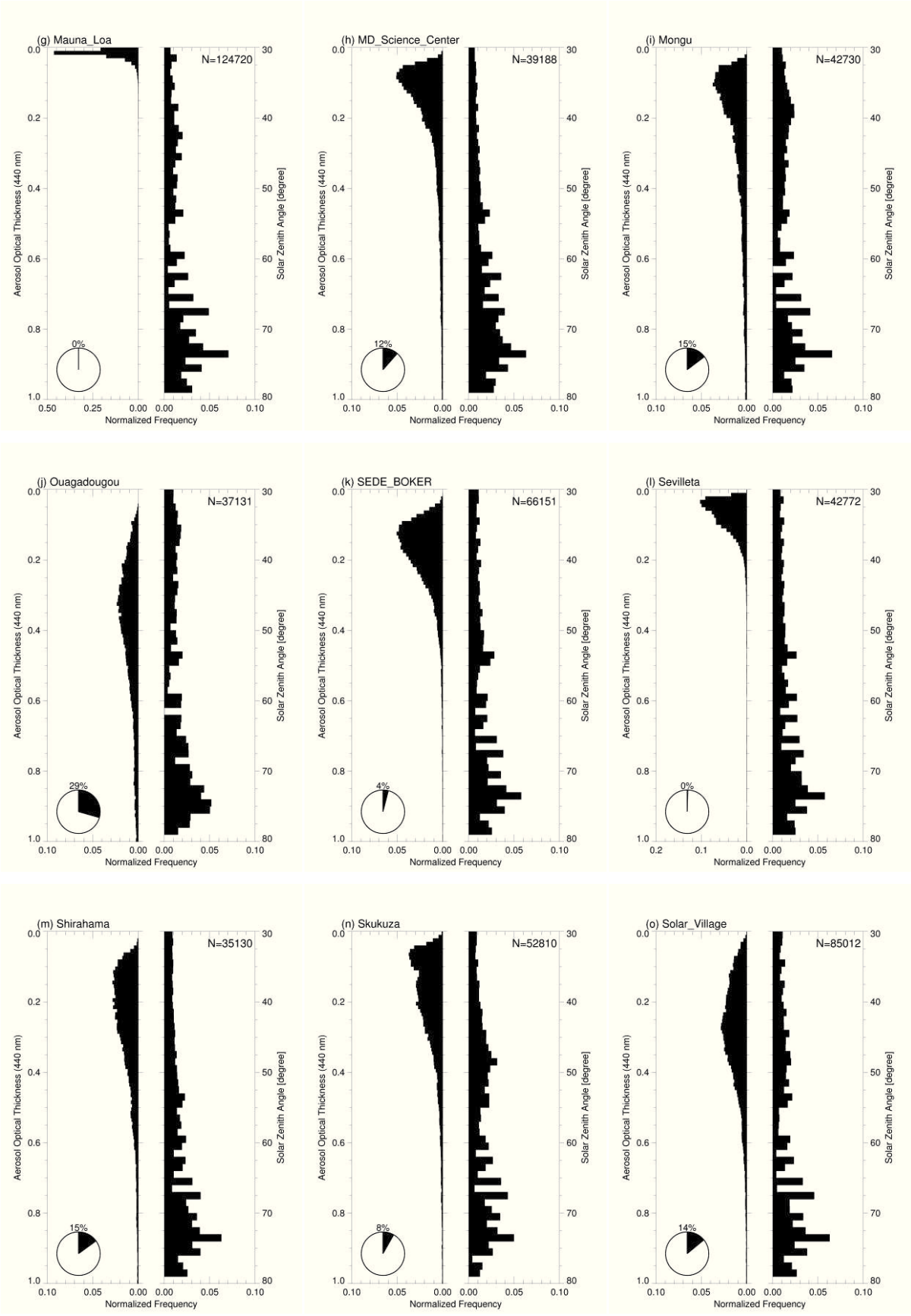

Fig. 5.4 (*Continued*)

desert dust aerosols. O'Neill et al. (2001a, 2001b, 2003, 2005) and Schuster et al. (2006) presented a detailed analysis and compared simulations with observations in order to investigate the relationship between aerosol size distribution and spectral dependence of the AOT. Gobbi et al. (2007) have set up a useful straight forward graphical framework easily applicable to classify aerosol fine mode fraction of the total AOT at 675 nm using ÅED as a measure of the curvature. They applied the graphical framework to AERONET data and were able to characterize different aerosol types such as pollution, mineral dust, and biomass burning. However, none of the above mentioned publications involved their methods in trend analyses. Here, a similar simulation as Gobbi et al. (2007) is built up in Fig. 5.5. The relationship between ÅE and ÅED is simulated using Mie code [Mishchenko et al., 1999b, 2002] with many bimodal volume size distributions consisting of mode radii, widths, fine volume fractions, and refractive indices (approximately 25000 combinations) shown in Tab. 5.2. Usually, negative ÅED shows a high proportion of fine mode aerosol for the same ÅE.

Tab. 5.2 Bimodal lognormal volume size distribution ($dV(r)/d\ln r$) parameters and refractive indices [Schuster et al., 2006] used to compute ÅE (440-870 nm) and ÅED (ÅE(440-675 nm)-ÅE(675-870 nm)) using Mie code in Fig. 5.5.

Parameter*	Values
r_{fine}	0.06, 0.09, 0.12, 0.15, 0.18, 0.21, 0.24, 0.27, 0.30
σ_{fine}	0.38, 0.50
r_{coarse}	1.9, 2.2, 2.7, 2.8, 3.0, 3.2, 3.4, 3.6, 3.7
σ_{coarse}	0.75, 1.00
n	1.34, 1.37, 1.40, 1.43, 1.47, 1.50, 1.54
k	0.003
C_{fine}/C_{total}	0.01, 0.10, 0.20, 0.30, 0.40, 0.50, 0.60, 0.70, 0.80, 0.90, 0.99

* The bimodal lognormal volume size distribution ($\frac{dV(r)}{d\ln r}$) is given by

$$\frac{dV(r)}{d\ln r} = \frac{C_{fine}}{\sqrt{2\pi}\sigma_{fine}} \exp\left[-\frac{(\ln r - \ln r_{fine})}{2\sigma_{fine}^2}\right] + \frac{C_{coarse}}{\sqrt{2\pi}\sigma_{coarse}} \exp\left[-\frac{(\ln r - \ln r_{coarse})}{2\sigma_{coarse}^2}\right],$$

where $C_{total,fine,coarse}$ represent the particle volume concentration for total, fine and coarse aerosol modes [$\mu m^3/\mu m^2$], $r_{fine,coarse}$ is the median or geometric mean radius [μm], and $\sigma_{fine,coarse}$ is the variance or width of each mode. n and k represent the real and imaginary parts of the complex refractive index, respectively.

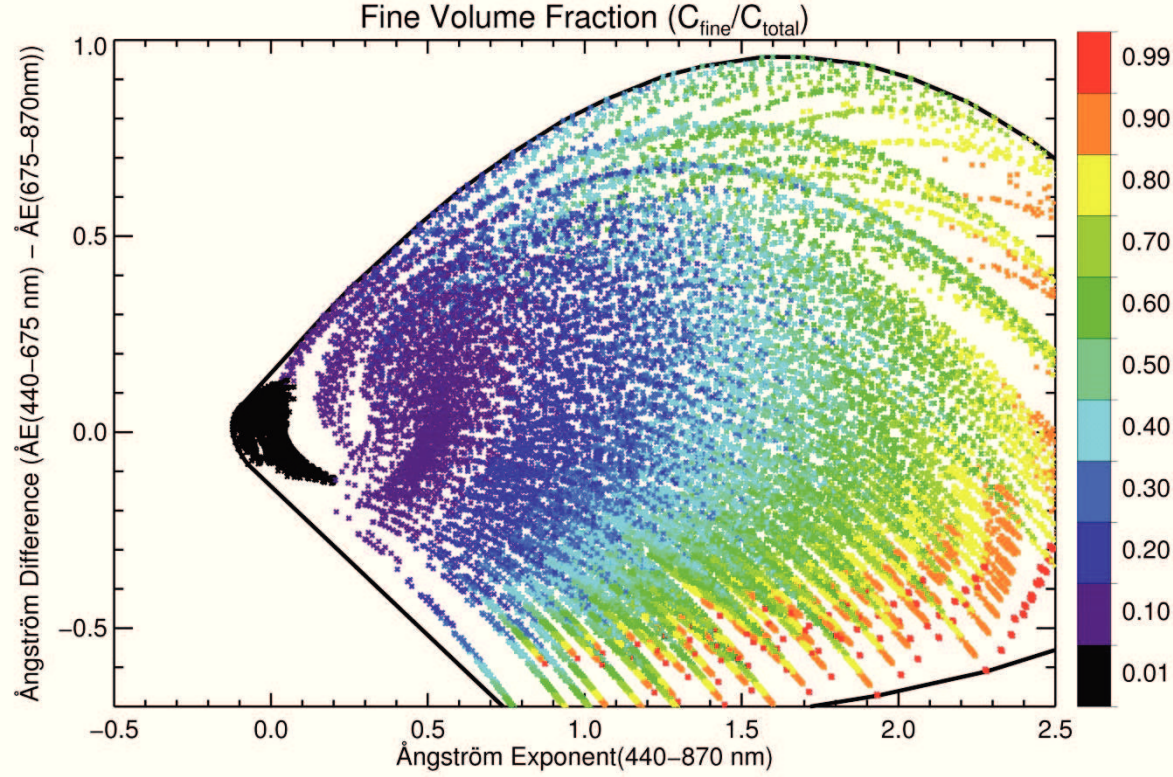

Fig. 5.5 Simulations of the fine volume fraction as a function of ÅE (440-870 nm) and ÅED (ÅE(440-675 nm)-ÅE(675-870 nm)) using Mie theory with all combinations of volume median radius, standard deviation, refractive indices, and fine volume fractions shown Tab. 5.2.

In this study, we set up the classification using both ÅE and ÅED by 50% fine volume fraction to total aerosol.

Generally, coarse-mode (fine-mode) dominant aerosols have been classified by lower (higher) values than ÅE of at least 1.0 (Kaufman, 1993) or 1.4 [Tanré et al., 2001; Pereira et al., 2011; Shinozuka et al., 2011]. However, one constant value of ÅE is not a good threshold to classify the aerosol types (coarse and fine dominant aerosols). Therefore, the new classification criteria determined by 50% fine volume fraction effectively discriminates coarse- and fine-mode dominant aerosols by higher accuracy (95.73%) than using other constant ÅEs (75.30% for ÅE of 1.0 and 80.82% for ÅE of 1.4) based on the Mie simulation in Fig. 5.5. Fig. 5.6 provides additional Mie simulations [Mishchenko et al., 1999b, 2002] based on aerosol characteristics of typical aerosols (urban-industrial and mixed, biomass

burning, desert dust, oceanic from Dubovik et al. (2002a)) to examine the red classification line (i.e. a variable ÅE and ÅED determined by 50% fine volume fraction). Coarse-mode dominant aerosols (desert dust and maritime aerosols) have smaller ÅE and positive ÅED according to the increase of aerosol loading. As already mentioned, the mean particle size of fine-mode dominant aerosols can increase by the increase of aerosol loading, despite of larger fine volume fractions. In addition, the range of ÅE (440-870 nm) for the typical aerosols from Dubovik et al. (2002a) (horizontal bar chart on the lower hand in Fig. 5.6) can explain why only one constant value of ÅE is not enough to classify coarse- or fine-mode dominant aerosols. These tendencies of ÅE and ÅED are more apparent when looking at application of AERONET data.

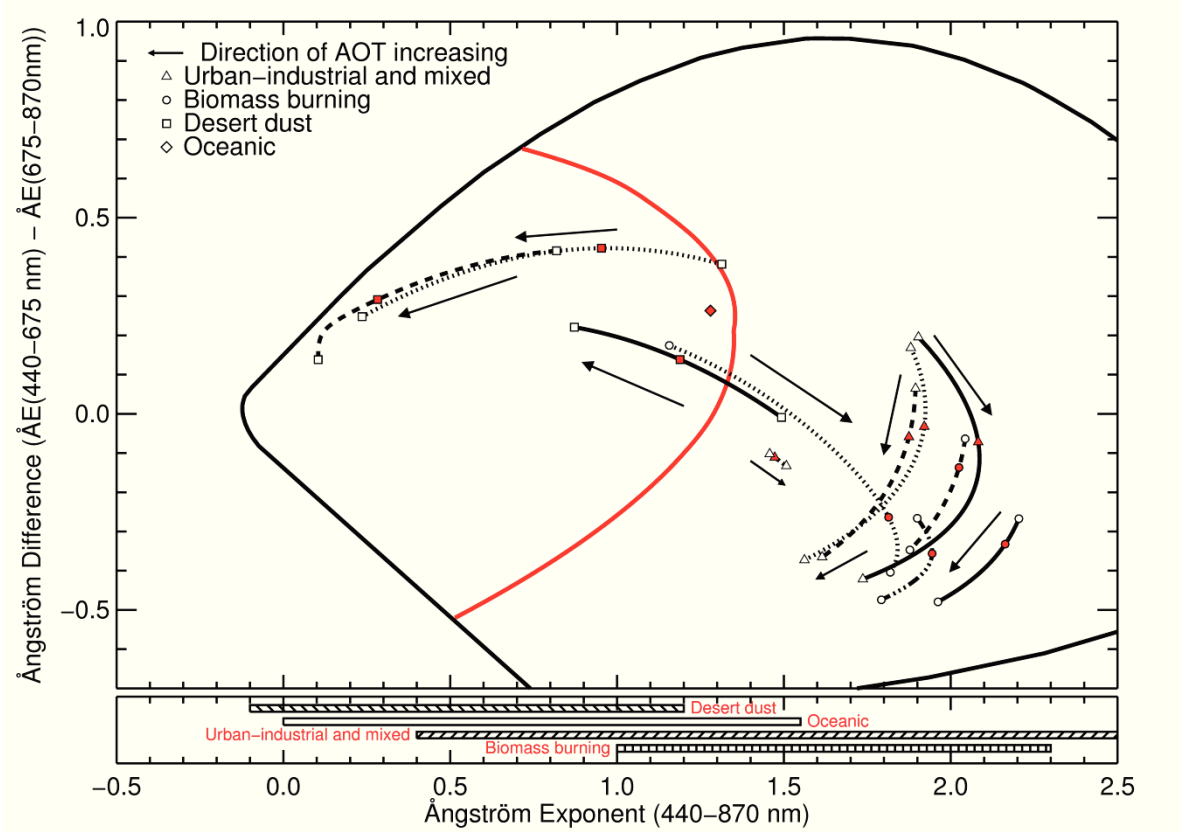

Fig. 5.6 Mie simulations (solid, dotted, dashed, dash-dot-dot lines) and range of Ångström Exponent (440-870 nm) for the typical aerosols (urban-industrial and mixed, biomass burning, desert dust, oceanic) summarized in Dubovik et al. (2002a). The red spot and red line represent the simulations for AOT mean of the typical aerosols and the classification line for two aerosol types (fine- and coarse-mode dominant aerosols), respectively.

Fig. 5.7 illustrates a scatterplot of ÅE and ÅED derived from AERONET datasets at fifteen stations including the red classification line. After applying the classification, the percentages of coarse-mode (C) and fine-mode (F) dominant aerosols are shown as a pie chart at the upper-left hand side. In order to avoid ÅE errors larger than 30%, those observations having an AOT at 440 nm larger than 0.15 have only been taken into account [Gobbi et al., 2007]. Most ÅEs and ÅEDs from the AERONET observations are positioned within the simulation border (thick black line) and their distributions according to increase of aerosol loading are similar with the Mie simulations in Fig. 5.6. As can be seen in Fig. 5.7, each AERONET station has a difference in percentage of coarse- and fine-mode dominant aerosols due to regionally different aerosol sources and atmospheric conditions. All stations over West Africa (Banizoumbou (C 99% >> F 1%), Dakar (C 99% >> F 1%), and Ouagadougou (C 97% >> F 3%)) and Middle East (SEDE_BOKER (C 71% > F 29%) and Solar_Village (C 97% >> F 3%)) are influenced by coarse-mode dominant aerosols because the regions are close to or within deserts. In contrast, industrial pollutants and biomass burning aerosols are dominant over Western Europe (Avignon (C 23% < F 77%) and Ispra (C 13% < F 87%)), South Africa (Mongu (C 6% << F 94%) and Skukuza (C 15% < F 85%)), and North America (GSFC (C 9% << F 91%) and MD_Science_Center (C 10% < F 90%)). Especially, typical anthropogenic aerosols caused by urbanization and industrialization as well as dust aerosols brought in by strong westerly winds are observed over East Asia (Beijing (C 62% > F 38%) and Shirahama (C 41% < F 59 %)). The classification is not applicable to data observed at Mauna_Loa and Sevilleta because most AOTs (440 nm) at these stations are less than 0.15. Finally, by applying the new aerosol classification, the present study can provide more reliable trends of Coarse- and Fine-mode dominant AOTs (CAOT and FAOT), which are more suitable to understand what major sources are influencing the AOT changes.

Tab. 5.3 Summary of aerosol optical properties for urban-industrial and mixed, biomass burning, desert dust, and oceanic types from Dubovik et al. (2002a) based on worldwide AERONET of ground-based radiometers. These properties are used to compute ÅE (440-870 nm) and ÅED (ÅE(440-675 nm)-ÅE(675-870 nm)) using Mie code and depicted by solid, dotted, dashed, dash-dot-dot lines sequentially in Fig. 5.6.

Urban-industrial and mixed	**GSFC, Greenbelt, MD (1993-2000)**	**Crete-Paris, France (1999)**	**Mexico City (1999-2000)**	**Maldives (INDOEX) (1999-2000)**
Range of optical thickness; <δ>*	0.1≤δ(440)≤1.0; 0.24	0.1≤δ(440)≤0.9; 0.26	0.1≤δ(440)≤1.8; 0.43	0.1≤δ(440)≤0.7; 0.27
Refractive indices (n; k)	1.41-0.03δ(440); 0.003	1.40; 0.009	1.47; 0.014	1.44; 0.007
r_{fine}[μm]; σ_{fine}	0.12+0.11δ(440); 0.38	0.11+0.13δ(440); 0.43	0.12+0.04δ(440); 0.43	0.18; 0.46
r_{coarse}[μm]; σ_{coarse}	3.03+0.49δ(440); 0.75	2.76+0.48δ(440); 0.79	2.72+0.60δ(440); 0.63	2.62+0.61δ(440); 0.76
C_{fine}[$\mu m^3/\mu m^2$]	0.15δ(440)	0.01+0.12δ(440)	0.12δ(440)	0.12δ(440)
C_{coarse}[$\mu m^3/\mu m^2$]	0.01+0.04δ(440)	0.01+0.05δ(440)	0.11δ(440)	0.15δ(440)
Biomass burning	**Amazonian forest, Brazil (1993-1994); Bolivia (1998-1999)**	**South American cerrado, Brazil (1993-1995)**	**African savanna, Zambia (1995-2000)**	**Boreal forest, United States and Canada (1994-1998)**
Range of optical thickness; <δ>	0.1≤δ(440)≤3.0; 0.74	0.1≤δ(440)≤2.1; 0.80	0.1≤δ(440)≤1.5; 0.38	0.1≤δ(440)≤2.0; 0.40
Refractive indices (n; k)	1.47; 0.00093	1.52; 0.015	1.51; 0.021	1.50; 0.0094
r_{fine}[μm]; σ_{fine}	0.14+0.13δ(440); 0.40	0.14+0.01δ(440); 0.47	0.12+0.025δ(440); 0.40	0.15+0.015δ(440); 0.43
r_{coarse}[μm]; σ_{coarse}	3.27+0.58δ(440); 0.79	3.27+0.51δ(440); 0.79	3.22+0.71δ(440); 0.73	3.21+0.2δ(440); 0.81
C_{fine}[$\mu m^3/\mu m^2$]	0.12δ(440)	0.1δ(440)	0.12δ(440)	0.01+0.1δ(440)
C_{coarse}[$\mu m^3/\mu m^2$]	0.05δ(440)	0.04+0.03δ(440)	0.09δ(440)	0.01+0.03δ(440)
Desert dust and oceanic	**Bahrain-Persian Gulf (1998-2000)**	**Solar-Vil.-Saudi Arabia (1998-2000)**	**Cape Verde (1993-2000)**	**Lanai, HI (1995-2000)**
Range of optical thickness; <δ>	0.1≤δ(1020)≤1.2; 0.22	0.1≤δ(1020)≤1.5; 0.17	0.1≤δ(1020)≤2.0; 0.39	0.01≤δ(1020)≤0.2; 0.04
Refractive indices (n)	1.55	1.56	1.48	1.36
Refractive indices (k(440/670/870/1020 nm))	0.0025/0.0014/0.001/0.001	0.0029/0.0013/0.001/0.001	0.0025/0.0007/0.0006/0.0006	0.0015
r_{fine}[μm]; σ_{fine}	0.15; 0.42	0.12; 0.40	0.12; 0.49+0.10δ(1020)	0.16; 0.48
r_{coarse}[μm]; σ_{coarse}	2.54; 0.61	2.32; 0.60	1.90; 0.63-0.10δ(1020)	2.70; 0.68
C_{fine}[$\mu m^3/\mu m^2$]	0.02+0.1δ(1020)	0.02+0.02δ(1020)	0.02+0.02δ(1020)	0.40δ(1020)
C_{coarse}[$\mu m^3/\mu m^2$]	-0.02+0.92δ(1020)	-0.02+0.98δ(1020)	0.9δ(1020)	0.80δ(1020)

* <δ> is total mean of AOT at λ nm (δ(λ)).

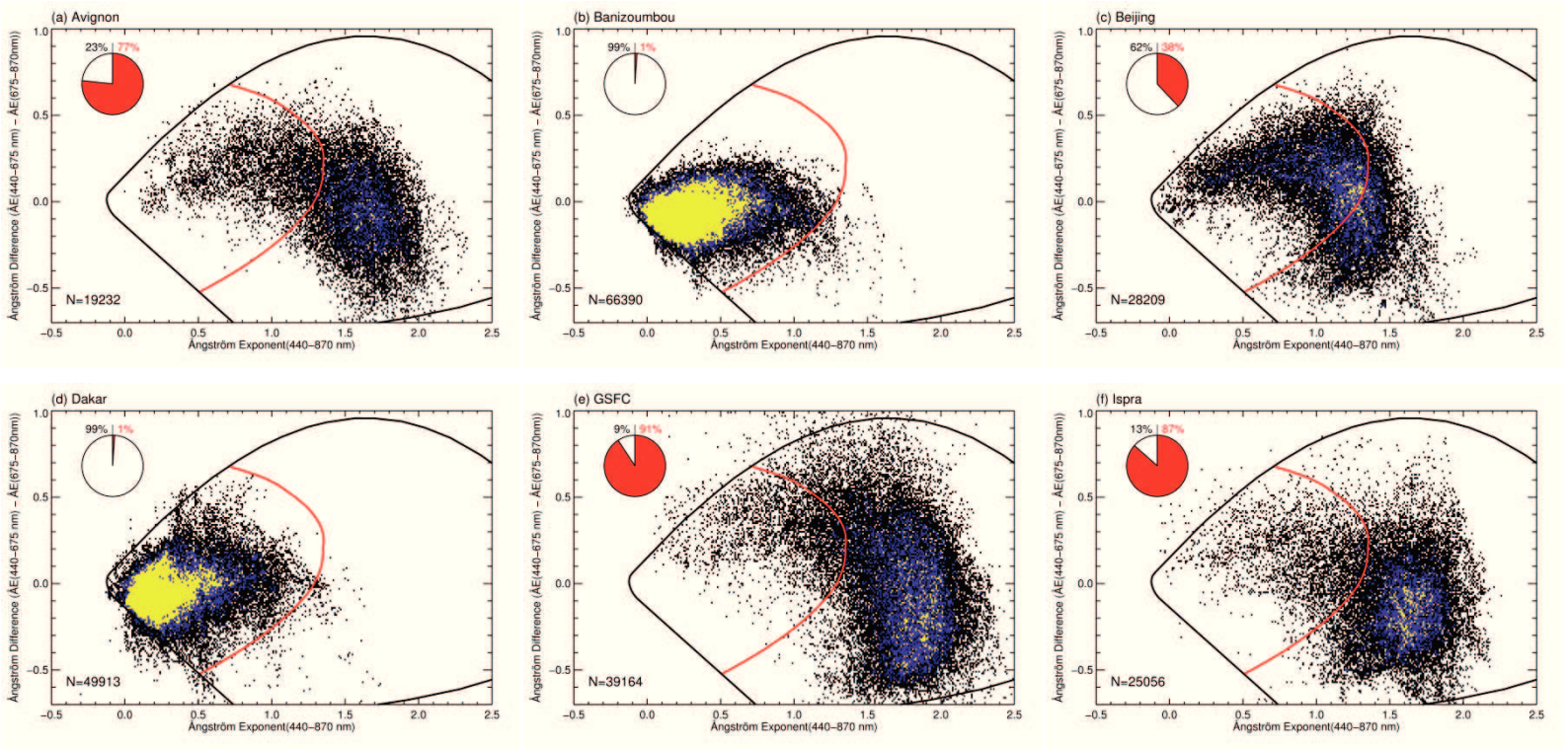

Fig. 5.7 Applications of the classification method to the AERONET datasets separated into two aerosol types as fine- and coarse-mode dominant aerosols at the several AERONET stations. The circle diagram on the upper-left hand means the percentage of coarse (black) and fine-mode (red) dominant aerosols to total observations (N). To avoid large errors in Ångström Exponent and its difference from low AOTs, only AERONET level 2.0 data with AOT (440 nm) > 0.15 are used.

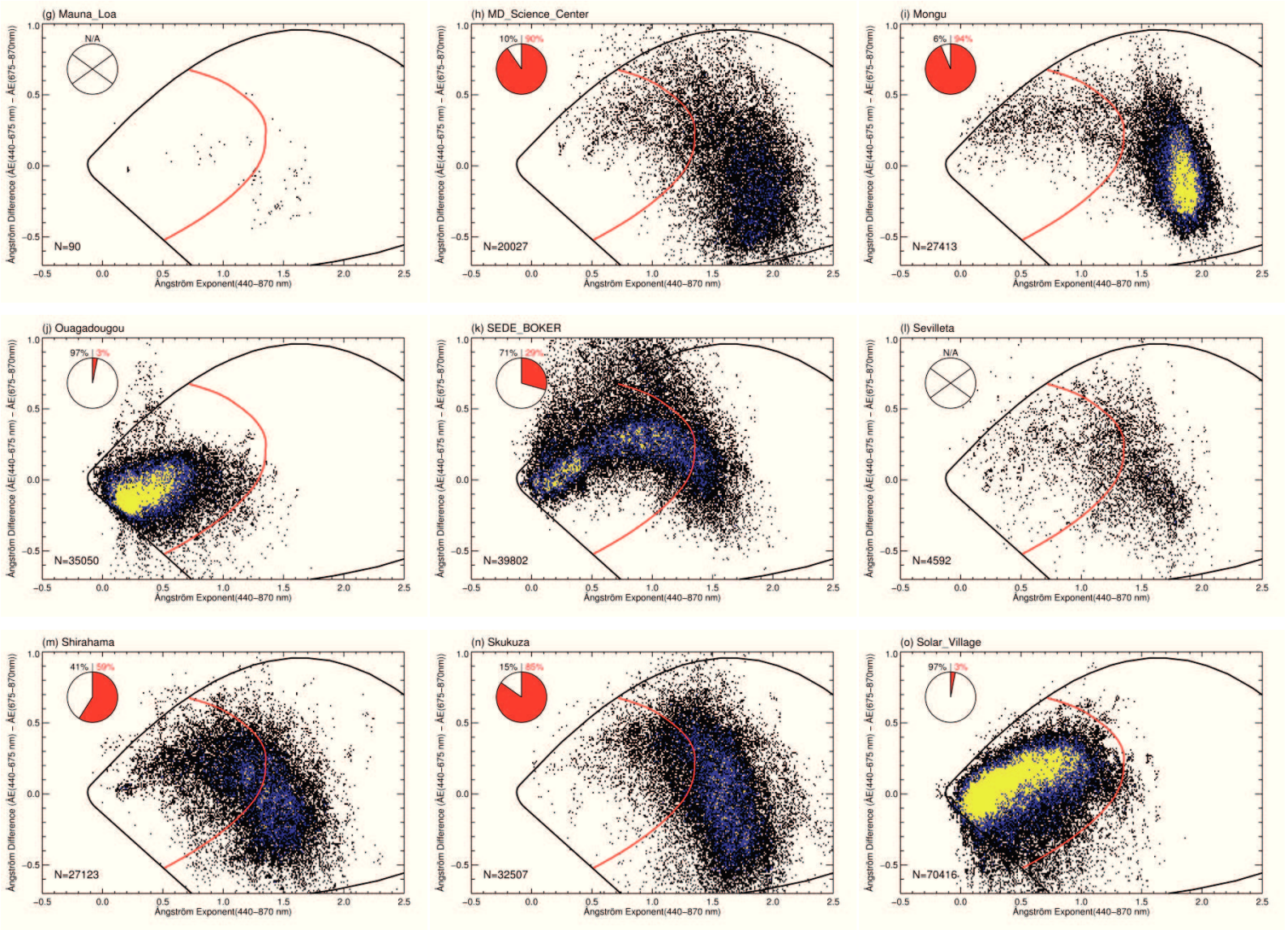

Fig. 5.7 (*Continued)*

5.2 Regional trend analysis

Shown in Fig. 5.8, the trends of ÅE (440-870 nm) and AOT (440 nm) are discussed at fifteen selected AERONET stations located in several regions (Western Europe, West Africa, South Africa, Middle East, East Asia, North America, and Free troposphere/Pacific). For clarity, the error bar is the standard error ($\sigma_t/\sqrt{n_t}$) scaled by a factor of 10. Comparison between unweighted (blue line and text on the left upper part) and weighted trends (red line and text on the right upper part) allows to estimate the uncertainty caused by cloud disturbance in the trend analysis. In this section, the main discussions of the aerosol trends are on the basis of the weighted trends. As previously mentioned, a classification of coarse- and fine-mode dominant aerosols is also introduced in the trend analysis (Fig. 5.10). Finally, the unweighted and weighted trends of ÅE (440-870 nm), AOT, CAOT, and FAOT (440 nm) in percent for most of AERONET stations are indicated on the global map in Figs. 5.9 and 5.11, and all specific values of both trend analyses are summarized in Tabs. 5.4 and 5.5.

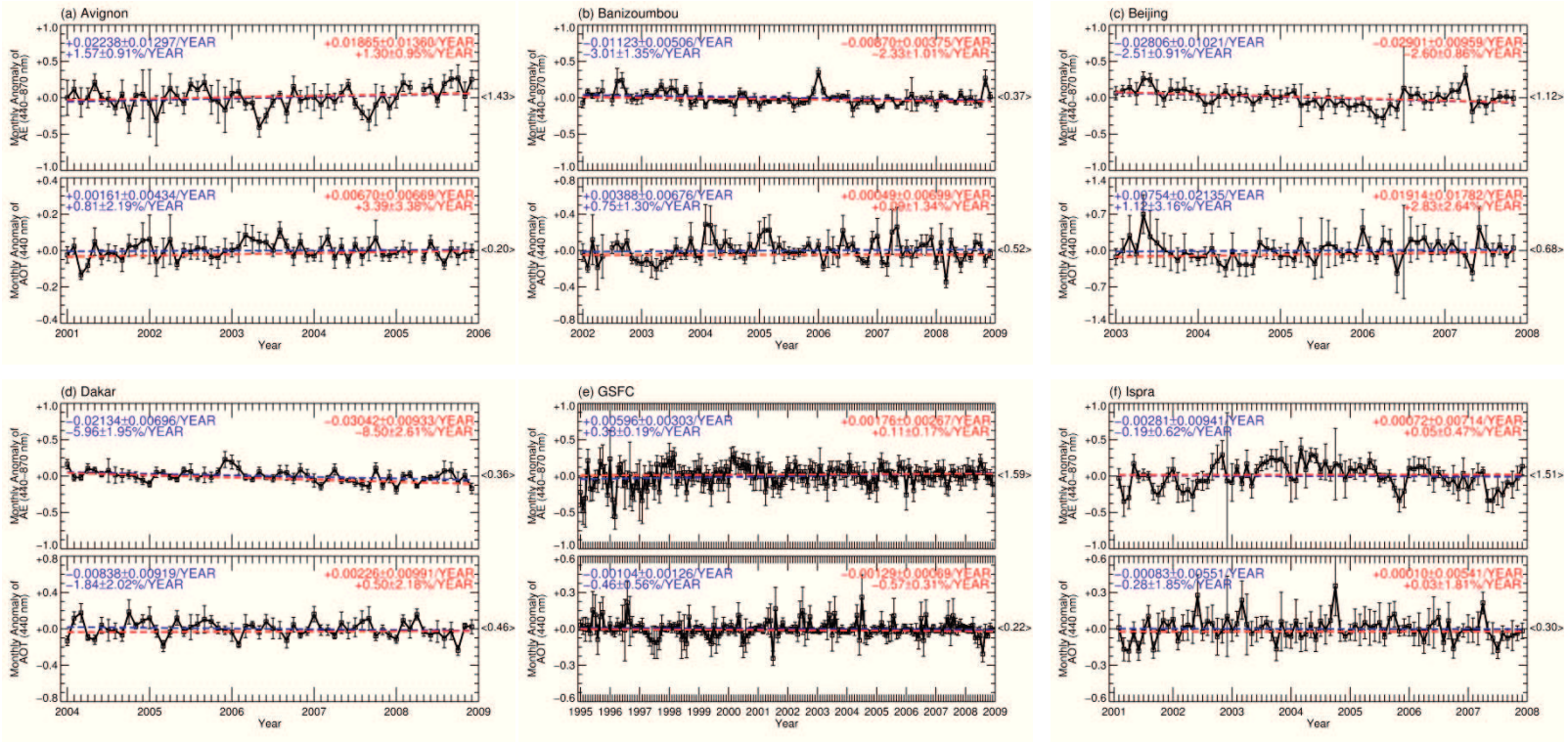

Fig. 5.8 Unweighted (blue one on the left upper part) and weighted (red one on the right upper part) trends of Ångström Exponent (440-870 nm) (α) and AOT (440 nm) (δ_{440}) at the several AERONET stations. The total means of α and δ_{440} (black one enclosed with parentheses) are shown on right vertical axis. The error bar means the 10 times of the standard error, which are used for the weighted trend analysis.

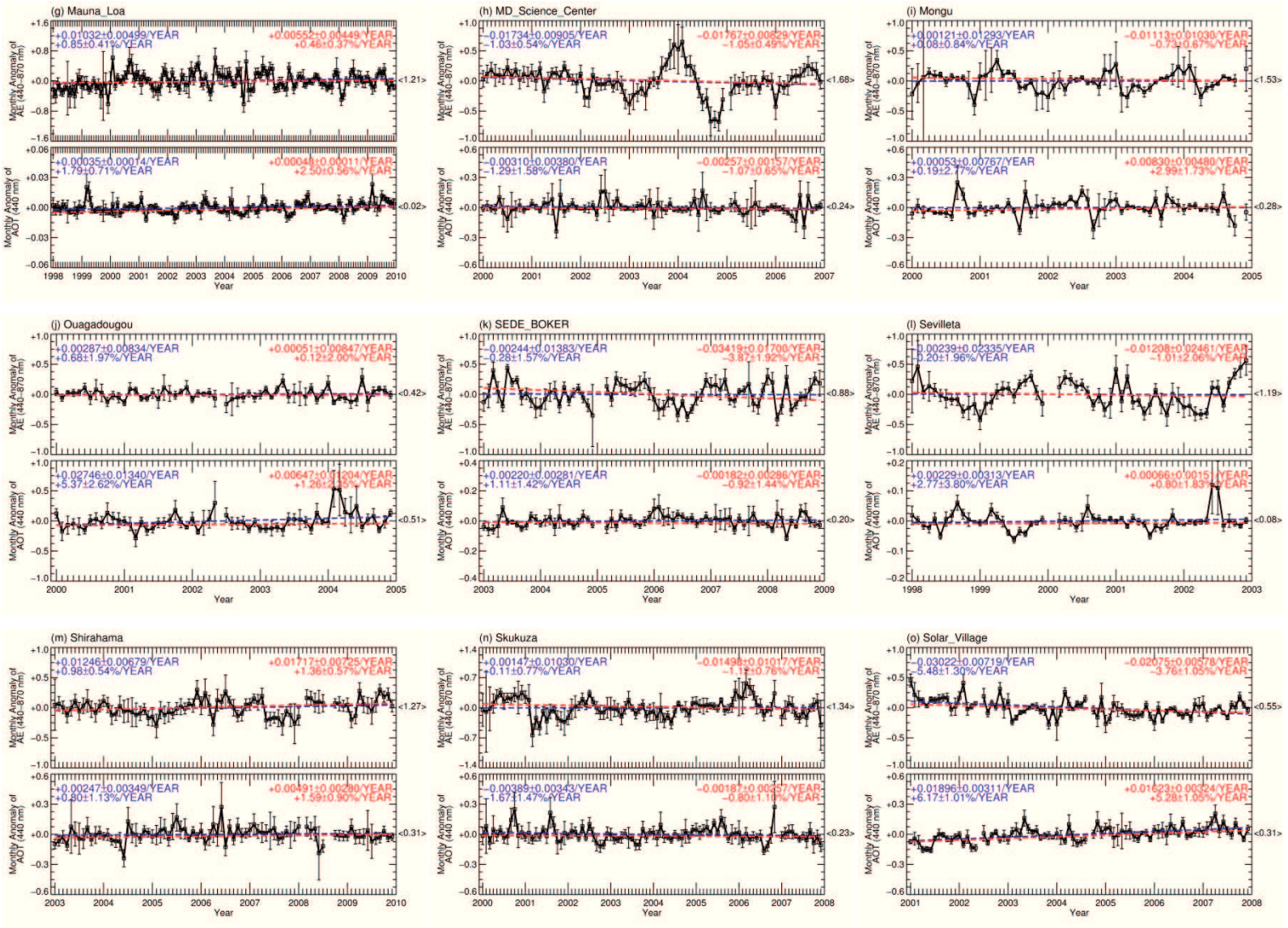

Fig. 5.8 (*Continued*)

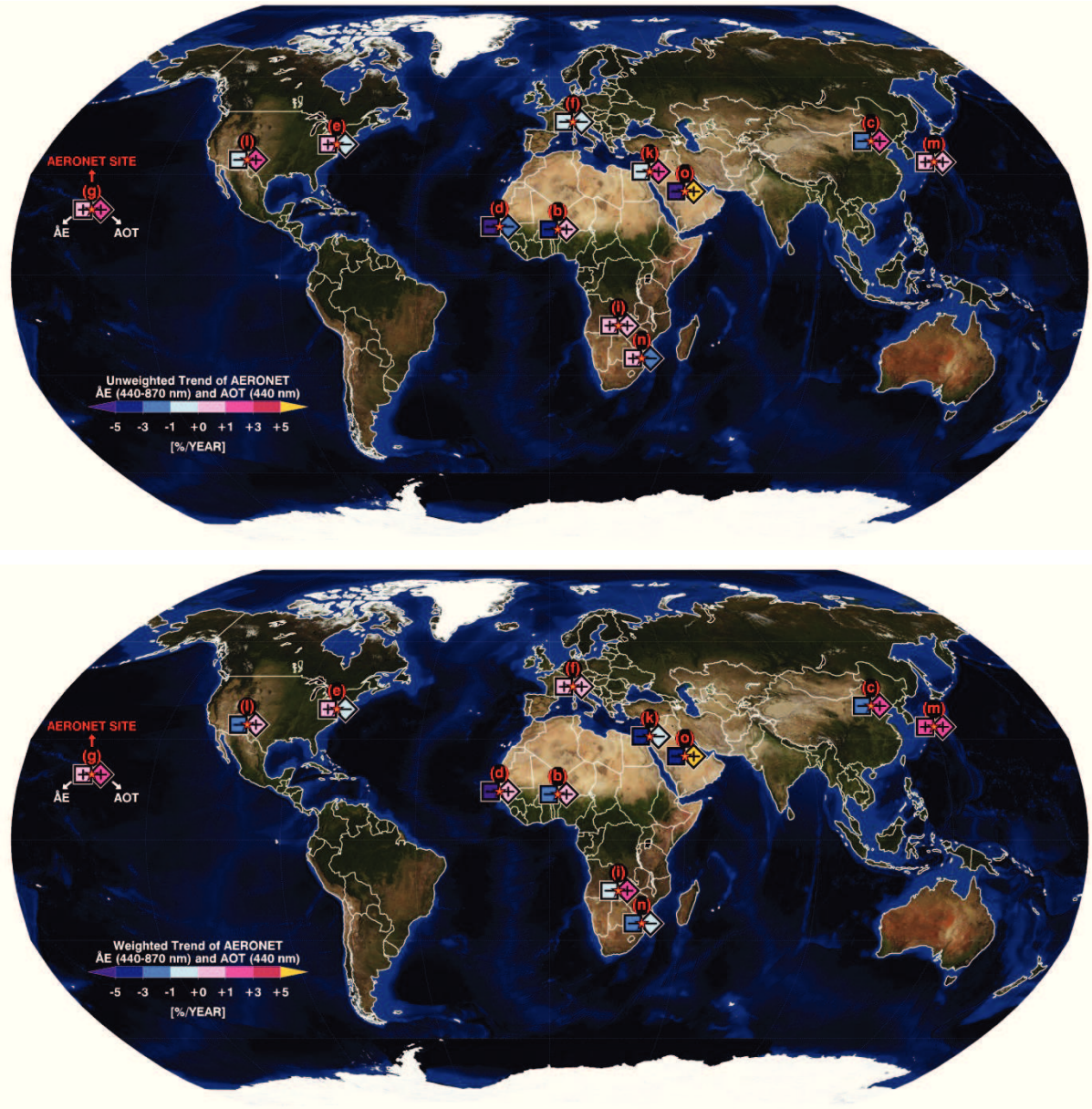

Fig. 5.9 Unweighted and weighted trends of ÅE (440-870 nm) (left square) and AOT (440 nm) (right diamond) in percent at the major stations except (a) Avignon over Western Europe, (h) MD_Science_Center over North America, and (j) Ouagadougou over West Africa.

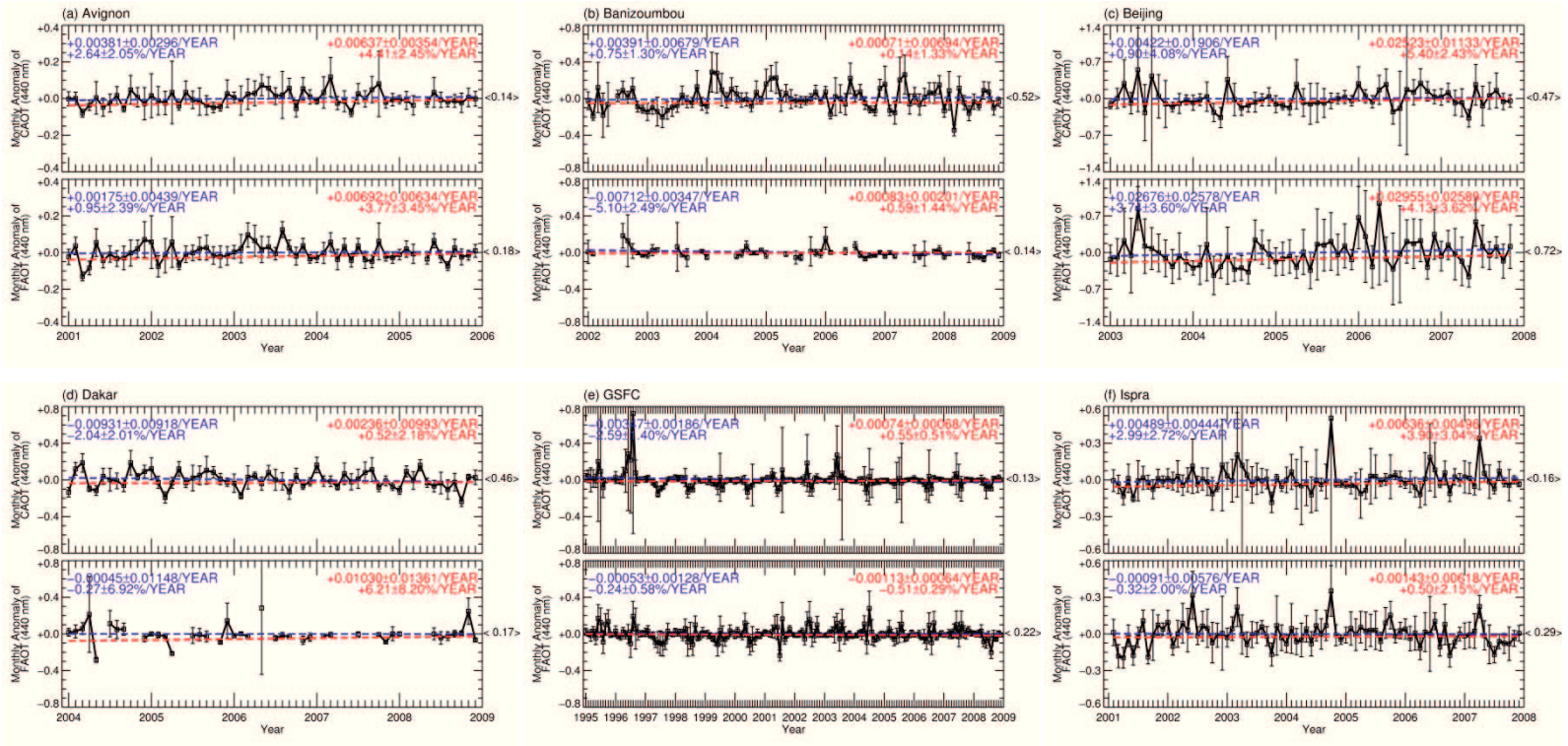

Fig. 5.10 As in Fig. 5.8, but for Coarse- and Fine-mode dominant AOT (440 nm) (CAOT and FAOT). Trend analysis of FAOT at (b) Banizoumbou, (d) Dakar, (j) Ouagadougou, and (o) Solar_Village may be insignificant because of incomplete yearly data sets.

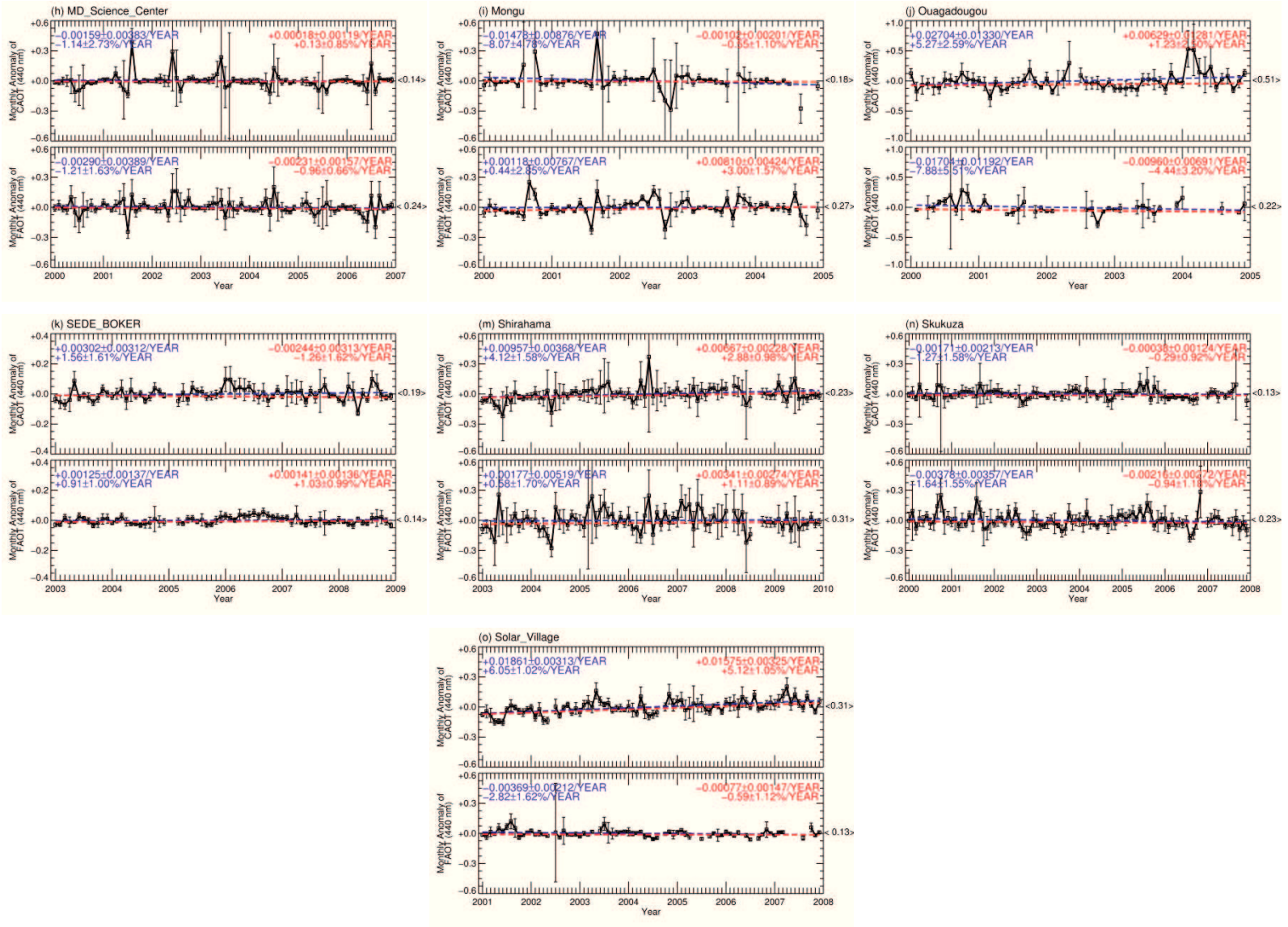

Fig. 5.10 (*Continued*)

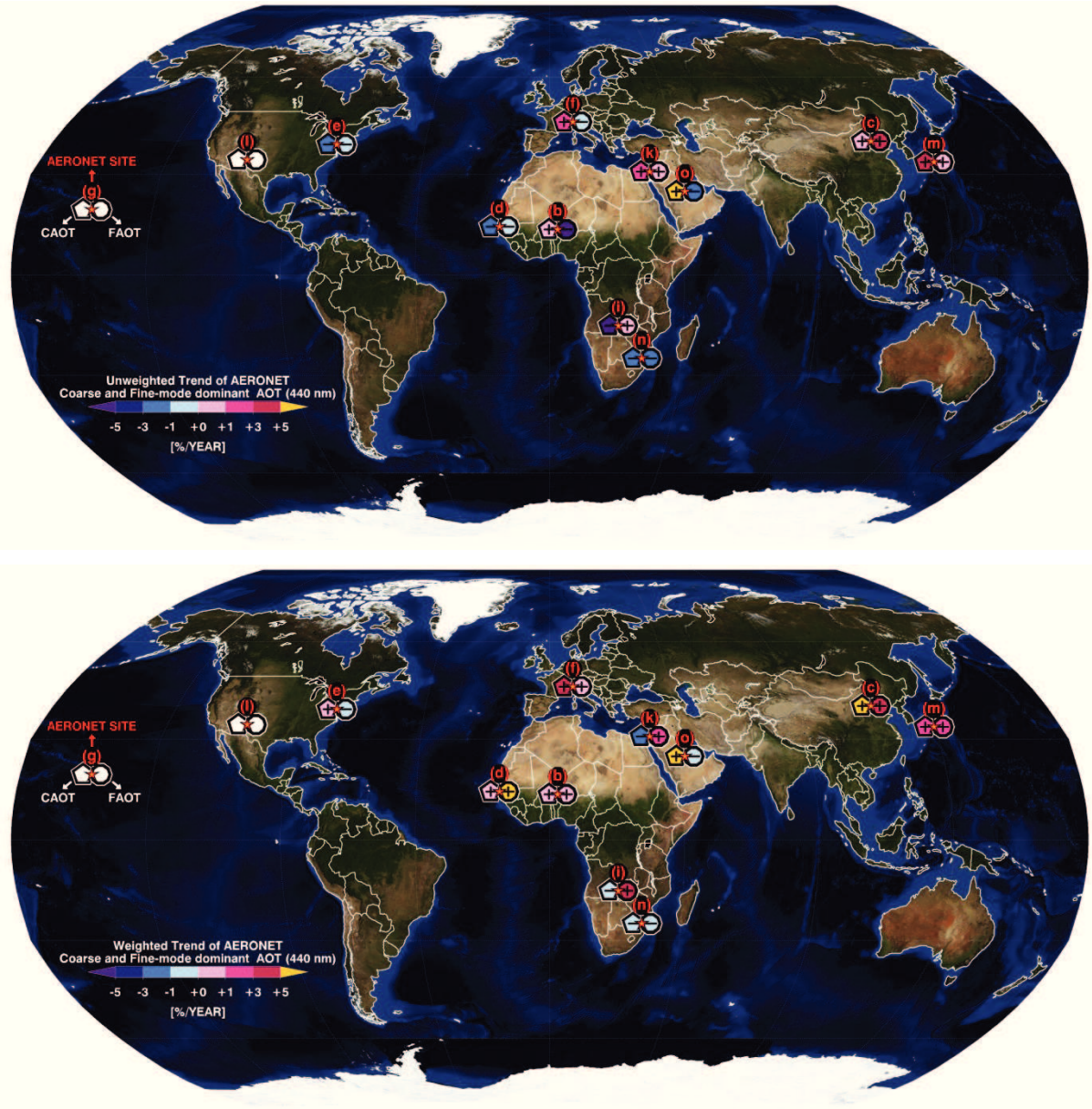

Fig. 5.11 As in Fig. 5.9, but for Coarse- (left pentagon) and Fine-mode (right circle) dominant AOT (440 nm) (CAOT and FAOT) except (a) Avignon over Western Europe, (h) MD_Science_Center over North America, and (j) Ouagadougou over West Africa. Non-applicable cases are shown as a white blank. Trend analysis of FAOT at (b) Banizoumbou, (d) Dakar, (j) Ouagadougou, and (o) Solar_Village may be insignificant because of incomplete yearly data sets.

Western Europe

The averages of ÅE shown in Fig. 5.8 at the stations Avignon (<ÅE> = 1.43) and Ispra (<ÅE> = 1.51) over Western Europe are influenced by industrial, urban, and traffic pollutants, such as ammonium salts of sulphate and nitrate [González et al., 2000; Benkovitz et al. 1996; Kambezidis and Kaskaoutis, 2008; Mazzola et al., 2010]. The AOTs over Western Europe exhibit a significant seasonal variation, which increases from spring to summer and decreases from autumn to winter. Basically, the AOT depends on the aerosol extinction coefficient (e.g., influenced by aerosol types, emission intensity, and relative humidity) and boundary layer height. Especially, industrial pollutants composed of sulphur are enhanced during summer due to stronger solar radiation [Marmer et al., 2007; Karnieli et al., 2009]. In addition, less removal process (e.g., rain/monsoon) as well as a higher boundary layer height causes higher AOTs over Europe in summer [Gerasopoulos et al., 2003; Bergamo et al., 2008; Venzac et al., 2009]. The weighted AOT trends over both stations are insignificant increasing or decreasing (+0.00161±0.00434 at Avignon and -0.00083±0.00551 yr^{-1} at Ispra). These tendencies are similar in FAOT trends at the stations, which are +0.00692±0.00634 at Avignon and +0.00143±0.00618 yr^{-1} at Ispra as shown in Fig. 5.10. Finally, these ground-based estimates are somewhat different to the decreasing trends [Smith et al., 2001; Streets et al., 2006; Zhao et al., 2008] over European regions most likely due to strict environmental regulations for mitigating climate change and improving air quality.

West Africa

Mineral dust mainly from the Saharan and Sahel regions is the most abundant aerosol type over West Africa (the stations Banizoumbou, Dakar, and Ouagadougou) year-round [Prospero and Lamb, 2003; Washington and Todd, 2005; Moulin and Chiapello, 2004; Reeves et al., 2010]. Besides, biomass burning is frequently advected by the West African

monsoon in summer from central Africa [Hao and Liu, 1994], and emitted from agricultural activity during the dry season (December-February) in West Africa [Johnson et al., 2008a]. The complex vertical distributions between mineral dust and biomass burning can make it difficult to assess the shortwave radiative effects [Johnson et al., 2008b]. Additionally, low AOT may occur as a result of efficient wet removal of aerosol particles due to strong precipitation [Reeves et al., 2010; Huang et al., 2009]. Insignificant increasing trends of dust aerosol are observed over most stations in West Africa (+0.00049±0.00699 at Banizoumbou, +0.00226±0.00991 at Dakar, and +0.00647±0.01204 yr^{-1} at Ouagadougou in Fig. 5.8). The weighted trends of ÅE and AOT at Dakar and Ouagadougou are different compared to unweighted trends due to frequent cloud disturbance. CAOT trends over West Africa (+0.00071±0.00694 at Banizoumbou, +0.00236±0.00993 at Dakar, and +0.00629±0.01281 yr^{-1} at Ouagadougou in Fig. 5.10) are generally similar with AOT trends.

South Africa

ÅE as well as AOT over the stations Mongu and Skukuza in South Africa exhibit a strong seasonality due to pronounced wet and dry seasons (see Fig. 5.8), and the presence of biomass burning aerosols [Tyson, 1986; Swap et al., 1996]. Frequent occurrence of burning activity in warm and dry seasons generates more biomass burning aerosols [Eck et al., 2001]. The area close to Skukuza (where there is less fire activity) is additionally influenced by aerosol mixtures with fossil fuel burning, industrial pollutant, and Aeolian coarse mode types [Eck et al., 2003]. In this region, the difference between unweighted and weighted trends is negligible because the burning activity generally happens before rainy season. A noticeable increases of AOT and FAOT at Mongu (+0.00830±0.00480 and +0.00810±0.00424 yr^{-1}) are most likely affected by biomass burning [Mishchenko and Geogdzhayev, 2007; Zhao et al., 2008], while insignificant decreases at Skukuza (-0.00187±0.00257 and -0.00216±0.00272

yr^{-1}) due to high variability of monthly AOTs in Figs. 5.8 and 5.10.

Middle East

The stations SEDE_BOKER and Solar_Village are located within the Middle East, and provide a long record of measurements because of stable and clear-sky weather conditions [Basart et al., 2009]. In this region, aerosol size and composition are dominated by mineral dust transported from the Anatolian plateau, Sahara, Negev, and Arabian deserts [Kubilay et al., 2003; Derimian et al., 2006; Sabbah et al., 2006; Smirnov et al., 2002; Tafuro et al., 2006] and industrial pollutants produced by the regional petroleum refining [Zhao et al., 2008; Basart et al., 2009]. The former explains the clear periodical pattern of ÅE and AOT seen in Fig. 5.8. The AOT over SEDE_BOKER tends to decrease (-0.00182±0.00286 yr^{-1}) due to a decrease in coarse particles (-0.00244±0.00313 yr^{-1} for CAOT in Fig. 5.10), while AOT over Solar_Village show a strong increase (+0.01623±0.00324 yr^{-1}) in the weighted trend probably related to an increase of mineral dust (+0.01575±0.00325 yr^{-1} for CAOT) caused by a change of atmospheric conditions (e.g. increase of wind speed and relative humidity) [Sabbah and Hasan, 2008]. Interestingly, there are clear differences between the unweighted and weighted trends at both stations due to a large standard error due to high variability of ÅE and AOT. The weighted FAOT trends of SEDE_BOKER and Solar_Village are insignificant (+0.00141±0.00136 and -0.00077±0.00147 yr^{-1}, respectively as seen in Fig. 5.10).

East Asia

Many emerging economies are found in East Asia, where, as a consequence, large amounts of anthropogenic aerosols are emitted. Additionally, mineral dust from the deserts in Mongolia and in Western and Northern China (mainly the Taklimakan and Badain Juran deserts) contributes around 70% of the total dust emissions in mid-latitude regions. Rapid

desertification caused by climate variation and human activities additionally can increase the aerosol amount [Zhang et al., 2003]. ÅE and AOT at Beijing exhibit very clear seasonal cycles, which have been explained by the complex combination of natural and anthropogenic aerosols, stagnant synoptic meteorological patterns, secondary aerosol formation, and hygroscopic growth [Kotchenruther et al., 1999; Dubovik et al., 2002a; Kim et al., 2007]. Because of industrialization, urbanization, and desertification over East Asia in the last twenty years, the aerosol loading over Beijing increases rapidly and the magnitude of the weighted trend is +0.01914±0.01782 yr^{-1} in Fig. 5.8. This trend is consistent with many previous studies [Streets et al., 2000, 2003, 2006; Smith et al., 2001, 2003; Massie et al., 2004; Mishchenko and Geogdzhayev, 2007; Zhao et al., 2008]. Such an increase is also observed in both aerosol types and more pronounced for weighted trends of CAOT and FAOT with increases of +0.02523±0.01133 and +0.02955±0.02589 yr^{-1}, respectively in Fig. 5.10. Shirahama is located along the south-western coast of Japan, far-off large cities, facing the Pacific Ocean [Mukai et al., 2006]. Hence, maritime aerosol is predominant, but there are occurrences of mineral dust and/or industrial aerosol transported by strong westerly winds from China [Sano et al., 2003; Mukai et al., 2005]. The seasonal cycles of ÅE and AOT are similar to those at Beijing due to similar meteorological conditions and aerosol sources. The upward trend of AOT is small (+0.00491±0.00280 yr^{-1}), while ÅE increases (+0.01717±0.00725 yr^{-1}), clearly seen in Fig. 5.8. The magnitudes of the CAOT and FAOT trends are +0.00667±0.00228 and +0.00341±0.00274 yr^{-1} in Fig. 5.10, which are similar with the trends at Beijing.

North America

The stations GSFC and MD_Science_Center are located on urban, while Sevilleta is positioned at shrub land over North America [Liu et al., 2004]. The main aerosol type

measured at GSFC and MD_Science_Center is due to urban-industrial pollution, mainly from vehicles and industries. The seasonal cycles of ÅE and AOT demonstrate that the variabilities are strongly dependent on the combination of natural and anthropogenic aerosols, fuel types, emission characteristic, relative humidity, boundary layer height, and scavenging by precipitation [Glen et al., 1996; Chen et al., 2001; Dubovik et al., 2002a; Andronache, 2004]. The negative trends of AOT (-0.00129±0.00069 at GSFC and -0.00257±0.00157 yr^{-1} at MD_Science_Center in Fig. 5.8) are consistent with the decrease of industrial emissions in the United States of America [Smith et al., 2001; Streets et al., 2006; Zhao et al., 2008]. A relatively small aerosol loading is observed at Sevilleta for the research periods. The weighted trends in Fig. 5.8 are -0.01208±0.02461 for ÅE and +0.00066±0.00151 yr^{-1} for AOT, clearly different from the unweighted ones (-0.00239±0.02335 for ÅE and +0.00229±0.00313 yr^{-1} for AOT). The most of monthly AOTs at Sevilleta are lower than 0.15, so that the classification cannot be applied. The weighted trends of fine-mode dominant aerosol (major aerosol type at GSFC and MD_Science_Center) are -0.00113±0.00064 and -0.00231±0.00157 yr^{-1}, respectively (see Fig. 5.10).

Mauna_Loa

Aerosols measured at Mauna_Loa (alt. ~ 3397m) in the Pacific are representative for *free tropospheric aerosol*. The free troposphere, which is characterized by being almost cloud-free in the subsiding branch of the Hadley cell [Garstang and Fitzjarrald, 1999; Schmeissner et al., 2011], is a good pathway for long-range transported aerosols (i.e., Asian mineral dust and pollution) over 6000 to 8000 km in spring [Perry et al., 1999; Eck et al., 2005]. In most cases, free tropospheric AOT (440 nm) does not exceed values of 0.05 except when affected by volcano eruption or transported mineral dust and pollution. Therefore, it is difficult to apply the classification due to significant errors of ÅE and ÅED [Gobbi et al., 2007;

Kaskaoutis et al., 2011a]. The main factors affecting the seasonal pattern of AOT are most likely long-range transported aerosols and seasonal meteorological conditions; the AOT trend for this station is positive (+0.00048±0.00011 yr^{-1} in Fig. 5.8). In addition, in order to investigate the trends in stratospheric or *free tropospheric aerosols*, the AOT data from March to May are excluded, and it is found that AOTs at 440 nm are increasing by +0.00049±0.00010 (+3.18±0.62%) yr^{-1} for unweighted and +0.00052±0.00011 (+3.36±0.71%) yr^{-1} for weighted trend analysis. However, because most of AOTs (440 nm) are close to the observation uncertainty (± 0.01) [Eck et al., 1999], these increasing tendencies at Mauna_Loa may be insignificant.

Tab. 5.4 Total means of Ångström Exponent (α) (440-870 nm) and AOTs (δ_λ) (440, 675, 870, and 1020 nm) and corresponding unweighted/weighted trends at the several AERONET stations.

	Total mean	Unweighted trend [/year]	Weighted trend [/year]	Total mean	Unweighted trend [/year]	Weighted trend [/year]	Total mean	Unweighted trend [/year]	Weighted trend [/year]
	(a) Avignon			**(b) Banizoumbou**			**(c) Beijing**		
α	1.43	+0.02238±0.01297	+0.01865±0.01360	0.37	-0.01123±0.00506	-0.00870±0.00375	1.12	-0.02806±0.01021	-0.02901±0.00959
δ_{440}	0.20	+0.00161±0.00434	+0.00670±0.00669	0.52	+0.00388±0.00676	+0.00049±0.00699	0.68	+0.00754±0.02135	+0.01914±0.01782
δ_{675}	0.11	+0.00033±0.00252	+0.00260±0.00361	0.47	+0.00589±0.00657	+0.00307±0.00656	0.43	+0.00759±0.01269	+0.01913±0.00895
δ_{870}	0.08	-0.00031±0.00185	+0.00057±0.00208	0.43	+0.00633±0.00607	+0.00388±0.00634	0.32	+0.00872±0.00895	+0.01685±0.00616
δ_{1020}	0.06	+0.00049±0.00172	+0.00053±0.00170	0.41	+0.00538±0.00577	+0.00301±0.00586	0.27	+0.00897±0.00732	+0.01430±0.00527
	(d) Dakar			**(e) GSFC**			**(f) Ispra**		
α	0.36	-0.02134±0.00696	-0.03042±0.00933	1.59	+0.00596±0.00303	+0.00176±0.00267	1.51	-0.00281±0.00941	+0.00072±0.00714
δ_{440}	0.46	-0.00838±0.00919	+0.00226±0.00991	0.22	-0.00104±0.00126	-0.00129±0.00069	0.30	-0.00083±0.00551	+0.00010±0.00541
δ_{675}	0.41	-0.00531±0.00880	+0.01009±0.00878	0.11	-0.00100±0.00067	-0.00080±0.00034	0.16	-0.00064±0.00299	-0.00059±0.00295
δ_{870}	0.38	-0.00298±0.00846	+0.01334±0.00830	0.07	-0.00078±0.00044	-0.00041±0.00023	0.11	-0.00001±0.00202	-0.00035±0.00208
δ_{1020}	0.36	-0.00277±0.00801	+0.01373±0.00764	0.06	-0.00058±0.00034	-0.00017±0.00021	0.09	-0.00016±0.00155	-0.00094±0.00189
	(g) Mauna_Loa			**(h) MD_Science_Center**			**(i) Mongu**		
α	1.21	+0.01032±0.00499	+0.00552±0.00449	1.68	-0.01734±0.00905	-0.01767±0.00829	1.53	+0.00121±0.01293	-0.01113±0.01030
δ_{440}	0.02	+0.00035±0.00014	+0.00048±0.00011	0.24	-0.00310±0.00380	-0.00257±0.00157	0.28	+0.00053±0.00767	+0.00830±0.00480
δ_{675}	0.01	+0.00009±0.00010	+0.00021±0.00007	0.12	-0.00142±0.00203	-0.00137±0.00080	0.14	-0.00077±0.00368	+0.00542±0.00222
δ_{870}	0.01	+0.00009±0.00008	+0.00022±0.00005	0.08	-0.00044±0.00127	-0.00019±0.00060	0.09	-0.00013±0.00226	+0.00507±0.00131
δ_{1020}	0.01	+0.00006±0.00007	+0.00017±0.00005	0.06	-0.00053±0.00106	-0.00061±0.00059	0.07	-0.00082±0.00171	+0.00336±0.00105
	(j) Ouagadougou			**(k) SEDE_BOKER**			**(l) Sevilleta**		
α	0.42	+0.00287±0.00834	+0.00051±0.00847	0.88	-0.00244±0.01383	-0.03419±0.01700	1.19	-0.00239±0.02335	-0.01208±0.02461
δ_{440}	0.51	+0.02746±0.01340	+0.00647±0.01204	0.20	+0.00220±0.00281	-0.00182±0.00286	0.08	+0.00229±0.00313	+0.00066±0.00151
δ_{675}	0.47	+0.00778±0.01732	-0.00495±0.01448	0.14	+0.00158±0.00267	-0.00174±0.00250	0.05	+0.00093±0.00167	+0.00068±0.00110
δ_{870}	0.41	+0.02454±0.01212	+0.00272±0.01114	0.12	+0.00237±0.00270	+0.00050±0.00222	0.04	+0.00121±0.00125	+0.00117±0.00094
δ_{1020}	0.38	+0.02655±0.01203	+0.00476±0.01077	0.11	+0.00148±0.00262	+0.00001±0.00266	0.03	+0.00116±0.00091	+0.00176±0.00078
	(m) Shirahama			**(n) Skukuza**			**(o) Solar_Village**		
α	1.27	+0.01246±0.00679	+0.01717±0.00725	1.34	+0.00147±0.01030	-0.01498±0.01017	0.55	-0.03022±0.00719	-0.02075±0.00578
δ_{440}	0.31	+0.00247±0.00349	+0.00491±0.00280	0.23	-0.00389±0.00343	-0.00187±0.00257	0.31	+0.01896±0.00311	+0.01623±0.00324
δ_{675}	0.18	+0.00023±0.00214	+0.00171±0.00194	0.12	-0.00251±0.00165	-0.00108±0.00126	0.25	+0.01793±0.00297	+0.01261±0.00290
δ_{870}	0.13	+0.00091±0.00166	+0.00130±0.00152	0.09	-0.00115±0.00106	-0.00018±0.00094	0.23	+0.01843±0.00298	+0.01202±0.00282
δ_{1020}	0.11	-0.00032±0.00138	-0.00037±0.00129	0.07	-0.00095±0.00082	-0.00029±0.00076	0.23	+0.01513±0.00294	+0.00826±0.00292

Tab. 5.5 Total means of CAOT and FAOT (440, 675, 870, and 1020 nm) and corresponding unweighted/weighted trends at the several AERONET stations except (g) Mauna_Loa and (l) Sevilleta where the classification is non-applicable.

	Coarse-mode dominant AOT (CAOT)			Fine-mode dominant AOT (FAOT)		
	Total mean	**Unweighted trend [/year]**	**Weighted trend [/year]**	**Total mean**	**Unweighted trend [/year]**	**Weighted trend [/year]**
			(a) Avignon			
δ_{440}	0.14	+0.00381±0.00296	+0.00637±0.00354	0.18	+0.00175±0.00439	+0.00692±0.00634
δ_{675}	0.09	+0.00207±0.00233	+0.00381±0.00237	0.09	+0.00042±0.00228	+0.00291±0.00341
δ_{870}	0.07	+0.00128±0.00205	+0.00253±0.00187	0.06	-0.00023±0.00142	+0.00077±0.00194
δ_{1020}	0.06	+0.00196±0.00209	+0.00256±0.00180	0.05	+0.00055±0.00122	+0.00046±0.00155
			(b) Banizoumbou*			
δ_{440}	0.52	+0.00391±0.00679	+0.00071±0.00694	*0.14*	*-0.00712±0.00347*	*+0.00083±0.00201*
δ_{675}	0.47	+0.00591±0.00635	+0.00330±0.00663	*0.10*	*-0.00356±0.00182*	*+0.00152±0.00145*
δ_{870}	0.43	+0.00633±0.00599	+0.00411±0.00626	*0.08*	*-0.00227±0.00122*	*+0.00050±0.00102*
δ_{1020}	0.41	+0.00538±0.00558	+0.00325±0.00589	*0.07*	*-0.00274±0.00105*	*-0.00053±0.00098*
			(c) Beijing			
δ_{440}	0.47	+0.00422±0.01906	+0.02523±0.01133	0.72	+0.02676±0.02578	+0.02955±0.02589
δ_{675}	0.32	+0.00349±0.01319	+0.01935±0.00702	0.43	+0.01852±0.01687	+0.01292±0.01774
δ_{870}	0.26	+0.00432±0.01042	+0.01578±0.00579	0.30	+0.01439±0.01164	+0.00931±0.01301
δ_{1020}	0.23	+0.00435±0.00952	+0.01314±0.00570	0.25	+0.01191±0.00890	+0.00717±0.01018
			(d) Dakar*			
δ_{440}	0.46	-0.00931±0.00918	+0.00236±0.00993	*0.17*	*-0.00045±0.01148*	*+0.01030±0.01361*
δ_{675}	0.41	-0.00642±0.00876	+0.00977±0.00883	*0.12*	*-0.00154±0.00569*	*+0.00706±0.00733*
δ_{870}	0.38	-0.00418±0.00832	+0.01296±0.00855	*0.10*	*-0.00007±0.00366*	*+0.00643±0.00562*
δ_{1020}	0.36	-0.00397±0.00818	+0.01338±0.00767	*0.09*	*-0.00021±0.00289*	*+0.00413±0.00441*
			(e) GSFC			
δ_{440}	0.13	-0.00347±0.00186	+0.00074±0.00068	0.22	-0.00053±0.00128	-0.00113±0.00064
δ_{675}	0.07	-0.00309±0.00137	+0.00037±0.00042	0.11	-0.00051±0.00068	-0.00080±0.00031
δ_{870}	0.06	-0.00274±0.00120	+0.00056±0.00038	0.07	-0.00029±0.00040	-0.00043±0.00021
δ_{1020}	0.05	-0.00252±0.00113	+0.00079±0.00038	0.05	-0.00009±0.00030	-0.00023±0.00018
			(f) Ispra			
δ_{440}	0.16	+0.00489±0.00444	+0.00636±0.00496	0.29	-0.00091±0.00576	+0.00143±0.00618
δ_{675}	0.10	+0.00240±0.00294	+0.00217±0.00303	0.15	-0.00061±0.00324	+0.00036±0.00335
δ_{870}	0.08	+0.00213±0.00245	+0.00172±0.00237	0.10	+0.00007±0.00204	+0.00071±0.00220
δ_{1020}	0.07	+0.00169±0.00212	+0.00101±0.00216	0.08	-0.00003±0.00155	+0.00020±0.00179
			(h) MD_Science_Center			
δ_{440}	0.14	-0.00159±0.00383	+0.00018±0.00119	0.24	-0.00290±0.00389	-0.00231±0.00157
δ_{675}	0.08	-0.00114±0.00242	+0.00017±0.00051	0.12	-0.00123±0.00203	-0.00113±0.00075
δ_{870}	0.06	-0.00055±0.00194	+0.00056±0.00046	0.08	-0.00025±0.00125	-0.00009±0.00054
δ_{1020}	0.05	-0.00084±0.00188	-0.00005±0.00044	0.06	-0.00034±0.00106	-0.00048±0.00055
			(i) Mongu			
δ_{440}	0.18	-0.01478±0.00876	-0.00102±0.00201	0.27	+0.00118±0.00767	+0.00810±0.00424
δ_{675}	0.11	-0.00934±0.00530	-0.00018±0.00134	0.13	-0.00039±0.00366	+0.00545±0.00194
δ_{870}	0.09	-0.00661±0.00418	+0.00093±0.00109	0.09	+0.00022±0.00214	+0.00501±0.00113
δ_{1020}	0.07	-0.00655±0.00362	+0.00062±0.00103	0.06	-0.00045±0.00153	+0.00300±0.00104
			(j) Ouagadougou*			
δ_{440}	0.51	+0.02704±0.01330	+0.00629±0.01281	*0.22*	*-0.01704±0.01192*	*-0.00960±0.00691*
δ_{675}	0.48	-0.00322±0.02365	-0.00577±0.02128	*0.19*	*-0.04916±0.01976*	*-0.01816±0.00689*
δ_{870}	0.41	+0.02432±0.01218	+0.00230±0.01132	*0.14*	*-0.02608±0.00974*	*-0.01356±0.00546*
δ_{1020}	0.39	+0.02628±0.01188	+0.00397±0.01116	*0.12*	*-0.02351±0.00923*	*-0.01157±0.00408*

* Some FAOT Trends represented in *smaller-italic* type may be insignificant because of incomplete yearly data sets.

Tab. 5.5 (*Continued*)

	Coarse-mode dominant AOT (CAOT)			Fine-mode dominant AOT (FAOT)		
	Total mean	**Unweighted trend [/year]**	**Weighted trend [/year]**	**Total mean**	**Unweighted trend [/year]**	**Weighted trend [/year]**
			(k) SEDE_BOKER			
δ_{440}	0.19	+0.00302±0.00312	-0.00244±0.00313	0.14	+0.00125±0.00137	+0.00141±0.00136
δ_{675}	0.14	+0.00241±0.00292	-0.00185±0.00256	0.08	+0.00076±0.00067	+0.00074±0.00067
δ_{870}	0.13	+0.00311±0.00278	-0.00035±0.00225	0.07	+0.00169±0.00069	+0.00187±0.00060
δ_{1020}	0.11	+0.00213±0.00282	-0.00113±0.00254	0.05	+0.00093±0.00075	+0.00122±0.00074
			(m) Shirahama			
δ_{440}	0.23	+0.00957±0.00368	+0.00667±0.00228	0.31	+0.00177±0.00519	+0.00341±0.00274
δ_{675}	0.15	+0.00483±0.00246	+0.00308±0.00164	0.17	-0.00084±0.00302	+0.00109±0.00187
δ_{870}	0.12	+0.00416±0.00211	+0.00263±0.00135	0.12	-0.00013±0.00200	+0.00095±0.00129
δ_{1020}	0.10	+0.00226±0.00189	+0.00101±0.00121	0.09	-0.00129±0.00154	-0.00063±0.00102
			(n) Skukuza			
δ_{440}	0.13	-0.00171±0.00213	-0.00038±0.00124	0.23	-0.00378±0.00357	-0.00216±0.00272
δ_{675}	0.08	-0.00204±0.00141	-0.00123±0.00099	0.12	-0.00237±0.00168	-0.00143±0.00134
δ_{870}	0.07	-0.00144±0.00121	-0.00024±0.00106	0.08	-0.00098±0.00103	-0.00055±0.00093
δ_{1020}	0.06	-0.00158±0.00112	-0.00047±0.00089	0.07	-0.00078±0.00079	-0.00058±0.00070
			(o) Solar_Village*			
δ_{440}	0.31	+0.01861±0.00313	+0.01575±0.00325	*0.13*	*-0.00369±0.00212*	*-0.00077±0.00147*
δ_{675}	0.26	+0.01756±0.00305	+0.01234±0.00282	*0.10*	*-0.00220±0.00152*	*+0.00053±0.00104*
δ_{870}	0.23	+0.01793±0.00301	+0.01170±0.00272	*0.08*	*-0.00018±0.00114*	*+0.00132±0.00097*
δ_{1020}	0.23	+0.01476±0.00299	+0.00820±0.00283	*0.09*	*-0.00339±0.00150*	*-0.00083±0.00119*

* Some FAOT Trends represented in *smaller-italic* type may be insignificant because of incomplete yearly data sets.

5.3 Aerosol optical properties

AERONET inversion products are useful to investigate climatological aerosol optical properties. Besides, aerosol retrieval accuracy using satellite remote sensing can be improved by providing those for LUT pre-calculation (see Section 3.4). In this section, various aerosol optical properties (i.e., AOT, SSA, phase function at 440, 675, 870, 1020 nm, and volume size distribution) as well as water vapor content are discussed over specific AERONET stations defined in Tab. 5.1. Appendix B describes major aerosol parameters for the theoretical understanding.

Figs. 5.12 and 5.13 provide various aerosol optical properties (i.e., AOTs, SSAs, phase functions at 440, 675, 870, 1020 nm, and volume size distribution) as well as water vapor content from AERONET level 2.0 inversion data. In these figures, various aerosol types (simply, anthropogenic and natural aerosols) are observed, and they are dependent on the local aerosol emission sources (e.g., industrial pollutant, biomass burning, desert dust, and sea salt) and seasonal meteorological conditions. Main aerosol characteristics at the stations (Avignon, Beijing, GSFC, Ispra, MD_Science_Center, Mongu, SEDE_BOKER, Shirahama, and Skukuza) near/in industrial or urban regions show anthropogenic type. The representative stations having typical desert dust are Banizoumbou, Dakar, Ouagadougou, and Solar_Village, as already mentioned in Section 5.2. Generally, AOTs observed at the stations Mauna_Loa (representative for the free troposphere) and Sevilleta (rural region) are small, but from different aerosol types (complicated compositions of transported and maritime aerosols at Mauna_Loa and regional soil dust at Sevilleta). SSA in Fig. 5.12 and Aerosol phase functions in Fig. 5.13 are very important to set up the aerosol database for refinement and improvement of future BAER based on LUT approach.

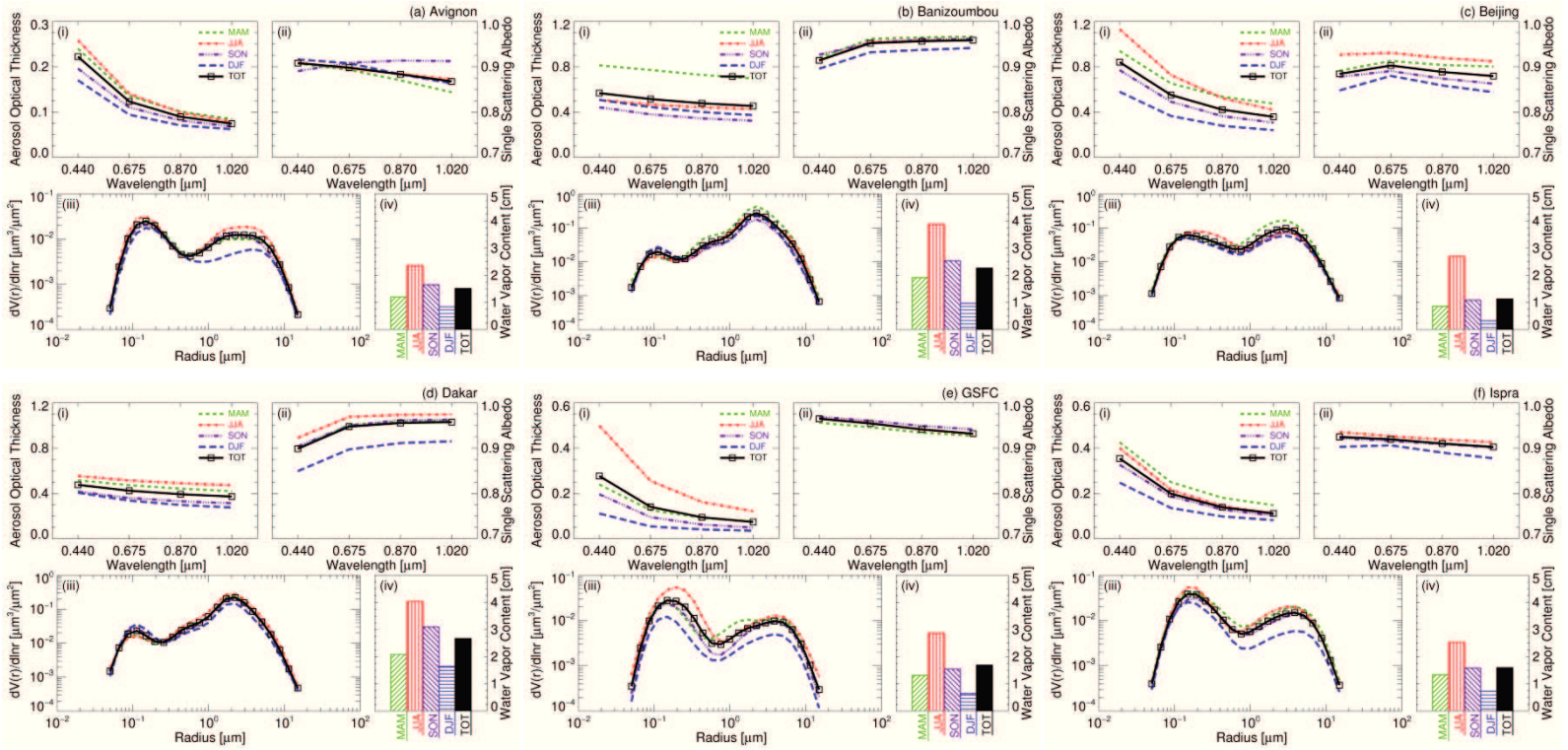

Fig. 5.12 Total and seasonal means of spectral (i) AOTs and (ii) SSAs at 440, 675, 870, 1020 nm, (iii) volume size distribution, and (iv) water vapour content at the several AERONET stations.

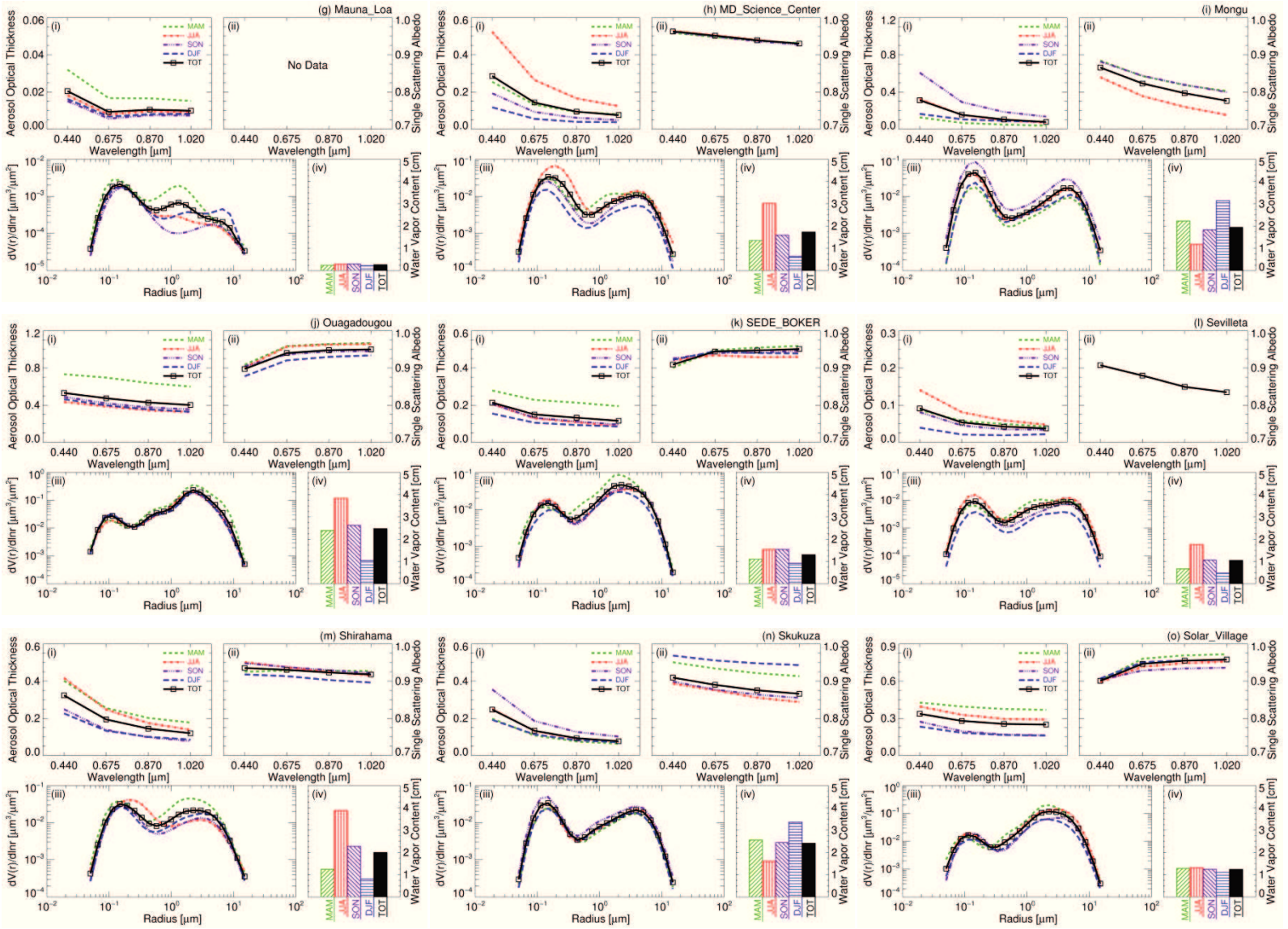

Fig. 5.12 (*Continued*)

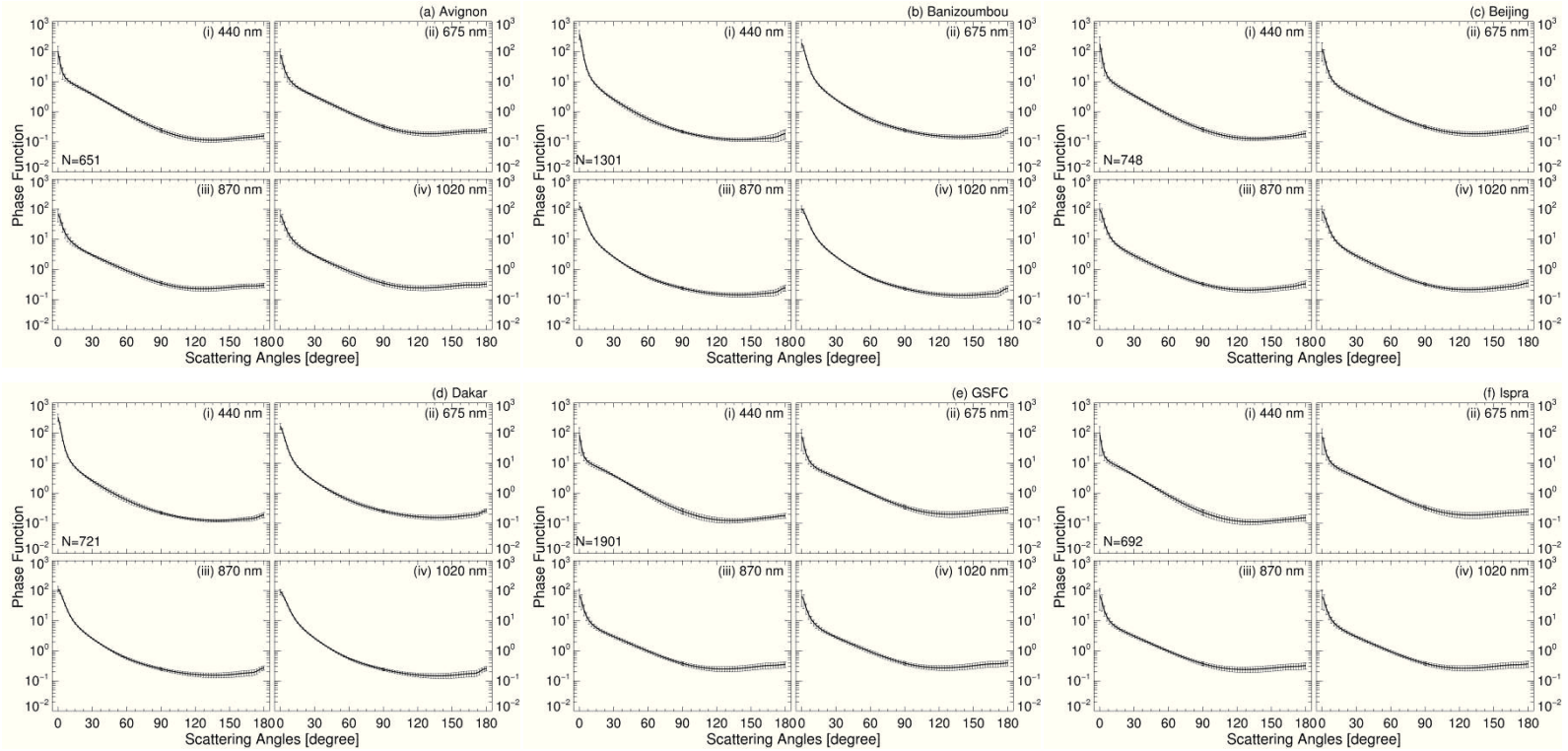

Fig. 5.13 Total means of spectral aerosol phase function at (i) 440, (ii) 675, (iii) 870, (iv) 1020 nm over the several AERONET stations.

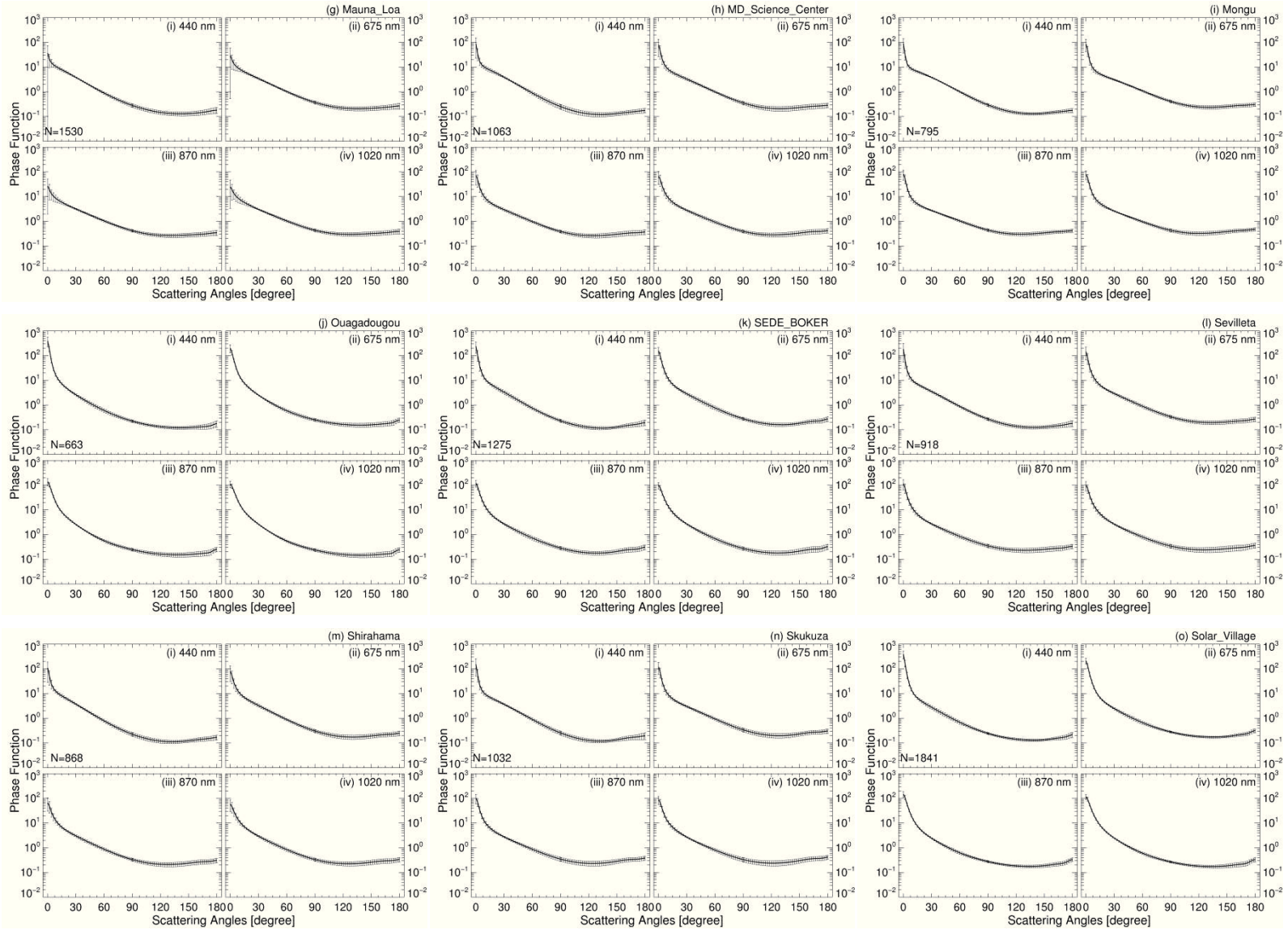

Fig. 5.13 (*Continued*)

6. Trend analysis of global AOT derived from polar orbiting satellites: Terra (MODIS and MISR), OrbView-2 (SeaWiFS), and Aqua (MODIS)

Many studies have discussed global distribution and temporal variation of aerosols using various satellite observations as referenced in Section 1.2. Recently, substantial improvements of aerosol retrieval accuracy over land have contributed to studies of anthropogenic and natural aerosols mostly emitted over land [Xie and Xia, 2008; Karnieli et al., 2009; de Meij et al., 2010; Koukouli et al., 2010; Kaskaoutis et al., 2011b; Dey and Di Girolamo, 2011; Kokhanovsky and de Leeuw, 2009]. However, unrepresentative aerosol sampling of polar-orbiting platforms (e.g., caused by frequent cloud disturbance and poor temporal resolution) is one of the serious limits, which can give a significant bias to the trend analysis of cloud-free AOT [Li et al., 2009; Ignatov et al., 2005; Kahn et al., 2007; Levy et al., 2009]. As discussed and demonstrated in the previous chapter, the influence of cloud disturbance can be minimized in the trend analysis by introducing the weighted least squares regression. However, the uncertainty caused by limited orbital periods (roughly 100 minutes for each orbit) and different sampling times of polar-orbiting platforms is an insurmountable obstacle. Therefore, using various polar-orbiting satellites: MODIS-Terra (MOD) and MISR-Terra (MIS), SeaWiFS-OrbView-2 (SEA), and MODIS-Aqua (MYD) possessing various sampling times, the present chapter attempts to minimize the uncertainty effect in trend analysis. The main content of this chapter is taken from the paper prepared to be submitted by Yoon et al. in *Geophysical Research Letters*, 2012.

6.1 Research data sets and methodology

High scientific quality of observations (which is directly linked to the sensor calibration status) is indispensable for analyzing the climatological AOT change. This study is based on MODIS, MISR, and SeaWiFS data, which have been kept in excellent calibration status [Kahn et al., 2005b; Bruegge et al., 2007; Li et al., 2009; Brenes et al., 2001; Gordon, 1998; Eplee et al., 2001]. Furthermore, many algorithms using these observations have been developed in order to retrieve and monitor global AOTs [Remer et al., 2005; Kaufman et al., 1997b; Higurashi and Nakajima, 1999; Mishchenko et al., 1999a; Jeong et al., 2005; Higurashi et al., 2000; Stowe et al., 1999; Heidinger et al., 2004; Torres et al., 2002; Di Girolamo and Wilson, 2003; Martonchik et al., 2004; Diner et al., 2006; Martins et al., 2002; von Hoyningen-Huene et al., 2011; Kokhanovsky and de Leeuw, 2009]. In the present study all trends are analyzed based on monthly products of MODIS AOT at 550 nm, MISR AOT at 558 nm, and SeaWiFS at 510 nm in order to reduce the uncertainty caused by limited orbital periods and different sampling times depending on the platforms. In addition, total means of monthly cloud fraction (CF) and its standard deviation (STD) derived from MODIS observations quantify the regional cloud occurrence and thus the frequency of clear-sky aerosol retrievals. More detailed information about the instruments/platform characteristics, calibration status, AOT retrieval accuracy, and research data sets are summarized in Tab. 6.1.

Tab. 6.1 Characteristics of on-board sensors and polar-orbiting satellites and summary of the sensor calibration approaches, aerosol retrieval accuracies, and data sets.

Sensor	**MODIS (Moderate Resolution Imaging Spectroradiometer)**		**MISR (Multi-angle Imaging SpectroRadiometer)**	**SeaWiFS (Sea-viewing Wide Field-of-view Sensor)**
Satellite	Terra	Aqua	Terra	OrbView-2
Local Equatorial Crossing Time	10:30 a.m.	01:30 p.m.	10:30 a.m.	12:20 p.m.
Launch Date	1999/12/18	2002/05/04	1999/12/18	1997/08/01
Orbit	Descending node	Ascending node	Descending node	Descending node
Swath (km)	2330		360	2801 (LAC) 1502 (GAC)
Resolution (m)	250 (bands 1-2) 500 (bands 3-7) 1000 (bands 8-36)		250	1100 (LAC) 4500 (GAC)
Number of Bands	36		4	8
Spectral Coverage (nm)	405-14385		446-867	402-885
View Angles (°)	nadir		0, ±26.1, ±45.6, ±60.0, and ±70.5	nadir
Reference Source	The International Ocean-Colour Coordinating Group (IOCCG) Homepage (http://www.ioccg.org); MODIS Homepage (http://modis.gsfc.nasa.gov); MISR Homepage (http://www-misr.jpl.nasa.gov); SeaWiFS Project Homepage (http://oceancolor.gsfc.nasa.gov/SeaWiFS)			
Sensor Calibration Method	On-board, Vicarious, and Lunar		On-board, Vicarious, and Lunar	On-board, Vicarious, Lunar, Comparison with situ
Calibration Accuracy or Precision	~2 % absolute, ~1 % precision		~3 % absolute, 1-2 % channel-to-channel relative, 1 % precision	0.5 % accuracy, ~0.3 % precision
Reference Source	Kahn et al. [2005b]; Bruegge et al. [2007]; Li et al. [2009]; Brenes et al. [2001]; Gordon [1998]; Eplee et al. [2001]			
AOT Retrieval Accuracy	±0.05 or ±15 % (Land) and ±0.05 or ±5 % (Ocean)		±0.03-0.05 or ±10-20 % (Land and Ocean)	±0.05 or ±20-25 % (Land and Ocean)
Reference Source	Kaufman et al. [1997b]; Remer et al. [2005, 2008]; Levy et al. [2010]		Kahn et al. [2005a, 2010]	von Hoyningen-Huene et al. [2003, 2006, 2011]
Studied Periods	2000/03-2009/12	2003/01-2008/12	2000/03-2010/12	1998/01-2007/12
Physical Parameters*	AOT (550 nm), CF	AOT (550 nm), CF	AOT (558 nm)	AOT (510 nm)
Data Type	Level 3 Collection 5	Level 3 Collection 5	Level 3 CGAS-F15	Level 3 Global Product
Data Resolution	1° × 1°	1° × 1°	0.5° × 0.5°	1° × 1°
Abbreviation	MOD	MYD	MIS	SEA

***** AOT and CF: Aerosol Optical Thickness and Cloud Fraction in daytime

Linear weighted model

For the AOT trend analysis, the linear weighted model approach is utilized as already discussed in Chapter 5. However, the weighting factor ($\sqrt{n_t}/(\sigma_t/y_t)$) is defined differently, namely as the ratio of square root of n_t ($\sqrt{n_t}$) and normalized standard deviation of monthly AOT by monthly AOTs (σ_t/y_t). n_t is inversely proportional to cloud occurrence as demonstrated in Chapter 5, and relatively large value of σ_t as compared to y_t is a good indicator of cloud contamination in AOT retrieval. Therefore, the combination of these parameters as a weighting factor allows minimizing the cloud disturbance in the trend analysis of cloud-free global AOT.

Outlier tests

In some cases, a small n_t leads to too large weighting factors (i.e., outliers) which can result in a strong bias in the trend analysis. In order to remove such outliers, additional steps are applied using two tests: 1) Grubbs test and 2) Gaussian test within 95% of confidence levels. Fig. 6.1 illustrates an example of outlier tests for significant weighting factors. Grubbs test [Grubbs, 1969; Stefansky, 1972] detects too large weighting factors under an approximately normal distribution (t-distribution).

$$G_i > \frac{(N-1)}{\sqrt{N}} \sqrt{\frac{t^2_{(\alpha/N,N-2)}}{N-2+t^2_{(\alpha/N,N-2)}}} \text{ with } G_i = \frac{wt_i - \mu_{wt}}{\sigma_{wt}} \quad (6.1)$$

where, N, μ_{wt}, and σ_{wt} are the total number, total mean, and total standard deviation of weights (wt_i), respectively. $t^2_{(\alpha/N,N-2)}$ denotes the critical value of the t-distribution with $(N-2)$ degrees of freedom and a significance level of (α/N). If G_i satisfies Equation (6.1), it is rejected as an outlier. After the first outlier removal by the Grubbs test, it can be assumed that the remaining data of weighting factors follow Gaussian distribution. In a second step,

the hypothesis about no outliers within approximately 95% of confidence intervals is discarded if wt_i is satisfied by the following equation:

$$wt_i > \mu_{wt} + 2\sigma_{wt} \text{ or } wt_i < \mu_{wt} - 2\sigma_{wt}. \quad (6.2)$$

Through these tests, the outliers are removed as shown in Fig. 6.1 (i.e., blue ones by Grubbs test and red ones by Gaussian test), and thereby the bias pressing for serious consideration can be minimized in linear weighted model.

Weighted mean for regional trends

Because of high temporal variability and spatial heterogeneity of cloud occurrence depending on the region, the regional trend (B_{region}) of the cloud-free AOT is estimated by the weighted mean method using the trends (B_g) on a grid scale (1° × 1° for MODIS and SeaWiFS or 0.5° × 0.5° for MISR):

$$B_{region} = \frac{\sum_g (B_g \times y_g)}{\sum_g (y_g)} \quad (6.3)$$

where, y_g is the monthly averaged AOTs for each grid within different research regions. Using this weighted mean method, it is possible to consider that some grid trends with larger AOT contribute more than others to the regional trend.

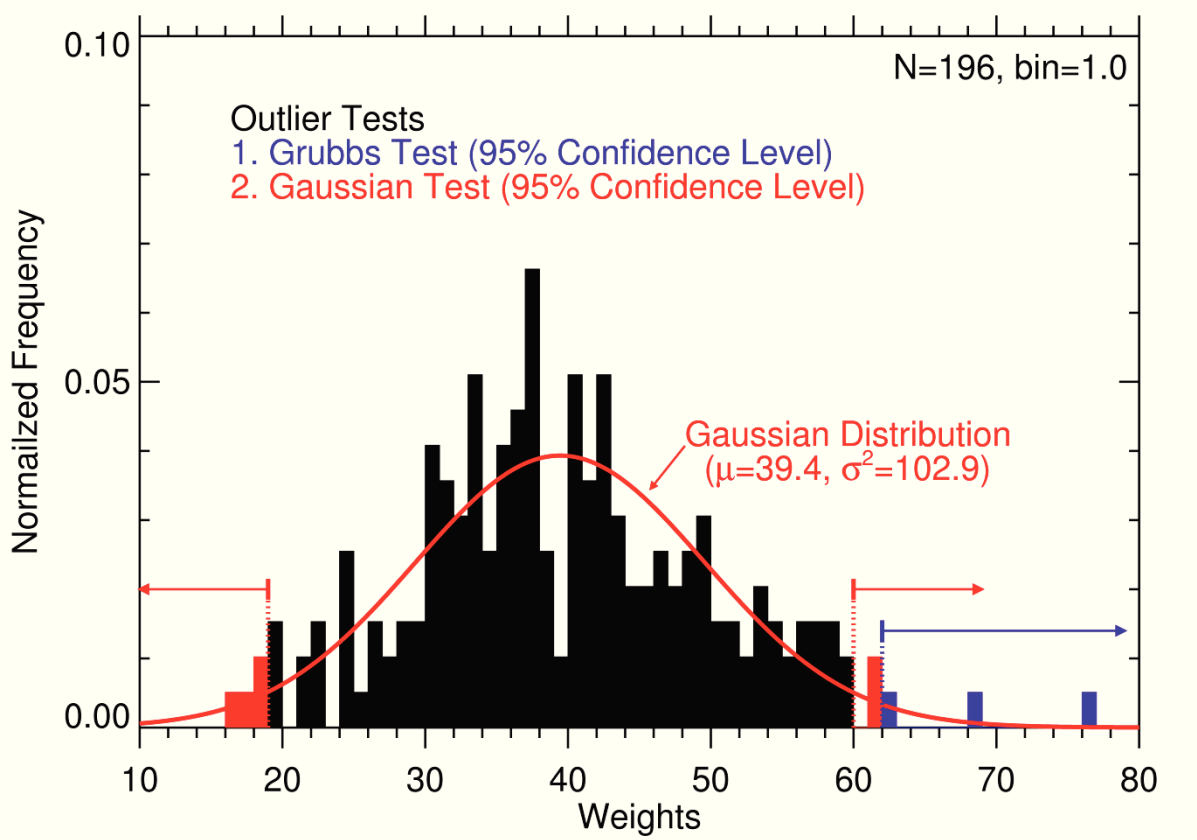

Fig. 6.1 Example of outlier tests (Grubbs and Gaussian tests within 95% of confidence levels) for significant weight factors.

6.2 Unrepresentative sampling in AOT trend analysis

Many studies have suggested various ways to reduce the uncertainty effects in the trend analysis of cloud-free AOT using polar-orbiting satellite observations, such as the instrument calibration, refinement of retrieval algorithms, and validation with AOT trends derived from ground observations. However, so far, no serious study has tried to discuss the unrepresentative sampling (e.g., induced by limited orbital periods, different sampling times, and cloud disturbance). In this section, the uncertainty caused by unrepresentative sampling is tested in AOT trend analysis.

For the aim of the uncertainty test to investigate how seriously unrepresentative sampling influences the trend analysis, it is assumed that the satellite products are perfectly matched up with the ground-based observations (AERONET) during the overpass time on the ground stations. Under the assumption, monthly AERONET AOTs at 550 nm (which are converted from AOTs at 440 nm using ÅE at 440-675 nm) from resamplings at the local equatorial crossing times (i.e., 10:30±30 a.m. for Terra, 12:20±30 p.m. for OrbView-2, and 01:30±30 p.m. for Aqua) are anomalized by the seasonal cycle of AOT as shown in Fig. 6.2.

Western Europe, where AERONET stations Avignon and Ispra are located, is influenced by enhanced industrial pollutants under less rain/monsoon during summer [Marmer et al., 2007; Karnieli et al., 2009; Gerasopoulos et al., 2003; Bergamo et al., 2008; Venzac et al., 2009]. The stations Banizoumbou, Dakar, and Ouagadougou in West Africa have different seasonal variation of AOT as compared to Western Europe because of different aerosol sources (mineral dust from the Saharan and Sahel regions and biomass burning from central Africa in summer) [Prospero and Lamb, 2003; Washington and Todd, 2005; Moulin and Chiapello, 2004; Reeves et al., 2010; Hao and Liu, 1994]. The stations Mongu and Skukuza in South Africa have an obvious seasonality of AOT due to emission of biomass burning aerosol in dry (June to September) seasons before rainy (December to February) periods

[Tyson, 1986; Swap et al., 1996]. Seasonal variation of AOT over Middle East (SEDE_BOKER and Solar_Village) under stable meteorological conditions is strongly influenced by mineral dust transported from the Anatolian plateau, Sahara, Negev, and Arabian deserts [Andreae et al., 2002; Kubilay et al., 2003; Derimian et al., 2006; Basart et al., 2009; Sabbah et al., 2001, 2006; Smirnov et al., 2002; Tafuro et al., 2006; Sabbah and Hasan, 2008]. The stations Beijing and Shirahama in East Asia have very clear seasonal cycles due to larger amount of mineral dust transported from Asian deserts, stagnant synoptic meteorological patterns, secondary aerosol formation, and hygroscopic growth in summer [Kotchenruther et al., 1999; Dubovik et al., 2002a; Kim et al., 2007]. The stations GSFC, MD Science Center, and Sevilleta over North America have similar seasonal variation of AOT, but the main aerosol sources are different (i.e., urban-industrial pollutions for GSFC and MD_Science_Center, and soil dust for Sevilleta). The seasonal cycle can be explained with the combination of natural and anthropogenic aerosols, fuel types, emission characteristic, relative humidity, boundary layer height, and scavenging by precipitation [Glen et al., 1996; Chen et al., 2001; Dubovik et al., 2002a; Andronache, 2004]. The station Mauna_Loa in the Pacific is in a good position to monitor *free tropospheric aerosol* due to its high altitude (around 3397 m). Long-range transported aerosols have been observed over this station, and can influence the seasonal cycle [Dubovik et al., 2002a; Garstang and Fitzjarrald, 1999; Schmeissner et al., 2011]. Generally, the seasonal cycles depending on the different sampling times look similar in Fig. 6.2, but it can be significant in the trend analysis based on the anomalies.

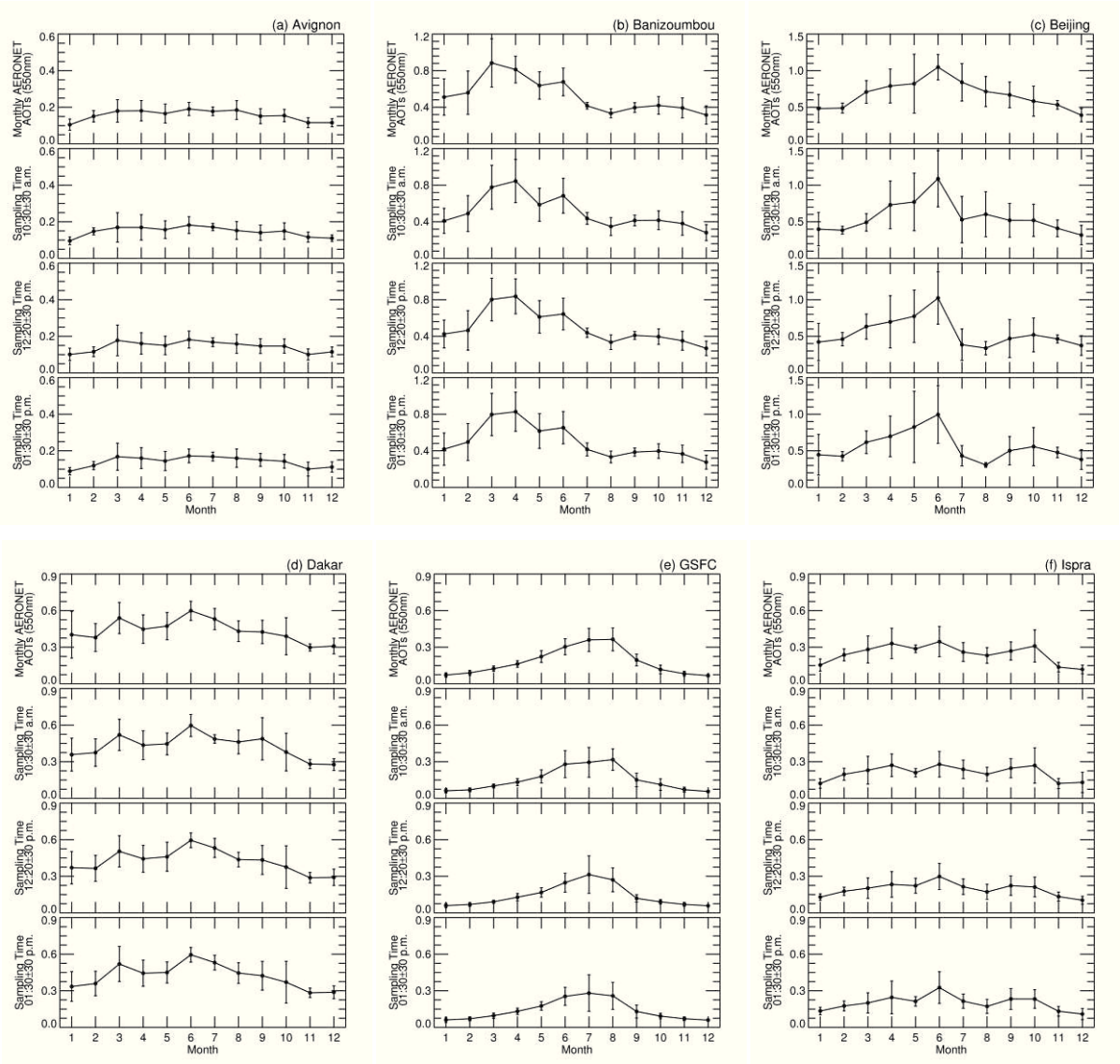

Fig. 6.2 Seasonal AOT (550 nm) cycles in different sampling times (i.e., all available sampling, 10:30±30 a.m., 12:20±30 p.m., and 01:30±30 p.m.) over the several AERONET stations.

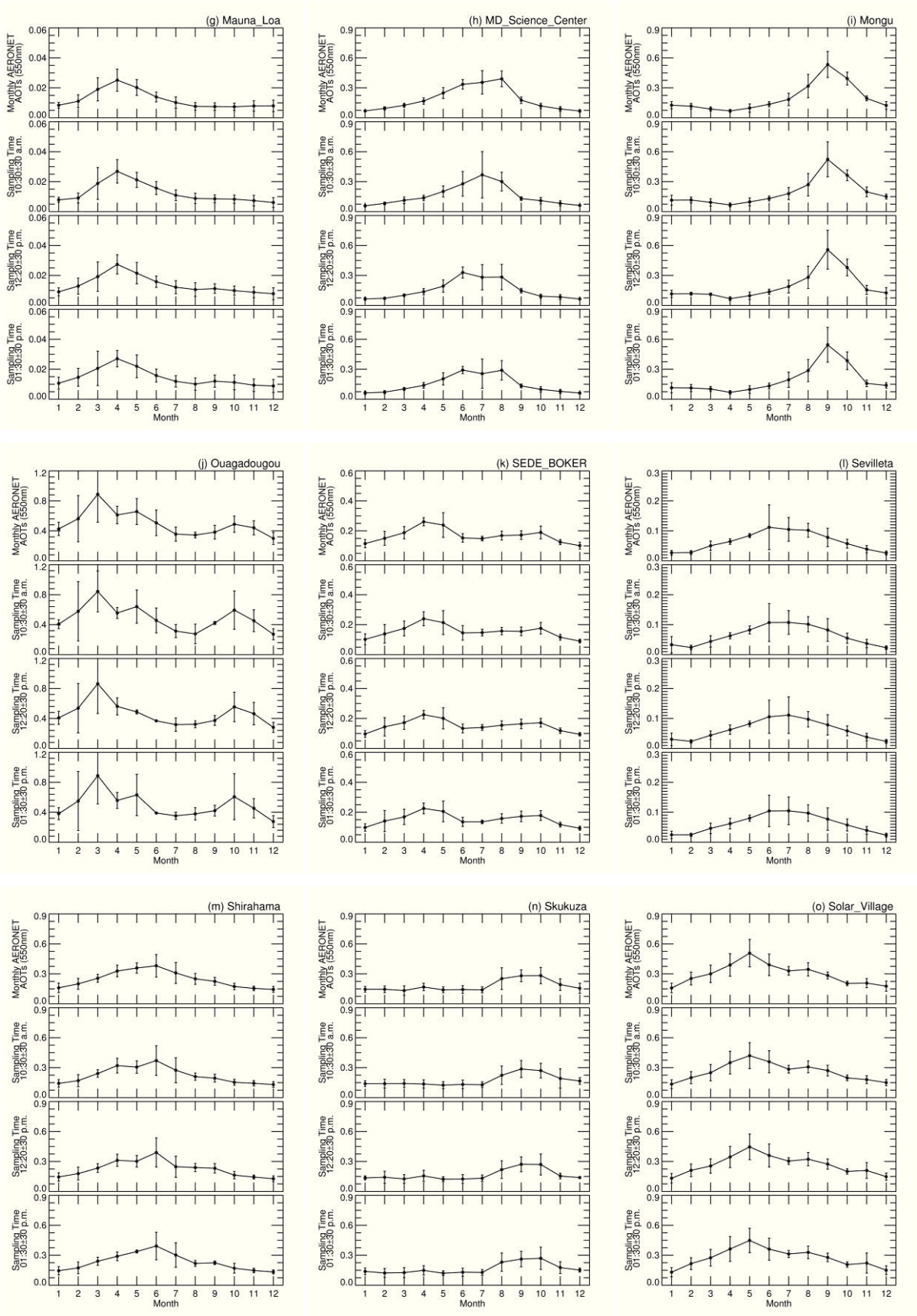

Fig. 6.2 (*Continued*)

The monthly anomalies of AERONET AOTs (550 nm) from the deseasonalization using these seasonal cycles are used for the trend analysis based on the simple linear (unweighted) regression (i.e. weighting factor (wt_t) = 1, see Section 5.1). Fig. 6.3 illustrates the linear trends of AOT anomalies for each sampling time at the several AERONET stations defined in Chapter 5. Surprisingly at all stations, the total means (<AOT>) as well as linear trends based on all available sampling are significantly different from ones in the different sampling times. These results are directly connected to the rapid temporal variability and diurnal patterns of AOT. Especially, the regions close to the emission source of anthropogenic aerosol can have a strong diurnal cycle of AOT [Smirnov et al., 2002], which induces a systematic bias in the trend analysis. Furthermore, the random-like error from non AOT retrievals caused by irregular cloud occurrences may lead to increased discrepancies between the trends since AOT can be retrieved only under clear-sky conditions [Remer et al., 1997; Dubovik et al., 2002a; Levy et al., 2009]. For these reasons, it is difficult to compare directly between the AOT trends based on different sampling times. Fig. 6.3 shows *true* trend (B_{true}, which is based on all available sampling) and the AOT trends ($B_{d.s.t.}$) in different sampling times (i.e., 10:30±30 a.m., 12:20±30 p.m., and 01:30±30 p.m.). For quantitative comparison, Tab. 6.2 presents the relative percent errors between them.

$$\text{Relative percent errors} = \frac{B_{d.s.t.} - B_{true}}{B_{true}} \times 100\% \qquad (6.4)$$

The relative percent errors over $|\pm 100\%|$ are shown as **bold** type in the table. Especially, the AOT trend with the errors less than -100% means that it is the opposite tendency (sign) to B_{true}. Except Mongu (because of almost negligible B_{true}) case, the stations close to urban or industrial regions (Avignon, Beijing, GSFC, Ispra, MD_Science_Center, Shirahama, and Skukuza) have larger relative percent errors between B_{true} and $B_{d.s.t.}$ (-156% ~ +399.2%) than the stations Banizoumbou, Dakar, Ouagadougou, SEDE_BOKER, and Solar_Village

near desert regions (-63.6% ~ +59.3%), where there is almost no influence of cloud disturbance and weak diurnal cycle of AOT all year round as shown in Fig. 6.4. Especially, Fig. 6.4 presents a clear diurnal cycle of AOT in the regions influenced by local aerosol sources [Smirnov et al., 2002] and meteorological conditions, and it surely leads to a bias in aerosol sampling. Near sparsely populated areas like Mauna_Loa (in *free troposphere* and

Tab. 6.2 Simple linear trends of AERONET AOT (550 nm) in different sampling times (i.e., all available sampling time, 10:30±30 a.m., 12:20±30 p.m., and 01:30±30 p.m.) and corresponding relative percent errors.

AERONET Stations	**Geolocations (lat.[°]/lon.[°] /alt.[m])**	**Research Periods**	**Simple Linear Trends of AERONET AOT (550 nm) in Different Sampling Times [/Year] and (Relative Percent Errors* [%])**			
			All Available	**10:30±30 a.m.**	**12:20±30 p.m.**	**01:30±30 p.m.**
Avignon	43.93/4.88/32	2001~2005	+0.00120	+0.00344 **(+186.7)**	+0.00599 **(+399.2)**	+0.00334 **(+178.3)**
Banizoumbou	13.54/2.66/250	2002~2008	+0.00538	+0.00857 (+59.3)	+0.00196 (-63.6)	+0.00700 (+30.1)
Beijing	39.98/116.38/92	2003~2007	+0.00537	+0.00624 (+16.2)	+0.01077 **(+100.6)**	-0.00047 **(-108.8)**
Dakar	14.39/-16.96/0	2004~2008	-0.00834	-0.00936 (+12.2)	-0.00907 (+8.8)	-0.01011 (+21.2)
GSFC	38.99/-76.84/87	1995~2008	-0.00219	-0.00054 (-75.3)	-0.00062 (-71.7)	+0.00038 **(-117.4)**
Ispra	45.80/8.63/235	2001~2007	-0.00496	+0.00101 **(-120.4)**	+0.00279 **(-156.3)**	+0.00019 **(-103.8)**
Mauna_Loa	19.54/-155.58/3397	1998~2009	+0.00014	-0.00000 **(-100.0)**	+0.00008 (-42.9)	+0.00014 (+0.0)
MD_Science_Center	39.28/-76.62/15	2000~2006	-0.00225	-0.00463 **(+105.8)**	-0.00043 (-80.9)	-0.00033 (-85.8)
Mongu	-15.25/23.15/1107	2000~2004	+0.00002	+0.00104 **(+5100.0)**	-0.00292 **(-14700.0)**	+0.00123 **(+6050.0)**
Ouagadougou	12.20/-1.40/290	2000~2004	+0.02895	+0.01635 (-43.5)	+0.01478 (-48.9)	+0.02017 (-30.3)
SEDE_BOKER	30.86/34.78/480	2003~2008	+0.00143	+0.00161 (+12.6)	+0.00116 (-18.9)	+0.00165 (+15.4)
Sevilleta	34.35/-106.89/1477	1998~2002	+0.00232	+0.00101 (-56.5)	+0.00104 (-55.2)	+0.00034 (-85.3)
Shirahama	33.69/135.36/10	2003~2009	+0.00107	+0.00263 **(+145.8)**	+0.00461 **(+330.8)**	+0.00218 **(+103.7)**
Skukuza	-24.99/31.59/150	2000~2007	-0.00463	-0.00022 (-95.2)	-0.00438 (-5.4)	-0.00468 (+1.1)
Solar_Village	24.91/46.40/764	2001~2007	+0.01965	+0.01531 (-22.1)	+0.01814 (-7.7)	+0.01875 (-4.6)

* The relative percent errors over |±100%| are shown as **bold** type in the table. Especially, the AOT trend having errors less than -100% is the opposite tendency (sign) to *true* trend.

open ocean) and Sevilleta (rural region), the main uncertainty factor is the cloud disturbance (as well as measurement uncertainty of AOT; ± 0.01 [Holben et al., 1998]), and the range of relative percent errors are from -100.0% to +0.0%. Additionally, Fig. 6.5 provides scatter plots to clarify the discrepancies between the trends. In spite of the high correlation (i.e., the ranges of correlation coefficient (R) and Relative Root-Mean-Square Difference (RMSD): $0.859 \leq R \leq 0.944$ and $0.03 \leq RMSD \leq 0.05$), $B_{d.s.t.}$ is underestimated by 24% to 36% approximately as compared to B_{true} due to the unrepresentative sampling. Especially, at some stations (Beijing, GSFC, and Ispra), the sign of $B_{d.s.t.}$ is even opposite to one of B_{true} (check the points in shaded areas in Fig. 6.5). Through the uncertainty test, it can be concluded that the unrepresentative sampling is an important factor and should be considered in the trend analysis of cloud-free AOT. In the next section, the trends derived from various satellite observations using the methodology to minimize the effect of unrepresentative sampling are validated with ground-based observation in order to investigate other uncertainty factors.

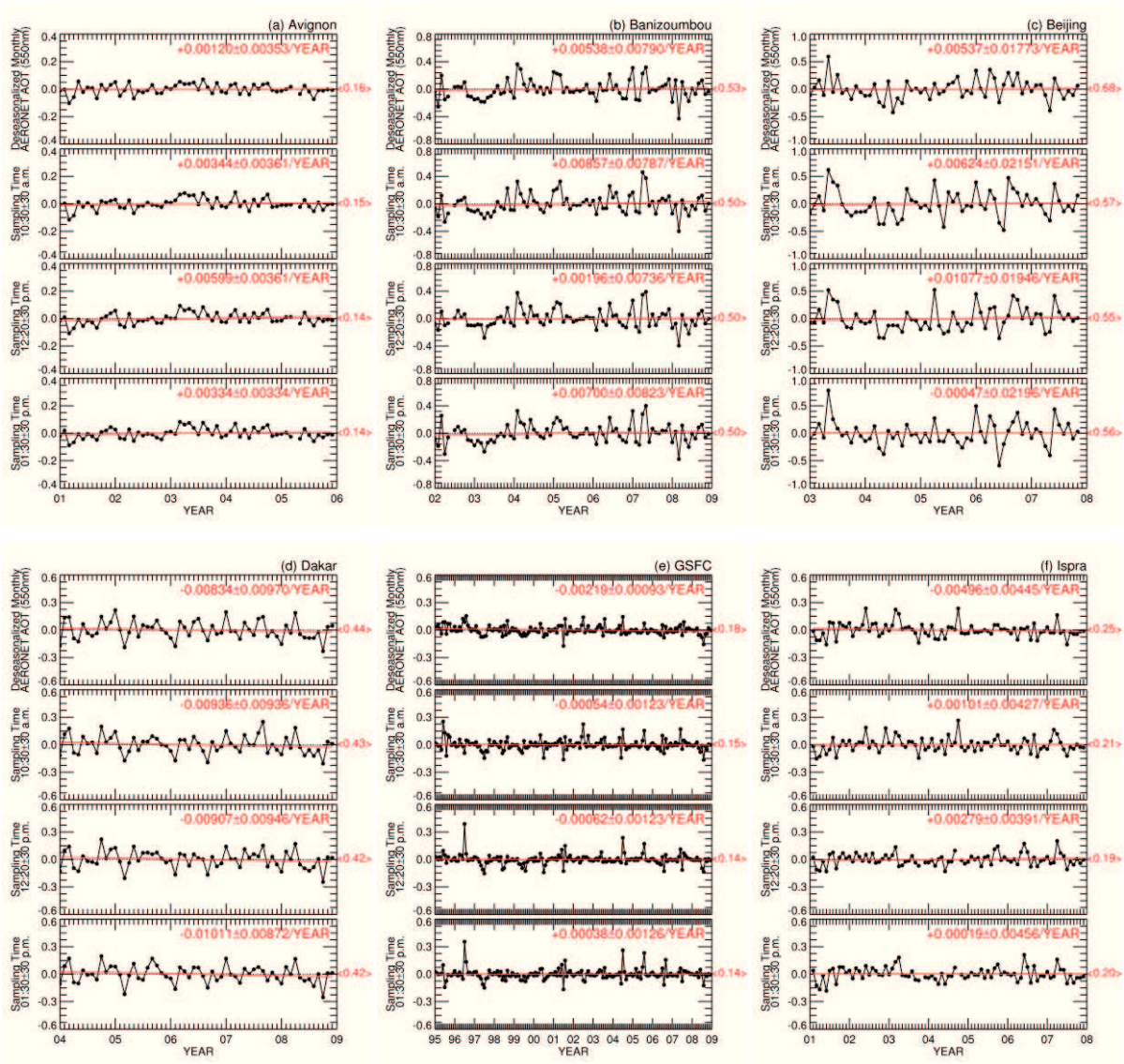

Fig. 6.3 Simple linear (unweighted) trends of AERONET AOT (550 nm) in different sampling times (i.e., all available sampling, 10:30±30 a.m., 12:20±30 p.m., and 01:30±30 p.m.) at the several AEROET stations.

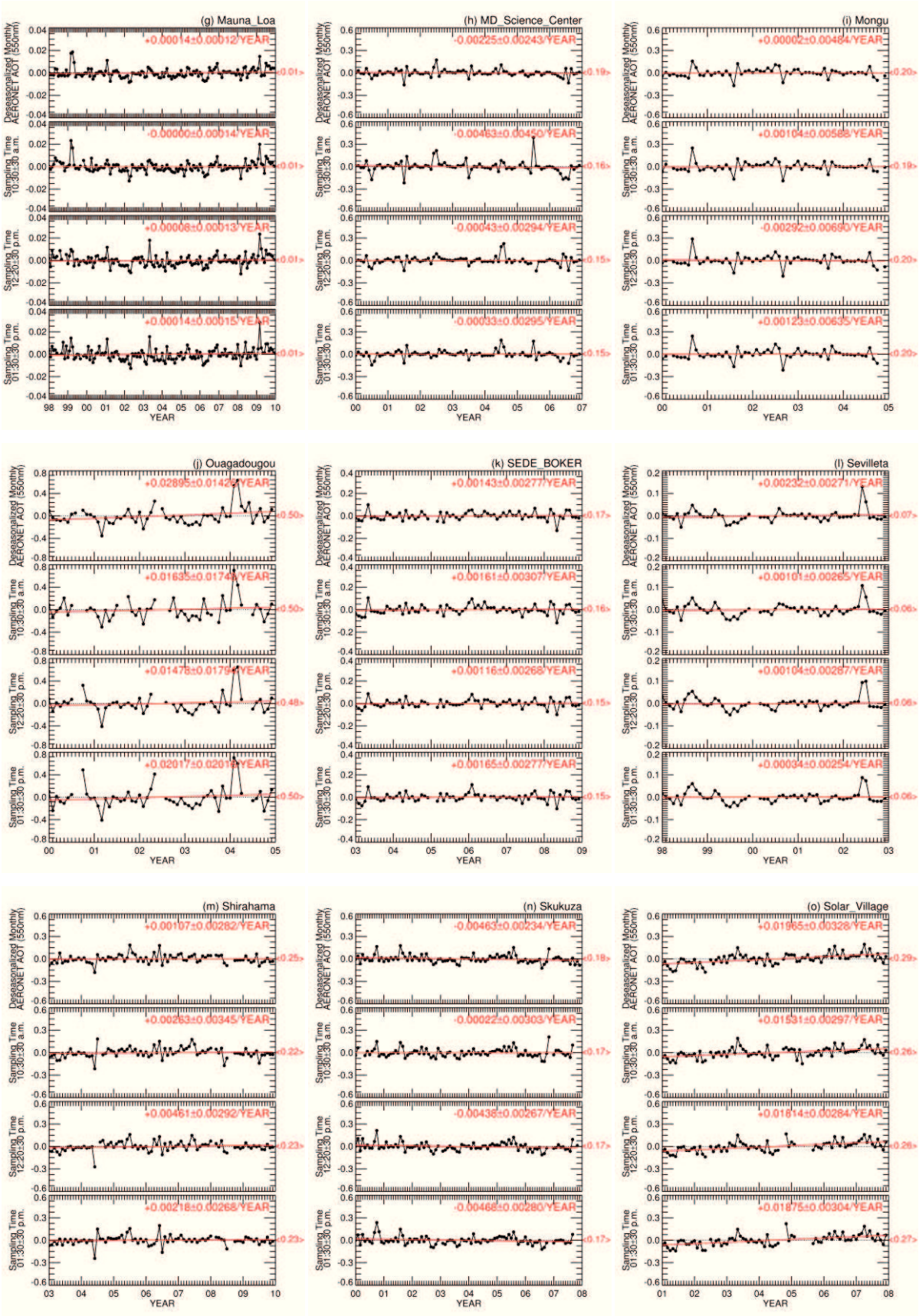

Fig. 6.3 (*Continued*)

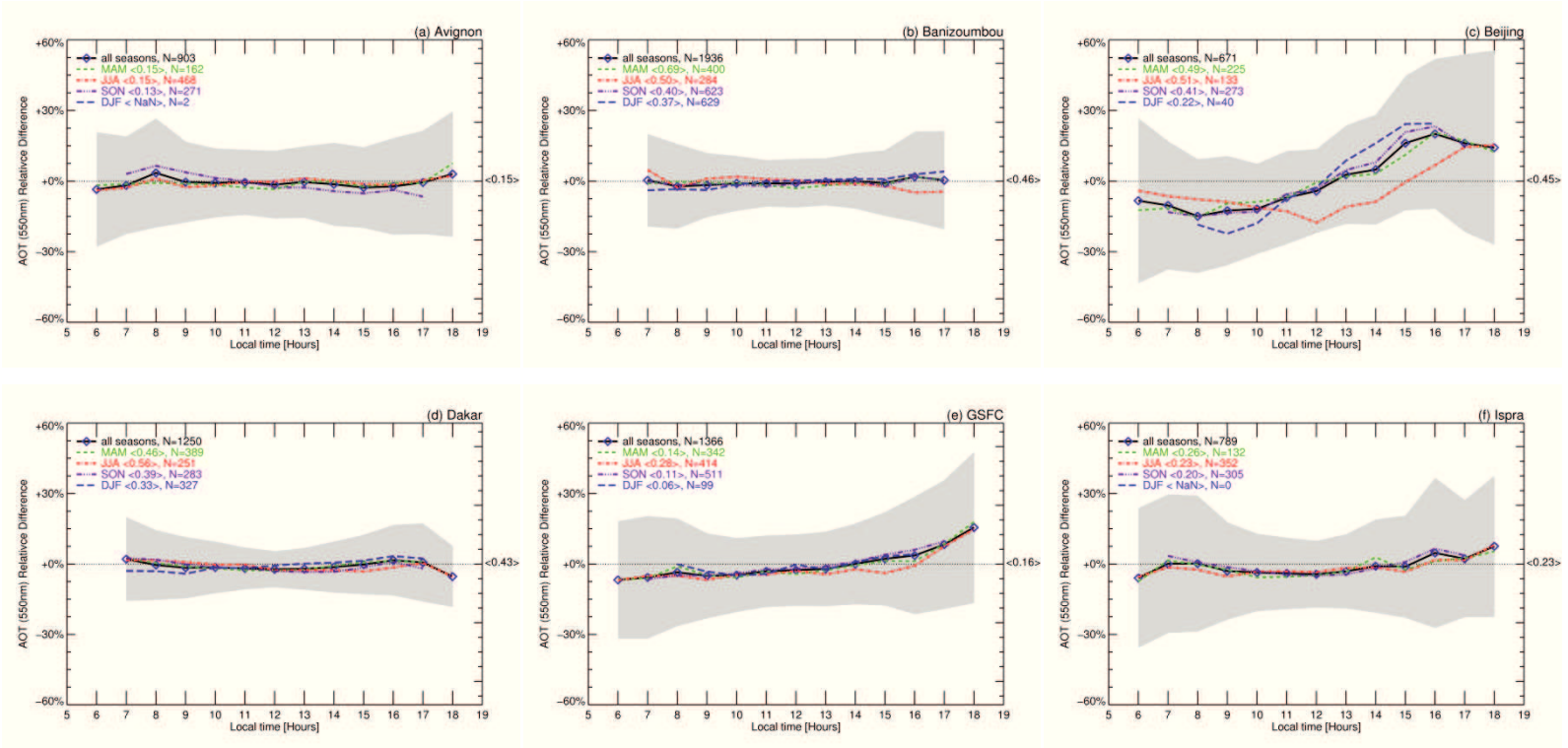

Fig. 6.4 Diurnal cycles of AERONET AOT (550nm) for seasons over the several AERONET stations. The diurnal AOT patterns in the regions are influenced by local aerosol sources and meteorological conditions.

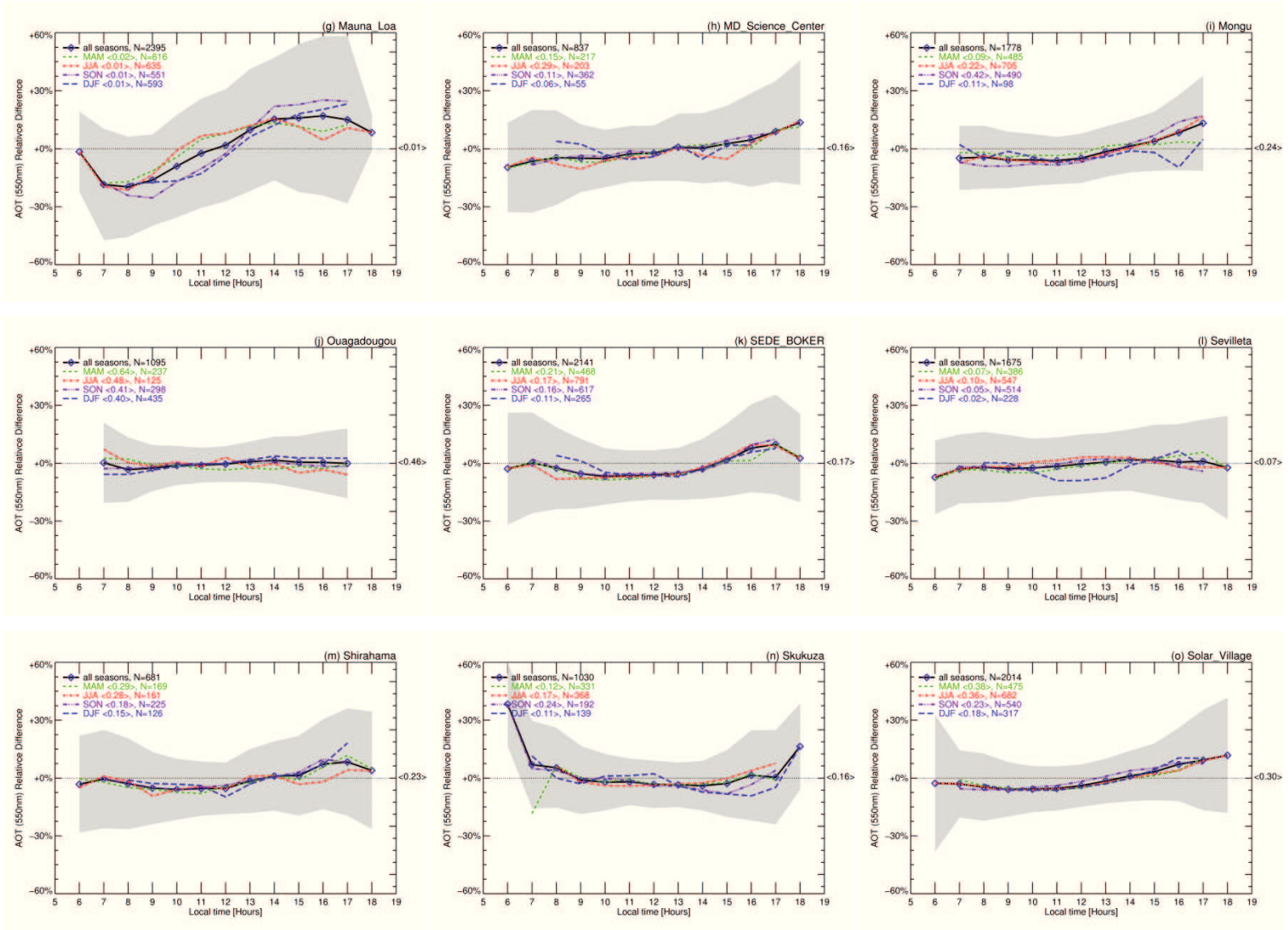

Fig. 6.4 (*Continued*)

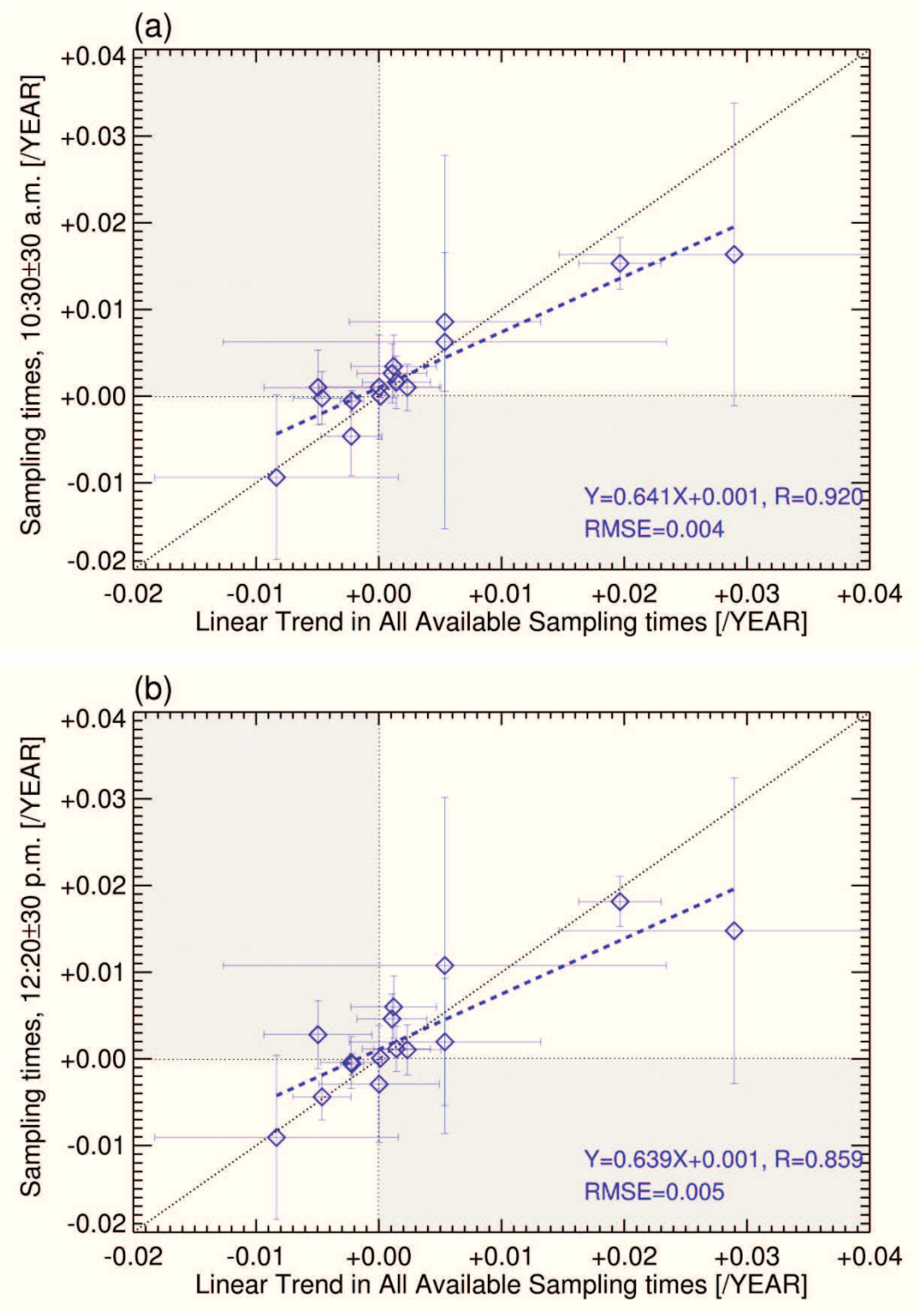

Fig. 6.5 Scatter plots for the comparison of AOT trends between all available sampling and (a) 10:30±30 a.m., (b) 12:20±30 p.m., and (c) 01:30±30 p.m. Shaded areas represent the opposite tendency (sign) of them.

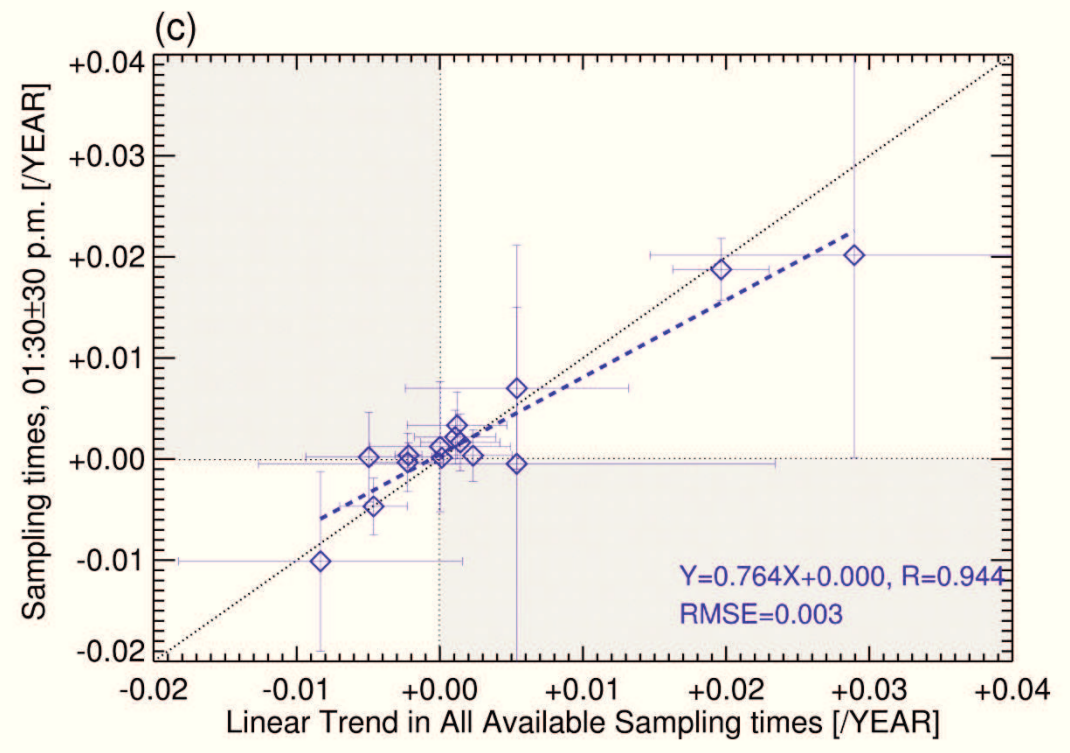

Fig. 6.5 (*Continued*)

6.3 Validation of AOT trends derived from satellites

As demonstrated in the previous section, it is difficult to compare AOT trends derived from different temporal samplings. Nevertheless, the trend validation with ground-based observations is needed since the reliability of AOT trends from satellite observations are also affected by other uncertainty factors (e.g. sensor calibration and retrieval accuracy). Therefore, AERONET level 2.0 data are used for the trend validation at the local stations as shown in Fig. 6.6. These stations are sorted out according to the periods of observation, which is longer than three years overlapped with each of satellite research periods in Fig. 6.7. More specific information of AERONET stations for the trend validation is summarized in Tab. 6.3.

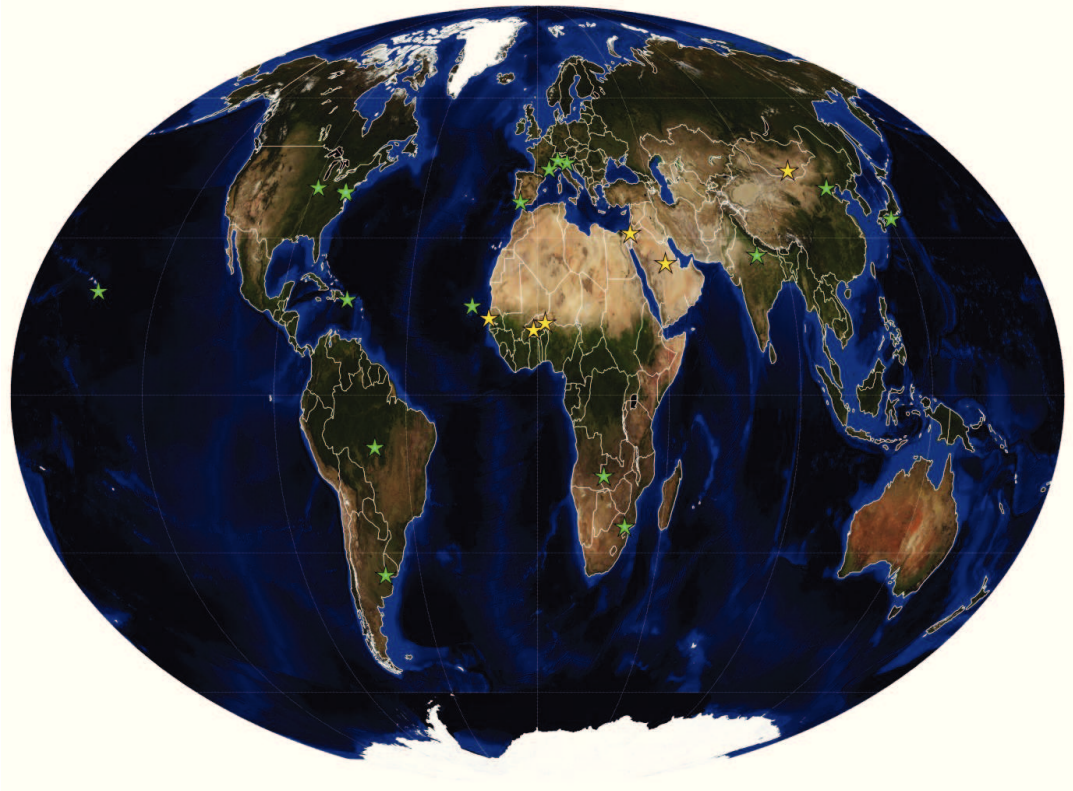

Fig. 6.6 Global AERONET stations for the validation of AOT trends derived from MODIS-Terra (MOD), MISR-Terra (MIS), SeaWiFS-OrbView-2 (SEA), and MODIS-Aqua (MYD). Yellow star symbol represents the AERONET stations only for the validation of MISR AOT trends (because MISR's multiple-viewing observation enables to retrieve AOTs near/in desert regions) while green star symbol shows the stations for all satellite trends.

Tab. 6.3 Geolocations of AERONET stations and research periodes of AERONET level 2.0 AOT data for the trend validations.

AERTONET Stations	Abbreviations	Geolocations (lat.[°]/lon.[°]/alt.[m])	Countires	Research Periods	Targets for Trend Validation
Alta_Floresta	ALTA	-9.87/-56.10/277	Brazil	2001~2004	MOD, SEA
Avignon	AVIG	43.93/4.88/32	France	2003~2005	MOD, MIS, SEA, MYD
Banizoumbou	BANI*	13.54/2.66/250	Niger	2003~2008	MIS
Beijing	BEIJ	39.98/116.38/92	China	2004~2007	MOD, MIS, SEA, MYD
BONDVILLE	BOND	40.05/-88.37/212	USA	2002~2006	MOD, MIS, SEA, MYD
Capo_Verde	CAPO	16.73/-22.94/60	Sal Island	2005~2008	MOD, MIS, SEA, MYD
CEILAP-BA	CEIL	-34.57/-58.50/10	Argentina	2000~2007	MOD, SEA, MYD
Dakar	DAKA*	14.39/-16.96/0	Senegal	2004~2007	MIS
Dalanzadgad	DALA*	43.58/104.42/1470	Mongolia	1999~2004	MIS
El_Arenosillo	EL_A	37.11/-6.73/0	Spain	2002~2005	MOD, MIS, SEA, MYD
GSFC	GSFC	38.99/-76.84/87	USA	1998~2008	MOD, MIS, SEA, MYD
Ispra	ISPR	45.80/8.63/235	Italy	2001~2007	MOD, MIS, SEA, MYD
Kanpur	KANP	26.51/80.23/123	India	2001~2006	MOD, MIS, SEA, MYD
La_Parguera	LA_P	17.97/-67.05/12	Puerto Rico	2006~2009	MOD, MIS, MYD
Mauna_Loa	MAUN	19.54/-155.58/3397	USA	1998~2009	MOD, MIS, SEA, MYD
MD_Science_Center	MD_S	39.28/-76.62/15	USA	2000~2006	MOD, MIS, SEA, MYD
Mongu	MONG	-15.25/23.15/1107	Zambia	1999~2008	MOD, MIS, SEA, MYD
Ouagadougou	OUAG*	12.20/-1.40/290	Burkina Faso	2000~2004	MIS
SEDE_BOKER	SEDE*	30.86/34.78/480	Israel	2004~2008	MIS
Shirahama	SHIR	33.69/135.36/10	Japan	2002~2009	MOD, MIS, SEA, MYD
Skukuza	SKUK	-24.99/31.59/150	South Africa	2001~2007	MOD, MIS, SEA, MYD
Solar_Village	SOLA*	24.91/46.40/764	Saudi Arabia	2001~2007	MIS
Venise	VENI	45.31/12.51/10	Italy	2000~2005	MOD, SEA, MYD

* represents the AERONET stations for the trend validation of MISR AOT only

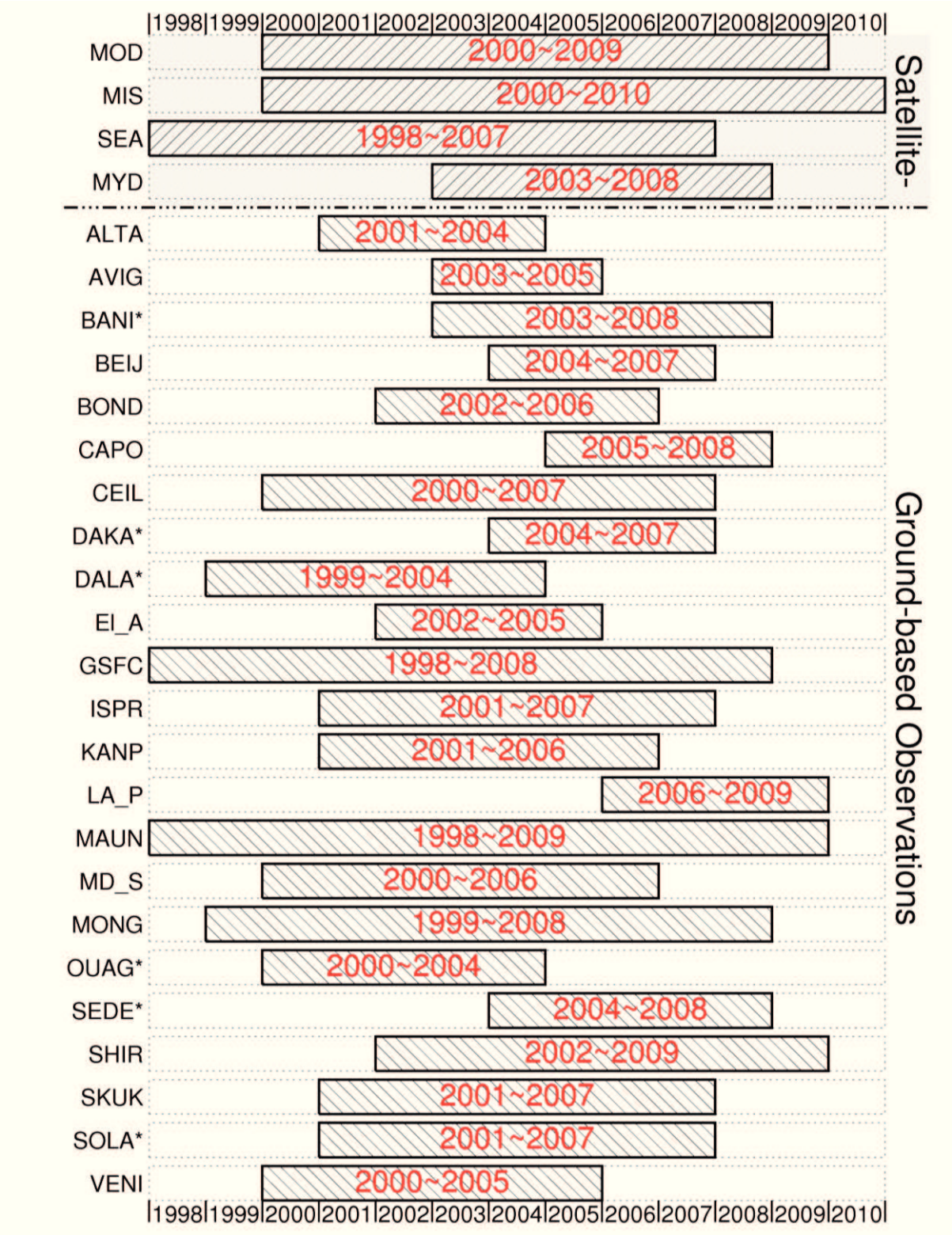

Fig. 6.7 Research periods of MODIS-Terra (MOD), MISR-Terra (MIS), SeaWiFS-OrbView-2 (SEA), MODIS-Aqua (MYD), and AERONET stations listed up in Tab. 6.3. These stations are selected by the periods of observation, which is longer than three years overlapped with each of satellite research periods. * represents the AERONET stations for the trend validation of MISR AOT only.

Figs. 6.8-6.11 provide an example of each comparison between AERONET and satellite AOT trends over the stations Beijing (for MOD AOT at 550 nm), Ouagadougou (for MIS AOT at 558 nm), Ispra (for SEA AOT at 510 nm), and GSFC (for MYD at 550 nm). The capital of China, Beijing, is one of the most populated and industrialized cities in the world. It is strongly influenced by anthropogenic aerosol due to the rapid economic development in the past decades as well as mineral dust transported from Asian deserts by strong westerly winds. In Fig. 6.8, AERONET and MOD AOTs are significantly increasing from 2004 to 2007. These similar tendencies also appear in the weighted trends. Coarse particle (i.e. mineral dust) is dominant over Ouagadougou located in Sahel regions throughout the year. Particularly, desertification is going on in surrounding areas due to the human activities and climate variations, which are observed in the analysis of AERONET and MIS AOT trends in Fig. 6.9. The third example for the validation of SEA AOT trend is presented in Fig. 6.10 including AERONET AOT trend over Ispra. Industrial and traffic pollutants are mainly observed over there, and significantly decreasing in AERONET AOT trend. Although linear trend of SEA AOT is opposite to the AERONET trend, the weighted trend shows a slightly negative tendency. Finally, in Fig. 6.11, the station GSFC positioned near Washington DC is influenced by industrial and traffic pollutants mainly emitted from vehicles and industries. The decreasing trends of AERONET and MYD AOTs are in good agreement, and the weighted trends with high significance are even better. The significance value ($\left|B_g/\sigma_{B_g}\right|$) defined as the absolute value of AOT trend (B_g) divided by its standard deviation (σ_{B_g}) will be discussed in more detail in the next section for statistical analysis. If the significance value is larger than two, the trend is significant within 95% confidence level [Tiao et al., 1990].

In this manner, the trend validation of each satellite AOT is performed at all available AERONET stations listed up in Tab. 6.3, and shown in Fig. 6.12 as scattering plots for

correlation analysis. Considering the discrepancy caused by limited orbital periods and different sampling times discussed in the previous section, it can be concluded that the AOT trends derived from satellite- and ground-based observations are strongly correlated (linear trend: $0.571 \leq R \leq 0.917$ and $0.006 \leq RMSD \leq 0.010$, and weighted trend: $0.396 \leq R \leq 0.934$ and $0.006 \leq RMSD \leq 0.015$). However, the primary discrepancies are caused by the sensor degradation, unscreened clouds, and aerosol retrieval accuracy. Firstly, the AERONET AOT trend shows better correlation with the MOD trend than with the MIS trend because MIS has a smaller spatial coverage, which leads to a lack of aerosol sampling, even though they are onboard on same space platform (Terra). Nonetheless, it is necessary to analyze the MIS trends over desert regions (where cloud disturbance and aerosol variability are less: see Figs. 5.2 and 6.4) because only MIS can retrieve AOT over these high reflecting surfaces using multiple-viewing observations. The weighted trends of SEA and AERONET AOTs generally give a better agreement with high correlation than the linear trends. However, the slightly low correlation slope of the SEA trends can be attributed to underestimation of SEA AOT (up to 20% near heavily polluted areas due to strong absorbing aerosols) [von Hoyningen-Huene et al., 2011] and OrbView-2 orbital drift (about two hours delay till end of 2007) [Yoon et al., 2011]. In contrast, MYD AOT trends are well correlated with and AERONET trends, but with relatively large deviation. In order to estimate more reliable AOT trends, these all complementary trends derived from various polar-orbiting satellites (i.e., MOD, MIS, SEA, and MYD) need to be analyzed. Specific values of the AOT trends are summarized in Tabs. C.1 - C.4 (Appendix C).

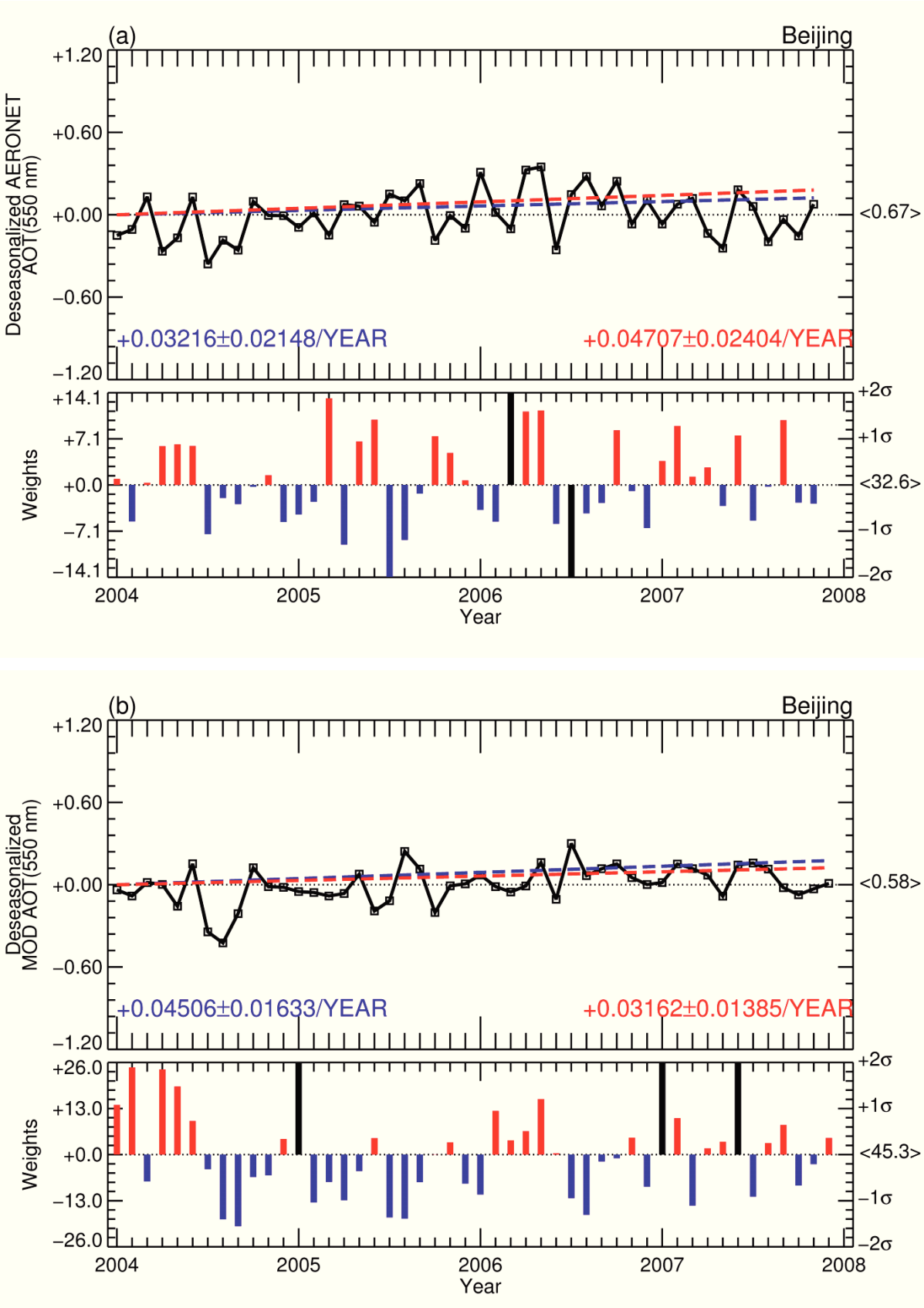

Fig. 6.8 Linear and weighted trends of (a) AERONET and (b) MOD anomalized (deseasonalized) AOTs at Beijing.

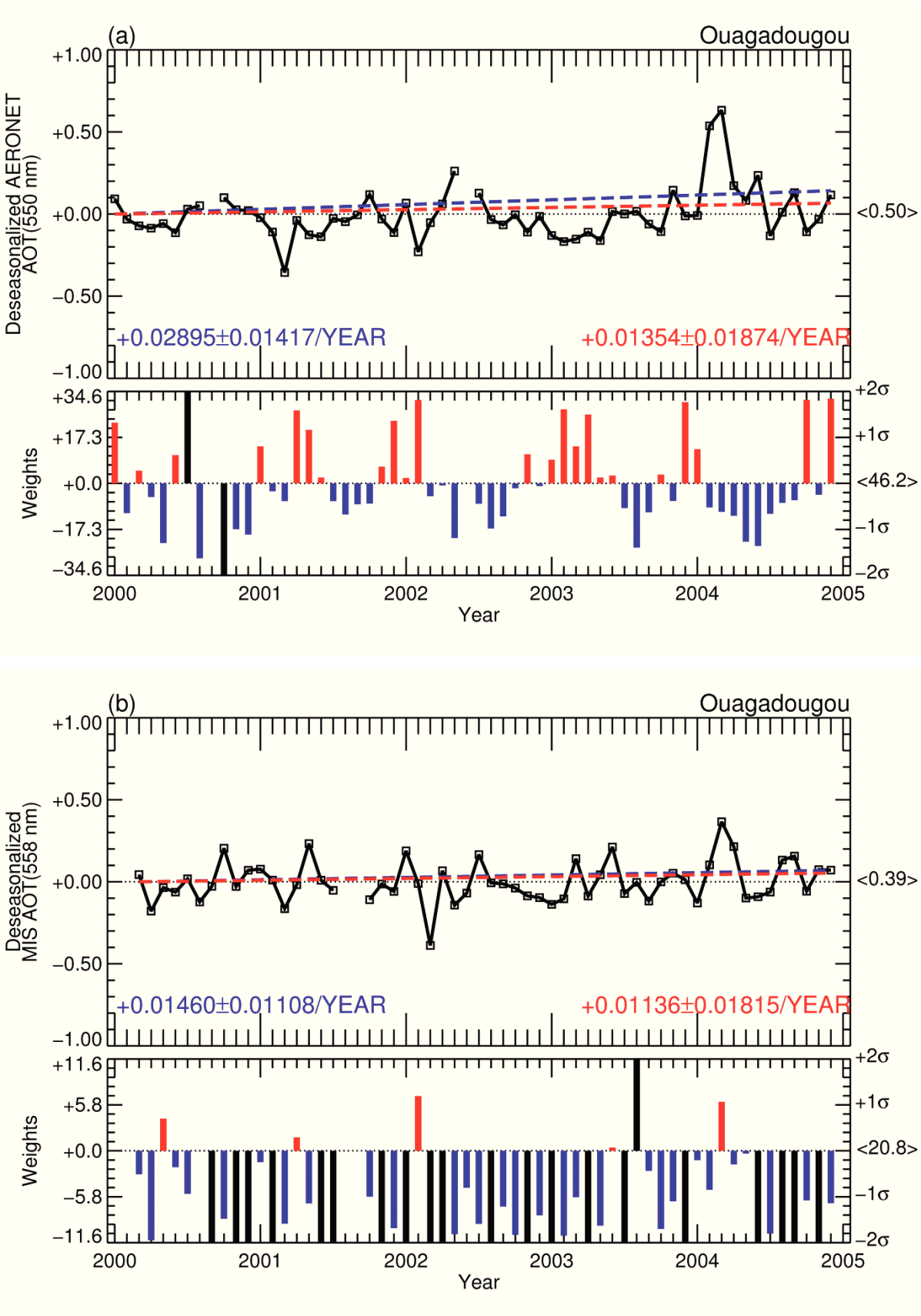

Fig. 6.9 As in Fig. 6.8, but (b) the trends of MIS anomalized (deseasonalized) AOTs at Ouagadougou.

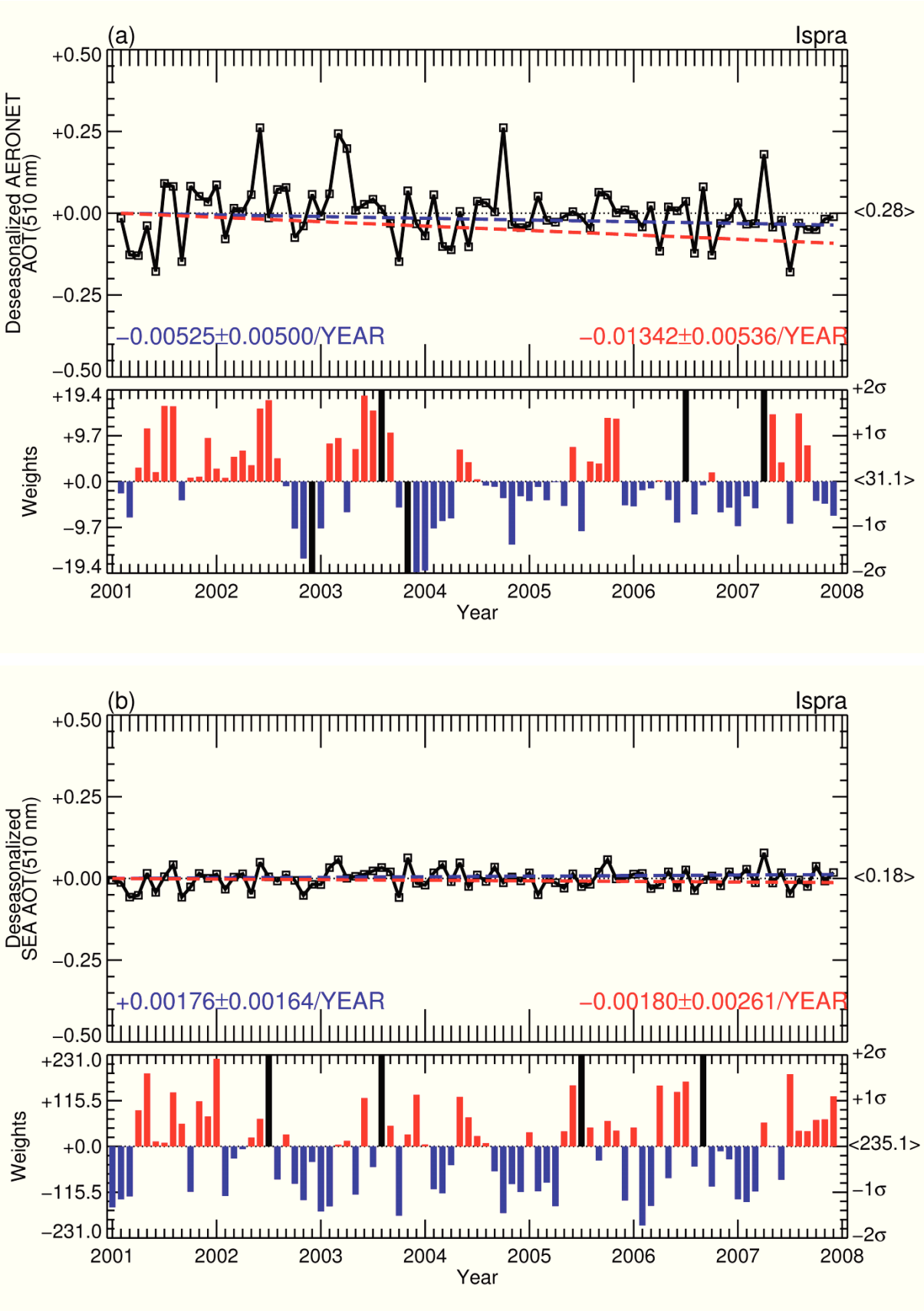

Fig. 6.10 As in Fig. 6.8, but (b) the trends of SEA anomalized (deseasonalized) AOTs at Ispra.

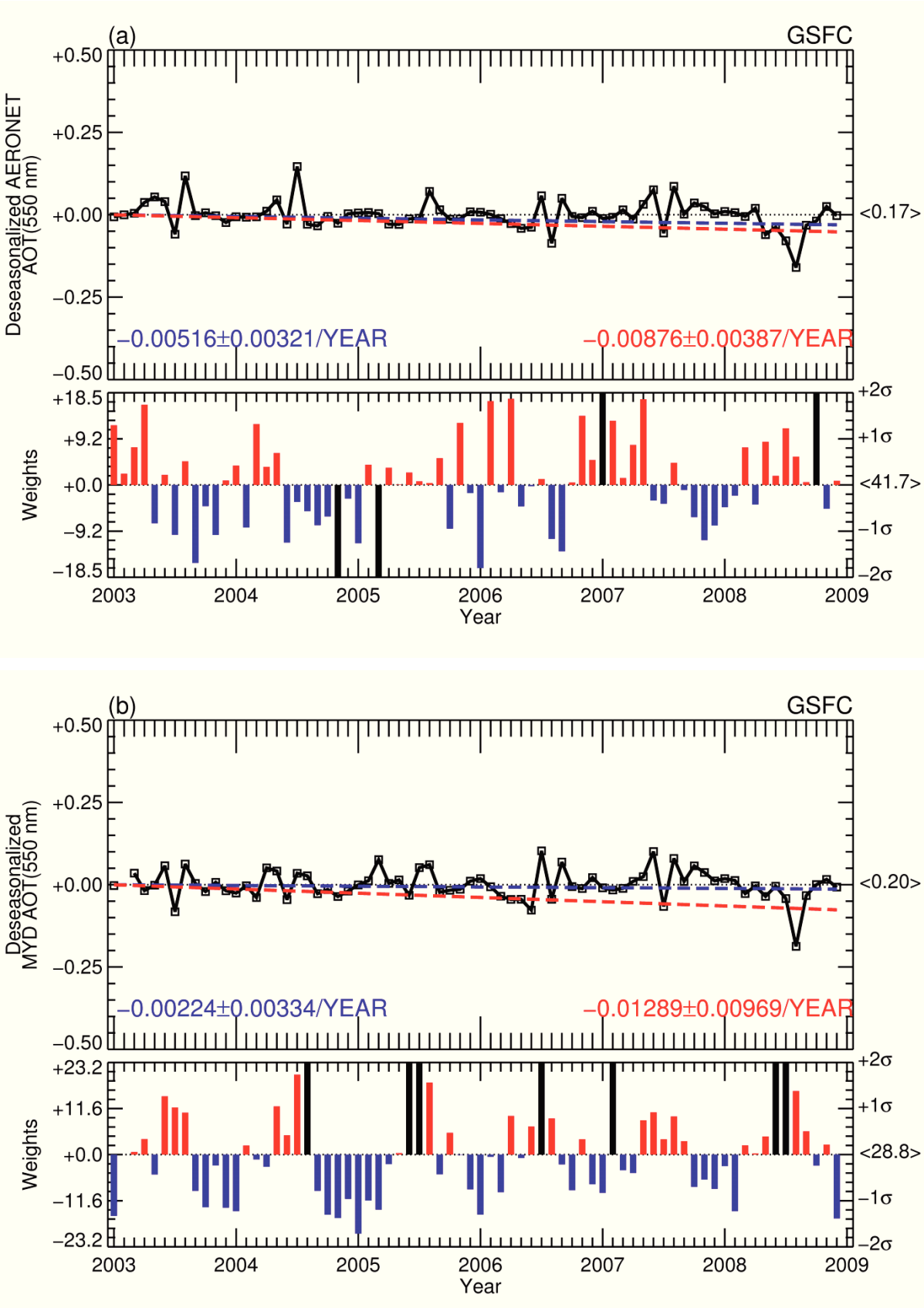

Fig. 6.11 As in Fig. 6.8, but (b) the trends of MYD anomalized (deseasonalized) AOTs at GSFC.

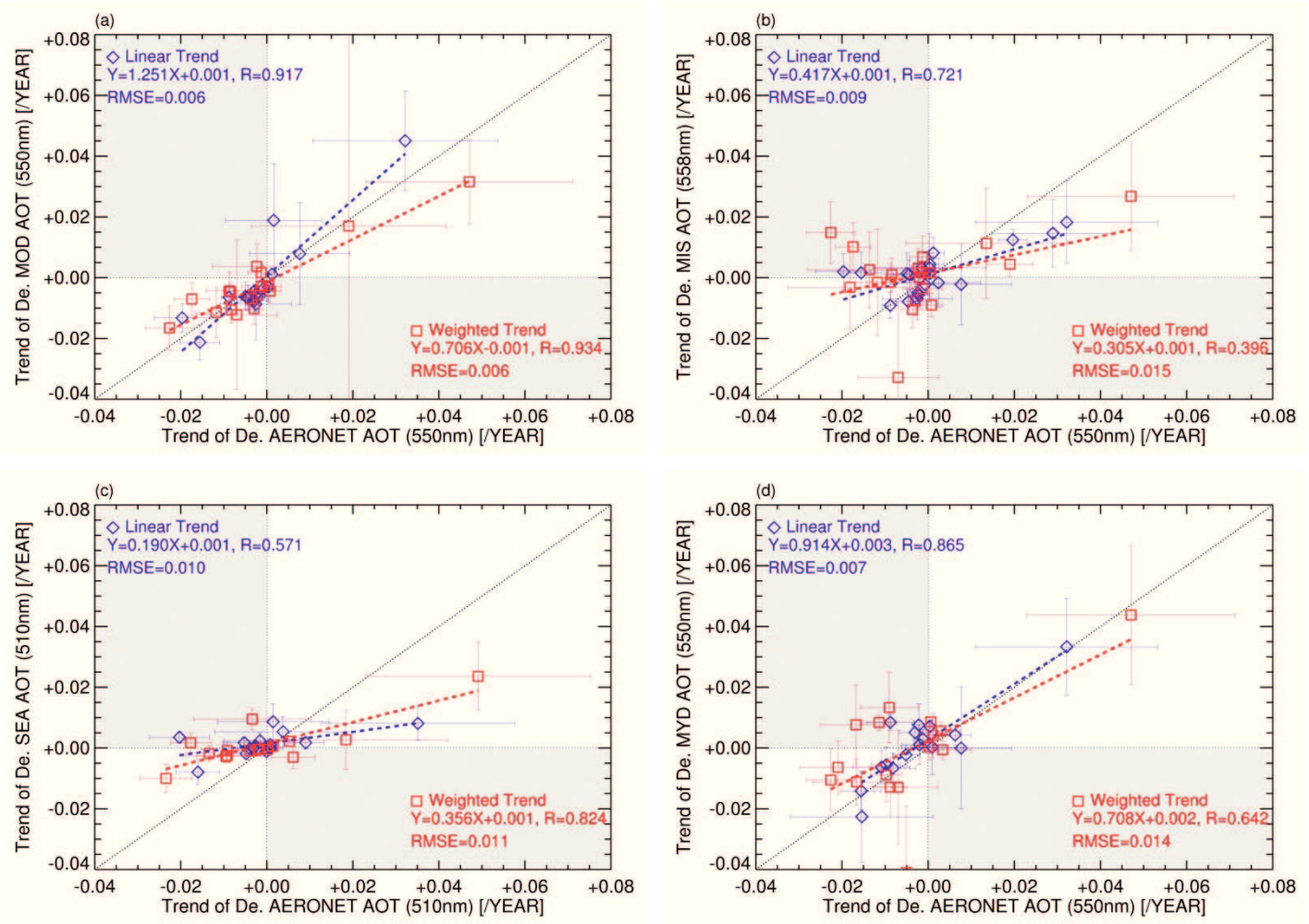

Fig. 6.12 Scattering plots of comparison between the trends of AERONET and (a) MOD, (b) MIS, (c) SEA, and (d) MYD anomalized (deseasonalized) AOTs.

6.4 Global and regional trend analyses

This section discusses the global and regional AOT (550 nm for MOD and MYD, 558 nm for MIS, and 510 nm for SEA) trends estimated from the polar-orbiting satellite observations by the methodologies mentioned in Section 6.1. For a meaningful analyses over specific regions, the present study takes into account the gridded trend (B_g) (1° × 1° for MOD, SEA, and MYD or 0.5° × 0.5° for MIS) with significance ($\left|B_g/\sigma_{B_g}\right|$) larger than one, which means that the trend uncertainty can range from -100% to +100%. If the significance is larger than two, it can be concluded that the trend is significant within 95% confidence level [Tiao et al., 1990]. The standard deviation of the gridded trend (σ_{B_g}) is calculated using the bootstrap method (aka, Monte Carlo error bars analysis) introduced in Section 5.1, and the number of resampling iteration is 5000 times for each grid. For regional analysis, Fig. 6.13 presents the specific regions coordinated in Zhao et al. (2008) and Streets et al. (2009) including

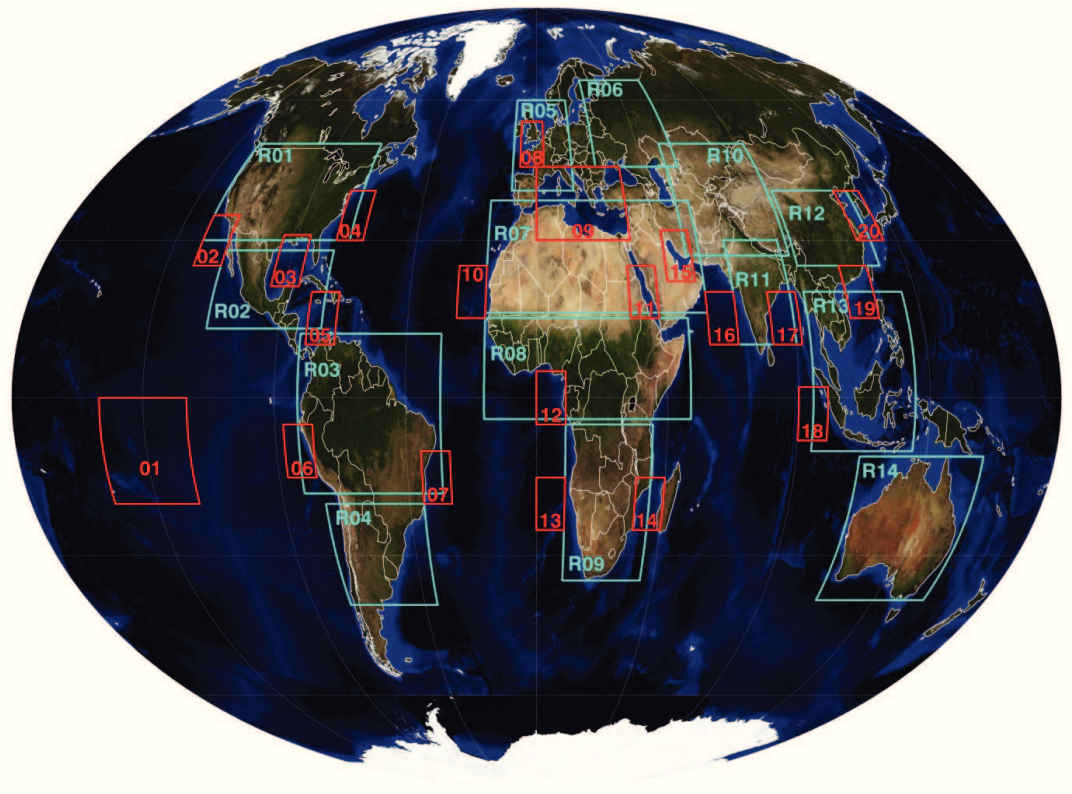

Fig. 6.13 Research regions over land and water (light bule square) and only oceanic areas (red square).

additional oceanic and desert areas having less cloudiness and variability. These regions are very important to monitor various aerosols (such as mineral dust, biomass burning aerosol, and industrial/traffic pollutant) transported from the downwind areas or emitted from the aerosol source regions.

In general, the global AOTs retrieved from the multiple observations show a similar distribution in Fig. 6.14. A strong emission of anthropogenic aerosols, especially industrial pollutants and biomass burning aerosols, is observed over South and East Asia [Zhang et al., 2003; Kaskaoutis et al., 2011b; Vadrevu et al., 2011], while a large amount of mineral dusts transported by winds from the deserts is detected in Middle East and Northern Africa [Derimian et al., 2006; Sabbah et al., 2006; Tafuro et al., 2006; Reeves et al., 2010]. Biomass burning (i.e. forest fires) in South Africa and South America is mainly generated by human activity for agriculture and land development [Eck et al., 2001; Swap et al., 1996; Zhu et al., 2011; Koppmann et al., 2005]. In North America and European regions, aerosol loadings composed of industrial, urban, and traffic pollutants are comparatively smaller [Mazzola et al., 2010; Zhao et al., 2008; Streets et al., 2006; Andronache, 2004]. Despite of a consistent global distribution of the AOTs, the corresponding trends can be different due to the various factors mentioned in the previous sections.

Many studies have attempted to discuss reliable temporal trends of the cloud-free AOTs using a simple linear model as shown in Fig. 6.15 [Mishchenko et al., 2007; Zhao et al., 2008; Yu et al., 2009; Karnieli et al., 2009; de Meij et al., 2010] and their significances ($\left|B_g/\sigma_{B_g}\right|$) in Fig. 6.16. Apparently, a similar tendency appears near/in the main industrialized/urbanized and desert regions (i.e. areas close to East and South Asia, Middle East, and African deserts). However, the linear AOT trends based on limited and different samplings show a large difference not only in intensity, but also in the sign (i.e. the complete opposite of the AOT tendencies) as demonstrated in previous chapters. Furthermore, a clear spatial division of the

AOT trends derived from the same sampling is found between nearby land and ocean even though they have a common aerosol source in land. For instance in Fig 6.15 (a), an increasing pattern of the trends over the India subcontinent is disconnected between land and ocean, and there is no positive signal over Brazil even though they are one of BRICs (a group of the countries: Brazil, Russia, India, and China leading a new and advanced economic development [Goldman Sachs, 2003]). Additionally, the MOD AOT trends over South Africa and its surrounding marine area are discontinuous. For MIS AOT trend in Fig 6.15 (b), although MISR is performing well in aerosol retrieval over desert areas (i.e. bright surfaces), there is a limit in trend analysis due to its small spatial coverage (see Tab. 6.1). Compared to other trends, it is difficult to recognize the discontinuity in SEA AOT trends along the coastline, but still a large difference is observed over Indian subcontinent in Fig 6.15 (c). MYD AOTs shows a large decreasing in South America and Central Africa while relatively large increases of aerosols are dominant over most of regions in Fig 6.15 (d). Obviously, these results should be discussed with respect to climate changes, human activity, platform characteristics, sensor calibration status, AOT retrieval accuracy, and research periods. However, the first and foremost fact to be considered for the trend analysis of cloud-free AOT is induced by the unrepresentative sampling. A major disturbing factor in the aerosol sampling by satellite observations is the presence of clouds. In other words, the trend analysis is almost impossible over regions where frequent cloud occurrence persists throughout the year (e.g., most of the marine areas and tropical rain/cloud forests in the equatorial zone). Fig.6.17 presents the total cloud fraction (CF) and its standard deviation (STD) in daytime from MOD and MYD observations during each research period, which can explain the cloud disturbance in aerosol sampling. Finally, even though the linear trend of cloud-free aerosol has a high significance in statistics, as shown in Fig.6.16, it cannot be significant without considering the cloud disturbance. Therefore, by using a linear weighted model, the

uncertainty caused by the cloud disturbance in the trend analysis can be minimized. Fig. 6.18 presents the weighted trends of cloud-free AOTs, which are improved over the problematic regions in the clear spatial division of linear trends between nearby land and ocean above mentioned (see Fig. 6.15). In particular, a discontinuous tendency of the MOD AOT between land and ocean over South Asia and South Africa has disappeared, and a positive trend can be found over South America (see Fig. 6.18 (a)). However, as already mentioned, the persistent and frequent cloud disturbance remains as an inescapable factor although using the weighted trend method. Therefore, for the regional trend analysis of cloud-free AOT, the present study attempts to select the research regions based on cloud fraction and variability as shown in Fig. 6.17. Furthermore, the gridded weighted trend (1° × 1° for MOD, SEA, and MYD or 0.5° × 0.5° for MIS) with the significance larger than one (see Fig. 6.19) are mainly used for a statistically meaningful analysis of regional and global trends.

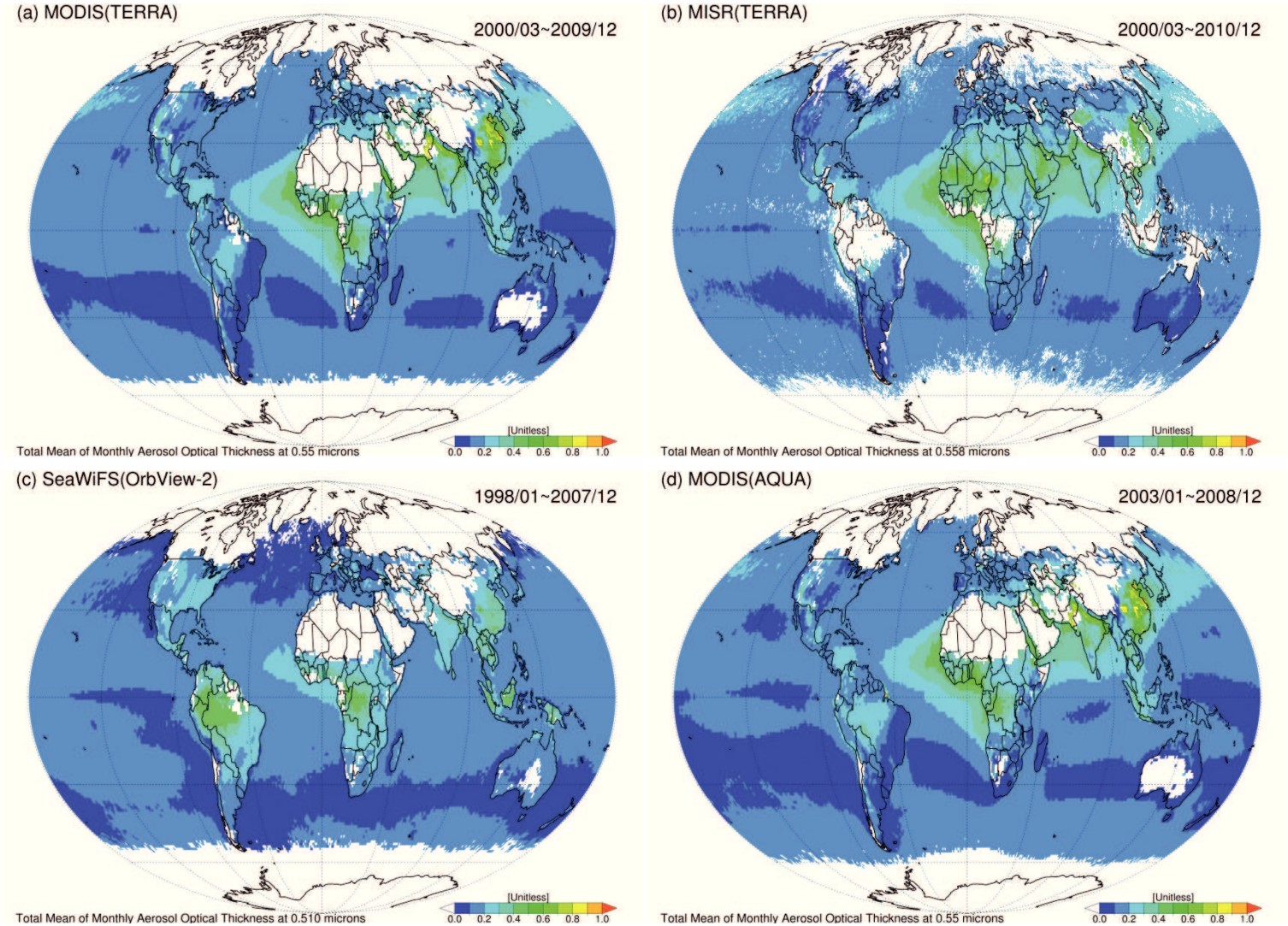

Fig. 6.14 Global distributions of total (a) MOD, (b) MIS, (c) SEA, and (d) MYD AOT means for each research period.

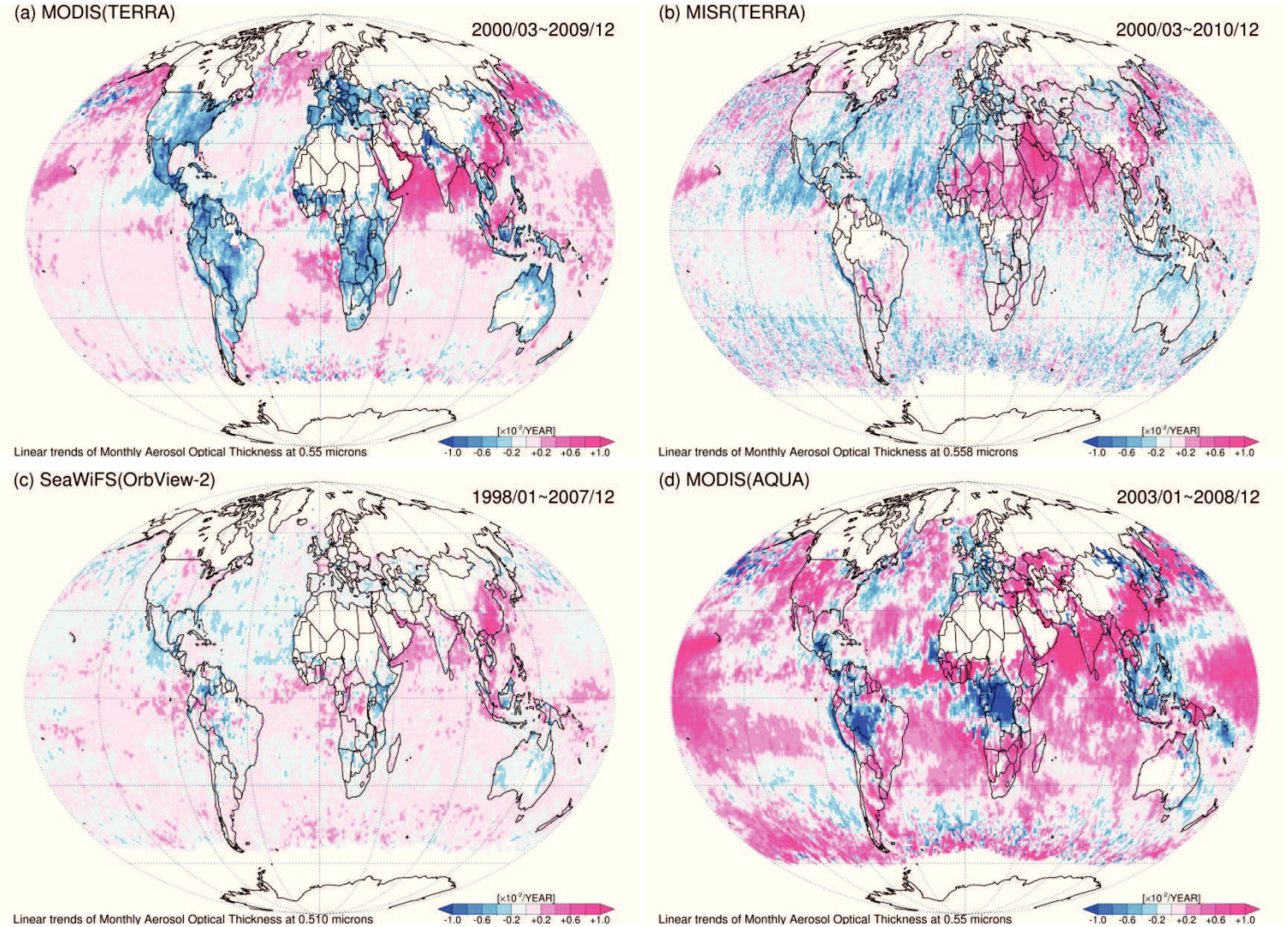

Fig. 6.15 Linear trends of global (a) MOD, (b) MIS, (c) SEA, and (d) MYD AOTs for each research period.

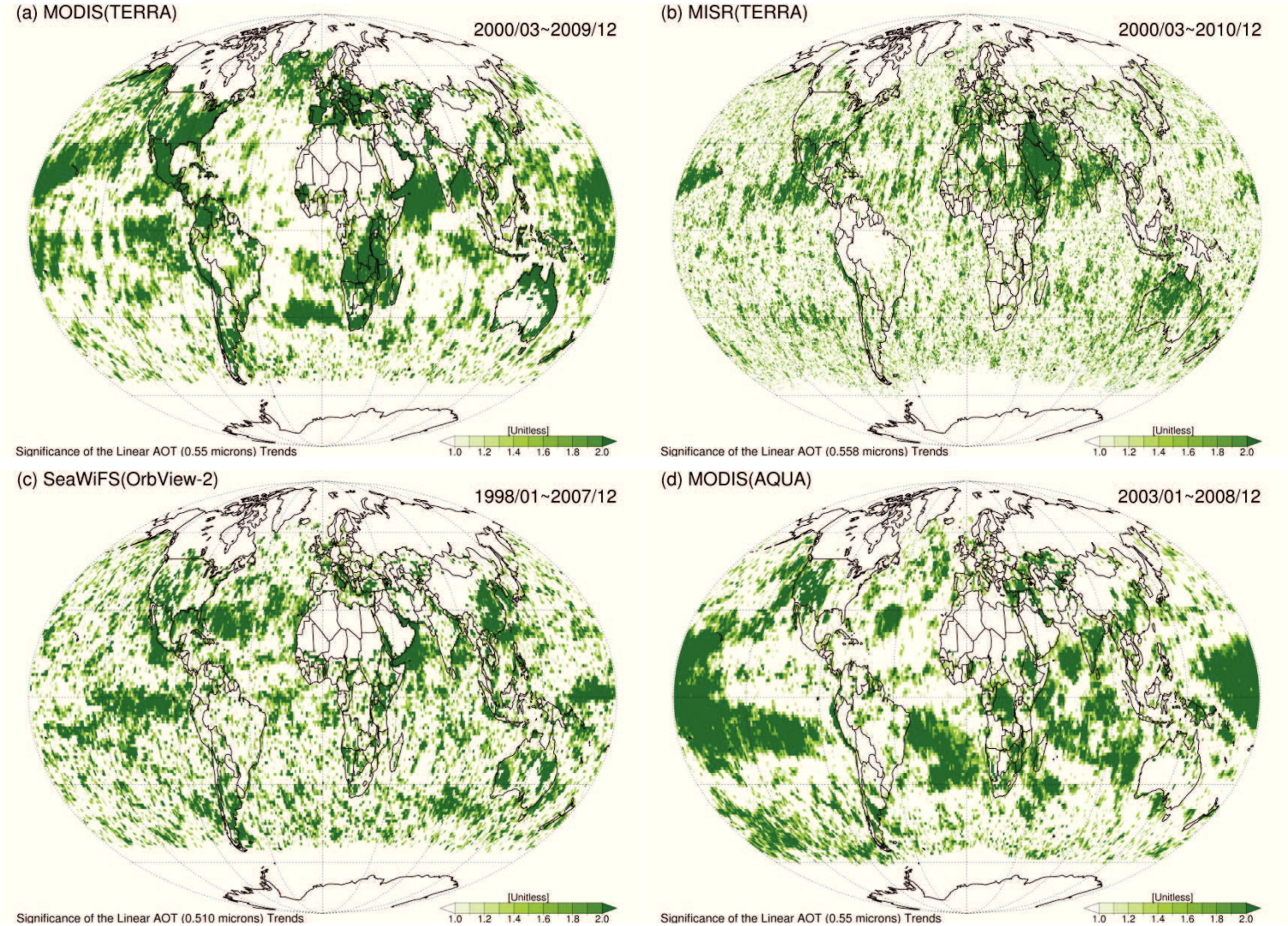

Fig. 6.16 Global significances ($\left|B_g/\sigma_{B_g}\right|$) of linear (a) MOD, (b) MIS, (c) SEA, and (d) MYD AOT trends for each research period.

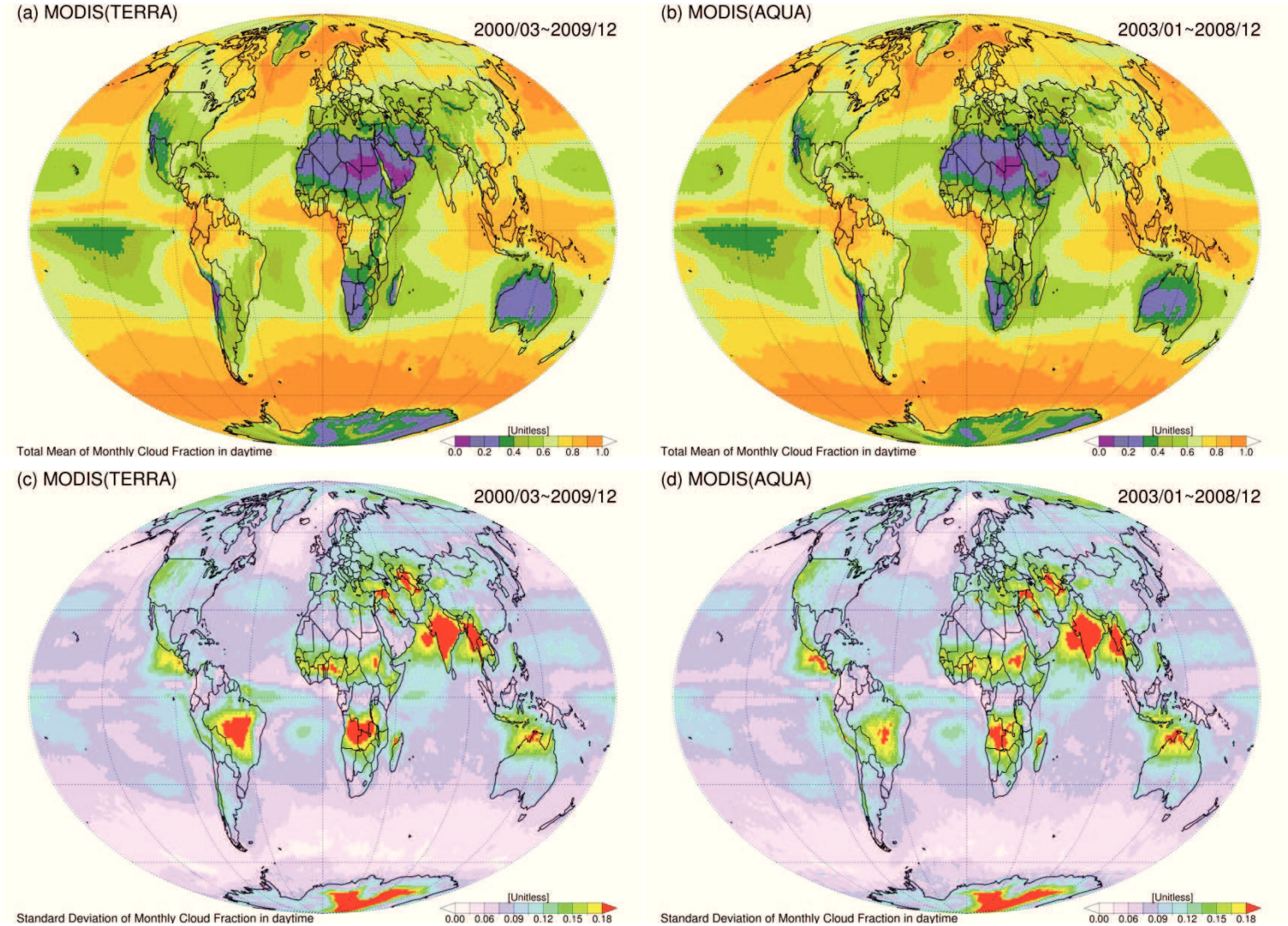

Fig. 6.17 Global distribution of total (a) MOD and (b) MYD CF means, and total (c) MOD and (d) MYD STD means for each research period in daytime.

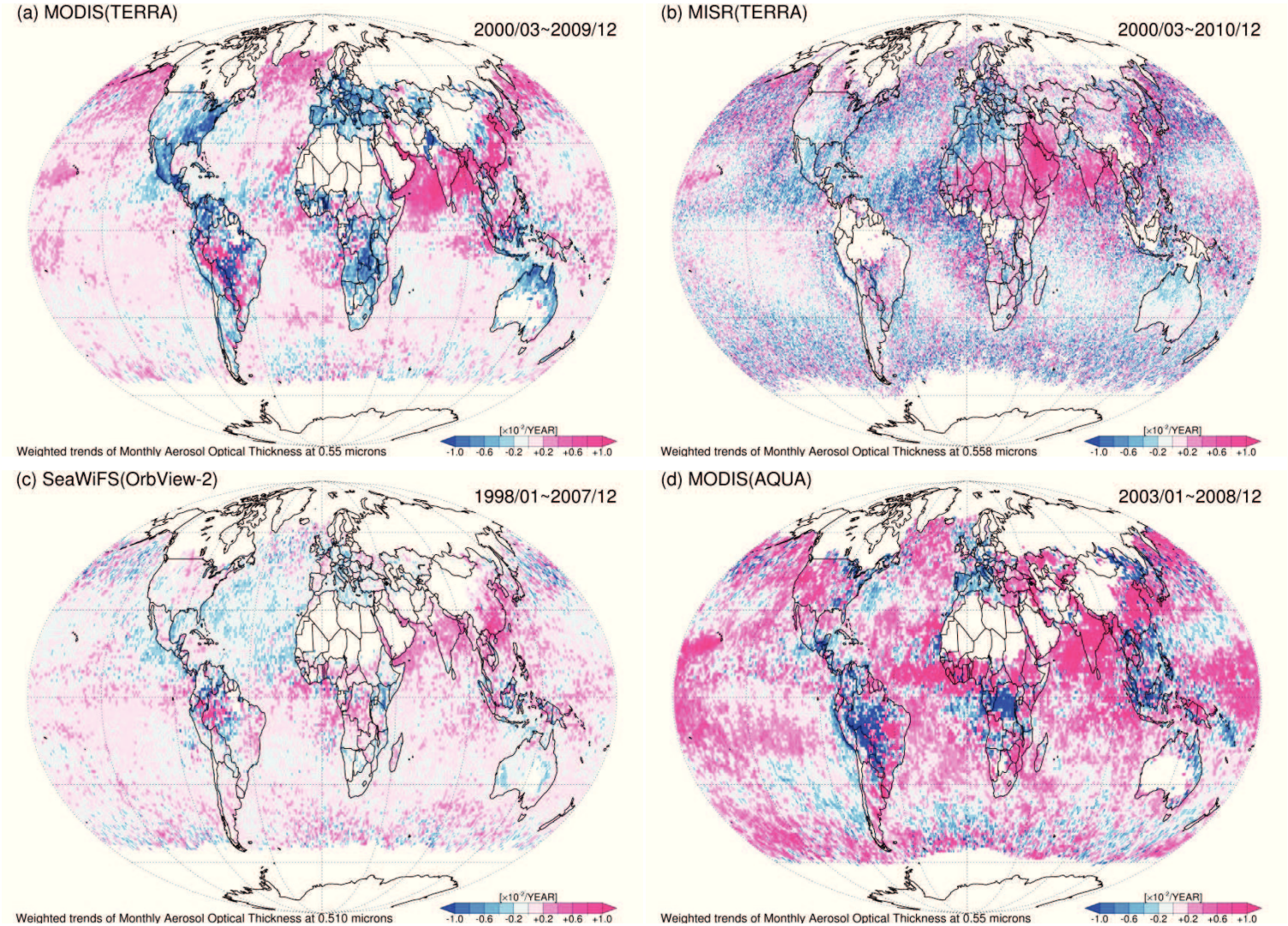

Fig. 6.18 Weighted trends of global (a) MOD, (b) MIS, (c) SEA, and (d) MYD AOTs for each research period.

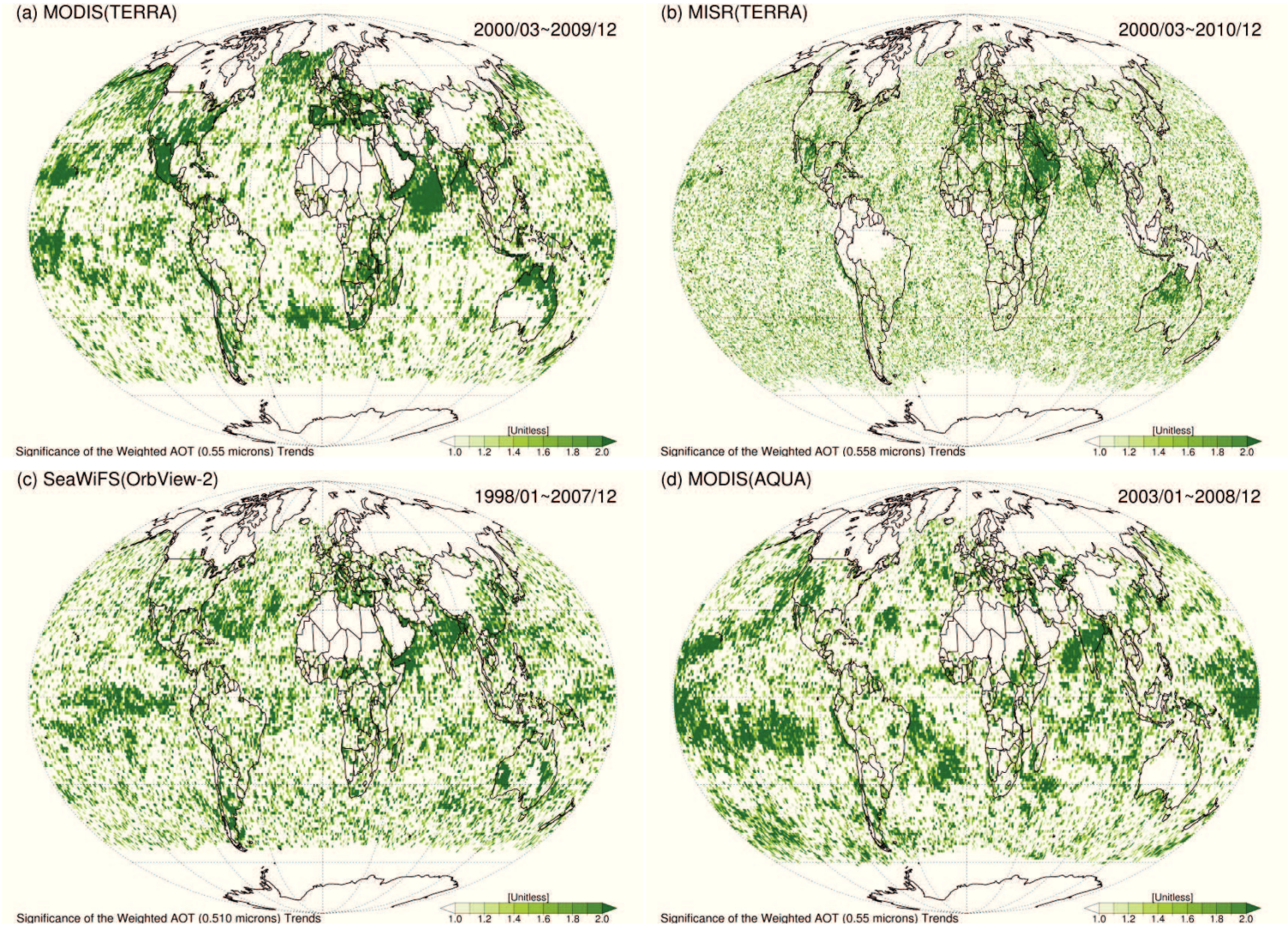

Fig. 6.19 Global significances ($\left|B_g/\sigma_{B_g}\right|$) of weighted (a) MOD, (b) MIS, (c) SEA, and (d) MYD AOT trends for each research period.

Linear and weighted trends of the cloud-free AOTs for the globe (GL), northern (NH), and southern hemisphere (SH) are illustrated in Fig. 6.20. Additionally, the trends are analyzed separately for land only, ocean only, and both regions. For the ocean regions, most of the sensors, except MISR which has a weakness in aerosol sampling due to small spatial coverage, consistently detect an increasing trend of AOT, which is opposite to the findings from AVHRR AOTs over water discussed in Mishchenko et al. (2007), Mishchenko and Geogdzhayev (2007), and Zhao et al. (2008). Clearly, there are many causes (e.g., different sampling times, research periods, retrieval accuracy, cloud-screening techniques, calibration status) being able to explain this inconsistency. Between the linear and weighted trends over marine areas, small differences occur because the weighted method does not work well due to large and persistent cloud disturbances. For the terrestrial areas, the AOTs over GL and NH regions show a positive trend, except for MOD AOT, while the decreasing trend is generally

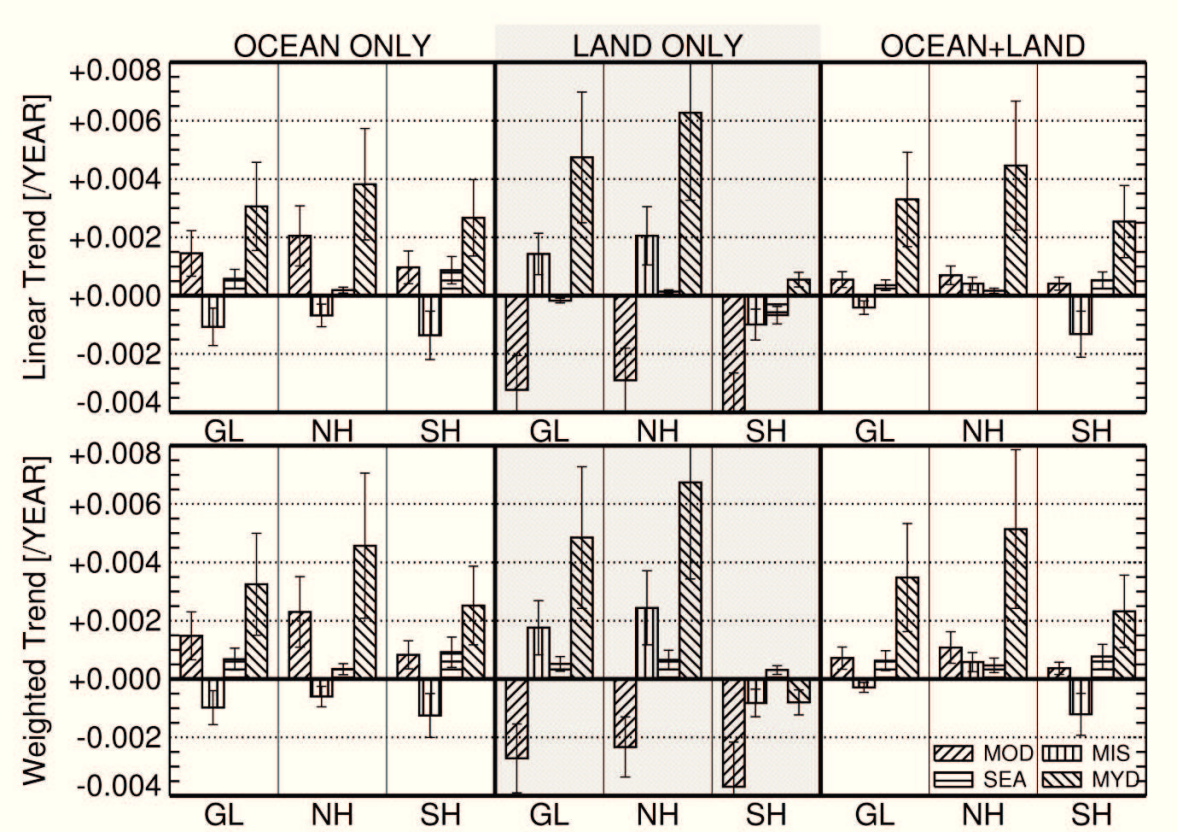

Fig. 6.20 Linear and weighted trends of cloud-free MOD, MIS, SEA, and MYD AOTs for GL, NH, and SH.

observed over SH region. Finally, throughout terrestrial and marine regions, increases of cloud-free AOTs are noticeably observed over GL, NH, and SH (although neagtive trends of MIS AOT are detected over GL and SH). These tendencies are mainly connected with the complicated changes of regional weather pattern and aerosol emission, which will be discussed in the following paragraphs (Figs. 6.21 and 6.22). The specific intensities and standard deviations of the AOT trends and CFs are summarized in Tab. D.1 (Appendix D).

Pacific region

In the tropical Pacific region, the region 01 (Fig. 6.13) over open oceans (which is far away from the terrestrial aerosol emission [Remer et al., 2006]) is selected because of less cloud disturbances as compared to surrounding regions (see Fig. 6.17). Especially, this region is one of the most sensitive areas to climate changes (i.e. El Niño/La Niña-Southern Oscillation or ENSO) [Rasmusson and Carpenter, 1982]. The main aerosol type over the remote ocean is sea-salt generated by the surface wind [Fan and Toon, 2011; Quinn et al., 1998]. Besides, asian mineral dusts, pollutants, and volcano ashes can be observed since they are long-rangely transported through the free troposphere [Dubovik et al., 2002a; Schmeissner et al., 2011]. Generally, the positive AOT trends with high significance are estimated in this area (except MIS AOT trend, but it is almost negligible: -0.00006±0.00004 yr^{-1} for weighted trend), and the intensities range from +0.00101±0.00060 to +0.00263±0.00113 yr^{-1} for linear and from +0.00116±0.00057 to +0.00281±0.00134 yr^{-1} for weighted trends. These positive tendencies are consistent with an increase of AERONET AOT at Mauna Loa reported in Chapter 5, which can be attributed to an increase of transported aerosols from East Asia. Especially, during the research periods for the MYD AOT trends (2003-2008), La Niña not only strengthened the pacific trade wind, but also shifted the precipitation area farther west than usual [Trenberth and Hoar, 1996; Philip and

van Oldenborgh, 2006]. These changes of the climate pattern can contribute to a more apparent positive trend of MYD AOTs. However, it is important to note that these trend analyses may be doubtable since most of oceanic AOTs are below 0.1 and close to the retrieval error ranges (see the aerosol retrieval accuracies in Tab. 6.1).

United States

The R02 and oceanic regions (02 and 04) are representative for US and its adjacent seas, where urban-industrial pollutants from vehicles and industries in Eastern US (near region 04) and biomass burning from wildfires in Western US (region 02) are dominant [Zhang et al, 2012]. Predominantly, a decrease trend of aerosols is estimated in the regions 04 and R02, and the magnitude of the weighted trends are up to -0.00488±0.00284 and -0.00412±0.00217 yr^{-1} respectively. Previous studies reflected similar results in US due to pollutant emission reduction [Smith et al., 2001; Streets et al., 2006; Zhao et al., 2008]. In contrast, a positive trend in the region 02 is also observed; in particular, the weighted trend of MYD AOT reaches +0.00320±0.00165 yr^{-1}. These opposite tendencies at a high significance level between Eastern and Western US are more apparently shown in Figs. 6.18-6.19 (a) and (d) (i.e., aerosol loadings observed by MOD in the morning temporally declines throughout the entire US area, while MYD AOT in the afternoon rises over Western US). The significant increase of MYD AOT can be related to wildfires, which are used to break out in the afternoon [Mu et al., 2011]. Furthermore, La Niña from 2003 to 2008 enhanced the fire activity providing the warmer/drier winter and increased spring/summer temperatures over Western US [Brenner, 1991; Luchs, 2010; Westerling et al., 2006]. These chain processes have been identified by Giglio et al. (2010) and Luchs (2010), which reported an increase of burned area as well as anti-correlation between Sea Surface Temperature (SST) anomaly and wildfire activity during this period. Finally, anthropogenic aerosol emmision over the US

continent seems to be controlled by environmental regulations while natural aerosol emmision highly depends on the climate changes.

Central America

Central America (the regions R02, 03, and 05) is influenced by smoke particles from tropical biomass region and anthropogenic aerosols from urban-industrial regions [Bergstrom et al., 2010; Barnard et al., 2008; Aiken et al., 2010]. Especially, the smoke particles combined with high humid oceaninc airs in each spring were studied as a trigger for deep convection and severe weather events over the Yucatan Peninsula, south Mexico, the Gulf of Mexico, and the US [Lyons et al, 1998; Murray et al, 2000]. Indeed, Wang et al. (2009) simulated the impact of smoke particles on the convective clouds over the south central US using coherent microphysical and meteorological mechanisms. The temporal weighted trends of cloud-free AOTs in these areas generally show negative trends; they are up to -0.00373±0.00202 for the region 03, -0.00363±0.00222 for the region 05, and -0.00412±0.00217 yr^{-1} for the region R02, which are consistant with findings of Zhao et al. (2008). In contrast, MYD AOT tends to increase in these areas (up to +0.00349±0.00212 for the region 03, +0.00061±0.00046 for the region 05, +0.00060±0.00037 yr^{-1} for the region R02). However, this increase is not certain due to the small significance values (see Figs. 6.18-6.19 (d)). Nevertheless, it is difficult to conclude that the aerosol emissions have been reduced since the aerosol products (i.e., MOD, MIS, SEA, and MYD AOTs) can only be retrieved under the cloud-free conditions, and the aerosols can be scavenged by cloud condensation [Twomey, 1974]. In order to estimate the changes of aerosol loading caused by cloud condensation over these areas, further stduies are needed to present a more direct evidence relating to interactions between atmospheric particulate matter and clouds.

Northern South America

The regions R03, 06, and 07 are selected as being representative for Northern South America where the the world's largest rainforest (i.e. the Amazon rainforest) is located. The rainforest plays an important role for regional and global climate changes [Ahlm et al., 2009; Eltahir and Bras, 1996; Li and Fu, 2004; Nepstad et al., 1999]. During past decades, massive biomass buring aerosols have been emitted due to the indiscriminate deforestation for subsistence agriculture [Davidson and Artaxo, 2004]. Recently, the accelerated deforestation led by Brazil for economic development has been intensified [Kirby et al., 2006]. As shown in Fig. 6.18, a more clear positive sign of weight trends over northern South America is found when compared to linear trends in Fig. 6.15. Nonetheless, increasing trends may be insignificant because of persistent cloudiness and low significance values (see Figs. 6.17 and 6.19). Negative weighted AOT trends in the regions R03 and 06 are dominant (up to -0.00384±0.00198 for the region R03 and -0.00400±0.00190 yr^{-1} for the region 06) while positive in the oceanic region 07 (+0.00278±0.00141 yr^{-1}). Apparently, the major tendency of temporal aerosol decrease can be explained by the decline of fire counts, growth of precipitation [Liebmann et al., 2004; Torres et al., 2010], and cloud nucleation processes [Twomey, 1974]. However, these possible explanations are not sufficient for understanding cloud-free AOT trends because of large and persistent clouds disturbing the aerosol sampling. Therefore, the significant positive trends of MYD AOT in the region 07, where there is less cloud occurences (Fig. 6.17), better reflects the temporal change of aerosol emissions linked to the deforestation.

Southern South America

As with previous research areas, biomass burning from tropical deforestation frequently occurs over the region R04 covering the Atlantic Forest for the various purposes: agricultural

land clearing, pest control, and grassland management [Pereira et al., 2009; Crutzen and Andreae, 1990; Liu et al., 2005; van der Werf et al., 2006]. The negative trends of MOD and MIS AOTs are estimated in the morning (up to -0.00169±0.00060 for linear and -0.00143±0.00062 yr^{-1} for weighted trends) while the positive trends of SEA and MYD AOTs are observed (up to +0.00276±0.00142 for linear and +0.00179±0.00097 yr^{-1} for weighted trends). Considering increased fire activity in the afternoon [Giglio, 2007], the trends of SEA and MYD AOTs are more relevant for investigations of the emission changes of biomas burning aerosol.

European regions

Various types of atmospheric aerosols exist over European regions (the regions R05, R06, 08, and 09). They are the industrial/traffic pollutant caused by human activity [Marmer et al., 2007; Karnieli et al., 2009], the biomass burning aerosol emitted from forest fires [Pace et al., 2006; Tafuro et al., 2008], and the mineral dust transported from northern African deserts [Hatzianastassiou et al., 2009]. Especially, over Russia partially contained in the region R06 (Eastern Europe), a massive emission of smoke aerosols from forest fires and industrial pollutants from urban areas has been reported in many studies [Hayn et al., 2009; Richter et al., 2005; Chubarova et al., 2011a, 2011b; Zhou et al., 2012]. The weighted trends in the OECD Europe region (R05) and oceanic neighborhood regions (08 and 09) are consistently decreasing (maximum intensity: -0.00530±0.00304 for the region R05, -0.00474±0.00258 for the region 08, and -0.00491±0.00252 yr^{-1} for the region 09), which results from the strict environmental regulations [Smith et al., 2001; Streets et al., 2006; Zhao et al., 2008]. Although the aerosol retrieval is limited in the region R06 due to large cloud disturbances and bright snow surface, a significant temporal increase of MYD AOT (+0.00885±0.00443 yr^{-1}) is observed in the afternoon, which is similar to the positive trends of natural aerosols [Streets

et al., 2006] and NOx emissions [Zhou et al., 2012].

Northern Africa and Middle East (Saharan and Arabian deserts)

Mineral dust from the Saharan and Arabian deserts is a dominant type over the region R07 [Reeves et al., 2010; Washington and Todd, 2005; Derimian et al., 2006; Sabbah et al., 2006; Tafuro et al., 2006], where stable and clear-sky weather conditions used to last most of the year [Basart et al., 2009]. Furthermore, fine-mode dominant aerosols emitted from the regional petroleum industry and its transport ships are frequently observed [Zhao et al., 2008; Basart et al., 2009]. Among the selected data sets in this study, only MISR AOTs are available for the trend analysis over these desert regions due to multiple-viewing capability of MISR instrument. Although the negative trend of MIS AOT with small significance (see Figs. 6.18-6.19 (b)) is estimated over northern part of the Sahara deserts, overall weighted trend in the region R07 (mainly in Middle East,) shows a significant increase (+0.00323±0.00150 yr^{-1} for MIS AOT) which is consistent with the weighted trend of AERONET AOT at Solar_Village station shown in Chapter 5. The oceanic regions (11 and 15) near the desert area have similar even stronger weighted trends which range from +0.00312±0.00148 to +0.01116±0.00677 yr^{-1} for the region 11 and from +0.00437±0.00133 to +0.01541±0.00438 yr^{-1} for the region 15. These tendencies can be attributed to a strong increase of coarse-mode dominant aerosols from deserts as well as, especially, fine-mode dominant aerosols from human activity over the Red Sea (transportations through the the Suez Canal connecting the Mediterranean Sea and the Red Sea; the transported freight volume by ship through the Suez Canal increased by 64% during June 2003 to June 2008) [de Ruyter de Wildt et al., 2012] and the Persian Gulf (oil industries near the world's largest single source of crude oil: ~65% of the world's oil reserves) [Sadrinasab and Kämpf, 2004]. In contrast, the mineral dust sensitive to climate changes is dominant over the region 10. The major trends in this area are negative (up

to -0.00580±0.00347 for linear and -0.00664±0.00386 yr^{-1} for weighted trends). The main cause for the negative trends can be about 10% reduction of surface wind speed [Zhao et al., 2011].

Central Africa

The regions R08 and 12 are located in Central Africa affected by mineral dust transported from the Saharan and Sahel regions and biomass burning aerosol emitted from agricultural activity during dry seasons [Reeves et al., 2010; Johnson et al., 2008a]. The desertification and drought caused by climate changes near the Sahel during the last decades [Held et al., 2005; Chung and Ramanathan, 2006] have provided an ideal condition for generating airborne aerosols. Some parts of the selected regions (especially, the region 12) are highly influenced by cloud, so the trend analysis of cloud-free aerosol can be contaminated (see Fig. 6.17). The positive weighted trend prevails over the region R08 (the maximun intensity: +0.00585±0.00320 yr^{-1}) while the weighted trends over the region 12 range from -0.00778±0.00469 to +0.00308±0.00167 yr^{-1}. These indefinite tendencies may be explained by different sampling times and interaction between aerosol and cloud particles.

South Africa

In the regions R09, 13, and 14 of South Africa, fine-mode dominant aerosols are observed, which are biomass burning aerosols in warm/dry seasons and industrial pollutants from fossil fuel burning [Eck et al., 2001, 2003]. Recently, a strong emission of anthropogenic aerosols and gases in the southern part of South Africa has been reported [Fleming and van der Merwe, 2002; Piketh and Walton, 2004; Vakkari et al., 2011]. The MOD and MIS AOTs over the region R09 temporally decrease in the morning (-0.00263±0.00127 for MOD and -0.00025±0.00016 for MIS weighted trends) while SEA and MYD AOTs increase

(+0.00038±0.00020 for SEA +0.00297±0.00169 yr^{-1} for MYD weighted trends) in the afternoon. Taking into account the peak of local emission from fires at mid afternoon [Smirnov et al., 2002], the afternoon samplings are more effective to monitor the temporal changes of biomass burning aerosols. The easterly wind pattern from South Africa [Piketh and Walton, 2004] is a good explanation for all increases (which range from +0.00043±0.00030 to +0.00432±0.00268 yr^{-1} of weighted trends) in the oceanic region 13 located in the western part to the continent. These postive tendencies are consistent with the increases of fine-mode dominant aerosols at AERONET stations Mongu and Skukuza discussed in the previous chapter. In contrast, the oceanic region 14 in the eastern part has somehow unclear weighted trends for each sensor: +0.00165±0.00091 for MOD, -0.00241±0.00137 for MIS, -0.00141±0.00075 for SEA, and +0.00390±0.00192 yr^{-1} for MYD weighted trends respectively.

Central Asia (Asian Deserts)

The region R10 is representative for a wide area in Central Asia, which straddles the Kyzyl Kum, Karakum, Taklamakan, and Gobi deserts. In particular, these deserts are expanding approximately 9% per decade accompanied by reduced precipitation and intensified warming in the 2000s [Jeong et al., 2011]. Accordingly, the influence of mineral dust blown by strong westerly winds from the deserts is growing in Asia. Only MIS AOTs are available over deserts and their linear/weighted trends are +0.00062±0.00036 and +0.00073±0.00043 yr^{-1} respectively, confirming the desertification.

Indian subcontinent (South Asia)

South Asia (the regions R11, 16, and 17) is influenced by various aerosols. These are anthropogenic aerosol from urban area [Kaskaoutis et al., 2011b], biomass burning aerosol

from forest fires [Vadrevu et al., 2011], and coarse-mode dominant aerosol (i.e., mineral dust and maritime aerosol) blown by the summer monsoon from deserts and surrounding oceans [Dey et al., 2004]. Not only rapid economic growth (8.5% GDP growth during 2010 and 2011) but also the second largest population in India (around 1.2 billion) [The Economist, 2010; The World Factbook, 2012] are two major factors contributing a significant enhancement of anthropogenic aerosol emmission in the atmosphere. Their impacts on the climate appear in many ways [Ramanathan et al., 2007a, 2007b; Lawrence and Lelieveld, 2010]. Significant AOT increases are observed at the all research areas in South Asia (the ranges of weighted trends: +0.00313±0.00128 ~ +0.01452±0.00615 for the region R11, +0.00243±0.00130 ~ +0.01274±0.00452 for the region 16, and +0.00346±0.00166 ~ +0.01292±0.00675 yr^{-1} for the region 17), which are in good agreement with the estimations in Streets et al. (2006) and Zhao et al. (2008).

East Asia

The regions R12 and 20 are located in/near China. Chinese economy is the second largest scale after US with approximately 10% of annual growth rates over the past decades [International Monetary Fund (IMF), 2012]. Moreover, China is the world's most populous country (more than 1.35 billion people) [Banister et al., 2010]. As a consequence, large amounts of anthropogenic aerosols are emitted into the atmosphere. Additionally, mineral dust from the expanding Asian deserts is transported by westerly winds [Zhang et al., 2003]. Similar to the AOT trends over South Asia, a significant temporal increase of all AOTs is estimated and their weighted trends range from +0.00342±0.00171 to +0.01939±0.00986 for the region R12 and +0.00476±0.00227 to +0.01794±0.00928 yr^{-1} for the region 20. These positive tendencies have been reported in various studies [Streets et al., 2000, 2003, 2006; Smith et al., 2001, 2003; Massie et al., 2004; Mishchenko and Geogdzhayev, 2007; Zhao et

al., 2008] as well as in the previous chapter (see the results at the AERONET station, Beijing) [Yoon et al., 2012].

Southeast Asia

The Southeast rainforest located in/near the regions R13, 18, and 19 plays an important role as source and sink of atmospheric aerosol particles (e.g., volatile organic compounds and secondary organic aerosols) [Whitehead et al., 2010]. In addition, biomass burning aerosol caused by volcanic activity, lightning, and (mainly) human activity is another dominant type [Taylor, 2010; Giglio et al., 2006a, 2006b]. These particles can potentially influence the cloud properties changing the Earth radiative balance [Facchini et al., 2000; McFiggans et al., 2005, 2006]. Except the negative weighted trend of MIS AOT (-0.00187±0.00113 yr^{-1}), all other AOTs show a positive tendency (+0.00030±0.00017 for MOD, +0.00163±0.00089 for SEA, and +0.00074±0.00046 yr^{-1} for MYD weighted trends). If ignoring less significant trends, the weighted trends can be estimated by SEA (+0.00874±0.00476 yr^{-1}) and MYD AOT trends (+0.00455±0.00218 yr^{-1}) in the regions 18 and 19, respectively. However, it is difficult to identify or conclude a clear trend over these areas because of the aerosol interaction with clouds as well as the aerosol removal by the precipitation [Irwin et al., 2011; Rotstayn and Lohmann, 2002].

Australia

Australian continental aerosol types are smokes from biomass burning in northern Australia and dusts from deserts in Central Australia [Qin and Mitchell, 2009; Giglio et al., 2006a, 2006b]. As already mentioned, only MIS AOTs can be used for the trend analysis in the region R14. The linear and weighted trends of MIS AOT show a decrease of -0.00170±0.00086 and -0.00183±0.00101 yr^{-1}. Given the afternoon peak in fire activity

[Giglio et al., 2006a, 2006b], the weighted trends of smokes can be an ignorable or a slight increase (-0.00053±0.00023 for SEA and +0.00148±0.00094 yr^{-1} for MYD weighted trends). All previous mentioned trends and CFs for regional analysis are listed in Tabs. D.2 and D.3 (Appendix D).

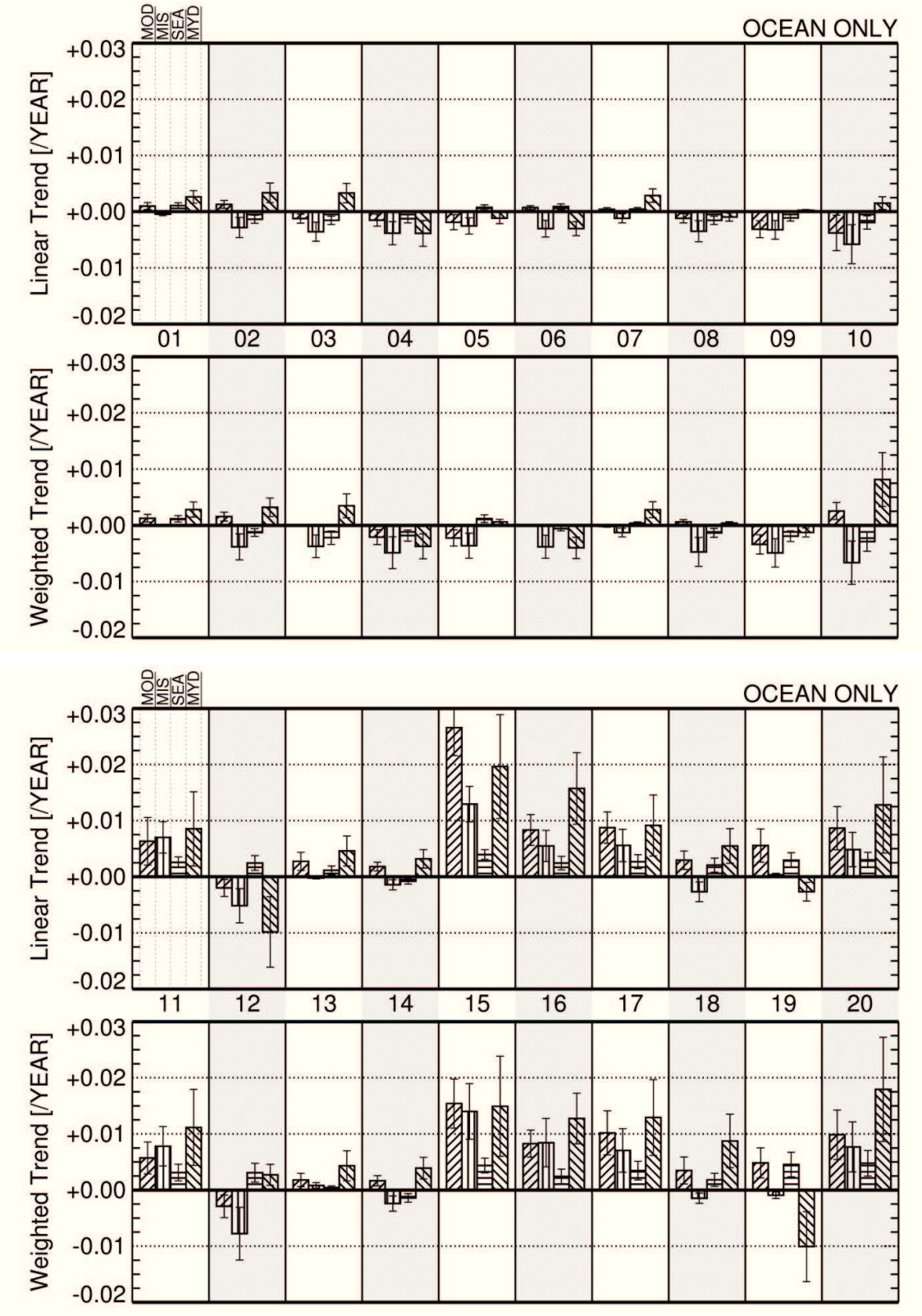

Fig. 6.21 Linear and weighted trends of cloud-free MOD, MIS, SEA, and MYD AOTs and corresponding uncertainty ranges (±σ) for the oceanic regions.

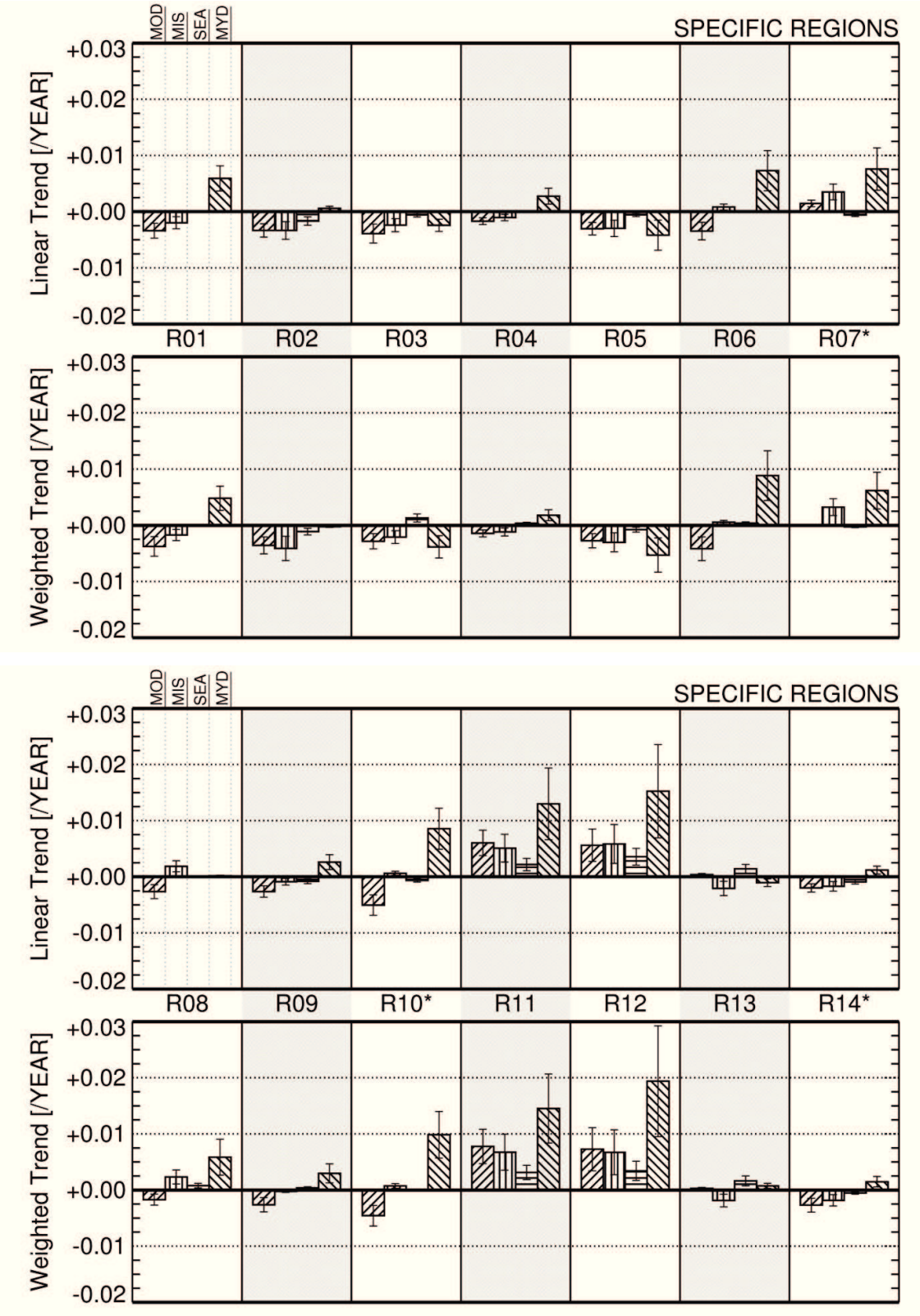

Fig. 6.22 Linear and weighted trends of cloud-free MOD, MIS, SEA, and MYD AOTs and corresponding uncertainty ranges (±σ) for the specific regions covering terrestrial and oceanic areas.

7. Summary and conclusions

The global and regional trends of cloud-free Aerosol Optical Thickness (AOT) have been investigated and analyzed using various satellite- and ground-based observations (i.e., MODIS-Terra (MOD), MISR-Terra (MIS), SeaWiFS-OrbView-2 (SEA), MODIS-Aqua (MYD), and AErosol RObotic NETwork (AERONET)). Using the entirely new approaches to consider large/persistent cloud disturbance all year round and the limited/different sampling of polar orbiting satellites (limited orbital periods and different sampling times), the investigation of aerosol temporal trends has been successfully addressed in this study. For a more accurate and reliable analysis of the global and regional AOT trends, several main key points have been discussed as follows:

a. Accuracy test of aerosol retrieval using satellite observations related to sensor calibration and algorithm performance.
b. Validation of the AOT trends derived from satellite retrievals with AERONET observations.
c. Minimization of the unrepresentative sampling effect caused by cloud disturbance and limited/different sampling.

Main results from this study

- This study provided global AOT retrieved by Bremen AErosol Retrieval (BAER) algorithm using SeaWiFS observations. The BAER retrieval accuracy was verified by comparison with AERONET AOTs: $\pm 0.05 \pm 0.25 \times AOT$.
- There were various uncertainty factors in the trend analysis, which are sensor calibration, aerosol retrieval accuracies, cloud disturbance, and limited/different sampling. However,

only a few previous studies discussed the limitations associated with unrepresentative sampling originating from the large/persistent cloud disturbance and limited/different sampling in polar orbiting satellite observation.

- From the uncertainty test based on more accurate ground-based AERONET AOT with higher temporal resolution, the error caused by unrepresentative sampling (i.e., large/persistent cloud disturbance and limited/different sampling) ranged between -24% to -36% approximately. Therefore, this study attempted to minimize the uncertainty effect of the unrepresentative sampling in the trend analysis of cloud-free AOTs by combining the multiple polar orbiting satellite observations (MOD from 03/2001 to 12/2009, MIS from 03/2001 to 12/2010, SEA from 01/1998 to 12/2007, and MYD from 01/2003 to 12/2008) and a weighted trend model.
- The weighted trends over Eastern US and OECD Europe showed a strong decreasing AOT (up to -0.00376±0.00174 for Eastern US and -0.00530±0.00304 yr^{-1} for OECD Europe) attributed to the recent environmental legislation and resulting regulation of emissions.
- A significant increase was observed over Saharan/Arabian deserts, South, and East Asia (up to +0.00618±0.00326, +0.01452±0.00615, and +0.01939±0.00986 yr^{-1} respectively). These in part dramatic increases are attributed to the amount of aerosol transported/emitted from industrialization, urbanization, deforestation, desertification, and climate change.
- The large and persistent cloud disturbance all year round over oceans remained as an inescapable uncertainty factor in the trend analysis of cloud-free AOTs even using the weighted trend method.

BAER's AOT retrieval Accuracy

Despite of long-term and well-calibrated SeaWiFS observations, it is difficult to investigate the global AOT trends because there was a lack of research on the atmospheric aerosol using radiances observed from SeaWiFS, which was mainly designed to study the ocean color. Therefore, part of this study has used Bremen AErosol Retrieval (BAER) algorithm for retrieving AOTs with SeaWiFS data, and validated them with AERONET AOTs. The main research regions were Europe and South China defined by the CityZen project. BAER retrieval accuracy was verified by comparison with AERONET AOTs, and the uncertainty range of BAER AOT retrieval was confirmed as ±0.05±0.25×AOT [von Hoyningen-Huene et al., 2011], which is comparable to other accuracies of MOD, MIS, and MYD AOTs (see details in Section 4.1). From this accuracy test related to SeaWiFS calibration and BAER performance, it could be concluded that BAER retrieved AOT using SeaWiFS data could contribute to the understanding of global/regional aerosol temporal change. Apparently, some retrieval errors can be reduced by suggestions in Section 3.4 for the refinement of the BAER algorithm in terms of cloud screening, surface reflectance, and a priori database of aerosol optical properties for Look-Up Table (LUT) approach.

Uncertainty factors in cloud-free AOT trend analysis

Many previous publications regarding global and regional AOT trends generally focused on the accuracy tests of satellite retrievals compared to ground-based AOT. As a consequence, they concluded that the temporal trends derived from validated AOTs are relevant. This approach is logical, but without validation of the AOT trend it is difficult to be convinced of the trend accuracy. Therefore, this study attempted to compare the BAER AOT trends with the trends from a better temporal-resolution and more accurate ground-based AERONET AOT. In spite of high accuracy of BAER retrieval, the AOT trends were clearly different in

magnitude due to cloud disturbance. Clouds directly influenced the retrieval accuracy as well as the possible number of satellite retrievals. Especially, the later one could be more serious in the trend analysis based on monthly AOTs because the sample size is crucial for the statistical representativeness of climatological means (e.g. monthly, seasonal, and annual averages). Therefore, the cloud disturbance should be considered in the trend analysis of cloud-free AOT.

The second uncertainty factor in this study was linked to limited orbital periods (roughly, 100 minutes for each orbit) and different sampling times (depending on space platform) of polar orbiting satellites (see Tab. 6.1). The fundamental limitation of polar orbiting satellites (i.e., limited orbital periods and different sampling times) could lead to biased results in the trend analysis. In order to estimate the uncertainty range caused by large/persistent cloud disturbance and limited/different sampling, the present study has tested the uncertainty under the assumption that the satellite retrievals are perfectly matched up with ground-based observations (AERONET) during the overpass times. In other words, using AERONET AOTs, the simple linear trends based on monthly mean of resampled AOTs by the local equatorial crossing times (i.e., 10:30±30 a.m. for Terra, 12:20±30 p.m. for OrbView-2, and 01:30±30 p.m. for Aqua) were compared with the trends derived from all available samplings. As a result, the trend for each sampling time was underestimated by 24% to 36% approximately due to unrepresentative sampling caused by large/persistent cloud disturbance and limited/different sampling (see details in Section 6.2). Therefore, for a more accurate and reliable analysis of global and regional AOT trends, it is necessary to minimize the uncertainty effect of unrepresentative sampling.

Minimization of the uncertainty caused by unrepresentative sampling

In order to minimize the cloud disturbance, this study introduced the weighted least

squares regression in the trend analysis. The weighting factor, key part of this approach, was defined as ratio of the two weights, which are sensitive to cloud occurrence. Applied to AERONET spectral observations, the weighted trend method was tested and thereby produced more reasonable trends at global AERONET stations.

It is nearly impossible to avoid a strong bias from limited/different sampling in satellite-based trend analysis (especially, when using polar orbiting satellites). In particular, this uncertainty effect was amplified over highly populated regions due to a strong diurnal aerosol cycle. Therefore, the present study introduced an alternative approach, which was the integrated trend analysis based on multiple and complementary aerosol products (MOD, MIS, SEA, and MYD AOTs). Although this might be not a perfect solution for the problem of limited/different sampling, it was quite succesful to draw a legitimate conclusion from an integrative analysis of global and regional AOT trends.

Global and regional AOT trends derived from multiple satellite observations

The global and regional AOT trends integrated from various satellite-based observations were analyzed. Due to a large and consistent cloud disturbance in most of the marine areas, the research regions over oceans were selected on the basis of cloudiness and its variability. Only the trends (B_g) for each grid (1° × 1° for MODIS and SeaWiFS or 0.5° × 0.5° for MISR) with significance ($\left|B_g/\sigma_{B_g}\right|$) larger than one were used in the trend analyses of global and regional AOTs. Throughout terrestrial and marine regions, temporal increase of cloud-free AOTs were dominat over the globe (GL), northern (NH), and southern hemisphere (SH) (up to +0.00348±0.00185 for GL, +0.00514±0.00272 for NH, and +0.00232±0.00124 yr^{-1} for SH). Generally, significant decreases of industiral and traffic pollutants were observed in Eastern US and OECD Europe (up to -0.00376±0.00174 for Eastern US and -0.00530±0.00304 yr^{-1}

for OECD Europe) due to the strict environmental regulations, while temporal increases of anthropogenic and natural aerosols prevailed in Saharan/Arabian deserts, South, and East Asia (up to +0.00618±0.00326, +0.01452±0.00615, and +0.01939±0.00986 yr^{-1} respectively) because of the enhanced emission of aerosol amount transported/emitted from industrialization, urbanization, deforestation, desertification, and climate change.

Further studies and open questions

In this study the global distribution and temporal variation of atmospheric aerosols have been discussed, which is an important contribution to the ongoing research on air quality associated with human health as well as aerosol's direct/indirect effects on the Earth radiative balance related to climate change. However, although several new attempts in this study were clearly effective to minimize the uncertainty in the trend analysis, they could not completely eliminate the fundamental limitations. First and foremost, the satellite retrievals should be refined and improved as suggested in Section 5.3 including additional considerations of the unidentified systematic and random errors caused by e.g., platform operating status and sensor calibration status. Furthermore, an intergrated analysis of independent aerosol and cloud data sets from a better sampling (i.e., various satellite-, ground-based, and in-situ observations) is needed to inter-compare the results estimated by modelling, and thereby can contribute to understanding of the effect of interaction between clouds and atmospheric aerosols in the trend analysis, which could not be covered in this study.

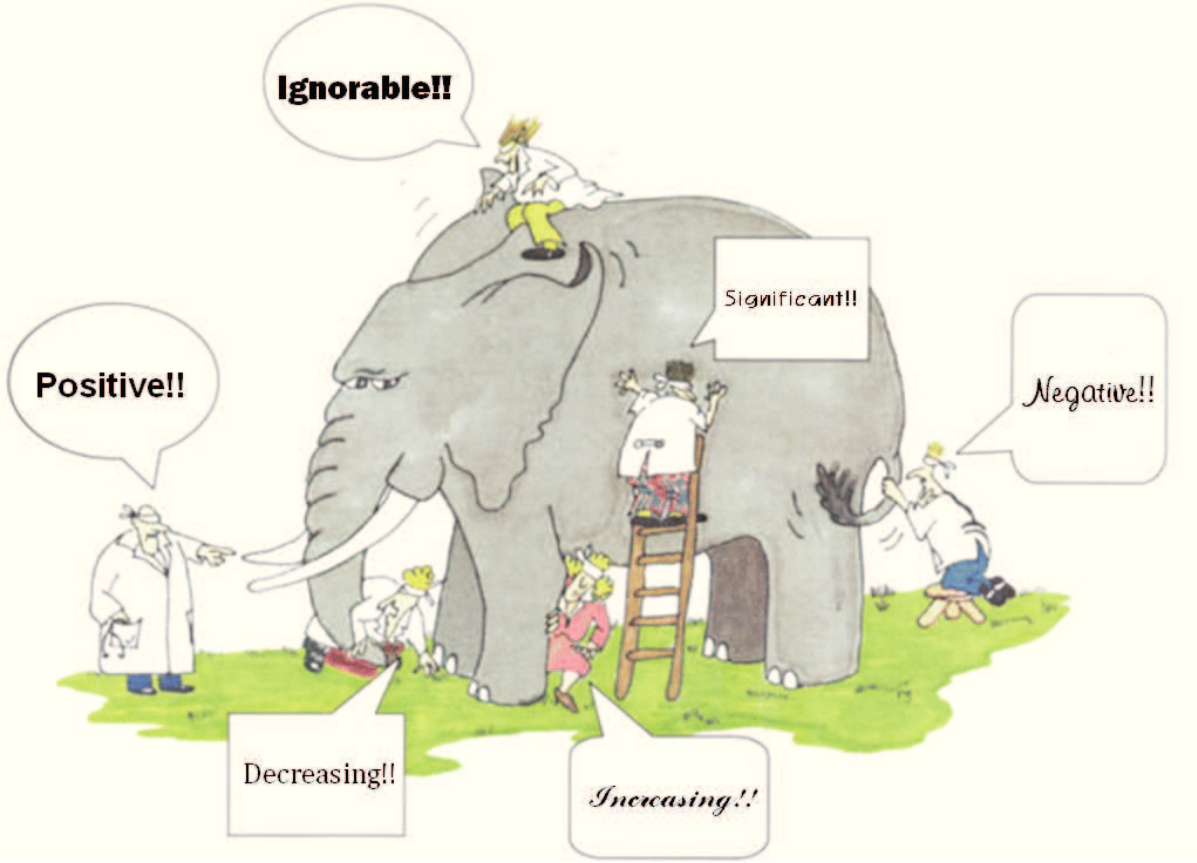

Fig. 7.1 The blind men and the elephant [http://www.nature.com]. It explains that the trend analysis based on limited data by unrepresentative sampling can lead to different conclusions with large errors.

Appendices

Appendix A: Abbreviations used in the dissertation

ACE-2	Aerosol Characterization Experiment-2
ÅE	Ångström Exponent
ÅED	Ångström Exponent Difference
AERONET	AErosol RObotic NETwork
AOT	Aerosol Optical Thickness
ATSR	Along Track Scanning Radiometer
AVHRR	Advanced Very High Resolution Radiometer
AVIRIS	Airborne Visible/Infrared Imaging Spectrometer
BAER	Bremen AErosol Retrieval
BeNeLux	Belgium/Netherlands/Luxemburg
BRDF	Bi-directional Reflection Distribution Function
BRICs	Brazil, Russia, India, and China
BRICS	Brazil, Russia, India, China, and South Africa
CAOT	Coarse-mode dominant Aerosol Optical Thickness
CF	Cloud Fraction
CGAS-F15	Component Global Aerosol Product version F15
CityZen	megaCity-Zoom for the environment
CTM	Chemical Transport Model
ENSO	El Niño/La Niña-Southern Oscillation
FAOT	Fine-mode dominant Aerosol Optical Thickness
GAC	Global-Area Coverage
GACP	Global Aerosol Climatology Project
GCM	General Circulation Model
GCOS	Global Climate Observing System
GDP	Gross Domestic Product
GL	GLobe
GMI	Global Modelling Initiative
GOCART	Goddard Chemistry Aerosol Radiation and Transport
GOME	Global Ozone Monitoring Experiment
IMF	International Monetary Fund
IOCCG	International Ocean-Colour Coordinating Group
IPCC	Intergovernmental Panel on Climate Change
LAC	Local-Area Coverage

LACE-98	Lindenberg Aerosol Characterization Experiment-98
LUT	Look-Up Table
MERIS	Medium Resolution Imaging Spectrometer
MIS	MISR-Terra
MISR	Multi-angle Imaging SpectroRadiometer
MOD	MODIS-Terra
MODIS	Moderate Resolution Imaging Spectroradiometer
MYD	MODIS-Aqua
NDPI	Normalized Differential Pigment Index
NDVI	Normalized Differential Vegetation Index
NH	North Hemisphere
NIC	Newly Industrializing Countries
OECD	Organization for Economic Co-operation and Development
OMI	Ozone Monitoring Instrument
OPAC	Optical Properties of Aerosols and Clouds
PATMOS	Pathfinder Atmosphere
PM	Particulate Matter
RMSD	Relative Root-Mean-Square Difference
ROT	Rayleigh Optical Thickness
RPV	Raman-Pinty-Verstraete model
RTM	Radiative Transfer Model
SAGE	Stratospheric Aerosol and Gas Experiment
SAMUM	Saharan Mineral Dust Experiment
SCIAMACHY	Scanning Imaging Absorption Spectrometer for Atmospheric CHartographY
SEA	SeaWiFS-OrbView-2
SeaWiFS	Sea-viewing Wide Field-of-view Sensor
SH	South Hemisphere
SSA	Single Scattering Albedo
STD	STandard Deviation
TOA	Top Of Atmosphere
TOMS	Total Ozone Mapping Spectrometer
TSP	Total Suspended Particulate
UNECE	United Nations Economic Commission for Europe
UNFCCC	United Nations Framework Convention on Climate Change
WHO	World Health Organization

Appendix B: Description of aerosol optical parameters

Most contents in Appendix B are cited from the book edited by Burrows et al. (2011) and the AERONET document about inversion products [http://aeronet.gsfc.nasa.gov/].

The incoming light beam to a medium containing aerosol is scattered or absorbed by the particles. This is described by the Beer-Lambert-Bouguer law:

$$I(\lambda) = I_0(\lambda)\exp\left(-\int_0^h b_{ext}(\lambda)dz\right) = I_0(\lambda)\exp\left(-\delta(\lambda)\right), \quad (B.1)$$

where I_0 and I denote the intensities of the incident and the transmitted light beams, b_{ext} is the aerosol extinction coefficient, and δ represents the optical thickness at wavelength (λ). The extinction coefficient ($b_{ext} = b_{scat} + b_{abs}$) is the sum of scattering and absorption coefficients (b_{scat} and b_{abs}). These coefficients depend on aerosol number size distribution ($n(r)$) and extiction/scattering/absorption efficiencies ($Q_{ext/scat/abs}(r, m, \lambda)$). The scattering coefficient is defined as following

$$b_{scat}(\lambda) = \int_{r_1}^{r_2} \pi r^2 n(r) Q_{scat}(r, m, \lambda) dr. \quad (B.2)$$

The scattering efficiency ($Q_{scat}(r, m, \lambda)$) for a particle having a radius (r) and complex refractive index ($m = n - ik$) at wavelength (λ), is given by:

$$Q_{scat}(r, m, \lambda) = C_{scat}(r, m, \lambda)/A(r), \quad (B.3)$$

where $C_{scat}(r, m, \lambda)$ is the scattering cross section and $A(r)$ is the geometric area of the particle. Absorption coeffieicent and efficiency are expressed in a similar way. The SSA ($\omega(\lambda)$) is defined as the ratio of scattering to extinction efficiency:

$$\omega(r, m, \lambda) = \frac{Q_{scat}(r,m,\lambda)}{Q_{ext}(r,m,\lambda)} = 1 - \frac{Q_{abs}(r,m,\lambda)}{Q_{ext}(r,m,\lambda)} \quad (B.4)$$

The extinction cross section and efficiency are the sums of scattering and absorption parameters, which are given by:

$$C_{ext}(r, m, \lambda) = C_{scat}(r, m, \lambda) + C_{abs}(r, m, \lambda) \quad (B.5)$$

$$\text{and } Q_{ext}(r, m, \lambda) = Q_{scat}(r, m, \lambda) + Q_{abs}(r, m, \lambda) \quad (B.6)$$

Based on these parameters, AOT (δ_{Aer}) indicating aerosol optical amount is defined as following:

$$\delta_{Aer}(\lambda) = \int_0^h b_{ext}(\lambda)dz. \quad (B.7)$$

The spectral dependence of AOTs with wavelength is often shown as ÅE (α), which is a good indicator of mean particle size.

$$\frac{\delta_{aer}(\lambda 1)}{\delta_{aer}(\lambda 2)} = \left(\frac{\lambda 1}{\lambda 2}\right)^{-\alpha} \tag{B.8}$$

In presenting the aerosol size distribution, the volume size distiribution, produced by AERONET inversion process, is assumed as log-normal distribution, which can be converted to the number size distribution as following

$$\frac{dV(r)}{d\ln r} = \frac{C_{fine}}{\sqrt{2\pi}\sigma_{fine}} \exp\left[-\frac{(\ln r - \ln r_{fine})}{2\sigma_{fine}^2}\right] + \frac{C_{coarse}}{\sqrt{2\pi}\sigma_{coarse}} \exp\left[-\frac{(\ln r - \ln r_{coarse})}{2\sigma_{coarse}^2}\right]$$

$$= V(r)\frac{dN(r)}{d\ln r} = V(r) r \frac{dN(r)}{dr}, \tag{B.9}$$

where $V(r)$ symbolizes the volume size distiribution, $N(r)$ is the number size distribution, $C_{total,fine,coarse}$ represents the particle volume concentration for total, fine and coarse aerosol modes ($\mu m^3/\mu m^2$), $r_{fine,coarse}$ is the median or geometric mean radius (μm), and $\sigma_{fine,coarse}$ is the variance or width of each mode. Another important parameter for the retrieval of aerosol properties from satellite observations is the angular distribution of the light scattering intensity ($F(\theta, x, m, \lambda)$). It is described by the phase function ($P(\theta, x, m, \lambda)$) defined as following:

$$P(\theta, x, m, \lambda) = 2\,F(\theta, x, m, \lambda) \Big/ \int_0^{\pi} F(\theta, x, m, \lambda) \sin\theta\, d\theta \tag{B.10}$$

$$\text{or } \frac{1}{2}\int_0^{\pi} P(\theta) \sin\theta\, d\theta = 1 \tag{B.11}$$

where θ is the scattering angle and x ($= \frac{2\pi r}{\lambda}$) is the size parameter.

Appendix C: Validations of AOT trends derived from various satellites

Tab. C.1 Linear and weighted trends of AERONET (AER) and MODIS-Terra (MOD) AOTs as shown in Fig. 6.12(a).

AERONET Stations	Validation Periods	Linear Trends ±1σ [/year]		Relative Percent Difference [%]	Weighted Trends ±1σ [/year]		Relative Percent Difference [%]
		AER AOT (550 nm)	MOD AOT (550 nm)		AER AOT (550 nm)	MOD AOT (550 nm)	
Alta_Floresta	2001~2004	+0.00159±0.01126	+0.01886±0.01868	+1083.06	+0.01906±0.02261	+0.01694±0.08579	-11.13
Avignon	2003~2005	-0.01555±0.00462	-0.02128±0.00572	+36.78	-0.02259±0.00568	-0.01658±0.00713	-26.59
Beijing	2004~2007	+0.03216±0.02148	+0.04506±0.01633	+40.12	+0.04707±0.02404	+0.03162±0.01385	-32.84
BONDVILLE	2002~2006	-0.01966±0.00649	-0.01322±0.00471	-32.78	-0.01743±0.00402	-0.00707±0.00546	-59.46
Capo_Verde	2005~2008	+0.00765±0.01163	+0.00790±0.01678	+3.32	-0.00701±0.00937	-0.01227±0.02465	+75.08
CEILAP-BA	2000~2007	-0.00294±0.00104	-0.00439±0.00226	+49.13	-0.00217±0.00107	-0.00571±0.00175	+162.68
El_Arenosillo	2002~2005	-0.00438±0.00377	-0.00659±0.00414	+50.50	-0.00874±0.00545	-0.00433±0.00623	-50.44
GSFC	2000~2008	-0.00241±0.00176	-0.00539±0.00229	+123.48	-0.00297±0.00212	-0.01025±0.00496	+245.65
Ispra	2001~2007	-0.00496±0.00450	-0.00617±0.00470	+24.26	-0.01177±0.00492	-0.01146±0.00827	-2.66
Kanpur	2001~2006	-0.00255±0.00827	-0.00872±0.01174	+242.52	-0.00233±0.01038	+0.00367±0.00736	-257.27
La_Parguera	2006~2009	-0.00879±0.00181	-0.00646±0.00287	-26.50	-0.00844±0.00163	-0.00451±0.00280	-46.58
Mauna_Loa	2000~2009	+0.00036±0.00012	-0.00305±0.00074	-943.37	+0.00042±0.00020	-0.00272±0.00078	-751.80
MD_Science_Center	2000~2006	-0.00225±0.00250	-0.00655±0.00128	+191.55	-0.00364±0.00250	-0.00675±0.00100	+85.34
Mongu	2000~2008	-0.00068±0.00196	-0.00347±0.00220	+409.25	+0.00078±0.00257	-0.00443±0.00363	-664.20
Shirahama	2002~2009	+0.00119±0.00255	+0.00106±0.00208	-11.33	-0.00131±0.00307	+0.00165±0.00261	-225.84
Skukuza	2001~2007	-0.00462±0.00276	-0.00656±0.00255	+42.08	-0.00127±0.00464	-0.00288±0.00207	+127.13
Venise	2000~2005	-0.00288±0.00325	-0.00761±0.00350	+164.36	-0.00827±0.00559	-0.01056±0.00451	+27.69

Tab. C.2 As in Tab. C.1, but AERONET (AER) and MISR-Terra (MIS) AOTs as shown in Fig. 6.12(b).

AERONET Stations	Validation Periods	Linear Trends ±1σ [/year]		Relative Percent Difference [%]	Weighted Trends ±1σ [/year]		Relative Percent Difference [%]
		AER AOT (550 nm)	MIS AOT (558 nm)		AER AOT (550 nm)	MIS AOT (558 nm)	
Avignon	2003~2005	-0.01555±0.00470	+0.00162±0.00684	-110.43	-0.02259±0.00559	+0.01484±0.01016	-165.71
Banizoumbou	2003~2008	+0.00235±0.00986	-0.00165±0.00795	-169.98	-0.01356±0.01440	+0.00258±0.01259	-119.05
Beijing	2004~2007	+0.03216±0.02118	+0.01826±0.01350	-43.20	+0.04707±0.02397	+0.02679±0.01775	-43.08
BONDVILLE	2002~2006	-0.01966±0.00650	+0.00197±0.00604	-109.99	-0.01743±0.00406	+0.01011±0.00787	-158.01
Capo_Verde	2005~2008	+0.00765±0.01173	-0.00220±0.01330	-128.73	-0.00701±0.00932	-0.03278±0.02460	+367.94
Dakar	2004~2007	+0.00032±0.01316	+0.00326±0.01124	+923.90	-0.01813±0.01435	-0.00320±0.01364	-82.37
Dalanzadgad	2000~2004	-0.00152±0.00247	+0.00329±0.00347	-316.81	-0.00165±0.00337	+0.00180±0.00236	-208.89
El_Arenosillo	2002~2005	-0.00438±0.00381	+0.00105±0.00480	-124.05	-0.00874±0.00568	-0.00148±0.00606	-83.05
GSFC	2000~2008	-0.00241±0.00181	-0.00497±0.00250	+106.10	-0.00297±0.00213	-0.00764±0.00481	+157.62
Ispra	2001~2007	-0.00496±0.00440	+0.00132±0.00675	-126.70	-0.01177±0.00492	-0.00157±0.01755	-86.68
Kanpur	2001~2006	-0.00255±0.00810	-0.00691±0.00688	+171.22	-0.00233±0.01025	+0.00306±0.00649	-231.08
La_Parguera	2006~2009	-0.00879±0.00180	-0.00913±0.00429	+3.79	-0.00844±0.00162	+0.00094±0.00546	-111.20
Mauna_Loa	2000~2009	+0.00036±0.00013	+0.00139±0.00104	+284.81	+0.00042±0.00020	+0.00159±0.00124	+281.06
MD_Science_Center	2000~2006	-0.00225±0.00248	-0.00564±0.00429	+150.89	-0.00364±0.00250	-0.01046±0.00615	+186.99
Mongu	2000~2008	-0.00068±0.00191	-0.00229±0.00267	+235.83	+0.00078±0.00254	-0.00900±0.00398	-1246.24
Ouagadougou	2000~2004	+0.02895±0.01417	+0.01460±0.01108	-49.57	+0.01354±0.01874	+0.01136±0.01815	-16.07
SEDE_BOKER	2004~2008	+0.00039±0.00336	+0.00443±0.00341	+1027.23	-0.00213±0.00404	+0.00020±0.00458	-109.49
Shirahama	2002~2009	+0.00119±0.00251	+0.00815±0.00509	+584.06	-0.00131±0.00309	+0.00681±0.00692	-620.34
Skukuza	2001~2007	-0.00462±0.00282	-0.00785±0.00379	+69.85	-0.00127±0.00462	-0.00358±0.00538	+182.18
Solar_Village	2001~2007	+0.01965±0.00333	+0.01243±0.00341	-36.75	+0.01898±0.00543	+0.00445±0.00397	-76.57

Tab. C.3 As in Tab. C.1, but AERONET (AER) and SeaWiFS-OrbView-2 (SEA) AOTs as shown in Fig. 6.12(c).

AERONET Stations	Validation Periods	Linear Trends ±1σ [/year]		Relative Percent Difference [%]	Weighted Trends ±1σ [/year]		Relative Percent Difference [%]
		AER AOT (510 nm)	SEA AOT (510 nm)		AER AOT (510 nm)	SEA AOT (510 nm)	
Alta_Floresta	2001~2004	+0.00147±0.01302	+0.00862±0.00589	+487.93	+0.01843±0.02361	+0.00266±0.00969	-85.56
Avignon	2003~2005	-0.01601±0.00508	-0.00793±0.00402	-50.47	-0.02342±0.00613	-0.00997±0.00463	-57.42
Beijing	2004~2007	+0.03511±0.02247	+0.00809±0.00562	-76.95	+0.04914±0.02609	+0.02362±0.01124	-51.94
BONDVILLE	2002~2006	-0.02031±0.00691	+0.00351±0.00166	-117.30	-0.01767±0.00477	+0.00173±0.00317	-109.77
Capo_Verde	2005~2007	+0.00378±0.01587	+0.00536±0.00502	+41.84	-0.00337±0.01363	+0.00948±0.00347	-381.44
CEILAP-BA	2000~2007	-0.00305±0.00114	+0.00015±0.00076	-104.88	-0.00212±0.00115	-0.00050±0.00116	-76.26
El_Arenosillo	2002~2005	-0.00392±0.00414	-0.00018±0.00159	-95.48	-0.00924±0.00722	-0.00251±0.00214	-72.81
GSFC	1998~2007	+0.00080±0.00142	-0.00008±0.00081	-110.01	+0.00138±0.00159	+0.00046±0.00130	-66.30
Ispra	2001~2007	-0.00525±0.00500	+0.00176±0.00164	-133.54	-0.01342±0.00536	-0.00180±0.00261	-86.58
Kanpur	2001~2006	-0.00160±0.00840	+0.00239±0.00268	-249.47	-0.00942±0.00939	-0.00280±0.00187	-70.29
Mauna_Loa	1998~2009	-0.00007±0.00015	-0.00113±0.00050	+1618.18	+0.00015±0.00023	-0.00038±0.00057	-355.10
MD_Science_Center	2000~2006	-0.00258±0.00278	+0.00058±0.00143	-122.51	-0.00401±0.00269	-0.00077±0.00187	-80.72
Mongu	1999~2007	+0.00078±0.00205	+0.00112±0.00078	+43.65	+0.00527±0.00312	+0.00228±0.00072	-56.85
Shirahama	2002~2007	+0.00903±0.00427	+0.00174±0.00199	-80.72	+0.00614±0.00511	-0.00301±0.00380	-149.07
Skukuza	2001~2007	-0.00480±0.00318	-0.00184±0.00169	-61.67	-0.00171±0.00533	-0.00021±0.00225	-87.84
Venise	2000~2005	-0.00318±0.00360	-0.00015±0.00190	-95.19	-0.00923±0.00612	-0.00076±0.00276	-91.73

Tab. C.4 As in Tab. C.1, but AERONET (AER) and MODIS-Aqua (MYD) AOTs as shown in Fig. 6.12(d).

AERONET Stations	Validation Periods	Linear Trends ±1σ [/year]		Relative Percent Difference [%]	Weighted Trends ±1σ [/year]		Relative Percent Difference [%]
		AER AOT (550 nm)	MYD AOT (550 nm)		AER AOT (550 nm)	MYD AOT (550 nm)	
Avignon	2003~2005	-0.01555±0.00469	-0.01412±0.00623	-9.21	-0.02259±0.00573	-0.01052±0.01022	-53.44
Beijing	2004~2007	+0.03216±0.02120	+0.03331±0.01595	+3.59	+0.04707±0.02414	+0.04381±0.02280	-6.94
BONDVILLE	2003~2006	-0.00201±0.00411	+0.00106±0.00653	-152.59	-0.00901±0.00669	+0.01329±0.01157	-247.50
Capo_Verde	2005~2008	+0.00765±0.01158	-0.00001±0.02014	-100.10	-0.00701±0.00931	-0.01297±0.01869	+85.11
CEILAP-BA	2003~2007	-0.00219±0.00166	+0.00756±0.00698	-446.09	+0.00020±0.00205	+0.00033±0.00408	+65.66
El_Arenosillo	2003~2005	-0.00818±0.00534	-0.00663±0.00487	-18.85	-0.01659±0.01014	-0.01120±0.00759	-32.51
GSFC	2003~2008	-0.00516±0.00321	-0.00224±0.00334	-56.66	-0.00876±0.00387	-0.01289±0.00969	+47.17
Ispra	2003~2007	-0.01082±0.00668	-0.00631±0.00540	-41.67	-0.01677±0.00820	+0.00766±0.01296	-145.68
Kanpur	2003~2006	-0.01541±0.01657	-0.02262±0.01499	+46.81	-0.00504±0.02455	-0.04097±0.02169	+712.55
La_Parguera	2006~2008	-0.00974±0.00340	-0.00552±0.00573	-43.28	-0.00973±0.00362	-0.00883±0.00892	-9.32
Mauna_Loa	2003~2008	+0.00037±0.00018	+0.00709±0.00134	+1821.95	+0.00061±0.00029	+0.00866±0.00155	+1331.07
MD_Science_Center	2003~2006	-0.00879±0.00546	+0.00846±0.00272	-196.24	-0.01137±0.00395	+0.00838±0.00268	-173.72
Mongu	2003~2008	-0.00121±0.00219	+0.00292±0.00316	-341.25	+0.00115±0.00347	+0.00415±0.00729	+262.16
Shirahama	2003~2008	+0.00626±0.00359	+0.00430±0.00322	-31.31	+0.00299±0.00450	+0.00561±0.00276	+87.21
Skukuza	2003~2007	-0.00304±0.00358	+0.00511±0.00347	-268.36	+0.00340±0.00660	-0.00063±0.00300	-118.57
Venise	2003~2005	+0.00096±0.00727	+0.00026±0.00907	-72.91	-0.02096±0.00882	-0.00639±0.00876	-69.53

Appendix D: Linear and weighted trends of cloud-free MOD (550 nm), MIS (558nm), SEA (510 nm), and MYD (550 nm) AOTs

Tab. D.1 Linear and weighted trends of cloud-free MOD, MIS, SEA, and MYD AOTs, Cloud Fraction (CF), and corresponding uncertainty ranges (±σ) for GL, NH, and SH.

Regions	Linear Trends ± STD [/year]				Weighted Trends ± STD [/year]				MOD CF	MYD CF
	MOD	MIS	SEA	MYD	MOD	MIS	SEA	MYD	± STD	± STD
Ocean Only										
NH	+0.00205±0.00103	-0.00068±0.00039	+0.00019±0.00010	+0.00382±0.00191	+0.00230±0.00121	-0.00060±0.00035	+0.00034±0.00019	+0.00457±0.00249	0.74±0.12	0.73±0.13
SH	+0.00097±0.00056	-0.00136±0.00083	+0.00087±0.00047	+0.00267±0.00131	+0.00083±0.00048	-0.00125±0.00075	+0.00092±0.00052	+0.00252±0.00135	0.78±0.08	0.76±0.08
GL	+0.00145±0.00078	-0.00107±0.00064	+0.00058±0.00032	+0.00306±0.00151	+0.00148±0.00082	-0.00098±0.00058	+0.00068±0.00038	+0.00325±0.00175	0.76±0.10	0.74±0.10
Land Only										
NH	-0.00290±0.00110	+0.00205±0.00100	+0.00014±0.00006	+0.00627±0.00300	-0.00233±0.00103	+0.00244±0.00127	+0.00066±0.00033	+0.00674±0.00331	0.58±0.15	0.61±0.15
SH	-0.00400±0.00135	-0.00099±0.00053	-0.00067±0.00030	+0.00055±0.00025	-0.00369±0.00153	-0.00082±0.00047	+0.00031±0.00015	-0.00080±0.00043	0.43±0.18	0.48±0.19
GL	-0.00323±0.00118	+0.00143±0.00071	-0.00017±0.00008	+0.00474±0.00224	-0.00272±0.00118	+0.00176±0.00093	+0.00052±0.00025	+0.00485±0.00243	0.52±0.16	0.56±0.17
Land and Ocean										
NH	+0.00070±0.00032	+0.00041±0.00022	+0.00017±0.00009	+0.00446±0.00221	+0.00108±0.00054	+0.00058±0.00033	+0.00047±0.00025	+0.00514±0.00272	0.67±0.13	0.68±0.14
SH	+0.00041±0.00022	-0.00132±0.00079	+0.00053±0.00028	+0.00254±0.00124	+0.00037±0.00021	-0.00121±0.00072	+0.00077±0.00042	+0.00232±0.00124	0.67±0.11	0.67±0.12
GL	+0.00055±0.00027	-0.00041±0.00023	+0.00036±0.00018	+0.00330±0.00162	+0.00072±0.00038	-0.00029±0.00017	+0.00063±0.00034	+0.00348±0.00185	0.67±0.12	0.68±0.13

Tab. D.2 As in Tab. D.1, but for the oceanic regions.

Regions	Linear Trends ± STD [/year]				Weighted Trends ± STD [/year]				MOD CF ± STD	MYD CF ± STD
	MOD	MIS	SEA	MYD	MOD	MIS	SEA	MYD		
01	+0.00101±0.00060	-0.00043±0.00028	+0.00108±0.00051	+0.00263±0.00113	+0.00126±0.00068	-0.00006±0.00004	+0.00116±0.00057	+0.00281±0.00134	0.45±0.10	0.45±0.09
02	+0.00129±0.00069	-0.00282±0.00178	-0.00135±0.00071	+0.00336±0.00174	+0.00155±0.00079	-0.00383±0.00230	-0.00129±0.00068	+0.00320±0.00165	0.68±0.12	0.64±0.12
03	-0.00124±0.00080	-0.00357±0.00169	-0.00154±0.00075	+0.00331±0.00174	+0.00005±0.00003	-0.00373±0.00202	-0.00220±0.00119	+0.00349±0.00212	0.58±0.11	0.58±0.11
04	-0.00151±0.00106	-0.00383±0.00206	-0.00125±0.00073	-0.00386±0.00230	-0.00210±0.00132	-0.00488±0.00284	-0.00182±0.00099	-0.00373±0.00221	0.71±0.11	0.70±0.12
05	-0.00188±0.00133	-0.00255±0.00144	+0.00076±0.00045	-0.00115±0.00099	-0.00225±0.00145	-0.00363±0.00222	+0.00119±0.00069	+0.00061±0.00046	0.62±0.13	0.61±0.15
06	+0.00073±0.00032	-0.00302±0.00147	+0.00090±0.00049	-0.00302±0.00124	+0.00000±0.00000	-0.00383±0.00204	-0.00059±0.00040	-0.00400±0.00190	0.78±0.16	0.72±0.18
07	+0.00041±0.00029	-0.00118±0.00081	+0.00044±0.00028	+0.00286±0.00120	-0.00020±0.00013	-0.00129±0.00077	+0.00038±0.00023	+0.00278±0.00141	0.52±0.09	0.51±0.10
08	-0.00118±0.00082	-0.00347±0.00188	-0.00154±0.00075	-0.00096±0.00073	+0.00060±0.00040	-0.00474±0.00258	-0.00134±0.00078	+0.00038±0.00026	0.71±0.10	0.69±0.11
09	-0.00313±0.00150	-0.00323±0.00167	-0.00110±0.00057	+0.00024±0.00014	-0.00339±0.00171	-0.00491±0.00252	-0.00193±0.00095	-0.00128±0.00078	0.46±0.19	0.45±0.20
10	-0.00379±0.00316	-0.00580±0.00347	-0.00193±0.00120	+0.00152±0.00113	+0.00254±0.00151	-0.00664±0.00386	-0.00289±0.00173	+0.00814±0.00481	0.65±0.13	0.61±0.13
11	+0.00633±0.00424	+0.00702±0.00280	+0.00257±0.00096	+0.00854±0.00661	+0.00572±0.00283	+0.00781±0.00352	+0.00312±0.00148	+0.01116±0.00677	0.50±0.15	0.44±0.16
12	-0.00199±0.00153	-0.00515±0.00305	+0.00246±0.00131	-0.00983±0.00628	-0.00290±0.00202	-0.00778±0.00469	+0.00308±0.00167	+0.00271±0.00186	0.85±0.08	0.83±0.09
13	+0.00275±0.00161	-0.00023±0.00014	+0.00116±0.00077	+0.00460±0.00267	+0.00180±0.00119	+0.00081±0.00051	+0.00043±0.00030	+0.00432±0.00268	0.77±0.11	0.69±0.12
14	+0.00182±0.00078	-0.00143±0.00091	-0.00079±0.00050	+0.00319±0.00165	+0.00165±0.00091	-0.00241±0.00137	-0.00141±0.00075	+0.00390±0.00192	0.43±0.14	0.42±0.15
15	+0.02658±0.00500	+0.01295±0.00316	+0.00397±0.00085	+0.01966±0.00925	+0.01541±0.00438	+0.01401±0.00496	+0.00437±0.00133	+0.01493±0.00892	0.43±0.17	0.42±0.16
16	+0.00834±0.00275	+0.00550±0.00278	+0.00244±0.00120	+0.01574±0.00639	+0.00827±0.00241	+0.00844±0.00431	+0.00243±0.00130	+0.01274±0.00452	0.56±0.25	0.55±0.27
17	+0.00876±0.00279	+0.00558±0.00288	+0.00269±0.00124	+0.00914±0.00543	+0.01019±0.00393	+0.00705±0.00388	+0.00346±0.00166	+0.01292±0.00675	0.70±0.23	0.68±0.25
18	+0.00296±0.00164	-0.00267±0.00176	+0.00207±0.00125	+0.00550±0.00308	+0.00349±0.00240	-0.00146±0.00091	+0.00182±0.00115	+0.00874±0.00476	0.84±0.09	0.84±0.09
19	+0.00557±0.00297	+0.00036±0.00025	+0.00297±0.00132	-0.00265±0.00167	+0.00484±0.00269	-0.00092±0.00057	+0.00455±0.00218	-0.01007±0.00624	0.74±0.13	0.73±0.14
20	+0.00866±0.00386	+0.00485±0.00306	+0.00302±0.00134	+0.01280±0.00857	+0.00985±0.00441	+0.00768±0.00447	+0.00476±0.00227	+0.01794±0.00928	0.69±0.11	0.69±0.11

Tab. D.3 As in Tab. D.1, but for the specific regions covering terrestrial and oceanic areas.

Regions	Linear Trends ± STD [/year]				Weighted Trends ± STD [/year]				MOD CF ± STD	MYD CF ± STD
	MOD	MIS	SEA	MYD	MOD	MIS	SEA	MYD		
R01	-0.00339±0.00133	-0.00197±0.00108	-0.00011±0.00005	+0.00592±0.00224	-0.00376±0.00174	-0.00172±0.00100	+0.00001±0.00000	+0.00481±0.00215	0.57±0.15	0.59±0.15
R02	-0.00334±0.00119	-0.00335±0.00157	-0.00167±0.00075	+0.00060±0.00037	-0.00357±0.00151	-0.00412±0.00217	-0.00112±0.00058	-0.00023±0.00014	0.55±0.14	0.56±0.15
R03	-0.00389±0.00168	-0.00241±0.00116	-0.00058±0.00036	-0.00242±0.00109	-0.00284±0.00136	-0.00209±0.00114	+0.00131±0.00071	-0.00384±0.00198	0.67±0.20	0.69±0.18
R04	-0.00169±0.00060	-0.00104±0.00058	+0.00003±0.00001	+0.00276±0.00142	-0.00143±0.00062	-0.00119±0.00070	+0.00037±0.00018	+0.00179±0.00097	0.55±0.13	0.55±0.13
R05	-0.00304±0.00112	-0.00296±0.00147	-0.00055±0.00031	-0.00418±0.00269	-0.00274±0.00126	-0.00303±0.00169	-0.00077±0.00044	-0.00530±0.00304	0.68±0.12	0.68±0.12
R06	-0.00346±0.00155	+0.00083±0.00054	+0.00013±0.00008	+0.00730±0.00358	-0.00416±0.00211	+0.00055±0.00032	+0.00039±0.00022	+0.00885±0.00443	0.68±0.16	0.71±0.15
R07	+0.00146±0.00058	+0.00351±0.00142	-0.00061±0.00026	+0.00758±0.00377	+0.00001±0.00000	+0.00323±0.00150	-0.00027±0.00014	+0.00618±0.00326	0.26±0.15	0.28±0.16
R08	-0.00264±0.00124	+0.00187±0.00098	+0.00015±0.00007	+0.00018±0.00009	-0.00171±0.00098	+0.00233±0.00125	+0.00079±0.00040	+0.00585±0.00320	0.58±0.17	0.59±0.17
R09	-0.00263±0.00100	-0.00088±0.00060	-0.00081±0.00042	+0.00262±0.00133	-0.00263±0.00127	-0.00025±0.00016	+0.00038±0.00020	+0.00297±0.00169	0.44±0.18	0.46±0.18
R10	-0.00505±0.00181	+0.00062±0.00036	-0.00065±0.00029	+0.00856±0.00366	-0.00457±0.00184	+0.00073±0.00043	+0.00003±0.00001	+0.00985±0.00415	0.45±0.20	0.49±0.19
R11	+0.00603±0.00226	+0.00510±0.00248	+0.00218±0.00111	+0.01300±0.00639	+0.00777±0.00306	+0.00675±0.00321	+0.00313±0.00128	+0.01452±0.00615	0.57±0.28	0.58±0.28
R12	+0.00562±0.00288	+0.00585±0.00345	+0.00357±0.00149	+0.01525±0.00830	+0.00727±0.00385	+0.00673±0.00401	+0.00342±0.00171	+0.01939±0.00986	0.67±0.13	0.70±0.12
R13	+0.00038±0.00021	-0.00208±0.00128	+0.00141±0.00079	-0.00104±0.00069	+0.00030±0.00017	-0.00187±0.00113	+0.00163±0.00089	+0.00074±0.00046	0.77±0.15	0.77±0.15
R14	-0.00198±0.00074	-0.00170±0.00086	-0.00091±0.00037	+0.00120±0.00070	-0.00269±0.00124	-0.00183±0.00101	-0.00053±0.00023	+0.00148±0.00094	0.42±0.15	0.45±0.16

Bibliography

Ackerman, A.S., Toon, O. B., Stevens, D. E., Heymsfield, A. J., Ramanathan, V., and Welton, E. J.: Reduction of tropical cloudiness by soot, *Science*, 288, 5468, 1042-1047, doi:10.1126/science.288.5468.1042, 2000.

Ahlm, L., Nilsson, E. D., Krejci, R., Mårtensson, E. M., Vogt, M., and Artaxo, P.: Aerosol number fluxes over the Amazon rain forest during the wet season, *Atmos. Chem. Phys.*, 9, 9381-9400, doi:10.5194/acp-9-9381-2009, 2009.

Aiken, A. C., de Foy, B., Wiedinmyer, C., DeCarlo, P. F., Ulbrich, I. M., Wehrli, M. N., Szidat, S., Prevot, A. S. H., Noda, J., Wacker, L., Volkamer, R., Fortner, E., Wang, J., Laskin, A., Shutthanandan, V., Zheng, J., Zhang, R., Paredes-Miranda, G., Arnott, W. P., Molina, L. T., Sosa, G., Querol, X., and Jimenez, J. L.: Mexico city aerosol analysis during MILAGRO using high resolution aerosol mass spectrometry at the urban supersite (T0) - Part 2: Analysis of the biomass burning contribution and the non-fossil carbon fraction, *Atmos. Chem. Phys.*, 10, 5315–5341, doi:10.5194/acp-10-5315-2010, 2010.

Albrecht, B.: Aerosols, cloud microphysics and fractional cloudiness, *Science*, 245, 4923, 1227-1230, doi:10.1126/science.245.4923.1227, 1989.

Andreae, T. W., Andreae, M. O., Ichoku, C., Maenhaut, W., Cafmeyer, J., Karnieli, A. and Orlovsky, L.: Light scattering by dust and anthropogenic aerosol at a remote site in the Negev desert, Israel, *J. Geophys. Res.*, 107(D2), 4008, doi:10.1029/2001JD900252, 2002.

Andronache, C.: Estimates of sulfate aerosol wet scavenging coefficient for locations in the Eastern United States, *Atmos. Environ.*, 38, 6, 795-804, doi:10.1016/j.atmosenv.2003.10.035, 2004.

Ångström, A.: On the atmospheric transmission of sun radiation and on dust in the air, *Geograf. Ann. Deut.*, 11, 156-166, 1929.

Ansmann, A., Wandinger, U., Wiedensohler, A., and Leiterer, U.: Lindenberg Aerosol Characterization Experiment 1998 (LACE 98): Overview, *J. Geophys. Res.*, 107(D21), 8129-8140, doi:10.1029/2000JD000233, 2002.

Arimoto, R., Balsam, W., and Schloesslin, C.: Visible spectroscopy of aerosol particles collected on filters: Iron-oxide minerals, *Atmospheric Environment*, 36, 89-96, doi:10.1016/S1352-2310(01)00465-4, 2002.

Baker, J., and Thornes, J. E.: Solar position within Monet's Houses of Parliament, Proc. R. Soc., A2006, 462, 3775-3788, doi:10.1098/rspa.2006.1754, 2006.

Banister, J., Bloom, D. E., and Rosenberg, L.: Population Aging and Economic Growth in China, *Program on the Global Demography of Aging Working Paper*, 53, 1-38, 2010.

Barnard, J. C., Volkamer, R., and Kassianov, E. I.: Estimation of the mass absorption cross section of the organic carbon component of aerosols in the Mexico City Metropolitan Area, *Atmos. Chem. Phys.*, 8, 6665-6679, doi:10.5194/acp-8-6665-2008, 2008.

Barnes, R. A., Eplee Jr., R. E., Schmidt, G. M., Patt, F. S., and Mc-Clain, C. R.: Calibration of SeaWiFS, I: Direct techniques, *Appl. Optics*, 40(36), 6682-6700, doi:10.1364/AO.40.006682, 2001.

Basart, S., Pérez1, C., Cuevas, E., Baldasano, J. M., and Gobbi, G. P.: Aerosol characterization in Northern Africa, Northeastern Atlantic, Mediterranean Basin and Middle East from direct-sun AERONET observations, *Atmos. Chem. Phys.*, 9, 8265-8282, doi:10.5194/acp-9-8265-2009, 2009.

Bell, M. L., Davis, D. L., and Fletcher, T.: A Retrospective Assessment of Mortality from the London Smog Episode of 1952: The Role of Influenza and Pollution, *Environ. Health Perspect.*, 112, 6-8, doi:10.1289/ehp.6539, 2004.

Benkovitz, C. M., Scholtz, M. T., Pacyna, J., Tarrason, L., Dignon, J., Voldner, E. C., Spiro, P. A., Logan, J. A., and Graedel, T. E.: Global gridded inventories of antropogenic emissions of sulphur and nitrogen, *J. Geophys. Res.*, 101, D22, 29239-29253, doi:10.1029/96JD00126, 1996.

Bergamo, A., Tafuro, A. M., Kinne, S., Tomasi, F. D., and Perrone, M. R.: Monthly-averaged anthropogenic

aerosol direct radiative forcing over the Mediterranean based on AERONET aerosol properties, *Atmos. Chem. Phys.*, 8, 6995-7014, doi:10.5194/acp-8-6995-2008, 2008.

Bergstrom, R. W., Schmidt, K. S., Coddington, O., Pilewskie, P., Guan, H., Livingston, J. M., Redemann, J., and Russell, P. B.: Aerosol spectral absorption in the Mexico City area: results from airborne measurements during MILAGRO/INTEX B, *Atmos. Chem. Phys.*, 10, 6333-6343, doi:10.5194/acp-10-6333-2010, 2010.

Brenner, J: Southern Oscillation Anomalies and Their Relation to Florida Wildfires, *Fire Management Notes*, 52(1), 28-32, doi:10.1071/WF9910073, 1991.

Bruegge, C. J., Diner, D. J., Kahn, R. A., Chrien, N., Helmlinger, M. C., Gaitley, B. J., and Abdou, W. A.: The MISR radiometric calibration process, *Rem. Sens. Environ.*, 107, 2-11, doi:10.1016/j.rse.2006.07.024, 2007.

Buchholz, A.: Rayleigh scattering calculations for the terrestrial atmosphere, *Appl. Opt.*, 34, 2765-2773, doi:10.1364/AO.34.002765, 1995.

Bundke, U., Hänel, G., Horvath, H., Kaller, W., Seidl, S., Wex, H., Wiedensohler, A., Wiegner, M., and Freudenthaler, V.: Aerosol optical properties during the Lindenberg Aerosol Characterization Experiment (LACE 98), *J. Geophys. Res.*, 107(D21), 8123-8137, doi:10.1029/2000JD000188, 2002.

Burrows, J. P., Platt, U., and Borrell, P.: The Remote Sensing of Tropospheric Composition from Space, *Springer Verlag, Heidelberg*, 259-313, doi:10.1007/978-3-642-14791-3, 2011.

Butz, A., Hasekamp, O. P., Frankenberg, C., and Aben, I.: Retrievals of atmospheric CO_2 from simulated space-borne measurements of backscattered near-infrared sunlight: accounting for aerosol effects, *Appl. Optics*, 48, 18, 3322-3336, doi: 10.1364/AO.48.003322, 2009.

Chen, L.-W. A., Doddridge, B. G., Dickerson, R. R.,Chow, J. C., Mueller, P. K., Quinn, J., and Butler, W. A.: Seasonal variations in elemental carbon aerosol, carbon monoxide and sulfur dioxide: Implications for sources, *Geophys. Res. Lett.*, 28, 9, 1711-1714, doi:10.1029/2000GL012354, 2001.

Chiang, Y. S., von Hoyningen-Huene, W., Chen, K. S., Ladstätter-Weißenmayer, A., and Burrows, J. P.: Evaluation of BAER Surface Model for Aerosol Optical Thickness Retrieval over Land Surface, *Atmos. Meas. Tech. Discuss.*, in preparation, 2012.

Chiapello, J., and Moulin, C.: TOMS and Meteosat satellite records of the variability of Saharan dust transport over the Atlantic during the last two decades (1979-1997), *Geophys. Res. Lett.*, 29, 8, 1176, doi:10.1029/2001GL013767, 2002.

Chiapello, I., Moulin, C., and Prospero, J. M.: Understanding the long-term variability of African dust transport across the Atlantic as recorded in both Barbados surface concentrations and large-scale total ozone mapping spectrometer (TOMS) optical thickness, *J. Geophys. Res.*, 110, D18S10, doi:10.1029/2004JD005132, 2005.

Chubarova, N. Y., Sviridenkov, M. A., Smirnov, A., and Holben, B. N.: Assessments of urban aerosol pollution in Moscow and its radiative effects, *Atmos. Meas. Tech.*, 4, 367-378, doi:10.5194/amt-4-367-2011, 2011a.

Chubarova, N., Nezval, Y., Sviridenkov, M., Smirnov, A., and Slutsker, I.: Smoke aerosol and its radiative effects during extreme fire event over Central Russia in summer 2010, *Atmos. Meas. Tech. Discuss.*, 4, 6351-6386, doi:10.5194/amtd-4-6351-2011, 2011b.

Chun, Y.: From Historical Dustfall to Early Warning of Asian Dust Events in Korea, Continuing Education Column, 446-452, 2000.

Chung, C. E. and Ramanathan, V.: Weakening of North Indian SST Gradients and the Monsoon Rainfall in India and the Sahel, *Journal of Climate*, 19, 2036-2045, doi:10.1175/JCLI3820.1, 2006.

Colette, A., Granier, C., Hodnebrog, Ø., Jakobs, H., Maurizi, A., Nyiri, A., Bessagnet, B., D'Angiola, A. D'Isidoro, M., Gauss, M., Meleux, F., Memmesheimer, M., Mieville, A., Rouïl1, L., Russo, F., Solberg, S., Stordal, F., and Tampieri, F.: Air quality trends in Europe over the past decade: a first multi-model assessment, *Atmos. Chem. Phys.*, 11, 11657-11678, doi:10.5194/acp-11-11657-2011, 2011.

Cracknell, A. P., Newcombe, S. K., Black, A. F., and Kirby, N. E.: The ABDMAP (Algal Bloom Detection, Monitoring and Prediction) Concerted Action, *Int. J. Remote Sens.*, 22, 205-247,

doi:10.1080/014311601449916, 2001.

Crutzen, P.J. and Andreae, M.O.: Biomass burning in the tropics: impact on atmospheric chemical and biochemical cycles, *Science*, 250, 1669-1678, doi:10.1126/science.250.4988.1669, 1990.

Davidson, E. A. and Artaxo, P.: Globally significant changes in biological processes of the Amazon Basin: Results of the Large-scale Biosphere-Atmosphere Experiment, *Global Change Biol.*, 10(5), 1-11, doi: 10.1111/j.1529-8817.2003.00779.x. 2004.

de Meij, A., Pozzer, A., and Lelieveld, J.: Global and regional trends in aerosol optical depth based on remote sensing products and pollutant emission estimates between 2000 and 2009, *Atmos. Chem. Phys. Discuss.*, 10, 30731-30776, doi:10.5194/acpd-10-30731-2010, 2010.

Derimian, Y., Karnieli, A., Kaufman, Y. J., Andreae, M. O., Andreae, T. W., Dubovik, O., Maenhaut, W., Koren, I. and Holben, B. N.: Dust and pollution aerosols over the Negev desert, Israel: Properties, transport, and radiative effect, *J. Geophys. Res.*, 111, D05205, doi:10.1029/2005JD006549, 2006.

de Ruyter de Wildt, M., Eskes, H., and Boersma, K. F.: The global economic cycle and satellite-derived NO_2 trends over shipping lanes, *Geophys. Res. Lett.*, 39, L01802, doi:10.1029/2011GL049541, 2012.

Dey, S., Tripathi, S. N., Singh, R. P., and Holben, B. N.: Influence of dust storms on the aerosol optical properties over the Indo-Gangetic plains, *J. Geophys. Res.*, 109, D20211, doi:10.1029/2004JD004924, 2004.

Di Girolamo, L. and Wilson, M. J.: A first look at banddifferenced angular signatures for cloud detection from MISR, *IEEE T. Geosci. Remote Sensing*, 41(7), 1730-1734, doi:10.1109/TGRS.2003.815659, 2003.

Dey, S., and L. Di Girolamo: A decade of change in aerosol properties over the Indian subcontinent, *Geophys. Res. Lett.*, 38, L14811, doi:10.1029/2011GL048153, 2011.

Diner, D. J., Abdou, W. A., Ackerman, T. P., Crean, K., Gordon, H. R., Kahn, R. A., Martonchik, J. V., Paradise, S. R., Pinty, B., Verstraete, M. M., Wang, M., and West, R. A.: Multi-angle Imaging SpectroRadiometer Level 2 Aerosol Retrieval Algorithm Theoretical Basis, Revision F. Jet Propulsion Laboratory, JPL D-11400, California Institute of Technology, 2006.

Dubovik, O. and King, M. D.: A flexible inversion algorithm for retrieval of aerosol optical properties from Sun and sky radiance measurements, *J. Geophys. Res.*, 105, D16, 20673-20696, doi:10.1029/2000JD900282, 2000.

Dubovik, O., Smirnov, A., Holben, B. N., King, M. D., Kaufman, Y. J., Eck, T. F. and Slutsker, I.: Accuracy assessment of aerosol optical properties retrieval from AERONET sun and sky radiance measurements, *J. Geophys. Res.*, 105, D8, 9791-9806, doi:10.1029/2000JD900040, 2000.

Dubovik, O., Holben, B. N., Eck, T. F., Smirnov, A., Kaufman, Y. J., King, M. D., Tanré, D., and Slutsker, I.: Variability of absorption and optical properties of key aerosol types observed in worldwide locations, *J. Atmos. Sci.*, 59, 3, 590-608, doi:10.1175/1520-0469(2002)059<0590:VOAAOP>2.0.CO;2, 2002a.

Dubovik, O., Holben, B. N., Lapyonok, T., Sinyuk, A., Mishchenko, M. I., Yang, P. and Slutsker, I.: Non-spherical aerosol retrieval method employing light scattering by spheroids, *Geophys. Res. Lett.*, 29, 10, 1415-1418, doi:10.1029/2001GL014506, 2002b.

Dubovik, O., Sinyuk, A., Lapyonok, T., Holben, B. N., Mishchenko, M., Yang, P., Eck, T. F., Volten, H., Munoz, O., Veihelmann, B., van der Zander, W. J., Leon, J. -F., Sorokin, M. and Slutsker, I.: Application of spheroid models to account for aerosol particle nonsphericity in remote sensing of desert dust, *J. Geophys. Res.*, 111, D11208, 34, doi:10.1029/2005JD006619, 2006.

Eck, T. F., Holben, B. N., Reid, J. S., Dubovik, O., Smirnov, A., O'Neill, N. T., Slutsker, I., and Kinne, S.: Wavelength dependence of the optical depth of biomass burning, urban, and desert dust aerosol, *J. Geophys. Res.*, 104, D24, 31333- 31349, doi:10.1029/1999JD900923, 1999.

Eck, T. F., Holben, B. N., Ward, D. E., Dubovik, O., Reid, J. S., Smirnov, A., Mukelabai, M. M., Hsu, N. C., O'Neill, N. T., and Slutsker, I.: Characterization of the optical properties of biomass burning aerosols in Zambia during the 1997 ZIBBEE Field Campaign, *J. Geophys. Res.*, 106, D4, 3425-3448, doi:10.1029/2000JD900555, 2001.

Eck, T. F. Holben, B. N., Ward, D. E., Mukelabai, M. M., Dubovik, O., Smirnov, A., Schafer, J. S., Hsu, N. C., Piketh, S. J., Queface, A., Le Roux, J., Swap, R. J., and Slutsker, I.: Variability of biomass burning aerosol optical characteristics in southern Africa during the SAFARI 2000 dry season campaign and a

comparison of single scattering albedo estimates from radiometric measurements, *J. Geophys. Res.*, 108, D13, 8477, doi:10.1029/2002JD002321, 2003.

Eck, T. F., Holben, B. N., Dubovik, O., Smirnov, A., Goloub, P., Chen, H. B., Chatenet, B., Gomes, L., Zhang, X.-Y., Tsay, S.-C., Ji, Q., Giles, D., and Slutsker, I.: Columnar aerosol optical properties at AERONET sites in central eastern Asia and aerosol transport to the tropical mid-Pacific, *J. Geophys. Res.*, 110, D06202, 18, doi:10.1029/2004JD005274, 2005.

Eltahir, E. A. B. and Bras, R. L.: Precipitation recycling, *Rev. Geophys.*, 34, 367-378, doi:10.1029/96RG01927, 1996.

Eplee Jr., R. E., Robinson, W. D., Bailey, S. W., Clark, D. K., Werdell, P. J., Wang, M., Barnes, R. A., and McClain, C. R.: The calibration of SeaWiFS, Part 2: Vicarious techniques, *Appl. Optics*, 40, 36, 6701-6718, doi:10.1364/AO.40.006701, 2001.

Eplee Jr., R. E., Patt, F. S., Barnes, R. A., and McClain, C. R.: SeaWiFS long-term solar diffuser reflectance and sensor noise analyses, *Appl. Optics*, 46, 5, 762-773, doi:10.1364/AO.46.000762, 2007.

Eplee Jr., R. E., Meister, G., Patt, F. S., Franz, B. A., and McClain, C. R.: Uncertainty Assessment of the SeaWiFS On-Orbit Calibration, *Proc. SPIE*, 8153, 81530B, doi:10.1117/12.892340, 2011.

Evan, A. T., Mahowald, N. M., and Remer, L. A.: Global Aerosols, *Bull. Am. Meteorol. Soc.*, 88, s1-s135, 2007.

Facchini, M. C., Decesari, S., Mircea, M., Fuzzi, S., and Loglio, G.: Surface tension of atmospheric wet aerosol and cloud/fog droplets in relation to their organic carbon econtent and chemical composition, *Atmos. Environ.*, 33, 4853-4857, 2000.

Fan, T. and Toon, O. B.: Modeling sea-salt aerosol in a coupled climate and sectional microphysical model: mass, optical depth and number concentration, *Atmos. Chem. Phys.*, 11, 4587-4610, doi:10.5194/acp-11-4587-2011, 2011

Fleming, G. and van der Merwe, M.: Spatial disaggregation of greenhouse gas emissions inventory data for Africa south of the equator, available at: http://gis.esri.com/library/userconf/proc00/professional/papers/PAP896/p896.htm, 2002.

Fonken, L. K., Xu, X., Weil, Z. M., Chen, G., Sun, Q., Rajagopalan, S., and Nelson, R. J.: Air pollution impairs cognition, provokes depressive-like behaviors and alters hippocampal cytokine expression and morphology, *Molecular Psychiatry*, 16, 987-995, doi:10.1038/mp.2011.76, 2011.

Foster, A. and Kumar, N.: Health effects of air quality regulations in Delhi, India, *Atmos. Environ.*, 45, 9, 1675-1683, doi:10.1016/j.atmosenv.2011.01.005, 2011.

Fotiadi, A., Hatzianastassiou, N., Matsoukas, C., Pavlakis, K. G., Drakakis, E., Hatzidimitriou, D., and Vardavas, I.: Analysis of the decrease in the tropical mean outgoing shortwave radiation at the top of atmosphere for the period 1984-2000, *Atmos. Chem. Phys.*, 5, 1721-1730, doi:10.5194/acp-5-1721-2005, 2005.

Franz, B. A., Bailey, S. W., Werdell, P. J., and McClain, C. R.: Sensorindependent Approach to the Vicarious Calibration of Satellite Ocean Color Radiometry, *Appl. Optics*, 46, 22, 5068-5082, doi:10.1364/AO.46.005068, 2007.

Frogner Kockum, P. C., Herbert, R. B., and Gislason, S. R.: A diverse ecosystem response to volcanic aerosols, *Chemical Geology*, 231, 57-66, doi:10.1016/j.chemgeo.2005.12.008, 2006.

Garstang, M. and Fitzjarrald, D. R.: Observations of Surface to Atmosphere Interactions in the Tropics, New York, USA, Oxford University Press, 1999.

GCOS - Global Climate Observing System: Systematic Observation Requirements for Satellite-based Products for Climate (Supplemental details to the satellite-based component of the "Implementation Plan for the Global Observing System for Climate in Support of the UNFCCC"), *World Meteorological Organization*, GCOS - 107, 2006.

GCOS - Global Climate Observing System: Systematic Observation Requirements for Satellite-based Products for Climate (Supplemental details to the satellite-based component of the "Implementation Plan for the Global Observing System for Climate in Support of the UNFCCC (2010 Update)"), *World Meteorological Organization*, GCOS - 154, 2011.

Gerasopoulos, E., Andreae, M. O., Zerefos, C. S., Andreae, T. W., Balis, D., P. Merlet, P., Amiridis, V., and Papastefanou, C.: Climatological aspects of aerosol optical properties in Northern Greece, *Atmos.*

Chem. Phys., 3, 2025-2041, doi:10.5194/acp-3-2025-2003, 2003.

Gerasopoulos, E., Amiridis, V., Kazadzis, S., Kokkalis, P., Eleftheratos, K., Andreae, M. O., Andreae, T. W., El-Askary, H., and Zerefos, C. S.: Three-year ground based measurements of aerosol optical depth over the Eastern Mediterranean: the urban environment of Athens, Atmos. Chem. Phys., 11, 2145-2159, doi:10.5194/acp-11-2145-2011, 2011.

Giglio, L., van der Werf, G. R., Randerson, J. T., Collatz, G. J., and Kasibhatla, P.: Global estimation of burned area using MODIS active fire observations, *Atmos. Chem. Phys.*, 6, 957-974, doi:10.5194/acp-6-957-2006, 2006a.

Giglio, L., Csiszar, I., and Justice, C. O.: Global distribution and seasonality of active fires as observed with the Terra and Aqua Moderate Resolution Imaging Spectroradiometer (MODIS) sensors, *J. Geophys. Res.*, 111, G02016, doi:10.1029/2005JG000142, 2006b.

Giglio, L.: Characterization of the tropical diurnal fire cycle using VIRS and MODIS observations, *Remote Sensing of Environment*, 108, 407-421, doi:10.1016/j.rse.2006.11.018, 2007.

Giglio, L., Randerson, J. T., van derWerf, G. R., Kasibhatla, P. S., Collatz, G. J., Morton, D. C., and DeFries, R. S.: Assessing variability and long-term trends in burned area by merging multiple satellite fire products, *Biogeosciences*, 7, 1171-1186, doi:10.5194/bg-7-1171-2010, 2010.

Glen, W. G., Zelenka, M. P., and Graham, R. C.: Relating meteorological variables and trends in motor vehicle emissions to monthly urban carbon monoxide concentrations, *Atmos. Environ.*, 30, 24, 4225-4232, doi:10.1016/1352-2310(96)00130-6, 1996.

Gobbi, G. P., Kaufman, Y. J., Koren, I., and Eck, T. F.: Classification of aerosol properties derived from AERONET direct sun data, *Atmos. Chem. Phys.*, 7, 453-458, doi:10.5194/acp-7-453-2007, 2007.

Goldman Sachs, Dreaming With BRICs: The Path to 2050, Global Economics Paper No: 99, 2003.

González, R. C., Veefkind, J. P., and de Leeuw, G.: Aerosol optical depth over Europe in August 1997 derived from ATSR-2 data, *Geophys. Res. Lett.*, 27, 7, 955-958, doi:10.1029/1999GL010962, 2000.

Gordon, H. R.: In-orbit calibration strategy for ocean color sensors, Remote Sens. Environ., 63, 265-278, 1998.

Grey, W. M. F., North, P. and Los, S.: Computationally efficient method for retrieving aerosol optical depth from ATSR-2 and AATSR data, *Appl. Optics*, 45, 2786-2795, doi:10.1364/AO.45.002786, 2006.

Grubbs, F.: Procedures for Detecting Outlying Observations in Samples, *Technometrics*, 11(1), 1-21, 1969.

Hansen, J., Sato, M., Ruedy, R., Lacis, A., and Oinas, V.: Global warming in the twenty-first century: An alternative scenario, *Proc. Natl. Acad. Sci. U.S.A.*, 97, 9875-9880, doi:10.1073/pnas.170278997, 2000.

Hansen, J., and Nazarenko, L.: Soot climate forcing via snow and ice albedos, *Proc. Natl. Acad. Sci. U.S.A.*, 101, 423-428, doi:10.1073/pnas.2237157100, 2004.

Hao, W. M., and Liu, M.: Spatial and temporal distribution of tropical biomass burning, *Glob. Biogeochem. Cycles*, 8, 4, 495-503, doi:10.1029/94GB02086, 1994.

Hatzianastassiou, N., Gkikas, A., Mihalopoulos, N., Torres, O., and Katsoulis, B. D.: Natural versus anthropogenic aerosols in the eastern Mediterranean basin derived from multiyear TOMS and MODIS satellite data, *J. Geophys. Res.*, 114, D24202, doi:10.1029/2009JD011982, 2009.

Hayn, M., Beirle, S., Hamprecht, F. A., Platt, U., Menze, B. H., and Wagner, T.: Analysing spatio-temporal patterns of the global NO_2-distribution retrieved from GOME satellite observations using a generalized additive model, *Atmos. Chem. Phys.*, 9, 6459-6477, doi:10.5194/acp-9-6459-2009, 2009.

Haywood, J. M., and Shine, K. P.: Multi-spectral calculations of the direct radiative forcing of tropospheric sulphate and soot aerosols using a column model, *Q. J. R. Meteorol. Soc.*, 123, 1907-1930, doi:10.1002/qj.49712354307, 1997.

Haywood, J. and Boucher, O.: Estimates of the direct and indirect radiative forcing due to tropospheric aerosols: A review, *Review of Geophysics*, 38, 4, 513-543, doi:10.1029/1999RG000078, 2000.

Haywood, J. M., Francis, P. N., Geogdzhayev, I., Mishchenko, M., and Frey, R.: Comparison of Saharan dust aerosol optical depths retrieved using aircraft mounted pyranometers and 2-channel AVHRR algorithms, *Geophys. Res. Lett.*, 28, 12, 2393-2396, doi:10.1029/2000GL012625, 2001.

Heidinger, A. K., Cao, C., and Sullivan, J.: Using Moderate Resolution Imaging Spectrometer (MODIS) to calibrate Advanced Very High Resolution Radiometer (AVHRR) reflectance channels, *J. Geophys. Res.*, 107(D23), 4702, doi:10,1029/2001JD002035, 2002.

Heidinger, A. K., Goldberg, M. D., Tarpley, D., Jelenak, A., and Pavolonis, M.: A new AVHRR cloud climatology. Applications with Weather Satellites II, Honolulu, Hawaii, 9-11 November 2004, Call Number: Reprint #4198, Proceedings SPIE-The International Society for Optical Engineering, Bellingham, WA, 197-205, 2004.

Held, I. M., Delworth, T. L., Lu, J., Findell, K. L., and Knutson, T. R.: Simulation of Sahel drought in the 20th and 21st centuries, *Proc. Natl. Acad. Sci. U.S.A.*, 102 (50), 17891-17896, doi:10.1073/pnas.0509057102, 2005.

Herman, J. R., Bhartia, P. K., Torres, O., Hsu, C., Seftor, C., and Celarier, E.: Global distribution of UV-absorbing aerosols from Nimbus 7/TOMS data, *J. Geophys. Res.*, 102(D14), 16911-16922, doi:10.1029/96JD03680, 1997.

Higurashi, A., and Nakajima, T.: Development of a two channel aerosol retrieval algorithm on global scale using NOAA AVHRR, *J. Atmos. Sci.*, 56, 924-941, doi:10.1175/1520-0469(1999)056<0924:DOATCA>2.0.CO;2, 1999.

Higurashi, A., Nakajima, T., Holben, B. N., Smirnov, A., Frouin, R., and Chatenet, B.: A study of global aerosol optical climatology with two-channel AVHRR remote sensing, *J. Climate*, 13(12), 2011-2027, doi:10.1175/1520-0442(2000)013<2011:ASOGAO>2.0.CO;2, 2000.

Holben, B. N., Eck, T. F., Slutsker, I., Tanré, D., Buis, J. P., Setzer, A., Vermote, E., Reagan, J. A., Kaufman, Y. J., Nakajima, T., Lavenu, F., Jankowiak, I., and Smirnov, A.: AERONET - A federated instrument network and data archive for aerosol characteristics, *Remote Sens. Environ.*, 66, 1, 1-16, doi:10.1016/S0034-4257(98)00031-5, 1998.

Holben, B. N., Tanré, D., Smirnov, A., Eck, T. F., Slutsker, I., Abuhassan, N., Newcomb, W. W., Schafer, J. S., Chatenet, B., Lavenu, F., Kaufman, Y. J., Vande Castle, J., Setzer, A., Markham, B., Clark, D., Frouin, R., Halthore, R., Karneli, A., O'Neill, N. T., Pietras, C., Pinker, R. T., Voss, K., and Zibordi, G.: An emerging ground-based aerosol climatology: Aerosol optical depth from AERONET, *J. Geophys. Res.*, 106, D11, 12067-12097, doi:10.1029/2001JD900014, 2001.

Hooker, S. B., Esaias, W. E., Feldman, G. C., Gregg, W. W., and McClain, C. R.: An Overview of SeaWiFS and Ocean Color, *NASA Tech. Memo.*, 1, 104566, 24, 1992.

Huang, J., Zhang, C., and Prospero, J. M.: African aerosol and large-scale precipitation variability over West Africa, *Environ. Res. Lett.*, 4, 015006, doi:10.1088/1748-9326/4/1/015006, 2009.

Husar, R. B., Prospero, J. M., and Stowe, L. L.: Characterization of tropospheric aerosols over the oceans with the NOAA advanced very high resolution radiometer optical thickness operational product, *J. Geophys. Res.*, 102(D14), 16889-16910, 1997.

Ignatov, A. and Stowe, L.: Sensitivity and information content of aerosol retrievals from AVHRR: Radiometric factors, *Appl. Optics*, 41(6), 991-1011, doi:10.1364/AO.41.000991, 2002.

Ignatov, A., Minnis, P., Loeb, N., Wielicki, B., Miller, W., Sun-Mack, S., Tanré, S., Remer, L., Laszlo, I., and Geier, E.: Two MODIS Aerosol Products over Ocean on the Terra and Aqua CERES SSF Datasets, *J. Atmos. Sci.*, 62, 1008-1031, doi: 10.1175/JAS3383.1, 2005.

International Monetary Fund: China Economic Outlook, 1-10, 2012.

IPCC: Changes in Atmospheric Constituents and in Radiative Forcing: Issues Related to Aerosols, 153-179, 2007.

Irwin, M., Robinson, N., Allan, J. D., Coe, H., and McFiggans, G.: Size-resolved aerosol water uptake and cloud condensation nuclei measurements as measured above a Southeast Asian rainforest during OP3, *Atmos. Chem. Phys.*, 11, 11157-11174, doi:10.5194/acp-11-11157-2011, 2011.

Jeong, M. -J., and Li, Z.: Quality, compatibility, and synergy analyses of global aerosol products of global aerosol products derived from the advanced very high resolution radiometer and Total Ozone Mapping Spectrometer, *J. Geophys. Res.*, 110, D10S08, doi:10.1029/2004JD004647, 2005.

Jeong, M. -J., Li, Z., Chu, D. A., and Tsay, S. -T.: Quality and compatibility analyses of global aerosol products derived from the advanced very high resolution radiometers and the moderate imaging spectroradiometer, *J. Geophys. Res.*, 110, D10S09, doi:10.1029/2004JD004648, 2005.

Jeong, S. -J., Ho, C. -H., Brown, M. E., Kug, J. -S., and Piao, S.: Browning in desert boundaries in Asia in recent decades, *J. Geophys. Res.*, 116, D02103, doi:10.1029/2010JD014633, 2011.

Johnson, B. T., Osborne, S. R., Haywood, J. M., and Harrison, M. A. J.: Aircraft measurements of biomass burning aerosol over West Africa during DABEX, *J. Geophys. Res.*, 113, D00C06, doi:10.1029/2007JD009451, 2008a.

Johnson, B. T., Heese, B., McFarlane, S. A., Chazette, P., Jones, A., and Bellouin, N.: Vertical distribution and radiative effects of mineral dust and biomass burning aerosol over West Africa during DABEX, *J. Geophys. Res.*, 113, D00C12, doi:10.1029/2008JD009848, 2008b.

Kahn, R. A., Gaitley, B., Martonchik, J., Diner, D., Crean, K., and Holben, B.: MISR global aerosol optical depth validation based on two years of coincident AERONET observations, *J. Geophys. Res.*, 110, D10S04, doi:10.1029/2004JD004706, 2005a.

Kahn, R., Li, W.-H., Martonchik, J., Bruegge, C., Diner, D., Gaitley, B., Abdou, W., Dubovik, O., Holben, B., Smirnov, S., Jin, Z., and Clark, D.: MISR low-light-level calibration, and implications for aerosol retrieval over dark water, *J. Atmos. Sci.*, 62(4), 1032-1062, doi:10.1175/JAS3390.1, 2005b.

Kahn, R., Garay, M., Nelson, D., Yau, K., Bull, M., and Martonchik, J.: Satellite-derived aerosol optical depth over dark water from MISR and MODIS: Comparisons with AERONET and implications for climatological studies, *J. Geophys. Res.*, 112, D18205, doi:10.1029/2006JD008175, 2007.

Kahn, R. A., Gaitley, B. J., Garay, M. J., Diner, D. J., Eck, T. F., Smirnov, A., and Holben, B. N.: Multiangle Imaging SpectroRadiometer global aerosol product assessment by comparison with the Aerosol Robotic Network, *J. Geophys. Res.*, 25(115), D23209, doi:10.1029/2010JD014601, 2010.

Kalivitis, N., Gerasopoulos, E., Vrekoussis, M., Kouvarakis, G., Kubilay, N., Hatzianastassiou, N., Vardavas, I., and Mihalopoulos, N.: Dust transport over the eastern Mediterranean derived from Total Ozone Mapping Spectrometer, Aerosol Robotic Network, and surface measurements, *J. Geophys. Res.*, 112, D03202, doi:10.1029/2006JD007510, 2007.

Kambezidisa, H. D. and Kaskaoutisa, D. G.: Aerosol climatology over four AERONET sites: An overview, *Atmos. Environ.*, 42, 8, 1892-1906, doi:10.1016/j.atmosenv.2007.11.013, 2008.

Karnieli, A., Derimian, Y., Indoitu, R., Panov, N., Levy, R. C., Remer, L. A., Maenhaut, W., and Holben, B. N.: Temporal trend in anthropogenic sulfur aerosol transport from central and eastern Europe to Israel, *J. Geophys. Res.*, 114, D00D19, doi:10.1029/2009JD011870, 2009.

Kaskaoutis, D. G. and Kambezidis, H. D.: Comparison of the Ångström parameters retrieval in different spectral ranges with the use of different techniques, *Meteorol. Atmos. Phys.*, 99, 3, 233-246, doi:10.1007/s00703-007-0279-y, 2008.

Kaskaoutis, D. G., Kambezidis, H. D., Hatzianastassiou, N., Kosmopoulos, P. G., and Badarinath, K. V. S.: Aerosol Climatology: Dependence of the angstrom exponent on wavelength over four AERONET sites. *Atmos. Chem. Phys. Discuss.*, 7, 7347-7397, doi:10.5194/acpd-7-7347-2007, 2007.

Kaskaoutis, D. G., Kharol, S. K., Sinha, P. R., Singh, R. P., Kambezidis, H. D., Rani Sharma, A., and Badarinath, K. V. S.: Extremely large anthropogenic-aerosol contribution to total aerosol load over the Bay of Bengal during winter season, *Atmos. Chem. Phys.*, 11, 7097-7117, doi:10.5194/acp-11-7097-2011, 2011a

Kaskaoutis, D. G., Kharol, S. K., Sinha, P. R., Singh, R. P., Badarinath, K. V. S., Mehdi, W., and Sharma, M.: Contrasting aerosol trends over South Asia during the last decade based on MODIS observations, *Atmos. Meas. Tech. Discuss.*, 4, 5275-5323, doi:10.5194/amtd-4-5275-2011, 2011b.

Kasten, F., and Young, A. T.: Revised optical air mass tables and approximation formula, *Appl. Opt.*, 28, 4735-4738, doi:10.1364/AO.28.004735, 1989.

Kaufman, Y. J.: Aerosol optical thickness and atmospheric path radiance, *J. Geophys. Res.*, 98, D2, 2677-2692, doi:10.1029/92JD02427, 1993.

Kaufman, Y. J., Tanré, D., Gordon, H. R., Nakajima, T., Lenoble, J., Frouin, R., Grassl, H., Herman, B. M., King, M. D., and Teillet, P. M.: Passive remote sensing of tropospheric aerosol and atmospheric correction for the aerosol effect, *J. Geoph. Res.*, 102, 16815-16830, doi:10.1029/97JD01496, 1997a.

Kaufman, Y. J., Tanré, D., Remer, L. A., Vermote, E. F., Chu, A., and Holben, B. N.: Operational remote sensing of tropospheric aerosol over land from EOS moderate resolution imaging spectroradiometer, *J. Geoph. Res.*, 102, 17,051-17,068, 1997b.

Kaufmann, R. K., Kauppi, H., Mann, M. L., and Stock, J. H.: Reconciling anthropogenic climate change with

observed temperature 1998-2008, *Proc. Natl. Acad. Sci. U.S.A.*, 108, 29, 11790-11793, doi:10.1073/pnas.1102467108/-/DCSupplemental, 2011.

Kikuchi, K., Sasaki, Y., Sasaki, W., Nomura, S.: Examination of the Dilution and Neutralization of Acid Droplets by Tree Leaves Using a pH-Imaging Microscope, *J. Meteor. Soc. Japan.*, 84, 1, 155-164, doi:10.2151/jmsj.84.155, 2006.

Kim, S. -W., Yoon, S. -C., Kim, J., and Kim, S. -Y.: Seasonal and monthly variations of columnar aerosol optical properties over East Asia determined from multi-year MODIS, LIDAR, and AERONET sun/sky radiometer measurements, *Atmos. Environ.*, 41, 8, 1634-1651, doi:10.1016/j.atmosenv.2006.10.044, 2007.

Kim, J., Yoon, J. -M., Ahn, M. H., Sohn, B. J., and Li, H. S.: Retrieving aerosol optical depth using visible and mid-IR channels from geostationary satellite MTSAT-1R, *International Journal of Remote Sensing*, 29, 6179-6190, doi:10.1080/01431160802175553, 2008.

Kirby, K. R., Laurance, W. F., Albernaz, A. K., Schroth, G., Fearnside, P. M., Bergen, S., Venticinque, E. M., and da Costa, C.: The future of deforestation in the Brazilian Amazon, *Futures*, 38, 432-453, doi:10.1016/j.futures.2005.07.011, 2006.

Kishcha, P., Starobinets, B., Kalashnikova, O., Long, C. N., and Alpert, P.: Variations of meridional aerosol distribution and solar dimming, *J. Geophys. Res.*, 114, D00D14, doi:10.1029/2008JD010975, 2009.

Kokhanovsky, A. A.: Reflection and transmission of polarized light by optically thick weakly absorbing random media, *J. Opt. Soc. Am.*, 18, 883-887, doi:10.1364/JOSAA.18.000883, 2001.

Kokhanovsky, A. and de Leeuw, G.: Satellite aerosol remote sensing over land, Springer, 2009.

Kokhanovsky, A. A., Deuzé, J. L., Diner, D. J., Dubovik, O., Ducos, F., Emde, C., Garay, M. J., Grainger, R. G., Heckel, A., Herman, M., Katsev, I. L., Keller, J., Levy, R., North, P. R. J., Prikhach, A. S., Rozanov, V. V., Sayer, A. M., Ota, Y., Tanré, D., Thomas, G. E., and Zege, E. P.: The inter-comparison of major satellite aerosol retrieval algorithms using simulated intensity and polarization characteristics of reflected light, *Atmos. Meas. Tech.*, 3, 909-932, doi:10.5194/amt-3-909-2010, 2010.

Koppmann, R., von Czapiewski, K. and Reid, J. S.: A review of biomass burning emissions, part I: gaseous emissions of carbon monoxide, methane, volatile organic compounds, and nitrogen containing compounds, *Atmos. Chem. Phys. Discuss.*, 5, 10455-10516, doi:10.5194/acpd-5-10455-2005, 2005.

Kotchenruther, R., Hobbs, P. V., and Hegg, D. A.: Humidification factors for atmospheric aerosols off the mid-Atlantic coast of the United States, *J. Geophys. Res.*, 104, D2, 2239-2251, doi:10.1029/98JD01751, 1999.

Koukouli, M.E., Kazadzis, S., Amiridis, V., Ichoku, C., Balis, D.S., Bais, A.F.: Signs of a negative trend in the MODIS aerosol optical depth over the Southern Balkans, *Atmos. Environ.*, 44, 1219-1228, doi:10.1016/j.atmosenv.2009.11.024, 2010.

Kubilay, N., Cokacar, T., and Oguz, T.: Optical properties of mineral dust outbreaks over the northeastern Mediterranean, *J. Geophys. Res.*, 108, D21, 4666, doi:10.1029/2003JD003798, 2003.

Larssen, T., and Carmichael, G. R.: Acid rain and acidification in China: The importance of base caption deposition, *Environ. Pollut.*, 110, 89-102, doi:10.1016/S0269-7491(99)00279-1, 2000.

Lawrence, M. G., and Lelieveld, J.: Atmospheric pollutant outflow from southern Asia: A review, *Atmos. Chem. Phys.*, 10, 11017-11096, doi:10.5194/acp-10-11017-2010, 2010.

Lee, K. H., Kim, Y. J., and von Hoyningen-Huene, W.: Estimation of aerosol optical thickness over northeast Asia from Sea-Viewing Wide Field-of-View Sensor (SeaWiFS) data during the 2001 ACE-Asia intensive observation period, *J. Geophys. Res.*, 109, D19S16, doi:10.1029/2003JD004126, 2004.

Lei, Y., Zhang, Q., He, K. B., and Streets, D. G.: Primary anthropogenic aerosol emission trends for China, 1990-2005, *Atmos. Chem. Phys.*, 11, 931-954, doi:10.5194/acp-11-931-2011, 2011.

Leibensperger, E. M., Mickley, L. J., Jacob, D. J., Chen, W.-T., Seinfeld, J. H., Nenes, A., Adams, P. J., Streets, D. G., Kumar, N., and Rind, D.: Climatic effects of 1950-2050 changes in US anthropogenic aerosols - Part 1: Aerosol trends and radiative forcing, *Atmos. Chem. Phys. Discuss.*, 11, 24085-24125, doi:10.5194/acpd-11-24085-2011, 2011.

Leitão, J., Richter, A., Vrekoussis, M., Kokhanovsky, A., Zhang, Q. J., Beekmann, M., and Burrows, J. P.: On the improvement of NO_2 satellite retrievals - aerosol impact on the airmass factors, *Atmos. Meas.*

Tech., 3, 475-493, doi:10.5194/amt-3-475-2010, 2010.

Lelieveld, J., Berresheim, H., Borrmann, S., Crutzen, P. J., Dentener, F. J., Fischer, H., Feichter, J., Flatau, P. J., Heland, J., Holzinger, R., Korrmann, R., Lawrence, M. G., Levin, Z., Markowicz, K. M., Mihalopoulos, N., Minikin, A., Ramanathan, V., de Reus, M., Roelofs, G. J., Scheeren, H. A., Sciare, J., Schlager, H., Schultz, M., Siegmund, P., Steil, B., Stephanou, E. G., Stier, P., Traub, M., Warneke, C., Williams, J., and Ziereis, H.: Global air pollution crossroads over the Mediterranean, *Science*, 298, 794-799, doi:10.1126/science.1075457, 2002.

Léon, J.-F., Chazette, P., and Dulac, F.: Retrieval and monitoring of aerosol optical thickness over an urban area by spaceborne and ground-based remote sensing, *Appl. Opt.*, 38(33), 6918-6926, doi:10.1364/AO.38.006918, 1995.

Léon, J.-F., Chazette, P., Dulac, F., Pelon, J., Bonnazola, M., Foret, G., Cautenet, S., Cachier, C., Alfaro, S. C., Gaudichet, A., Gomes, L., Rajot, J.-L., Lavenu, F., Inamdar, S. R., Sarode, P. R., and Kadadevarmath, J. S.: Large scale advection of continental aerosols during INDOEX, *J. Geophys. Res.*, 106, D22, 28427-28439, doi:10.1029/2001JD900023, 2001.

Levy, R. C., Leptoukh, G. G., Kahn, R., Zubko, V., Gopalan, A., and Remer, L. A.: A Critical Look at Deriving Monthly Aerosol Optical Depth From Satellite Data, *IEEE T. Geosci. Remote Sensing*, 47 (8), 2942-2956, doi:10.1109/TGRS.2009.2013842, 2009.

Levy, R. C., Remer, L. A., Kleidman, R. G., Mattoo, S., Ichoku, C., Kahn, R., and Eck, T. F.: Global evaluation of the Collection 5 MODIS dark-target aerosol products over land, *Atmos. Chem. Phys.*, 10, 10399-10420, doi:10.5194/acp-10-10399-2010, 2010.

Li, W. and Fu, R.: Transition of the large-scale atmospheric and land surface conditions from dry to wet season over Amazonia as diagnosed by the ECMWF re-analysis, *J. Climate*, 17, 2637-2651, doi:10.1175/1520-0442(2004)017<2637:TOTLAA>2.0.CO;2, 2004.

Li, Z., Zhao, X., Kahn, R., Mishchenko, M., Remer, L., Lee, K.-H., Wang, M., Laszlo, I., Nakajima, T., and Maring, H.: Uncertainties in satellite remote sensing of aerosols and impact on monitoring its long-term trend: a review and perspective, *Ann. Geophys.*, 27, 2755-2770, doi:10.5194/angeo-27-2755-2009, 2009.

Liebmann, B., Vera, C. S., Carvalho, L. M. V., Camilloni, I. A., Hoerling, M. P., Allured, D., Barros, V. R., Báez, J., and Bidegain, M.: An Observed Trend in Central South American Precipitation, *Journal of Climate*, 17(22), 4357-4367, doi:10.1175/3205.1, 2004.

Liu, J., Drummond, J. R., Li, Q., Gille, J. C., Ziskin, D. C.: Satellite mapping of CO emission from forest fires in Northwest America using MOPITT measurements, *Remote Sensing of Environment*, 95, 502-516, doi:10.1016/j.rse.2005.01.009, 2005.

Liu, Y., Sarnat, J. A., Coull, B. A., Koutrakis, P., and Jacob, D. J.: Validation of Multiangle Imaging Spectroradiometer (MISR) aerosol optical thickness measurements using Aerosol Robotic Network (AERONET) observations over the contiguous United States, *J. Geophys. Res.*, 109, D06205, doi:10.1029/2003JD003981, 2004.

Luchs, S.: Increased Fire Danger Predicted for 2011: La Niña and Wildfire Activity in Florida, *Florida Forest Service- FDACS*, 2010.

Lyons,W. A., Nelson, T. E., Williams, E. R., Crarmer, J. A. and Turner, T. R.: Enhanced positive cloud-to-ground lightning in thunderstorms ingesting smoke from fires, *Science*, 282, 77-80, doi:10.1126/science.282.5386.77, 1998.

Maignan, F., Brèon, F.-M., and Lacaze, R.: Bidirectional reflectance of Earth targets: evaluation of analytical models using a large set of spaceborne measurements with emphasis on the Hot Spot, *Remote Sens. Environ.*, 90, 210-220, doi:10.1016/j.rse.2003.12.006, 2004

Marmer, E., Langmann, B., Fagerli, H., and Vestreng, V.: Direct shortwave radiative forcing of sulphate aerosol over Europe from 1900 to 2000, J. Geophys. Res., 112, D23S17, doi:10.1029/2006JD008037, 2007.

Martins, J. V., Remer, L., Kaufman, Y. J., Mattoo, S., and Levy, R.: MODIS cloud screening for remote sensing of aerosols over oceans using spatial variability, *Geophys. Res. Lett.*, 29(12), 8009, doi:10.1029/2001GL013252, 2002.

Martonchik, J. V., Diner, D. J., Kahn, R. A., Gaitley, B. J., and Holben, B. N.: Comparison of MISR and

AERONET aerosol optical depths over desert sites, *Geophys. Res. Lett.*, 31, L16101, doi:10.1029/2004GL019807, 2004.

Massie, T. S., Torres, O., and Smith, S. J.: Total ozone mapping spectrometer (TOMS) observations of increases in Asian aerosol in winter from 1979 to 2000, *J. Geophys. Res.*, 109, D18211, doi:10.1029/2004JD004620, 2004.

Mazzola, M., Lanconelli, C., Lupi, A., Busetto, M., Vitale, V., and Tomasi, C.: Columnar aerosol optical properties in the Po Valley, Italy, from MFRSR data, *J. Geophys. Res.*, 115, D17206, doi:10.1029/2009JD013310, 2010.

McFiggans, G., Alfarra,M., Allan, J., Bower, K., and Coe, H.: Simplification of the representation of the organic component of atmospheric particulates, *Fara. Discuss.*, 130, 341-362, doi:10.1039/b419435g, 2005.

McFiggans, G., Artaxo, P., Baltensperger, U., Coe, H., Facchini, M. C., Feingold, G., Fuzzi, S., Gysel, M., Laaksonen, A., Lohmann, U., Mentel, T. F., Murphy, D. M., O'Dowd, C. D., Snider, J. R., and Weingartner, E.: The effect of physical and chemical aerosol properties on warm cloud droplet activation, *Atmos. Chem. Phys.*, 6, 2593-2649, doi:10.5194/acp-6-2593-2006, 2006.

Mishchenko, M. and Geogdzhayev, I. V.: Satellite remote sensing reveals regional tropospheric aerosol trends, *Opt. Express*, 15(12), 7423-7438, doi:10.1364/OE.15.007423, 2007.

Mishchenko, M. I., Geogdzhayev, I. V., Cairns, B., Rossow, W. B., and Lacis, A. A.: Aerosol retrievals over the ocean by use of channels 1 and 2 AVHRR data: sensitivity analysis and preliminary results, *Applied Optics*, 38, 7325-7341, doi:10.1364/AO.38.007325, 1999a.

Mishchenko, M. I., Dlugach, J. M., Yanovitskij, E. G., and Zakharova, N. T.: Bidirectional reflectance of flat, optically thick particulate laters: an efficient radiative transfer solution and applications to snow and soil surfaces, *J. Quant. Spectrosc. Radiat. Transfer*, 63, 2, 409-432, doi:10.1016/S0022-4073(99)00028-X, 1999b.

Mishchenko, M. I., Travis, L. D., and Lacis, A. A.: Scattering, Absorption, and Emission of Light by Small Particles, Cambridge University Press, 2002.

Mishchenko, M., Geogdzhayev, I. V., Rossow, W. B., Cairns, B., Carlson, B. E., Lacis, A. A., Liu, L., and Travis, L. D.: Long-term satellite record reveals likely recent aerosol trend, *Science*, 315, 1543, doi:10.1126/science.1136709, 2007.

Moulin, C. and Chiapello, I.: Evidence of the control of summer atmospheric transport of African dust over the Atlantic by Sahel sources from TOMS satellites (1979-2000), *Geophys. Res. Lett.*, 31, L02107, doi:10.1029/2003GL018931, 2004.

Mu, M., Randerson, J. T., van der Werf, G. R., Giglio, L., Kasibhatla, P., Morton, D., Collatz, G. J., DeFries, R. S., Hyer, E. J., Prins, E. M., Griffith, D. W. T., Wunch, D., Toon, G. C., Sherlock, V., and Wennberg, P. O.: Daily and 3-hourly variability in global fire emissions and consequences for atmospheric model predictions of carbon monoxide, *J. Geophys. Res.*, 116, D24303, doi:10.1029/2011JD016245, 2011.

Mudelsee, M.: Climate Time Series Analysis: Classical Statistical and Bootstrap Methods (Atmospheric and Oceanographic Sciences Library), *Springer*, ISBN-13: 978-9048194810, 2010.

Mukai, S., Sano, I., and Holben, B.N.: Aerosol properties over Japan by sun/sky photometry, *Water Air Soil Pollut.: Focus*, 5, 3-6, 133-143, doi:10.1007/s11267-005-0731-2, 2005.

Mukai, S., Sano, I., Satoh, M., Holben, B. N.: Aerosol properties and air pollutants over an urban area, *Atmos. Res.*, 82, 3-4, 643-651, doi:10.1016/j.atmosres.2006.02.020, 2006.

Murray, N. D., Orville, R. E., and Huffines, G. R.: Effect of pollution from Central American fires on cloud-to-ground lightning in May 1998, *Geophys. Res. Lett.*, 27, 2249-2252, doi:10.1029/2000GL011656, 2000.

Nakićenović, N. and Swart, R.: Special Report on Emission Scenarios. A Special Report of the Working Group III of Intergovernmental Panel on Climate Change, in: A Special Report of the Working Group III of Intergovernmental Panel on Climate Change, Cambridge University Press, Cambridge, UK and New York, NY USA, 569, 2000.

Nepstad, D., Veríssimo, A., Alencar, A., Nobres, C., Lima, E., Lefebvre, P., Schlesinger, P., Potter, C., Moutinho, P., Mendoza, E., Cochrane, M., and Brooks, V.: Large-scale impoverishment of

Amazonian forests by logging and fire, *Nature*, 398, 505-508, 1999.

Norris, J. R. and Wild, M.: Trends in aerosol radiative effects over Europe inferred from observed cloud cover, solar "dimming," and solar "brightening", *J. Geophys. Res.*, 112, D08214, doi:10.1029/2006JD007794, 2007.

Ohmura, A.: Observed long-term variations of solar irradiance at the Earth's surface, *Space Sci. Rev.*, 125, 1-4, 111-128, doi:10.1007/s11214-006-9050-9, 2006.

O'Neill, N. T., Dubovik, O., and Eck, T. F.: Modified Angstrom coefficient for the characterization of submicron aerosols, *Appl. Opt.*, 40, 15, 2368-2375, doi:10.1364/AO.40.002368, 2001a.

O'Neill, N. T., Eck, T. F., Holben, B. N., Smirnov, A., and Dubovick, O.: Bimodal size distribution influences on the variation of Angstrom derivatives in spectral and optical depth space, *J. Geophys. Res.*, 106, D9, 9787-9806, doi:10.1029/2000JD900245, 2001b.

O'Neill, N. T., Eck, T. F., Smirnov, A., Holben, B. N., and Thulasiraman, S.: Spectral discrimination of coarse and fine mode optical depth, *J. Geophys. Res.*, 108, D17, 4559, doi:10.1029/2002JD002975, 2003.

O'Neill, N. T., Thulasiraman, S., Eck, T. F., and Reid, J.S.: Robust optical features of fine mode size distributions: Application to the Quebec smoke event of 2002, *J. Geophys. Res.*, 110, D11207, doi:10.1029/2004JD005157, 2005.

Ortore, E. and Francione, V.: On the aerosols monitoring by satellite observations, *Clean Technol. Environ. Policy*, 10, 137-145, doi:10.1007/s10098-007-0134-3, 2008.

Oxford Economics: The Economic Impacts of Air Travel Restrictions Due to Volcanic Ash, 1-12, 2011.

Pace, G., di Sarra, A., Meloni, D., Piacentino, S., and Chamard, P.: Aerosol optical properties at Lampedusa (Central Mediterranean). 1. Influence of transport and identification of different aerosol types, *Atmos. Chem. Phys.*, 6, 697-713, doi:10.5194/acp-6-697-2006, 2006.

Papadimas, C. D., Hatzianastassiou, N., Mihalopoulos, N. , Querol, X., and Vardavas, I.: Spatial and temporal variability in aerosol properties over the Mediterranean basin based on 6-year (2000-2006) MODIS data, *J. Geophys. Res.*, 113, D11205, doi:10.1029/2007JD009189, 2008.

Parker, D. E., Wilson, H., Jones, P. D., Christy, J. R., and Folland, C. K.: The Impact of Mount Pinatubo on World-Wide Temperatures, International Journal of Climatology, 16, 5, 487-497, doi: 10.1002/(SICI)1097-0088(199605)16:5<487::AID-JOC39>3.0.CO;2-J, 1996.

Patt, F.: SeaWiFS Status, MODIS Science Meetings, February 5, 2010.

Penner, J.E., Andreae, M., Annegarn, H., Barrie, L., Feichter, J., Hegg, D., Jayaraman, A., Leaitch, R., Murphy, D., Nganga, J., Pitari, G., Ackerman, A., Adams, P., Austin, P., Boers, R., Boucher, O., Chin, M., Chuang, C., Collins, B., Cooke, W., DeMott, P., Feng, Y., Fischer, H., Fung, I., Ghan, S., Ginoux, P., Gong, S. -L., Guenther, A., Herzog, M., Higurashi, A., Kaufman, Y., Kettle, A., Kiehl, J., Koch, D., Lammel, G., Land, C., Lohmann, U., Madronich, S., Mancini, E., Mishchenko, M., Nakajima, T., Quinn, P., Rasch, P., Roberts, D. L., Savoie, D., Schwartz, S., Seinfeld, J., Soden, B., Tanré, D., Taylor, K., Tegen, I., Tie, X., Vali, G., Van Dingenen, R., van Weele, M., and Zhang, Y.: Aerosols, their direct and indirect effects, *Cambridge University Press*, Cambridge, United Kingdom and New York, NY, USA, 289-348, 2001.

Pereira, G., Freitas, S. R., Moraes, E. C., Ferreira, N. J., Shimabukuro, Y. E., Rao, V. B., and Longo, K. M.: Estimating trace gas and aerosol emissions over South America: Relationship between fire radiative energy released and aerosol optical depth observations, *Atmos. Environ.*, 43, 6388-6397, doi:10.1016/j.atmosenv.2009.09.013, 2009.

Pereira, S. N., Wagner, F., and Silva, A. M.: Seven years of measurements of aerosol scattering properties, near the surface, in the southwestern Iberia Peninsula, *Atmos. Chem. Phys.*, 11, 17-29, doi:10.5194/acp-11-17-2011, 2011.

Perry, K. D., Cahill, T. A., Schnell, R. C., and Harris, J. M.: Long-range transport of anthropogenic aerosols to the National Oceanic and Atmospheric Administration baseline station at Mauna Loa Observatory, Hawaii, *J. Geophys. Res.*, 104, D15, 18521-18533, doi:10.1029/1998JD100083, 1999.

Philip, S. and van Oldenborgh, G. J.: Shifts in ENSO coupling processes under global warming, *Geophys. Res. Lett.*, 33, L11704, doi:10.1029/2006GL026196, 2006.

Piketh, S. J. and Walton, N. M.: Characteristics of Atmospheric Transport of Air Pollution for Africa, *The*

Handbook of Environmental Chemistry, 4, 173-195, doi:10.1007/b94527, 2004.

Pincus, R., and Baker, M. B.: Effect of precipitation on the albedo susceptibility of clouds in the marine boundary layer, *Nature*, 372, 250-252, doi:10.1038/372250a0, 1994.

Prospero, J. M., and Lamb, J. P.: African droughts and dust transport to the Caribbean: climate change and implications, *Science*, 302, 5647, 1024-1027, doi:10.1126/science.1089915, 2003.

Qin, Y., and Mitchell, R. M.: Characterisation of episodic aerosol types over the Australian continent, *Atmos. Chem. Phys.*, 9, 1943-1956, doi:10.5194/acp-9-1943-2009, 2009.

Quinn, P. K., Coffman, D. J., Kapustin, V. N., Bates, T. S., and Covert, D. S.: Aerosol optical properties in the marine boundary layer during the First Aerosol Characterization Experiment (ACE1) and the underlying chemical and physical aerosol properties, *J. Geophys. Res.*, 103(D13), 16547-16563, doi:10.1029/97JD02345, 1998.

Ramanathan, V., Crutzen, P. J., Kiehl, J. T., and Rosenfeld, D.: Atmosphere: aerosols, climate, and the hydrological cycle, Science, 294, 2119-2124, doi: 10.1126/science.1064034, 2001.

Ramanathan, V., Li, F., Ramana, M. V., Praveen, P. S., Kim, D., Corrigan,, C. E., Nguyen, H., Stone, E. A., Schauer, J. J., Carmichael, G. R., Adhikary, B., and Yoon, S. C.: Atmospheric brown clouds: Hemispherical and regional variations in long-range transport, absorption, and radiative forcing, *J. Geophys. Res.*, 112, D22S21, doi:10.1029/2006JD008124, 2007a.

Ramanathan, V., Ramana, M. V., Roberts, G., Kim, D., Corrigan, C., Chung, C., and Winker, D.: Warming trends in Asia amplified by brown cloud solar absorption, *Nature Letters*, 448, 575-578, doi:10.1038/nature06019, 2007b.

Rasmusson, E. M. and Carpenter, T. H.: Variations in Tropical Sea Surface Temperature and Surface Wind Fields Associated with the Southern Oscillation/El Niño, *Mon. Wea. Rev.,* 110, 354-384, doi:10.1175/1520-0493(1982)110<0354:VITSST>2.0.CO;2, 1982.

Reeves, C. E., Formenti, P., Afif, C., Ancellet, G., Attié, J.-L., Bechara, J., Borbon, A., Cairo, F., Coe, H., Crumeyrolle, S., Fierli, F., Flamant, C., Gomes, L., Hamburger, T., Jambert, C., Law, K. S., Mari, C., Jones, R. L., Matsuki, A., Mead, M. I., Methven, J., Mills, G. P., Minikin, A., Murphy, J. G., Nielsen, J. K., Oram, D. E., Parker, D. J., Richter, A., Schlager, H., Schwarzenboeck, A., and Thouret, V.: Chemical and aerosol characterisation of the troposphere over West Africa during the monsoon period as part of AMMA, *Atmos. Chem. Phys.*, 10, 7575-7601, doi:10.5194/acp-10-7575-2010, 2010.

Reid, J. S., Eck, T. F., Christopher, S. A., Hobbs, P. V., and Holben, B. N.: Use of the Ångstrom exponent to estimate the variability of optical and physical properties of aging smoke particles in Brazil, *J. Geophys. Res.*, 104, D22, 27473-27489, doi:10.1029/1999JD900833, 1999.

Remer, L. A., Gasso, S., Hegg, D. A., Kaufman, Y. J., and Holben, B. N.: Urban/industrial aerosol: Ground-based sun/sky radiometer and airborne in situ measurements, *J. Geophys. Res.*, 102, D14, 16849-16859, doi:10.1029/96JD01932, 1997.

Remer, L. A., Kaufman, Y. J., Tanré, D., Mattoo, S., Chu, D. A., Martins, J. V., Li, R.-R., Ichoku, C., Levy, R. C., Kleidman, R. G., Eck, T. F., Vermote, E., and Holben, B. N.: The MODIS Aerosol Algorithm, Products, and Validation, *J. Atmos. Sci.*, 62, 947-973, doi:10.1175/JAS3385.1, 2005.

Remer, L. A., Kaufman, Y. J., and Kleidman, R.G.: Comparison of Three Years of Terra and Aqua MODIS Aerosol Optical Thickness Over the Global Oceans, *IEEE Geosci. Remote Sensing Letters*, 3 (4), 537-540, doi:10.1109/LGRS.2006.879562, 2006.

Remer, L. A., Kleidman, R. G., Levy, R. C., Kaufman, Y. J., Tanré, D., Mattoo, S., Martins, J. V., Ichoku, C., Koren, I., Yu, H., and Holben, B. N.: Global aerosol climatology from the MODIS satellite sensors, *J. Geophys. Res.*, 113, D14S07, doi:10.1029/2007JD009661, 2008.

Richter, A., Burrows, J. P., Nüß, H., Granier, C., and Niemeier, U.: Increase in tropospheric nitrogen dioxide over China observed from space, *Nature*, 437(7055), 129-132, doi:10.1038/nature04092, 2005.

Robinson, W. D., Franz, B. A., Patt, F. S., Bailey, S. W., and Werdell, P. J.: Masks and flags updates, NASA Goddard Space Flight Center, Greenbelt, Maryland, edited by: Hooker, S. B. and Firestone, E. R., SeaWiFS Postlaunch Technical Report Series Vol. 22, NASA Tech. Memo. 2003-206892, 2003.

Rossow,W. B. and Schiffer, R. A.: Advances in understanding clouds from ISCCP, B. *Am. Meteorol. Soc.*, 80(11), 2261-2287, doi:10.1175/1520-0477(1999)080<2261:AIUCFI>2.0.CO;2, 1999.

Rotstayn, L. D., and Lohmann, U.: Tropical Rainfall Trends and the Indirect Aerosol Effect, *Journal of Climate*, 15, 2103-2116, doi: 0.1175/1520-0442(2002)015<2103:TRTATI>2.0.CO;2, 2002.

Sabbah, I. and Hasan, F. M.: Remote sensing of aerosols over the Solar Village, Saudi Arabia, *Atmos. Res.*, 90, 2-4, 170-179, doi:10.1016/j.atmosres.2008.02.004, 2008.

Sabbah, I., Ichoku, C., Kaufman, Y. J., and Remer, L.: Full year cycle of desert dust spectral optical thickness and precipitable water vapor over Alexandria Egypt, *J. Geophys. Res.*, 106 (D16), 18305-18316, doi:10.1029/2000JD900410, 2001.

Sabbah, I., Saeed, T., Al Jassar, H.K., and Rao, K.S.: Remote sensing of desert dust in Kuwait, *J. of Sci. Eng.*, 33, 1, 101-117, 2006.

Sadrinasab, M. and Kämpf, J.: Three-dimensional flushing times of the Persian Gulf, *Geophys. Res. Lett.*, 31, L24301, doi:10.1029/2004GL020425, 2004.

Sano, I., Mukai, S., Okada, Y., Holben, B.N., Ohta, S., and Takamura, T.: Optical properties of aerosols during APEX and ACE-Asia experiments, *J. Geophys. Res.*, 108, 8649, doi:10.1029/2002JD003263, 2003.

Schmeissner, T., Krejci, R., Ström, J., Birmili1, W., Wiedensohler, A., Hochschild, G., Gross, J., Hoffmann, P., and Calderon, S.: Analysis of number size distributions of tropical free tropospheric aerosol particles observed at Pico Espejo (4765m a.s.l.), Venezuela, *Atmos. Chem. Phys.*, 11, 3319-3332, doi:10.5194/acp-11-3319-2011, 2011.

Schuster, G. L., Dubovick, O., and Holben, B. N.: Angstrom exponent and bimodal aerosol size distributions, *J. Geophys. Res.*, 111, D07207, doi:10.1029/2005/JD006328, 2006.

Shinozuka, Y., Redemann, J., Livingston, J. M., Russell, P. B., Clarke, A. D., Howell, S. G., Freitag, S., O'Neill, N. T., Reid, E. A., Johnson, R., Ramachandran, S., McNaughton, C. S., Kapustin, V. N., Brekhovskikh, V., Holben, B. N., and McArthur, L. J. B.: Airborne observation of aerosol optical depth during ARCTAS: vertical profiles, inter-comparison and fine-mode fraction, *Atmos. Chem. Phys.*, 11, 3673-3688, doi:10.5194/acp-11-3673-2011, 2011.

Sinyuk, A., Dubovik, O., Holben, B. N., Eck, T. F., Breon, F. -M., Martonchik, J., Kahn, R., Diner, D. J., Vermote, E. F., Roger, J. -C., Lapyonok, T., and Slutsker, I.: Simultaneous retrieval of aerosol and surface properties from a combination of AERONET and satellite data, *Remote Sens. of Environ.*, 107, 1-2, 90-108, doi:10.1016/j.rse.2006.07.022, 2007.

Smirnov, A., Holben, B. N., Eck, T. F., Dubovik, O., and Slutsker, I.: Cloud screening and quality control algorithms for the AERONET data base, *Rem. Sens. Env.*, 73, 3, 337-349, doi:10.1016/S0034-4257(00)00109-7, 2000.

Smirnov, A., Holben, B. N., Dubovik, O., Neil, N., and Eck, T. F.: Atmospheric aerosol optical properties in the Persian Gulf, *Atmos. Sci.*, 59, 3, 620-634, doi:10.1175/1520-0469(2002)059<0620:AAOPIT>2.0.CO;2, 2002.

Smith, S. J., Pitcher, H., and Wigley, T. M. L.: Global and regional anthropogenic sulfur dioxide emissions, *Global Planet. Change*, 29, 1-2, 99-119, doi:10.1016/S0921-8181(00)00057-6, 2001.

Smith, S. J., Andres, R., Conception, E., and Lurz, J.: Historical sulfur dioxide emissions 1850-2000: Methods and results, PNNL Res. Rep. 14537, Pac. Northwest Natl. Lab., Richland, Wash, 2003.

Stanhill, G.: A perspective on global warming, dimming, and brightening, *EOS Trans. Amer. Geophys. Union*, 88, 5, 58, doi:10.1029/2007EO050007, 2007.

Stefansky, W.: Rejecting Outliers in Factorial Designs, *Technometrics*, 14, 469-479, 1972.

Stowe, L. L., Davis, P. A., and McClain, E. P.: Scientific basis and initial evaluation of the CLAVR-1 global clear/cloud classification algorithm for the Advanced Very High Resolution Radiometer, *J. Atmos. Ocean. Tech.*, 16(6), 656-681, doi:10.1175/1520-0426(1999)016<0656:SBAIEO>2.0.CO;2, 1999.

Streets, D. G., Tsai, N. Y., Akimoto, H., and Oka, K.: Sulfur dioxide emissions in Asia in the period 1985-1997, *Atmos. Environ.*, 34, 26, 4413-4424, doi:10.1016/S1352-2310(00)00187-4, 2000.

Streets, D. G., Bond, T. C., Carmichael, G. R., Fernandes, S. D., Fu, Q., He, D., Klimont, Z., Nelson, S. M., Tsai, N. Y., Wang, M. Q., Woo, J. -H., and Yarber, K. F.: An inventory of gaseous and primary aerosol emissions in Asia in the year 2000, *J. Geophys. Res.*, 108, D21, 8809, doi:10.1029/2002JD003093, 2003.

Streets, D. G., Wu, Y., and Chin, M.: Two-decadal aerosol trends as a likely explanation of the global

dimming/brightening transition, Geophys. Res. Lett., 33, L15806, doi:10.1029/2006GL026471, 2006.

Streets, D. G., Yan, F., Chin, M., Diehl, T., Mahowald, N., Schultz, M., Wild, M., Wu, Y., and Yu, C.: Anthropogenic and natural contributions to regional trends in aerosol optical depth, 1980-2006, *J. Geophys. Res.*, 114, D00D18, doi:10.1029/2008JD011624, 2009.

Swap, R., Garstang, M., Macko, S. A., Tyson, P. D., Maenhaut, W., Artaxo, P., Kållberg, P. and Talbot, R.: The long-range transport of southern African aerosols to the tropical South Atlantic, *J. Geophys. Res.*, 101, D19, 23777-23791, doi:10.1029/95JD01049, 1996.

Tafuro, A.M., Barnaba, F., De Tomasi, F., Perrone, M.R., and Gobbi, G.P.: Saharan dust particle properties over the central Mediterranean, *Atmos. Res.*, 81, 1, 67-93, doi:10.1016/j.atmosres.2005.11.008, 2006.

Tafuro, A. M., De Tomasi, F., and Perrone, M. R.: Remote Sensing of Aerosols by Sunphotometers and Lidar Techniques, Chapter 14, in: Advanced Environmental Monitoring, edited by: Kim, Y. J., Platt, U., ISBN 978-1-4020-6363-3, XXII, Springer, 179-189, 2008.

Tanré, D., Bréon, F. M., Deuzé, J. L., Herman, M., Goloub, P., Nadal, F., and Marchand, A.: Global observation of anthropogenic aerosols from satellite, *Geophys. Res. Lett.*, 28, 24, 4555-4558, doi:10.1029/2001GL013036, 2001.

Taylor, D.: Biomass burning, humans and climate change in Southeast Asia, *Biodivers. Conserv.*, 19, 1025-1042, doi:10.1007/s10531-009-9756-62010, 2010.

The Economist: India's economy, India's surprising economic miracle, available at: http://www.economist.com/node/17147648?story_id=17147648&fsrc=rss, 2010.

The World Factbook: India, *Central Intelligence Agency*, available at: https://www.cia.gov/library/publications/the-world-factbook/geos/in.html, 2012.

Thomas, G. E., Carboni, E., Sayer, A. M., Poulsen, C. A., Siddans, R., and Grainger, R. G.: Oxford-RAL Aerosol and Cloud (ORAC): Aerosol retrievals from satellite radiometers, in: Aerosol remote sensing over land, edited by: Kokhanovsky, A. A. and de Leeuw, G., Springer, Berlin, 2009.

Thomas, G. E., Poulsen, C. A., Siddans, R., Sayer, A. M., Carboni, E., Marsh, S. H., Dean, S. M., Grainger, R. G., and Lawrence, B. N.: Validation of the GRAPE single view aerosol retrieval for ATSR-2 and insights into the long term global AOD trend over the ocean, *Atmos. Chem. Phys.*, 10, 4849-4866, doi:10.5194/acp-10-4849-2010, 2010.

Tiao, G. C., Reinsel, G. C., Xu, D., Pedrick, J. H., Zhu, X., Miller, A. J., DeLuisi, J. J., Mateer, C. L., and Wuebbles, D. J.: Effects of autocorrelation and temporal sampling schemes on estimates of trend and spatial correlation, *J. Geophys. Res.*, 95, 20507-20517, doi:10.1029/JD095iD12p20507, 1990.

Torres, O., Bhartia, P. K., Herman, J. R., Ahmad, Z., and Gleason, J.: Derivation of aerosol properties from satellite measurements of backscattered ultraviolet radiation: Theoretical basis, *J. Geophys. Res.*, 103(D14), 17099-17110, doi:10.1029/98JD00900, 1998.

Torres, O., Bhartia, P. K., Herman, J. R., Sinyuk, A., and Holben, B.: A long term record of aerosol optical thickness from TOMS observations and comparison to AERONET measurements, *J. Atmos. Sci.*, 59, 398-413, doi:10.1175/1520-0469(2002)059<0398:ALTROA>2.0.CO;2, 2002.

Torres, O., Chen, Z., Jethva, H., Ahn, C., Freitas, S. R., and Bhartia, P. K.: OMI and MODIS observations of the anomalous 2008-2009 Southern Hemisphere biomass burning seasons, *Atmos. Chem. Phys.*, 10, 3505-3513, doi:10.5194/acp-10-3505-2010, 2010.

Trenberth, K. E. and Hoar, T. J.: The 1990-1995 El Niño-Southern Oscillation event: Longest on record, *Geophys. Res. Lett.*, 23(1), 57-60, doi:10.1029/95GL03602, 1996.

Twomey, S.A.: The influence of pollution on the shortwave albedo of clouds, *J. Atmos. Sci.*, 34, 7, 1149-1152, doi:10.1175/1520-0469(1977)034<1149:TIOPOT>2.0.CO;2, 1977.

Tyson, P. D.: Climatic Change and Variability in Southern Africa, Oxford Univ. Press, 220, 1986.

Vadrevu, K. P., Ellicott, E., Badarinath, K. V. S., and Vermote, E.: MODIS derived fire characteristics and aerosol optical depth variations during the agricultural residue burning season, north India, *Environ. Pollut.*, 159(6), 1560-1569, doi:10.1016/j.envpol.2011.03.001, 2011.

Vakkari, V., Laakso, H., Kulmala, M., Laaksonen, A., Mabaso, D., Molefe, M., Kgabi, N., and Laakso, L.: New particle formation events in semi-clean South African savannah, *Atmos. Chem. Phys.*, 11, 3333-3346, doi:10.5194/acp-11-3333-2011, 2011.

van der Werf, G. R., Randerson, J. T., Giglio, L., Collatz, G. J., Kasibhatla, P. S., and Arellano Jr., A. F.: Interannual variability in global biomass burning emissions from 1997 to 2004, *Atmos. Chem. Phys.*, 6, 3423-3441, doi:10.5194/acp-6-3423-2006, 2006.

Veefkind, J. P., de Leeuw, G., and Durkee, P. A.: Retrieval of aerosol optical depth over land using two-angle view satellite radiometry during TARFOX, *Geophys. Res. Lett.*, 25, 3135-3138, doi:10.1029/98GL02264, 1998.

Venzac, H., Sellegri, K., Villani, P., Picard, D., and Laj, P.: Seasonal variation of aerosol size distributions in the free troposphere and residual layer at the puy de Dme station, France, *Atmos. Chem. Phys.*, 9, 1465-1478, doi:10.5194/acp-9-1465-2009, 2009.

von Hoyningen-Huene, W., Freitag, M., and Burrows, J. P.: Retrieval of aerosol optical thickness over land surfaces from top-of-atmosphere radiance, *J. Geophys. Res.*, 108, D94260, doi:10.1029/2001JD002018, 2003.

von Hoyningen-Huene, W., Kokhanovsky, A. A., Burrows, J. P., Bruniquel-Pinel, V., Regner, P., and Baret, F.: Simultaneous Determination of Aerosol- and Surface Characteristics from Top-of-Atmosphere Reflectance using MERIS on board of ENVISAT, *J. Adv. Space Res.*, 37, 2172-2177, doi:10.1016/j.asr.2006.03.017, 2006.

von Hoyningen-Huene, W., Yoon, J., Vountas, M., Istomina, L. G., Rohen, G., Dinter, T., Kokhanovsky, A. A., and Burrows, J. P.: Retrieval of spectral aerosol optical thickness over land using ocean color sensors MERIS and SeaWiFS, *Atmos. Meas. Tech.*, 4, 151-171, doi:10.5194/amt-4-151-2011, 2011.

Wang, J., van den Heever, S. C., and Reid, J. S.: A conceptual model for the link between Central American biomass burning aerosols and severe weather over the south central United States, *Environ. Res. Lett.*, 4(015003), doi:10.1088/1748-9326/4/1/015003, 2009.

Wang, Z., Akimoto, H., and Uno, I.: Neutralization of soil aerosol and its impact on the distribution of acid rain over east Asia: Observations and model results, *J. Geophys. Res.*, 107, D19, 4389, doi:10.1029/2001JD001040, 2002.

Wang, M. and Shi, W.: Estimation of ocean contribution at the MODIS near-infrared wave lengths along the east coast of the U.S.: Two case studies, *Geophys. Res. Lett.*, 32, L13606, doi:13610.11029/12005GL022917, 2005.

Ward, P. L.: Sulfur Dioxide Initiates Global Climate Change in Four Ways, Thin Solid Films, 517, 11, 3188-3203, doi:10.1016/j.tsf.2009.01.005, 2009.

Washington, R., and Todd, M. C.: Atmospheric controls on mineral dust emission from the Bodélé depression, chad: the role of the low level jet, *Geophys. Res. Lett.*, 32, L17701, doi:10.1029/2005GL023597, 2005.

Weatherhead, E. C., Reinsel, G. C., Tiao, G. C., Meng, X.-L., Choi, D., Cheang, W.-K., Keller, T., DeLuisi, J., Wuebbles, D. J., Kerr, J. B., Miller, A. J., Oltmans, S. J., and Frederick, J. E.: Factors affecting the detection of trends: Statistical considerations and applications to environmental data, *J. Geophys. Res.*, 103, 17149-17161, doi:10.1029/98JD00995, 1998.

Westerling, A. L., Hidalgo, H. G., Cayan, D. R., Swetnam, T. W.: Warming and Earlier Spring Increase Western U.S. Forest Wildfire Activity, *Science*, 313(940), doi:10.1126/science.1128834, 2006.

Whitehead, J. D., Gallagher, M. W., Dorsey, J. R., Robinson, N., Gabey, A. M., Coe, H., McFiggans, G., Flynn, M. J., Ryder, J., Nemitz, E., and Davies, F.: Aerosol fluxes and dynamics within and above a tropical rainforest in South-East Asia, *Atmos. Chem. Phys.*, 10, 9369-9382, doi:10.5194/acp-10-9369-2010, 2010.

WHO - World Health Organization: Air quality guidelines for Europe, No. 23, 1987.

WHO - World Health Organization: Air quality guidelines for Europe, No. 91, 2000.

WHO - World Health Organization: Air quality guidelines for Europe, 18-20, 2005.

Wilcox, R. R.: BASIC STATISTICS Understanding Conventional Methods and Modern Insights, *Oxford University Press, Inc.*, ISBN 978-0-19-531510-3, 2009.

Wild, M., Gilgen, H., Roesch, A., Ohmura, A., Long, C. N., Dutton, E. G., Forgan, B., Kallis, A., Russak, V., Tsvetkov, A.: From dimming to brightening: Decadal changes in solar radiation at Earth's surface, *Science*, 308, doi:10.1126/science.1103215, 847 - 850, 2005.

Wild, M., Ohmura, A., and Makowski, K.: Impact of global dimming and brightening on global warming, *Geophys. Res. Lett.*, 34, L04702, doi:10.1029/2006GL028031, 2007.

Xiao, R., Takegawa, N., Zheng, M., Kondo, Y., Miyazaki, Y., Miyakawa, T., Hu, M., Shao M., Zeng, L., Gong, Y., Lu, K., Deng, Z., Zhao, Y., and Zhang, Y. H.: Characterization and source apportionment of submicron aerosol with aerosol mass spectrometer during the PRIDE-PRD 2006 campaign, *Atmos. Chem. Phys.*, 11, 6911-6929, doi:10.5194/acp-11-6911-2011, 2011.

Xie, J. and Xia, X.: Long-term trend in aerosol optical depth from 1980 to 2001 in north China, *Particuology*, 6, 2, 106-111, doi:10.1016/j.partic.2007.11.002 , 2008.

Yoon, J. -M., Kim, J., Lee, J. H., Cho, H. K., Shon, B. J., and Ahn, M. H.: Retrieval of Aerosol Optical Depth over East Asia from a Geostationary Satellite, MTSAT-1R, *Journal of the Korean Meteorological Society*, 43, 133-142, 2007.

Yoon, J. , von Hoyningen-Huene, W., Vountas, M., and Burrows, J. P.: Analysis of linear long-term trend of Aerosol Optical Thickness derived from SeaWiFS using BAER over Europe and South China, *Atmos. Chem. Phys.*, 11, 12149-12167, doi:10.5194/acp-11-12149-2011, 2011.

Yoon, J., von Hoyningen-Huene, W., Kokhanovsky, A. A., Vountas, M., and Burrows, J. P.: Trend analysis of the Aerosol Optical Thickness and Ångström Exponent derived from the global AERONET spectral observations, *Atmos. Meas. Tech.*., 5, 1271-1299, doi:10.5194/amt-5-1271-2012, 2012.

Yoon, J., Vountas, M., von Hoyningen-Huene, W., Chang, D. Y., and Burrows, J. P.: Trend analysis of global AOT derived from polar orbiting satellites: Terra (MODIS and MISR), OrbView-2 (SeaWiFS), and Aqua (MODIS), *Geophys. Res. Lett.*, in preparation, 2012.

Yu, H., Chin, M., Remer, L. A., Kleidman, R. G., Bellouin, N., Bian, H., and Diehl, T.: Variability of marine aerosol fine-mode fraction and estimates of anthropogenic aerosol component over cloud-free oceans from the Moderate Resolution Imaging Spectroradiometer (MODIS), *J. Geophys. Res.*, 114, D10206, doi:10.1029/2008JD010648, 2009.

Zhang, J. and Reid, J. S.: A decadal regional and global trend analysis of the aerosol optical depth using a data-assimilation grade over-water MODIS and Level 2 MISR aerosol products, *Atmos. Chem. Phys.*, 10, 10949-10963, doi:10.5194/acp-10-10949-2010, 2010.

Zhang, X. Y., Gong, S. L., Zhao, T. L., Arimoto, R., Wang, T. Q., and Zhou, Z. J.: Sources of Asian dust and role of climate change versus desertification in Asian dust emission, *Geophys. Res. Lett.*, 30, 2272, doi:10.1029/2003GL018206, 2003.

Zhang, Y. H., Hu, M., Zhong, L. J., Wiedensohler, A., Liu, S. C., Andreae, M. O., Wang, W., and Fan, S. J.: Regional integrated experiments on air quality over Pearl River Delta 2004 (PRIDEPRD2004): Overview, *Atmos. Environ.*, 42, 6157-6173, doi:10.1016/j.atmosenv.2008.03.025, 2008.

Zhang, Y., Yu, H., Eck, T. F., Smirnov, A., Chin, M., Remer, L. A., Bian, H., Tan, Q., Levy, R., Holben, B. N., and Piazzolla, S.: Aerosol Daytime Variations over North and South America Derived from Multi-year AERONET Measurements, *J. Geophys. Res.*, 117, D05211, doi:10.1029/2011JD017242, 2012.

Zhao, C., Liu, X., Leung, L. R., and Hagos, S.: Radiative impact of mineral dust on monsoon precipitation variability over West Africa, *Atmos. Chem. Phys.*, 11, 1879-1893, doi:10.5194/acp-11-1879-2011, 2011.

Zhao, T. X.-P., Laszlo, I., Guo, W., Heidinger, A., Cao, C., Jelenak, A., Tarpley, D., and Sullivan, J.: Study of long-term trend in aerosol optical thickness observed from operational AVHRR satellite instrument, *J. Geophys. Res.*, 113, D07201, doi:10.1029/2007JD009061, 2008.

Zhou, Y., Brunner, D., Hueglin, C., Henne, S., and Staehelin, J.: Changes in OMI tropospheric NO_2 columns over Europe from 2004 to 2009 and the influence of meteorological variability, *Atmospheric Environment*, 46, 482-495, Doi:10.1016/j.atmosenv.2011.09.024, 2012.

Zhu, L., Martins, J. V., and Remer, L. A.: Biomass burning aerosol absorption measurements with MODIS using the critical reflectance method, *J. Geophys. Res.*, 116, D07202, doi:10.1029/2010JD015187, 2011.

Zhu, T, Liu, X., Connelly, P. R., and Zhong, J.: An optimized wild bootstrap method for evaluation of measurement uncertainties of DTI-derived parameters in human brain, *NeuroImage*, 40, 1144-1156, doi:10.1016/j.neuroimage.2008.01.016, 2008.

Acknowledgements

It has been three years and more since I came here, and I was very happy because I was not alone during my PhD. There were many friends, colleagues, and advisers whom I would like to thank specifically for their supports. For sure, it would never have been completed without their help and encouragement.

First of all, my most sincere thanks go to **Prof. J. P. Burrows**, whose constructive criticism, kind encouragement, and willing assistance helped bring the dissertation to a successful conclusion.

I sincerely thank **Prof. J. Notholt** and **other committee members** for examining this dissertation.

Dr. W. von Hoyningen-Huene supervised my doctoral work in Bremen. He has overseen the planning of this dissertation and has given my work minute consideration over three years.

In writing my dissertation, I have contracted many debts. I should like to thanks **Dr. M. Vountas** for encouraging me to think about the topic and then offering constant assistance while this dissertation was being written.

I am very grateful to **Dr. A. A. Kokhanovsky**. As ever, I benefited from his vast knowledge and originality of mind.

Many colleagues have offered useful suggestions and invaluable supports for my dissertation and life in a variety of ways, and I would like to give particular thanks to **L. Lelli, Dr. C. Schlundt, Dr. L. Istomina, Dr. H. S. Negi, Y. Chiang, Dr. A. Richter, L. Mei, J. Heymann, Dr. T. Dinter, Dr. A. Sadeghi, F. Azam, V. Nenakhov, C. Gebhardt, F. Ebojie, T. Frost, and M. Jäger.**

I would like to express my deep and sincere gratitude to my former supervisors, **Prof. H. K. Cho and Prof. J. Kim** in Yonsei University (South Korea), who gave me enormous amount of scientific support and encouragement.

I want to take this opportunity to thank a few members of **my family**. They installed in me the belief that intellectual pursuit is the highest calling, and that ideas do have the power to change people's lives. In dedicating this dissertation to my dead grandfather, **Dr. J.-S. Yoon**, I wish to recognize a bond that is unlike any other.

To **everyone in IUP**, I was very happy with you standing by and studying by me.

I am grateful to the CityZen Project, the University of Bremen, and the DFG Project for supporting this work; NASA teams for providing SeaWiFS, MODIS, MISR, and AERONET data; Dr. M. I. Mishchenko for providing the Mie code; Dr. D. G. Kaskaoutis, Dr. O. Dubovik, and Dr. D. G. Street for providing useful comments to improve conclusions in this study.